GEOMETRY AND MECHANICS OF PNEUMATIC TIRES

F. KOUTNÝ

Zlín, CZE • 2007

CONTENTS

PREFACE

This text is based on a compiling work written under the same title in 1996. Thus, it might look a bit old fashioned. But as I am still regularly reading two journals on tires, namely Tire Science and Technology and Tire Technology International, I see that old motives preserve their repeated appearing practically unchanged. That is why I decided to translate the work and update it in view of the present stage of my knowledge.

Fast development of electronics, computers, numerical methods and all the complex structure of contemporary science has produced immense packets of specialized knowledge in every technical branch. The mathematical point of view, very often underestimated in the past, has finally found its place also in many areas traditionally considered for purely empirical ones. Tire production and exploitation is one of them. Today mathematical modeling is taken as a necessary part of inventing and designing every new rubber product and a tool to enhancing the quality and efficiency of production processes, accelerating development cycles, removing expensive tests on prototypes etc.

The following chapters offer a short look at the tire structure and illustrate nonlinearities in behavior of basic tire materials. The role of the compressed air filling is emphasized by evaluating its prevailing contribution to total energy accumulated in tire. Then the problem of loading the tire structure with the internal air pressure is solved under the assumption that the energy accumulated in tire wall is neglected. This assumption enables setting up the so called belt model and solving simple cases of tire loading in analytical form within a very short time, i.e. instantly from the practical point of view. The belt model may serve in many application areas like rolling resistance, tire uniformity etc.

The text may seem to be sometimes too concise. But all the needed mathematics with sufficient details could be found in Courses on this website (www.koutny-math.com). I take it as a shapeable material and may be some supplementary sections could be added in the future.

There are also more comprehensive works at hand today like

Mechanics of Pneumatic Tires edited by S. K. Clark or

The Pneumatic Tires edited by A. N. Gent and J. D. Walter.

It is just and fair to remind also Russian authors (Biderman, Bukhin and many others) who significantly contributed to the theory of pneumatic tires as well.

I would like to apologize for my imperfectness, numerous mistakes, bad formulations and many linguistic trespasses.

F. Koutny

The mathematician is characterized not by computing but by his clear thinking and his ability to omit irrelevant things.

Rósza Péter

1 INTRODUCTION

Various vehicles such as cars and trucks in the first place, tractors, agricultural and forestry machinery etc. as well as aircrafts and jets belong to inevitable technical means of the present time. It is clear that the wheels of high performance vehicles cannot be built somehow by blind trials but modern construction means are needed in their design and development.

Computers and robots are attributes of technological development almost in all branches of human activities in the last decade. Outputs of projecting works are completely automated and transferred to CNC machines. Laser optics and CCD cameras are used in optical control, computer tomography creates spatial view of the internal structure of goods etc. So mathematical methods have found a fertile soil also in many areas where they were completely ignored a few years ago.

Though the pneumatic tire was invented and patented already in 1845 (Thomson) and reinvented in 1888 (Dunlop) [1] the first theoretical works concerning its construction appeared only in 1950ies (Hofferberth) [2]. The theory, however, was too complicated (integration of a function with a singularity) and its practical applications were conditioned by use of computers that were then only in napkins. In decades 1970 and 1980 graphical-numerical methods were used also and to make their application easier special nomographs were published [3-7]. At that time also analog computers were used to obtain the meridian curve of the tire. But with mass applications of digital computers, especially PC's, those methods declined very quickly. Developments of electronics and numerical methods have had a strong influence also in various branches of rubber industry (machinery, automating technology, construction, testing).

Here the basic knowledge concerning the construction and properties of tires will be discussed. It is obvious that the pneumatic tire as a real object must be represented in a very simplified way if the corresponding mathematical models are to be successful in search for answers to properly formulated questions.

Theoretical results of any model need to be compared with the experimental ones whenever possible. As a rule, sooner or later experimental facts are discovered that do not agree with the theoretical predictions. Then the model must be adapted, if possible, or abandoned completely and substituted by a better model. This process is repeated again and again and the spiral-like development is a characteristic feature of general recognition (see Prelude to Probability … on this website).

Experiment is a basic element of natural and technical sciences. Its reproducibility and repeatability assures the objectivity of science. This feature of experimental work is closely connected to applications of statistical methods.

●

But let us turn to the object of pneumatic tire again. Radial tire lettering is a sequence of figures and letters with the following meaning:

Outer width (mm) / aspect ratio + (Speed category) R + Rim diameter (inch) + Tread pattern.

Tire wall consists of three main components (Figure 1.1):

- approximately homogeneous and isotropic outer rubber layers of the sidewall and tread with patterned grooves needed for transmission of forces and moments in the interface tire/road,
- reinforced parts (carcass, belt, beads) of cord/rubber composites carrying main part of stresses produced by the internal air overpressure and external dynamic loads between rim and road,
- homogeneous layer of innerliner rubber material with small diffusion coefficient to preserve the inner overpressure in the tire cavity.

This complicated structure is very uncomfortable to describe mathematically. Moreover, there are very large differences in physical characteristics of individual tire layers, significant dependence of rubber behavior (and also of some cords behavior) on temperature, general nonlinearity in stress/strain relation and hysteresis. Also strains that cannot be considered small and tire geometry, though approximated by an axisymmetric body as usual, do not belong to simplifying facts.

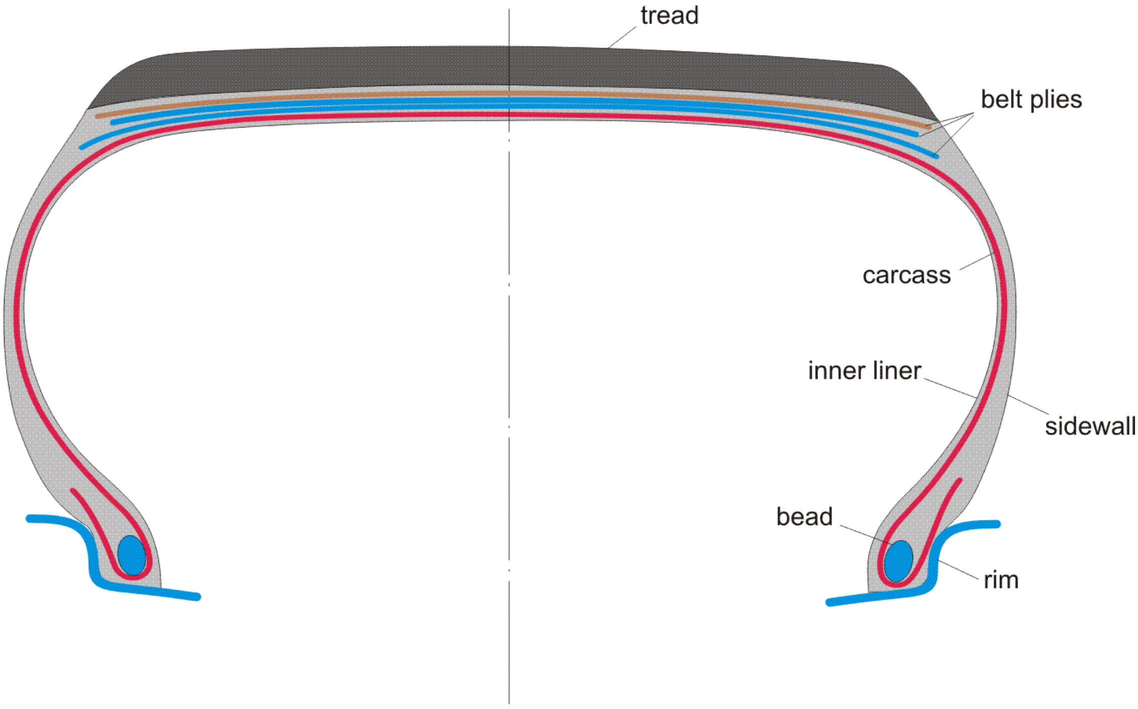

Figure 1.1 – A schematic picture of the cross-section of a radial tire.

The equilibrium shape theory, strength and tire building calculations take into account the load/deflection curves of corresponding reinforcing cords, wires etc. Rubber is considered just as a sealing and completely deformable material. But in calculations of tire reactions to the external loads the deflection of tread must be considered too. Therefore, also basic stress-strain behavior of rubber needs to be somehow described.

Traffic safety requires that the tire as a pressure vessel retains its integrity during its whole service life. But its components are exposed to cyclic loadings so their strength drops necessarily. Study of the fatigue behavior of individual tire components in exploitation is expensive, because strengths measurement means total destruction of the tire. E.g. acquiring the bead strength drop after traveling a fixed distance would need a burst test of tire with pressurized water. Preserving the material strength above a given level needs to know something on how it depends on stress-strain conditions and what the working conditions of tire are like. A qualified estimate of deflection of the traveling tire is the first step to it. Conditions in regular exploitation, however, are a mixture of deterministic and stochastic components. Therefore, realistic simulation of the cord loading is very difficult in laboratory. The carcass cord in running tire is periodically unloaded and bent during its passing the contact area. So estimates of the upper and lower levels of the cord tension and deflection would be very useful to describe the fatigue regime. This, however, needs a suitable tire model.

Systemizing experimental data can help to reveal some relations (or structures) that in some cases may be explicitly expressed in mathematical form. Mathematical models enable prediction and theoretical results can be confronted with experimental data in the experimentally feasible domains. On the other hand, theoretical results can transcend the possibilities of experiments.

A system of ideas, hypothesis or theory can be considered scientific in the sense of K. Popper only if it includes the possibility of its falsifiability, e.g. by experimental disprovability. As far as the horizon of the investigation is broad enough while the area of knowledge is small several concurrent theories may exist contemporarily. The subjective standpoint may be influenced by the temporary philosophy, ideological fashion, social or political boosts or constrictions etc.

●

The Greek word “pneuma” means the air, which emphasizes etymologically the role of the compressed air in the pneumatic tire. The German “Luftreifen” is the verbatim equivalent of the pneumatic tire.

The behavior of the system (tire wall/air) is controlled by the principle of minimum energy. The today so popular finite element method (FEM) finds this minimum via numerical solution of large systems of equations corresponding to individual elements and their constrictions. Neglecting the tire wall energy, however, simplifies the problem substantially. This can lead to a relatively simple and analytically solvable problem, whose solution can be obtained very fast by numerical methods.

Direct measuring the inflation pressure increase in two car tires during their radial loading in laboratory by mercury manometer [12] provided a justification for such a neglecting. Rhyne's regression formula for radial stiffness [13] transformed for SI units,

$$K_z = 2.68\, p \sqrt{WD} + 33.1$$

(p is the inflation pressure in MPa, W and D are the width and diameter of tire in mm), was verified in several large tire groups and confirms the overwhelming role of the compressed air in the pneumatic tire. It gives the ratio of the radial stiffness (N/mm) of a flat tire (p = 0) and the radial stiffness of the same inflated tire

$$\frac{33.1}{2.68\, p \sqrt{WD} + 33.1}$$

As mentioned above, those ideas create a basis of the belt model of radial tire that enables to predict its external behavior, i.e. load/deflection curves in radial, lateral, circumferential directions quite good. It can also be used to predict average stresses in supporting elements inside the tire structure. Nevertheless, computing local stress peaks or determining stresses and strains maps need finer means (FEA).

In the tread/road interface local strains are influenced by the macroscopic and microscopic bumps and asperities on the road surface. Corresponding stresses may exceed the critical level of material strength. Then microscopic particles are torn out of the surface. This destructive process is manifested as the tread wear. Wear rate depends on tread rubber compound, road surface quality, interface temperature etc.

As said in Preface this text is a commented summary on author's former publications in different journals. Its main goal is to show that relatively simple methods and means can still be useful in such a large application area like the geometry, technology and mechanics of pneumatic tires.

P

2 TIRE MATERIALS

Properties of macromolecular materials for tire production belong in the area of physics of polymers [14]. However, there is a substantial difference in response of real tire compounds and the ideal elastomer considered in the kinetic theory of rubber elasticity.

For example, the ideal material is stiffening with increasing temperature while the real tire rubber compounds become softer. To illustrate the complexity of real tire materials several examples are presented below.

2.1 Rubber

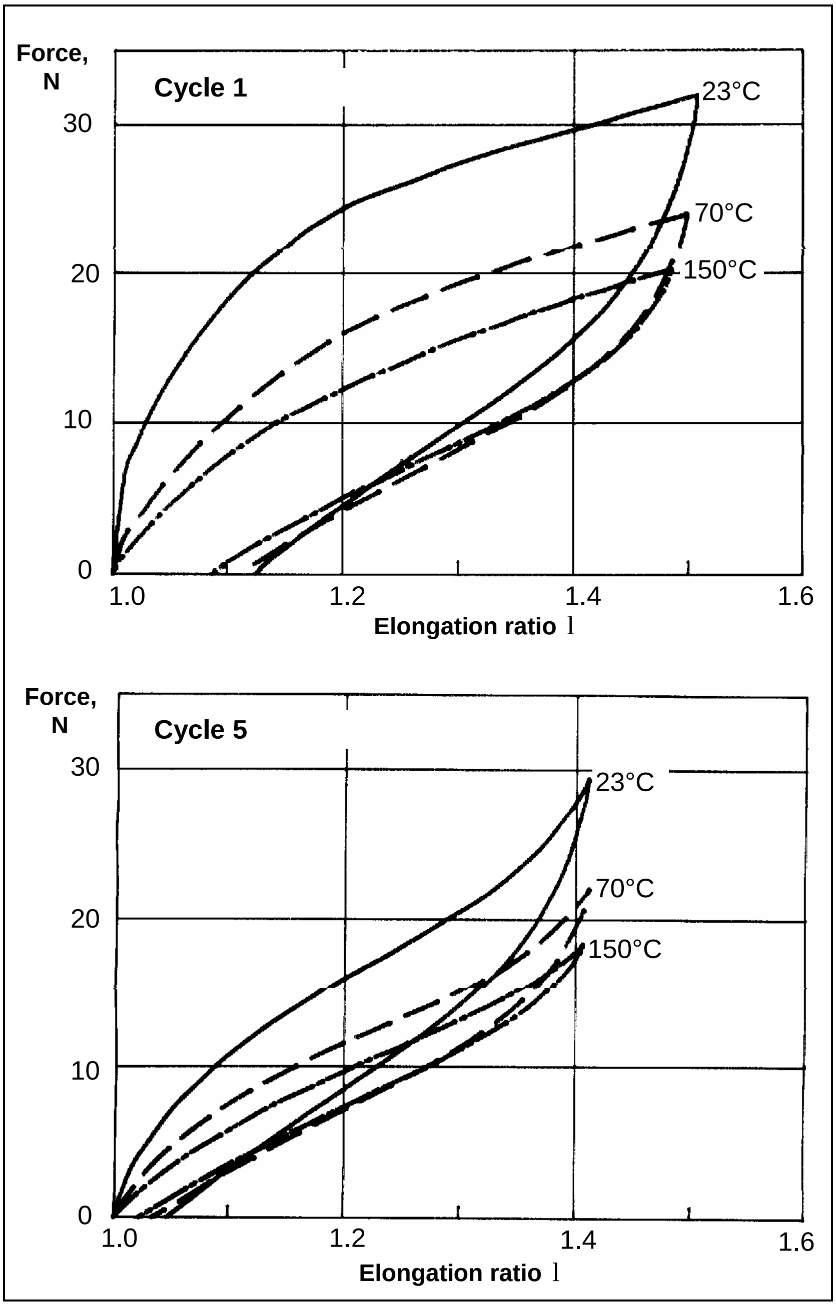

Figure 2.1 – Hysteresis loops of the vulcanization bladder rubber in the first and fifth strain cycle.

Figure 2.1 demonstrates complexity of stress strain behavior in rubber. There are shown hysteretic loops of test pieces prepared of bladder rubber at different temperatures in the first and the fifth strain cycles. It is surely difficult to clarify what could be meant under the Young modulus in such a case and why.

The information value of the Young modulus is low for the majority of the people who develop rubber compounds. On the other hand the evaluation criterions used by those people cannot be used in the regular physical description of rubber.

To compute tangential forces in radial tire the shear modulus of tread compound is needed. This, however, is not measured as a rule. To determine the shear stiffness of rubber, the device shown in Figure 2.2 was made. It enabled to record the tensile force $F(x)$ at displacement x of jaws by INSTRON TTCM machine [15]. Though the torque $F(x).R$ represents an average of shear stresses the linear elasticity gives proportionality between the shear modulus G and the ratio $F(x)/x$. However, tensile force $F(x)$ showed nonlinearity, which implies variability of G with x and the shear angle (Figure 2.3).

Both the dynamic (oscillation) and static torsion tests with standard shear test pieces were carried out.

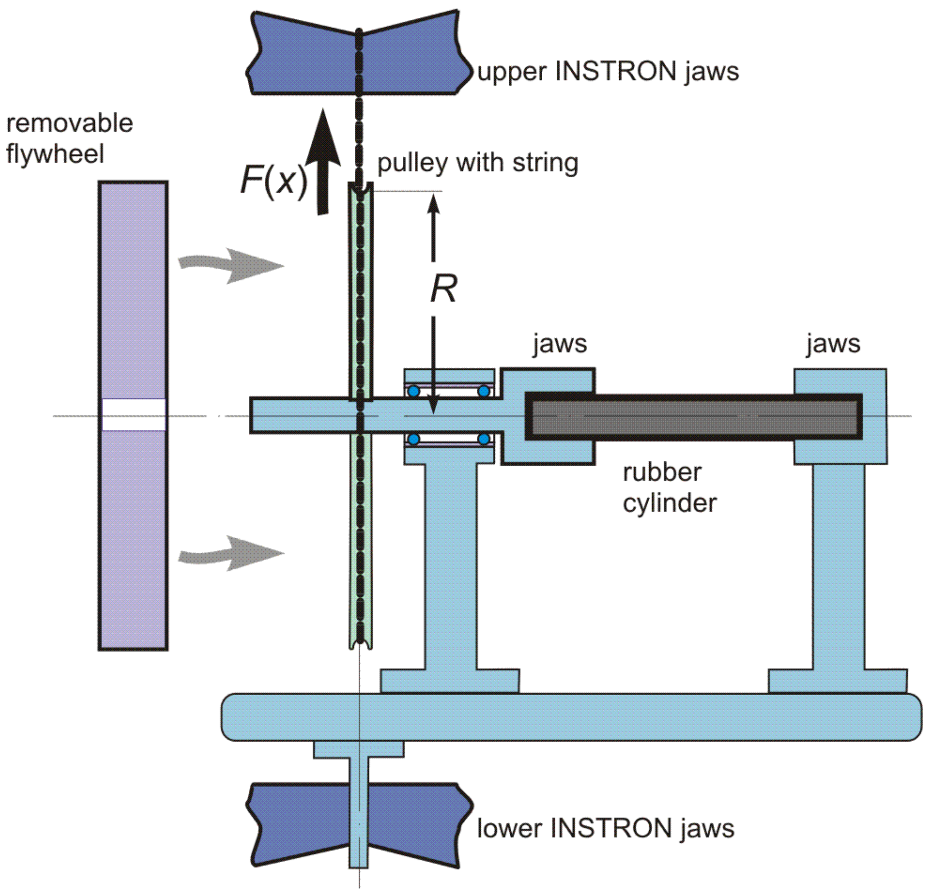

Figure 2.2 – A device for rubber torsion testing either statically on INSTRON TTCM (the distance between horizontal axis and vertical tension axis is the pulley radius) or dynamically by flywheel.

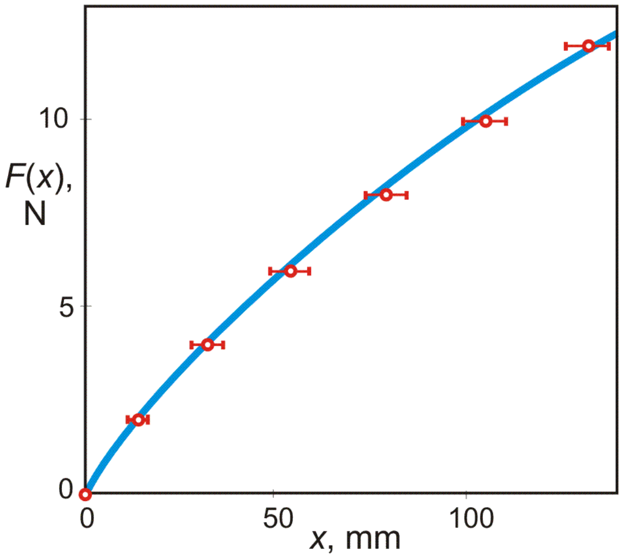

Figure 2.3 – Nonlinear relationship between the displacement of INSTRON jaws and force.

In some parts of the tire the pressure stress is dominant, e.g. in tread. Therefore, also pressure tests were performed on cylindrical test pieces cut out either of laboratory rubber plates [16] or directly from treads of tires [17].

Stress/strain characteristics were taken in the 3rd or 5th strain cycle. To illustrate the dependence on temperature (°C) pressure moduli are shown at different temperatures. In tread compounds an exponential drop with the absolute temperature was ascertained (Figure 2.4). But these approximations cannot be used for extrapolations (e.g. at temperatures lower than 10°C the materials become stiffer than predicted).

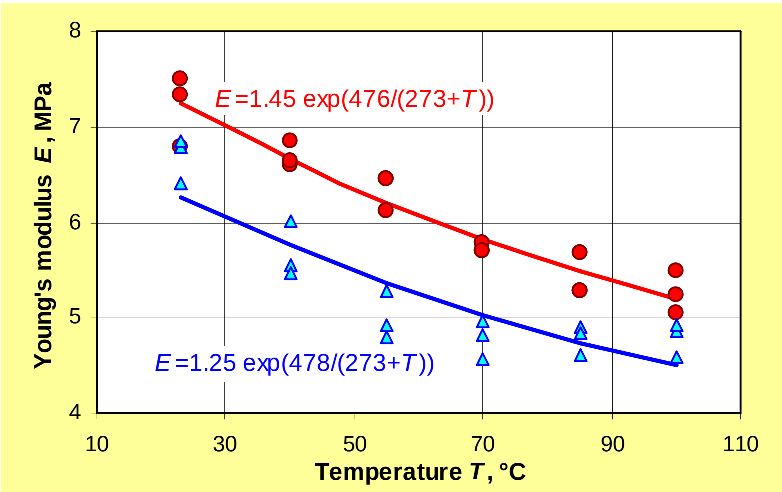

Figure 2.4 – Young's pressure modulus decrease in truck tire treads with increasing temperature;
● Michelin, Δ Semperit.

In hysteresis a similar decrease may be observed. Figure 2.5 shows the drop of hysteresis with increasing temperature in rubber matrix of belt cord layer. Hysteresis losses were calculated directly from force/displacement records of INSTRON 6025. But the resilience measurement by Lüpke method proved to be easier and more acceptable due to lower variance.

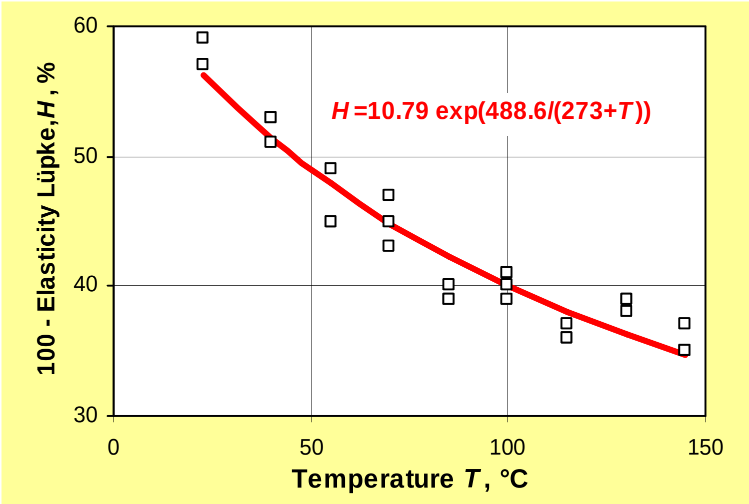

Figure 2.5 – Hysteresis decrease with increasing temperature in belt rubber matrix of a truck tire.

The displayed regression function would reach the level of H = 100% at $T \approx -53$°C, i.e. approximately at the glass transition temperature of the rubber. With this temperature the regression functions from Figure 2.4 would be transferred to

$$E_{Michelin}(T) = 3.85 \exp\frac{49.55}{53+T}, \qquad E_{Semperit}(T) = 3.22 \exp\frac{52.95}{53+T}.$$

Those formulas also adequately fit the experimental data and are acceptable in a broader range of temperature.

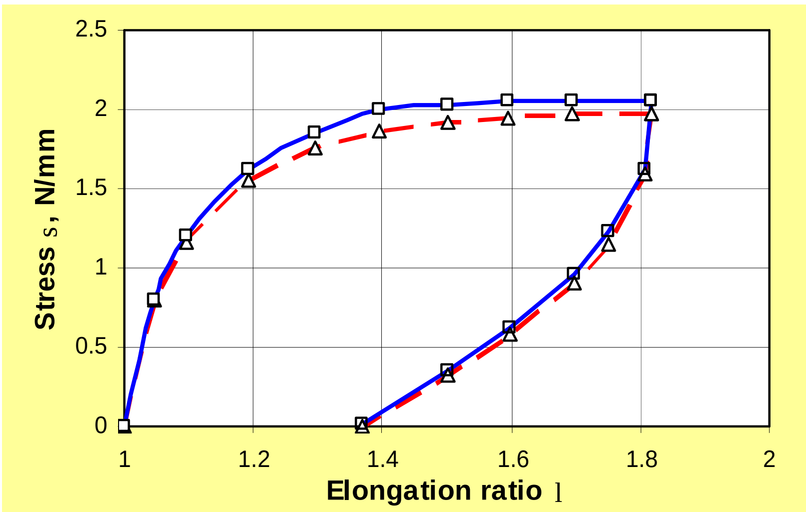

Figure 2.6 – Hysteresis loops of rubberized steel cord strip of 50mm width before tire building.

It might be convenient to realize that the tire building technology is based on small stiffness and large plasticity of raw rubber compounds. The plasticity is manifested by large area of the hysteresis loop as shown in Figure 2.6.

2.2 Cords

Considerable nonlinearity in dependence of tension and corresponding elongation can be seen in all textile cords, high elongation steel cords and other kinds of cords. Figure 2.7 shows hysteresis loops of cords produced of four different materials. The upper limit of load is 20N. In the initial part of load curve the cord filaments are rearranged, ordered and cord structure is tightened. Elasticity of primary filaments causes a puff up of cord structure. They must be rearranged first (the cord is compacted and its outer diameter reduced) and then they start to carry their parts of the total load. This can be seen very clearly in Kevlar cord, where this process requires the strain of about one percent.

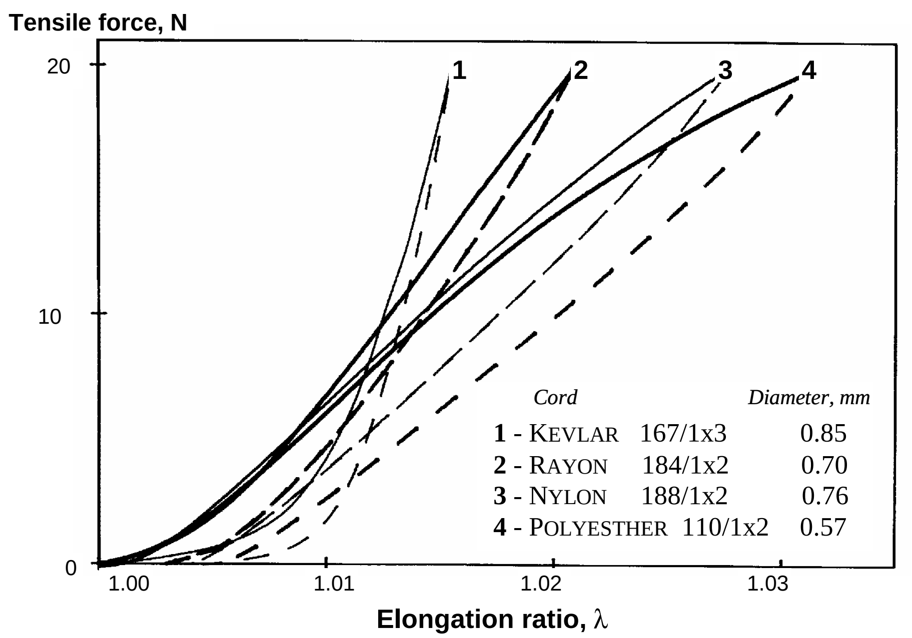

Figure 2.7 – Loading and unloading curves of different textile cords.

Cord properties are depending on temperature – similarly as the rubber properties. This can be seen very explicitly in nylon and polyester cords. If temperature increases the nylon fiber shrinks like a strained rubber strip. But the shrinkage in nylon is much less and, moreover, the nylon cord yielding increases at higher temperatures as shown in Figure 2.8 [18]. So the often proclaimed contracting effect of nylon cap layer seems improbable. The positive effect should be assigned more probably to creating a transition layer and blurring this way the steep stress change between stiff steel cord belt layers and soft tread rubber. Simple measurement showed that the increment of circumferential length due to the same change of inflation pressure was greater in heated up radial tire than in the same cold tire. The plasticity of nylon cords at higher temperatures also reduces problems arisen possibly due to high circumferential stiffness when the tire expands into vulcanization mold.

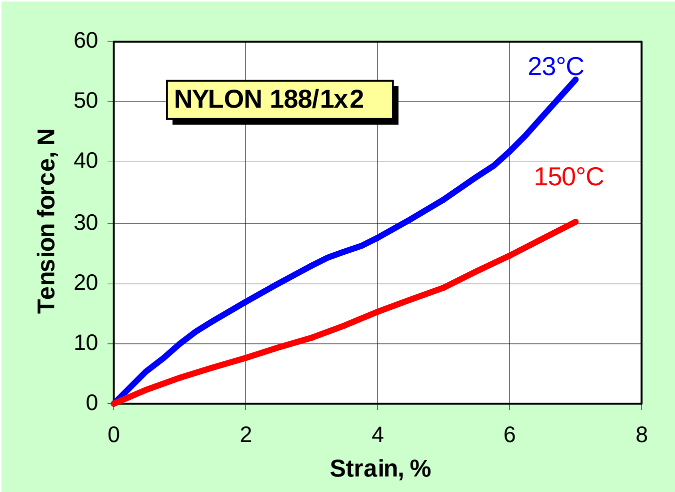

Figure 2.8 – Influence of temperature on tension stiffness of nylon cord.

Time dependence of nylon cord strain $e(t)$ at a constant tension load (creep) can be described in a simple engineering form

$$e(t) = a \ln t + b,$$

where parameters a, b depend on the cord load, temperature etc. For example, in the nylon cord from Figure 2.8 the tension of 27.5N and the time in minutes gave

$e_{23}(t) = 0.010 \ln t + 0.040$ for the temperature $T = 23°C$,

$e_{100}(t) = 0.001 \ln t + 0.065$ for the temperature $T = 100°C$.

For more details see [18].

r

Special devices are needed in experimental work with steel cords. E.g. a properly dimensioned tensile testing machine is required for establishing the strength of a steel cord. Clamping the cord in jaws must also be solved satisfactorily to obtain undistorted results.

Figure 2.9 shows tensile curves in several steel cords. They are practically linear up to 1% strain at least. The high-elongation (HE) cord appears very soft at small values of elongation and all the displacement in the tensile force direction is consumed on spatial packing the primary fibers. Only then the fibers are forced to elongate in the cord axis direction with a much greater stiffness. The strength of cord fiber steel is significantly higher than that in common steels of similar composition due to technology of drawing the rod.

Though the hysteresis in steel cords is considerable it is difficult to record precisely the unloading curve with common tensile testing machine. Our attempts to find out a suitable and simple method for measuring hysteresis of steel cord were unsuccessful.

The steel still represents one of the materials with a very high strength. But the strength of the common spider web fiber is also very high at much lower specific weight. Obviously, the mere existence of such materials is a provocative challenge for development of materials with similar strength/mass ratio.

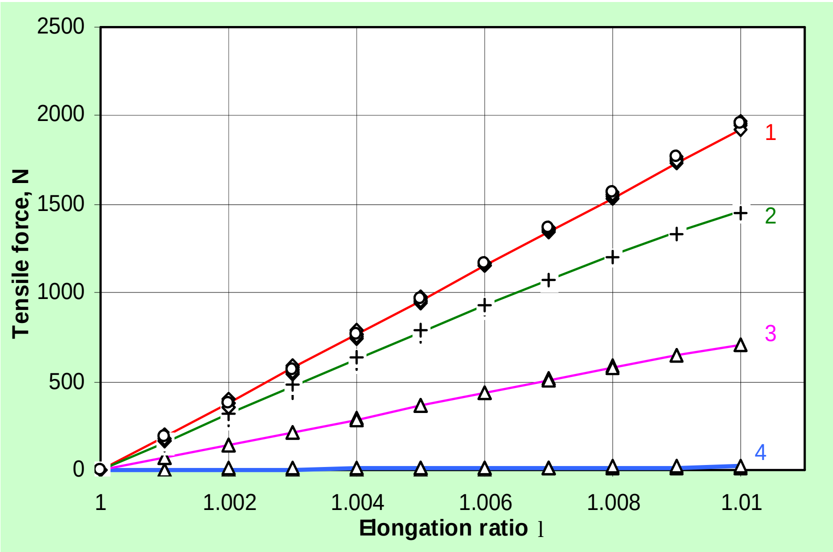

Figure 2.9 – Tensile curves of several steel cords.
1 - BEKAERT 7x4x0.22+1 *(D* =1.81mm*)* *and* 3+9+15x0.22+1 *(D* =1.62mm*)*
2 - BEKAERT 3x0.20+6x0.38 *(D* =1.19mm*),*
3 - ZDB 3x0.15+6x0.27 *(D* =0.85mm*),*
4 - BEKAERT HE 3x7x0.22 *(D* =1.51mm*).*

2.3 Cord Strain and Energy Distribution in Tire

Tire wall occupies just a relatively small part of the total volume limited by the outer surfaces of the tire and the rim. The prevailing part of the total tire volume, tire cavity, is filled with almost ideally elastic medium – the compressed air (or other gas, e.g. neutral nitrogen). The air overpressure produces strains in the tire wall corresponding to its structure and stress/strain parameters of materials. It is well known that the dimensional changes in radial tires are smaller that those in diagonal tires due to the orientation of tough cords close to the direction of main components of stress.

To show different behavior of the compressed air and cords let us consider a simple system shown in Figure 2.10. It consists of sealed cylinder with a piston of a negligible mass. The initial distance of the piston from the bottom be h, its area be A. Let p_a = 98kPa denote the usual atmospheric pressure and initial pressure under the piston. If the piston is loaded via a piece of the elastic cord then the pressure under the piston increases. The isotherm compression is characterized by constant product pV, i.e. a displacement x of the piston changes the pressure to $p(x) = p_a\, h/(h–x)$, $0<x<h$ due to Boyle law. The overpressure in the lower part of cylinder $p(x) – p_a = p_a(h/(h–x) – 1\,) = p_a\, x/(h–x)$ produces the pressure force on the piston

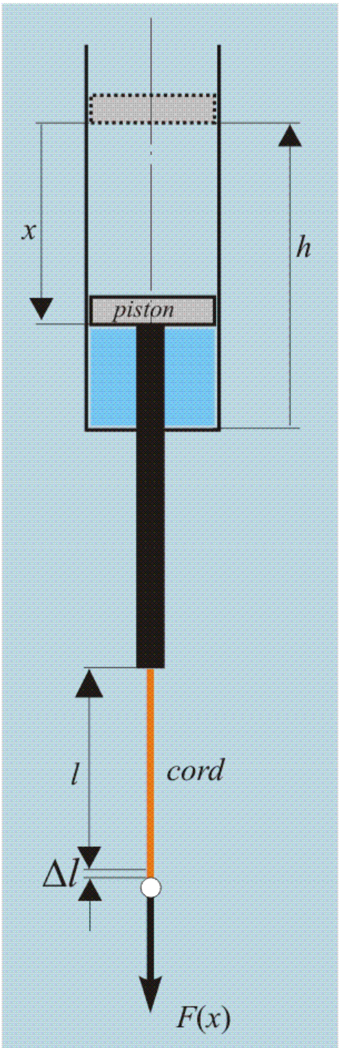

Figure 2.10 – A simple model to illustrate the energies stored in cord and compressed air.

$$F(x) = A\,p_a\,x/(h-x).$$

If l is the initial length of the cord section, Δl its change due to a force F and k the cord elasticity constant,

$$F \approx k\,\Delta l,$$

then the same force $F(x)$ results in the cord elongation $\Delta l(x) \approx F(x)/k$. The work accumulated in the cord is

$$W_{cord}(x) \approx (k/2)\,\Delta l^2(x) = (k/2)\,(F(x)/k)^2 = (A\,p_a\,x/(h-x))^2/(2k)$$

and the work accumulated in the compressed air in cylinder is

$$W_{air}(x) = -\int_0^x F(x)\,\mathrm{d}x = -A\,p_a \int_0^x \frac{x}{h-x}\,\mathrm{d}x = -A\,p_a \int_0^x \frac{x-h+h}{h-x}\,\mathrm{d}x = A\,p_a \left[x - h\ln\frac{h}{h-x} \right].$$

Thus the quotient

$$Q(x) = \frac{W_{cord}(x)}{W_{air}(x)} = \frac{\dfrac{A^2 p_a^2 x^2}{2k(h-x)^2}}{A p_a \left(x - h\ln\dfrac{h}{h-x}\right)} = \frac{A p_a}{2k} \frac{x^2}{(h-x)^2 \left(x - h\ln\dfrac{h}{h-x}\right)} = \frac{A p_a}{2kh} \frac{-(x/h)^2}{(1-x/h)^2\,(\ln(1-x/h) + x/h)}.$$

Obviously, $Q(0) = Ap_a/(kh)$ and $Q(x) \to +\infty$ as $x \to h-0$. Limited cord strength and elongation at brake keep $Q(x)$ near $Q(0)$ if values of l/h are not extremely great.

r

The next example is more difficult. The corresponding theory will be explained later in Chapter 4 and computer programs are needed to make the calculation of considered quantities easier.

Let us consider the carcass of a radial tire now, e.g. that of 445/65R22.5 tire, and suppose its beads absolutely stiff. Carcass equator radius in that tire is 544.0mm and the volume enclosed by the carcass inner surface is 0.230012m^3. The carcass cord tension due to the inflation pressure 900kPa is 331N. If the belt were removed, the carcass would expand radially as shown in Figure 2.11. The assumption of inextensible carcass cord would result into free carcass equator radius of 623.0mm and the increased volume 0.263122m^3. This, however, would reduce the overpressure to

$$p = (998\times0.230012/0.263122 - 98) = 774\text{kPa},$$

while the cord tension would increase to 579N. Let carcass cord be the steel *cord 1* from Figure 2.9. The elongation ratio corresponding to the load 579N is λ = 1.003. For the initial carcass cord length 814.18mm the tension difference 579 – 331 = 248N would produce an increased cord length l_f = 815.0mm, a new equator radius of 623.33mm and volume V_f = 0.263654m^3.

The total energy of the compressed air contained in the cavity of the free carcass at the isothermal expansion is defined by the volume V_a annulling the overpressure 774kPa, i.e. reducing the absolute air pressure from (774 + 98)kPa = 872kPa to 98kPa, $V_a = \dfrac{774+98}{98} V_f$ = 2.343331m^3,

$$W_{air} = 872\,000 \times 0.263654 \ln \frac{872}{98} = 502.534\text{kJ}.$$

The energy stored in the carcass corresponds to the energy spent on the volume decrement due to the cord length reduction, $l_c = l_f /\lambda$ = 815.0/1.003 = 812.56mm. The volume $V(l_c)$ = 0.262008m^3. Thus,

$$W_{cords} = 872\,000 \times 0.263654 \times \ln \frac{0.263654}{0.262008} = 1.440\text{kJ}.$$

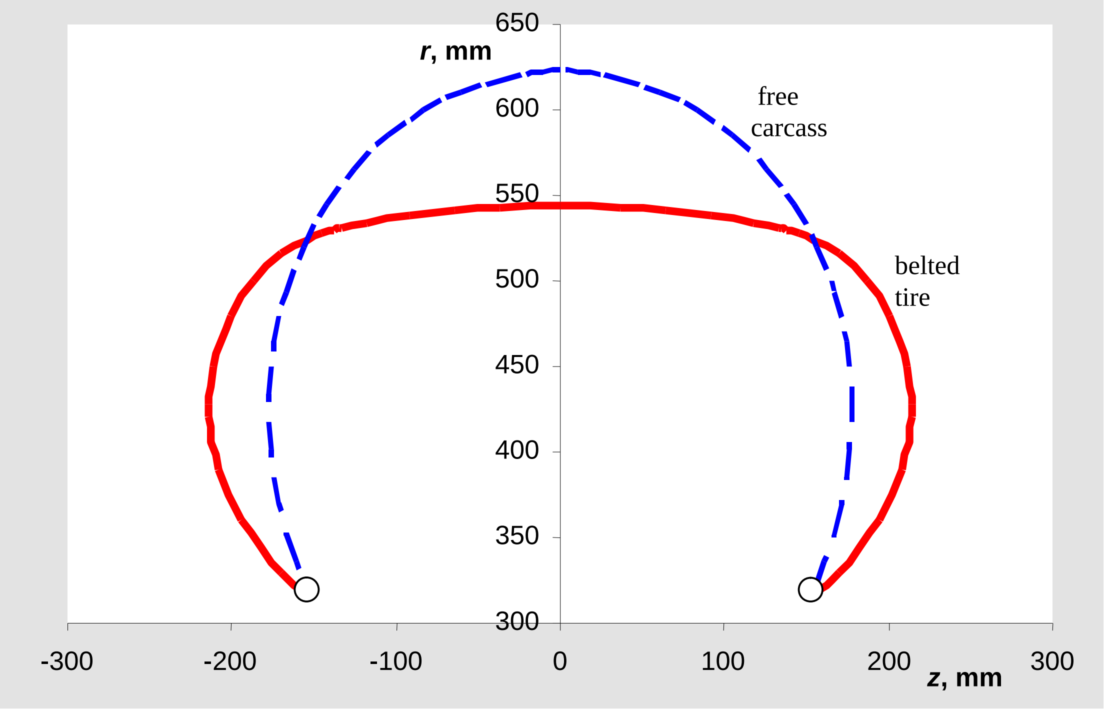

Figure 2.11 – Carcass meridian of the 445/65R22.5 tire.

These simple estimates show that the tire wall contribution to the total energy accumulated in the inflated tire must be expected very small.

In real tire, however, the bead wire is extensible as much as the steel cords at least. Also the bead is rotated by some angle due to the tension stress in the carcass cord layer winded around the bead wire bundle (Figure 1.1). Thus, the real meridian length increments in the area beyond the rim shoulders due to inflation pressure are much greater than those we have taken into account so far.

Figure 2.12 shows how the energy accumulated in the tire carcass is increasing with an elastic increase of cord length.

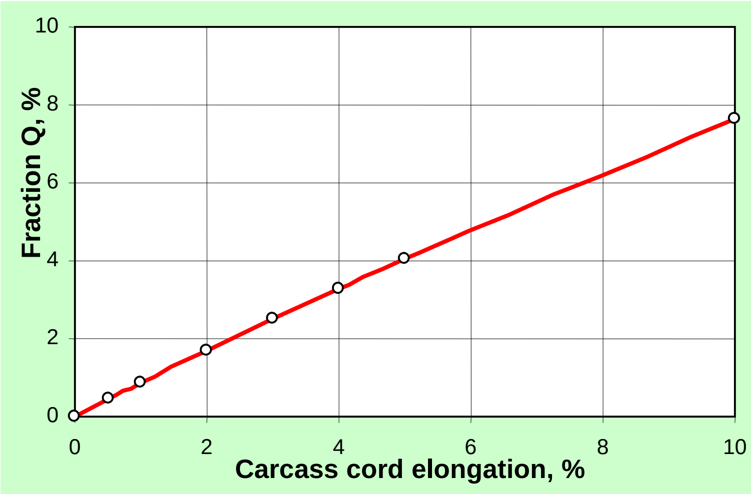

Figure 2.12 – The ratio of elastic carcass meridian elongation energy and the air energy of tire.

If the tire were filled with water, i.e. practically incompressible medium, the energy accumulated in the pressure medium would be negligible and the dominant role would belong to the elastic energy of tire wall [19]. That can be seen in tire burst tests. If the tire wall were inextensible the pressure in tire would drop instantly after an opening has arisen. But in real tire a stream of water is driven out by the relaxing wall materials through the arisen opening with a high kinetic energy. So safety measures are necessary to prevent destructive effects of that water stream.

P

3 DIAGONAL CARCASS GEOMETRY

The reinforcing cord system plays a fundamental role in shaping the tire. In diagonal carcass the cord plies are laid so that the cords in one ply cross over the cords in the neighboring ply under the opposite angle regarding the circumferential direction. In this way the cords shape diagonals in curvilinear quadruples generated by meridians and parallels on the axisymmetric surface. A single cord trajectory in cross-ply tire is then a spatial curve on that surface of revolution as shown in Figure 3.1. It arises from a helix on the building drum by its radial expansion while reducing the axial distance of beads contemporarily.

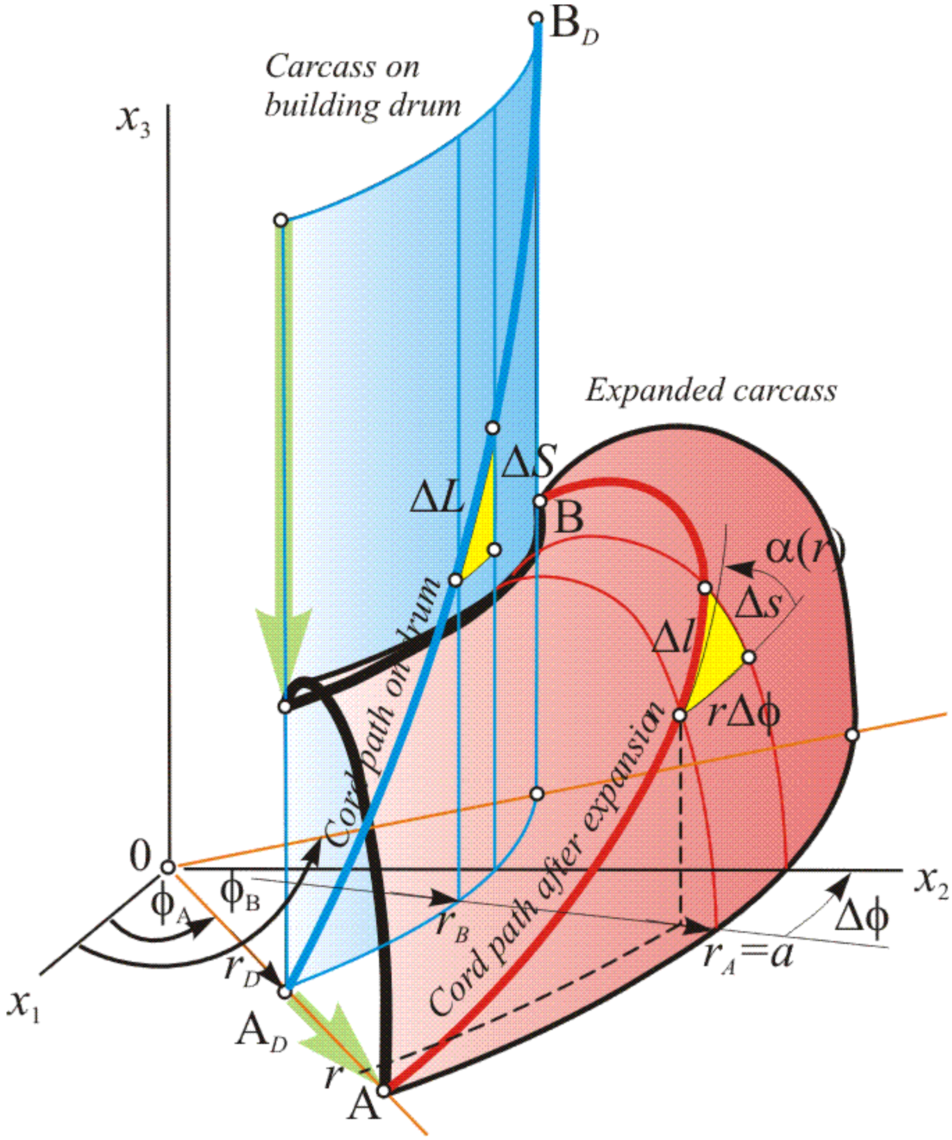

Figure 3.1 – Cord path in a diagonal tire and the schematic of diagonal carcass expansion after its building.

3.1 Cord Trajectory in Tire Carcass

To describe the cord trajectory it is necessary to introduce a convenient coordinate system. Because a tire, in a simplified view, can be considered as an axisymmetric body with a further symmetry with respect to the equator plane it is natural to choose the intersection point of the axis of revolution x_3 and the equator plane for the center 0 of Cartesian coordinate system $0x_1x_2x_3$. This enables to define cylindrical coordinates r, ϕ, z as follows

$$\left.\begin{aligned} x_1(r, \phi, z) &= r \cos \phi, \\ x_2(r, \phi, z) &= r \sin \phi, \\ x_3(r, \phi, z) &= z. \end{aligned}\right\} \tag{3.1}$$

The square of length element $\mathrm{d}l = |\mathrm{d}\mathbf{x}(r, \phi, z)|$ on the surface of revolution in Cartesian and cylindrical coordinates (**.** denotes the scalar product, [9,10])

$$\begin{aligned} \mathrm{d}l^2 &= \mathrm{d}\mathbf{x}.\mathrm{d}\mathbf{x} = \mathrm{d}\,x_1^2 + \mathrm{d}\,x_2^2 + \mathrm{d}\,x_3^2 \\ &= (\mathrm{d}r \cos \phi - r \sin \phi\, \mathrm{d}\phi)^2 + (\mathrm{d}r \sin \phi + r \cos \phi\, \mathrm{d}\phi)^2 + \mathrm{d}z^2 \\ &= \mathrm{d}r^2 + r^2\mathrm{d}\phi^2 + \mathrm{d}z^2 \,. \end{aligned} \tag{3.2}$$

As well known the equality r = const. defines a parallel and ϕ = const. a meridian curve on the surface of revolution [9] which can be described as the graph of a function $z(r, \phi)$. The parallels and meridian curves generate together orthogonal grid of curves on the surface of revolution. Namely, the derivatives of the vector $\mathbf{x}$ with respect to the azimuth ϕ and radius r are

$$\mathbf{x}_\phi = \frac{\partial \mathbf{x}}{\partial \phi} = (-r \sin \phi, r \cos \phi, 0)^{\mathrm{T}} \qquad \text{for the parallel and}$$

$$\mathbf{x}_r = \frac{\partial \mathbf{x}}{\partial r} = (\cos \phi, \sin \phi, z_r)^{\mathrm{T}} \qquad \text{for the meridian,}$$

and their scalar product $\mathbf{x}_\phi . \mathbf{x}_r = 0$.

The angle between the cord trajectory and the parallel of radius r

$$\alpha = \arccos (\mathbf{x}_\phi\, \mathrm{d}\phi/\mathrm{d}\mathbf{x})$$

can be measured by relatively simple means so its use is advantageous. The infinitesimal triangle from Figure 3.1 shows that

$$\mathrm{d}l \cos \alpha = r\, \mathrm{d}\phi.$$

Thus,

$$\mathrm{d}l^2 = \mathrm{d}r^2 + \mathrm{d}l^2 \cos^2 \alpha + \mathrm{d}z^2$$

and

$$\mathrm{d}l^2 (1 - \cos^2\alpha) = \mathrm{d}l^2 \sin^2\alpha = \mathrm{d}r^2 + \mathrm{d}z^2 \,.$$

For the sake of simplicity let ϕ, z and α be differentiable functions of r up to a sufficiently high order and $0<\alpha<\pi$. Then $\mathrm{d}z(r) = z'(r)\,\mathrm{d}r$, $\mathrm{d}\phi(r) = \phi'(r)\,\mathrm{d}r$ and further

$$\mathrm{d}l(r) = \frac{\sqrt{\mathrm{d}x^2 + \mathrm{d}z^2(r)}}{\sin \alpha(r)} = \frac{\sqrt{1 + z'^2(r)}}{\sin \alpha(r)}\, \mathrm{d}r$$

Putting this into Equation (3.2) gives

$$\frac{1+z'^2(r)}{\sin^2\alpha(r)}\,\mathrm{d}r^2 = \mathrm{d}r^2 + r^2\mathrm{d}\phi^2 + z'^2(r)\,\mathrm{d}r^2 ,$$

and by simple rearrangement one obtains

$$\mathrm{d}\phi(r) = \frac{\sqrt{1+z'^2(r)}}{r\,\tan\alpha(r)}\,\mathrm{d}r .$$

The total length of the spatial curve and the azimuth angle between the endpoints A, B (Figure 3.1) is then

$$\left.\begin{aligned} l_{AB} &= \int_{r_B}^{r_A} \frac{\sqrt{1+z'^2(r)}}{\sin\alpha(r)}\,\mathrm{d}r , \\ \phi_{AB} &= \int_{r_B}^{r_A} \frac{\sqrt{1+z'^2(r)}}{r\,\tan\alpha(r)}\,\mathrm{d}r . \end{aligned}\right\} \tag{3.3}$$

The derivative $z'(r)$ for $r\to r_A$ tends to infinity, $\lim\limits_{r\to r_A-} z'(r) = -\infty$, and both integrals (3.3) are singular. But for $|r_A-r_B| < 2R$ the length of the arc of the circle

$$(r-(r_A-R))^2 + z^2 = R^2$$

expressed by the integral

$$\int_{r_A}^{r_B} \sqrt{1+z'^2(r)}\,\mathrm{d}r$$

is final evidently. The same is true also for $0<\alpha(r)\leq\pi/2$ and any reasonable meridian curve $z(r)$. If $\alpha(r) = \pi/2$ (radial carcass),

$$l_{AB} = \int_{r_B}^{r_A} \sqrt{1+z'^2(r)}\,\mathrm{d}r , \qquad \phi_{AB} = \int_{r_B}^{r_A} 0\,\mathrm{d}r = 0 .$$

Problems with singularity may be avoided by transforming the integrals (3.3) to line integrals of the first kind [9]. The infinitesimal length of the meridian curve is

$$\mathrm{d}s(r) = \sqrt{1+z'^2(r)}\,\mathrm{d}r.$$

Thus, if s_{AB} is the total meridional length between the parallels $r = r_B$ and $r = r_A$, then

$$l_{AB} = \int_0^{s_{AB}} \frac{1}{\sin\alpha(r(s))}\,\mathrm{d}s , \qquad \phi_{AB} = \int_0^{s_{AB}} \frac{1}{r(s)\tan\alpha(r(s))}\,\mathrm{d}s . \tag{3.4}$$

These formulas together with numerical computing the integrals [10] played very useful role several decades ago, because then the tires used to be given merely by its cross-sectional drawings and both values l_{AB}, ϕ_{AB} had to be computed manually [20]. For example, the 3-nodal Gauss' quadrature formula needs three radii r_{-1}, r_0, r_1 shown in Figure 3.2a. This may be even simplified, when calculating over the whole meridian arc as shown in Figure 3.2b (with a greater error).

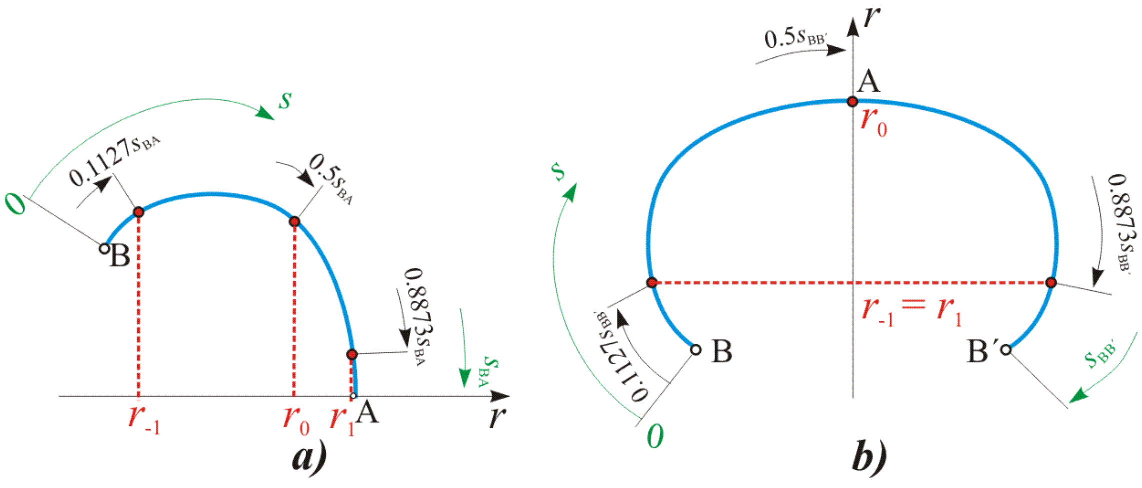

Figure 3.2 – Radii used in Gauss formula for computing integrals (3.4).

3.2 Geodesic Line on the Surface of Revolution

Let a convex surface of revolution be given by its meridian curve $z(r)$ and let the shortest line connecting its two fixed endpoints be found (a tensioned fiber laid on the surface so that it goes through two given points on it). On the interval (r_B, r_A) of uniqueness of the functions z and ϕ this problem may be written as follows

$$l_{AB}[\phi] = \int_{r_B}^{r_A} \sqrt{1+z'^2(r)+r^2\phi'^2(r)}\,\mathrm{d}r = \int_{r_B}^{r_A} f(r,\phi')\,\mathrm{d}r \ \rightarrow \text{minimum}.$$

This is a simple problem when using the calculus of variations [9]. The corresponding Euler-Lagrange equation

$$\frac{\mathrm{d}}{\mathrm{d}r}\left(\frac{\partial f(r,\phi')}{\partial\phi'}\right) = 0$$

has its first integral

$$\frac{\partial f(r,\phi')}{\partial\phi'} = \frac{r^2\phi'(r)}{\sqrt{1+z'^2(r)+r^2\phi'^2(r)}} = r\,\frac{r\,\mathrm{d}\phi}{\mathrm{d}l} = \text{const.}$$

But $\dfrac{r\,\mathrm{d}\phi}{\mathrm{d}l} = \cos\alpha$ (Figure 3.1). Therefore the geodesic line on the surface of revolution is characterized by the following equation

$$r\cos\alpha(r) = \text{const.}$$

(*Clairaut's equation*).

The choice $r = a$ presents the simplest case – the cylindrical surface (a circular tube) – on which the geodesic line, helix, runs under a constant elevation angle (lead). This curve was found in [9] as a solution of a problem concerning the conditioned maximum.

Imagine a thin elastic axisymmetric membrane (tube) and a uniform net of fibers (free cords without any rubber matrix) fixed only to two parallels in beads and otherwise freely frictionless movable on the membrane. The overpressure in the fluid within the membrane would force the cords to reshape in such a way that the volume enclosed by the membrane is maximal:

$$\left(\int_{r_B}^{r_A} r\, z(r)\, dr \;\middle|\; \int_{r_B}^{r_A} \sqrt{1 + z'^2(r) + r^2\, \phi'^2(r)}\, dr = l_{BA} \right) \longrightarrow \mathit{max.}$$

Such problems, however, will be solved later in Chapter 4.

3.3 Carcass Expansion and the Angle $a(r)$

The cord net in tire carcass on the building drum is embedded in the matrix of raw rubber compound. The expansion of raw carcass can be viewed as a radial displacement of the cord system in a very viscous liquid or something like this. Problems of this type are probably difficult to solve even today. That is why different models were set up to capture the behavior of the cord net embedded in the rubber. Ignoring the possibility of local shear displacement of cord plies there are two extreme cases to distinguish:

- § If the cord length has to be preserved, which is in full accord with reality, the cord net is modeled locally as a combination of two systems of parallel rods connected together in fixed joints (Figure 3.3).
- § Between every two parallel rods is an incompressible material and the distance between neighboring cords in the corresponding layer must be preserved, i.e. joints must be displaced (Figure 3.4).

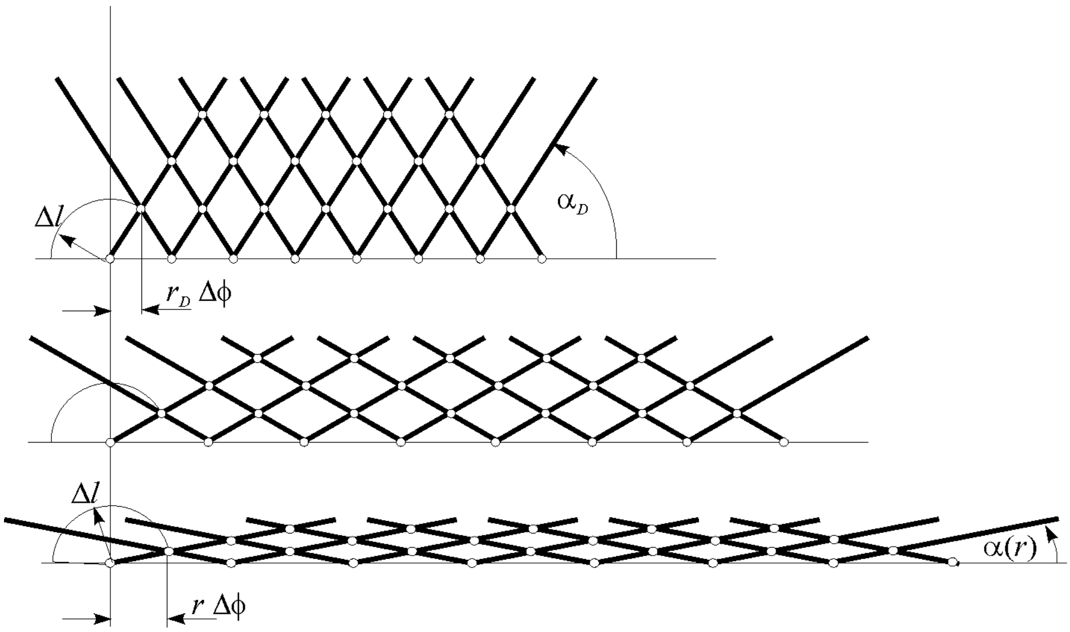

Figure 3.3 – Pantographic model of the carcass cord net.

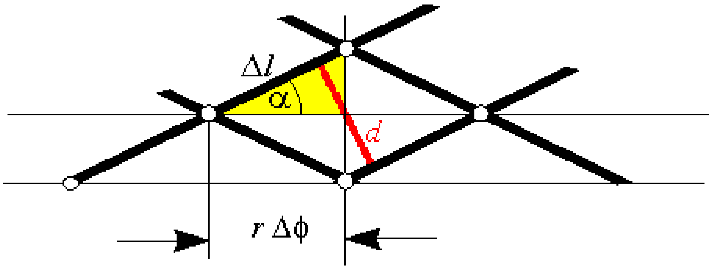

Figure 3.4 – An element of the cord net.

In the first case the distances Δl between the neighboring nodes of parallelepipeds are constant, which implies

$$\Delta l = r\,\Delta\phi \,/\, \cos\alpha(r) \;=\; r_D\,\Delta\phi \,/\, \cos\alpha_D \,,$$

i.e.

$$\frac{\cos\alpha(r)}{r} = \frac{\cos\alpha(r_D)}{r_D} = \text{const.} \qquad \text{(cos)}$$

This is the traditionally used *cosine* or *pantographic rule*.

The area of one parallelepiped of the net is

$$A(\alpha) = \Delta l^2 \sin(2\alpha)\,.$$

This means that A tends to 0 if $\alpha \to 0+$ as indicated in the lower part of Figure 3.3. The maximum expansion ratio is then $r/r_D = 1/\cos\alpha_D$ and $\cos\alpha(r_D/\cos\alpha_D) = 1$.

One can, however, suppose that the rubber matrix surrounding cords would resist such squeezing out. The distance of two neighboring cords is (Figure 3.4)

$$d(r) = 2r\,\Delta\phi\,\sin\alpha(r).$$

The assumption $d(r)$ = const. leads to the following equations

$$d(r) = 2r\,\Delta\phi\,\sin\alpha(r) = 2r_D\,\Delta\phi\,\sin\alpha_D = d(r_D),$$

i.e.

$$r\sin\alpha(r) = r_D \sin\alpha_D = \text{const.} \qquad \text{(sin)}$$

This is the so called *sine rule* [21].

Requirement of preserving the area $A(\alpha)$ is a compromise between those extreme cases. The distance Δl between two neighboring nodes on the same cord is now variable but the area A can be expressed by diagonals in the parallelepiped in Figure 3.4. The horizontal diagonal $u_h = 2r\,\Delta\phi$, the vertical one $u_v = u_h \tan\alpha$, therefore

$$A(\alpha(r)) = \frac{1}{2}u_v\,u_h = \frac{1}{2}(2r\,\Delta\phi)^2\tan\alpha(r) \;=2\,(r_D\,\Delta\phi)^2\tan\alpha_D = \text{const.}$$

Then

$$r^2\tan\alpha(r) \;= r_D^{\,2}\tan\alpha_D \;= \text{const.} \qquad \text{(tan)}$$

This may be called the *tangent rule*.

Another compromise rule is the *generalized cosine rule*

$$\cos\alpha(r) = \left(\frac{r}{r_D}\right)^E \cos\alpha_D\,. \tag{E}$$

It comprises as special cases either $E = -1$, i.e. the Clairaut's relation for geodesic line on a surface of revolution, and $E = 1$, i.e. the usual cosine rule.

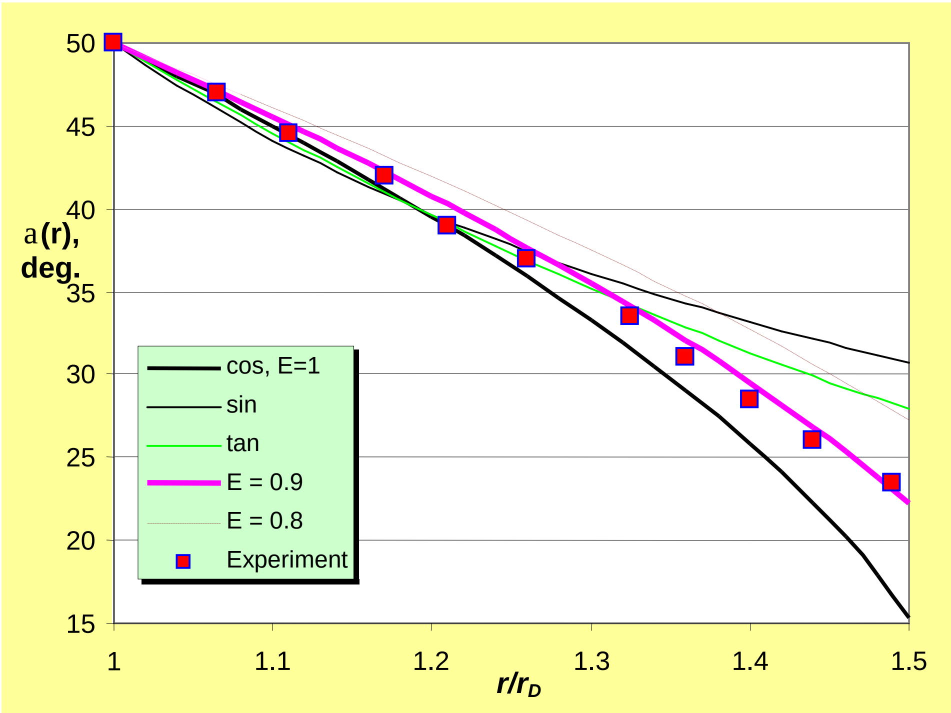

Figure 3.5 – Comparison of angles $\alpha(r)$ *computed with the mentioned rules to the measured values in a strip cut of two raw rubberized cord plies assembled with angles* $\alpha_D = \pm 50°$.

Figure 3.5 shows the angles $\alpha(r)$ computed by the mentioned rules compared to results obtained by stretching the strip of width 0.1m made of two raw rubberized textile cord layers with angles $\alpha_D = \pm 50°$. The rule (E) with $E = 0.9$ fits the measured values quite well. But the straight line through the point (1, 50°),

$$\alpha(r) = 50 - 52.95(r/r_D - 1),$$

fits the measured data also good and F-test [11] shows statistical equivalency of both the functions,

$$F = \frac{\sum_{k=1}^{11}(\alpha_{E,0.9}(r_k) - \alpha_k)^2}{\sum_{k=1}^{11}(50 - 52.95(r_k/r_D - 1) - \alpha_k)^2} = 1.764155 < 3.47370 = F_{0.025}(11, 11)\,.$$

The dependence

$$\alpha(r) = \alpha_D - c\left(\frac{r}{r_D} - 1\right) \tag{L}$$

can be taken as a further expansion rule, the *linear rule*.

Though the radial tires are clearly dominant today, the description of crossed cord systems deserves some attention. Belts of radial tires are still built as diagonal systems and it is important to realize that a small expansion at angles round 20° introduces the reduction of width of the corresponding ply,

$$\frac{W}{W_D} = \frac{\sin\alpha(r)}{\sin\alpha_D},$$

which may be significant. For example if the original width is W_D = 200mm, the angle α_D=22° and the expansion ratio 1.02 (2 percent), then the rule (E) with E = 0.9 gives

$$\alpha = \arccos(1.02^{0.9}\cos(22°)) = 19.29° \text{ and}$$

$$W = W_D \frac{\sin\alpha(r)}{\sin\alpha_D} = 200 \frac{\sin 19.29°}{\sin 22°} = 176.4\text{mm}.$$

The reduction of the corresponding belt ply is therefore almost 24mm, i.e. 12 percent.

3.4 Tire Building Parameters

The rubberized cord fabric is cut so that cord plies of rhomboid shape with prescribed width are prepared. The cutting angle α_C is approximately equal to the angle α_D (given by the angle α_A on tire equator and expansion rule) but sometimes it needs to be a bit corrected, e.g. with respect to possible circumferential elongation.

Another quantity that must be set up is the width W_D of the building drum. It is essentially determined by the cord length l_{BAB} = $2l_{AB}$ equal to the length of the helix representing the cord path on the building drum and the angle α_D :

$$W_D \approx 2l_{AB} \sin\alpha_D.$$

There are several technical details concerning the shape of bead parts that must be respected in practical determining the values of α_C, W_D and carcass ply widths for individual tires and building drums.

Mathematical analysis of relationships among the angles in tire and on the building drum, the cord elongation and the building drum width was in a more detailed way presented in [22,23].

In radial carcass there is $\alpha(r) = \pi/2$, of course. Then, obviously, $\alpha_C = \alpha_D = \pi/2$ and $W_D \approx 2l_{AB}$ with respect to possible increase due tightening cords in beads.

P

4 EQUILIBRIUM SHAPE

So far the carcass expansion with no respect to the final shape has been dealt with. The carcass expands to a fixed shape in the vulcanization press when it is pressed against the mold surface by heating medium in the bladder within the tire cavity. If there is no outer support then the carcass itself must resist the pressure on its internal surface and change its shape in accordance with the general principle of energy minimum.

The energy of inflated tire at zero velocity is composed of the elastic energy of tire wall and the energy of the air compressed in tire cavity, $E_{pot} = E_{elast} + E_{air}$. It was shown in Section 2.3 that the energy E_{elast} can be taken negligible. Then the tire wall can be reduced to a surface of revolution whose final shape is fully determined by the carcass cord net.

4.1 Air Volume Theory of the Tire Meridian Curve

We will consider the unloaded inflated tire rotating with angular velocity ω. Variable thickness and density of the tire wall is reflected in surface density ρ (kg/m^2) of the surface A representing the upper half of the tire ($z \geq 0$). Let P be a point on A. The kinetic energy of the whole surface is

$$E_{kin} = 2\,\frac{\omega^2}{2} \int_A \rho(\mathrm{P})\, r^2(\mathrm{P})\, \mathrm{d}A(\mathrm{P})\,.$$

Let the rotating tire be considered as an energetically closed system. The surface A in cylindrical coordinates is expressed by a function

$$z = f(r, \phi).$$

Local measuring lengths and angles a point P of the surface is performed in tangential plane at this point, i.e. in the plane determined by two independent tangential vectors at that point [9]. The square of the length element is

$$\mathrm{d}l^2 = g_{rr}\,\mathrm{d}r^2 + g_{\phi\phi}\,\mathrm{d}\phi^2 + 2\,g_{r\phi}\,\mathrm{d}r\,\mathrm{d}\phi\,,$$

where $\mathbf{g} = \begin{pmatrix} g_{rr} & g_{r\phi} \\ g_{r\phi} & g_{\phi\phi} \end{pmatrix}$ is the local metric tensor.

In the case of axial symmetry with respect to the axis 0z the surface is given completely by its meridian curve $z = f(r)$. Using (3.2) gives

$$g_{rr} = 1 + f'^2(r), \qquad g_{r\phi} = 0, \qquad g_{\phi\phi} = r^2.$$

Thus,

$$\mathrm{d}A(r, \phi) = \sqrt{g_{rr}g_{\phi\phi} - g_{r\phi}^2}\;\mathrm{d}r\,\mathrm{d}\phi = \sqrt{(1+f'^2(r))r^2}\;\mathrm{d}r\,\mathrm{d}\phi = r\sqrt{1+f'^2(r)}\;\mathrm{d}r\,\mathrm{d}\phi$$

and

$$E_{kin} = \omega^2 \int_{(r_B,r_A)\times(0,2\pi)} \rho(r, \phi)\, r^2\, r\sqrt{1+f'^2(r)}\;\mathrm{d}r\,\mathrm{d}\phi = \omega^2 \int_{r_B}^{r_A}\int_0^{2\pi} \rho(r, \phi)\, r^3 \sqrt{1+f'^2(r)}\,\mathrm{d}r\,\mathrm{d}\phi.$$

The mass is supposed to be distributed axisymmetrically, $\rho(r, \phi) = \rho(r)$. Due to finality of r and $\rho(r)$ the existence of the integral on the right hand side is obvious and the Fubini theorem [9, Section 3.4] gives

$$E_{kin}[f] = 2\pi\omega^2 \int_{r_B}^{r_A} \rho(r)\, r^3 \sqrt{1+f'^2(r)}\; \mathrm{d}r\,.$$

The volume of the cavity T corresponding to the meridian curve $z = f(r)$ is

$$V[f] = \int_{\mathrm{T}} \mathrm{d}x_1 \mathrm{d}x_2 \mathrm{d}x_3.$$

Transition to cylindrical coordinates and the substitution theorem [9, Section 3.4] yields

$$V[f] = 2\int_{\Omega} \left|\frac{\partial(x_1, x_2, x_3)}{\partial(r, \phi, z)}\right| \mathrm{d}r\, \mathrm{d}\phi\, \mathrm{d}z\,,$$

where

$$\Omega = \{(r, \phi, z) : r_B < r < r_A,\ 0 < \phi < 2\pi,\ 0 < z < f(r)\ \}.$$

The Jacobian

$$\frac{\partial(x_1, x_2, x_3)}{\partial(r, \phi, z)} = \det\begin{pmatrix} \cos\phi & -r\sin\phi & 0 \\ \sin\phi & r\cos\phi & 0 \\ 0 & 0 & 1 \end{pmatrix} = \det\begin{pmatrix} \cos\phi & -r\sin\phi \\ \sin\phi & r\cos\phi \end{pmatrix} = r.$$

Thus,

$$V[f] = 2\int_{r_B}^{r_A}\int_0^{2\pi}\int_0^{f(r)} r\, \mathrm{d}r\, \mathrm{d}\phi\, \mathrm{d}z\,.$$

Using the Fubini theorem gives

$$V[f] = 2\int_{r_B}^{r_A} 2\pi\, r\, f(r)\, \mathrm{d}r = 4\pi \int_{r_B}^{r_A} r\, f(r)\, \mathrm{d}r.$$

The potential energy is considered equal to the energy of the air compressed in the tire cavity, i.e.

$$U_{pot}[f] = p_0 V_0 \ln\frac{V_0}{V[f]} = -p_0 V_0 \ln\left(1 - \frac{V_0 - V[f]}{V_0}\right) \approx -p_0 V_0\left(-\frac{V_0 - V[f]}{V_0}\right)$$
$$= p_0\,[\, V_0 - 4\,\pi \int_{r_B}^{r_A} r\, f(r)\, \mathrm{d}r]\,,$$

where V_0, p_0 are the initial volume and absolute pressure, respectively.

The total energy

$$E[f] = E_{kin}[f] + U_{pot}[f]$$

is then a functional depending on f and in real conditions $E[f]$ is always minimized,

$$E[f] \to \min.$$

The function f is supposed to be smooth sufficiently and satisfy conditions of preserving the following two invariants of expansion,

$$L[f] = \int_{r_B}^{r_A} \frac{\sqrt{1+f'^2(r)}}{\sin\alpha(r)}\,\mathrm{d}r = l_{AB}, \quad \Phi[f] = \int_{r_B}^{r_A} \frac{\sqrt{1+f'^2(r)}}{r\tan\alpha(r)}\,\mathrm{d}r = \phi_{AB}. \quad (4.1)$$

Search for the conditioned minimum of the energy of rotating tire may be shortly written as follows

$$(E[f] \mid L[f] = l_{AB}, \Phi[f] = \phi_{AB}) \to \min.$$

This is the so called isoperimetric problem with two isoperimetric restrictions [9, Chapter 6]. The standard way for its solution is based on finding a stationary point of an auxiliary functional

$$H = E + \mu L + \nu\Phi,$$

where μ and ν are unknown constants (Lagrange multipliers).
Obviously, omitting the constant V_0 and putting $p = p_0$ one gets

$$H[f] = \int_{r_B}^{r_A} h(r, f, f')\,\mathrm{d}r,$$

where

$$h(r, f, f') = \omega^2\rho(r)\,r^3\sqrt{1+f'^2(r)} - 4\pi p r f + \mu\frac{\sqrt{1+f'^2(r)}}{\sin\alpha(r)} + \nu\frac{\sqrt{1+f'^2(r)}}{r\tan\alpha(r)}$$

$$= \left[\omega^2\rho r^3 + \frac{\mu}{\sin\alpha} + \frac{\nu}{r\tan\alpha}\right]\sqrt{1+f'^2} - 4\pi p r f.$$

The corresponding Euler-Lagrange equation sounds

$$0 = \frac{\mathrm{d}}{\mathrm{d}r}\left(\frac{\partial h}{\partial f'}\right) - \frac{\partial h}{\partial f} = \frac{\mathrm{d}}{\mathrm{d}r}\left(\left[\omega^2\rho r^3 + \frac{\mu}{\sin\alpha} + \frac{\nu}{r\tan\alpha}\right]\frac{f'}{\sqrt{1+f'^2}}\right) + 4\pi p r.$$

Integrating this equation gives

$$\left(\left[\omega^2\rho r^3 + \frac{\mu}{\sin\alpha} + \frac{\nu}{r\tan\alpha}\right]\frac{f'}{\sqrt{1+f'^2}}\right) = 2\pi p(C - r^2),$$

where C is a constant. Further simplification may be attained by introducing the angle θ by equation

$$\tan\theta(r) = f'(r).$$

Then

$$\left[\omega^2\rho r^3 + \frac{\mu}{\sin\alpha} + \frac{\nu}{r\tan\alpha}\right]\sin\theta(r) = 2\pi p(C - r^2)$$

and

$$\sin\theta(r) = -\frac{2\pi p(r^2 - C)}{\left[\omega^2\rho r^3 + \frac{\mu}{\sin\alpha} + \frac{\nu}{r\tan\alpha}\right]} = -\frac{2\pi p(r^2 - C)}{\left[\omega^2\rho r^3 + \frac{1}{\sin\alpha}\left(\mu + \nu\frac{\cos\alpha}{r}\right)\right]}. \quad (4.2)$$

On the right side there are three constants, C, μ, ν, that are to be determined by other conditions. The function f is differentiable on (r_B, r_A), thus, its derivative f'

vanishes at its maximum representing the "width" W of the tire carcass (Figure 4.1). Denoting the corresponding radius r_w, it is obviously $f'(r_w) = 0$. This implies

$$\sin\theta(r_w) = -\frac{2\pi p(r_w^2 - C)}{\left[\omega^2 \rho\, r_w^3 + \frac{1}{\sin\alpha}\left(\mu + \nu\frac{\cos\alpha}{r_w}\right)\right]} = 0$$

and

$$C = r_w^{\,2}\,.$$

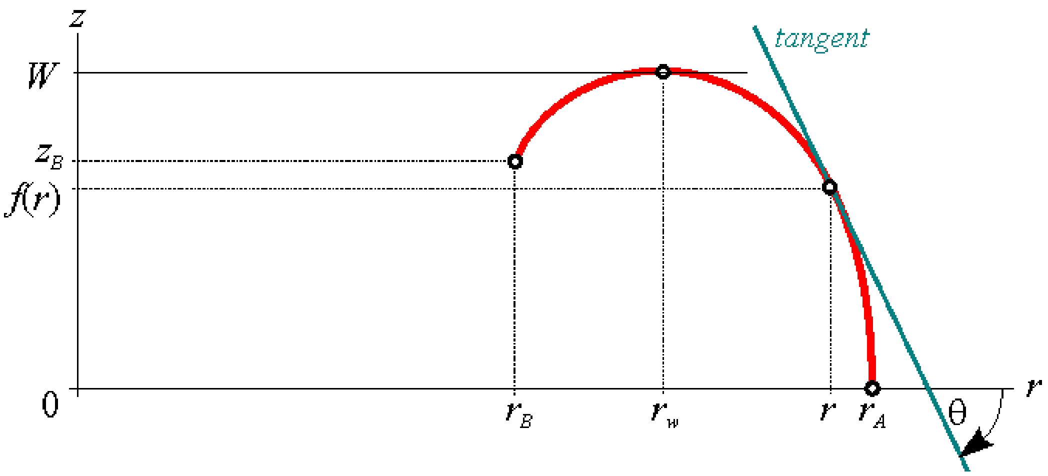

Figure 4.1 – Sketch of a typical carcass meridian curve.

The maximum radius – the upper boundary of the domain of function f is defined by the equality

$$\theta(a) = -\pi/2\,.$$

This in many cases represents the carcass equator with radius a, especially in diagonal tires or in tires without belt. Then (like in Figure 4.1)

$$a = r_A, \quad f(a) = 0.$$

For $r = a$ the equation (4.2) yields

$$\sin\theta(a) = -\frac{2\pi p(a^2 - r_w^2)}{\left[\omega^2 \rho(a)\, a^3 + \frac{1}{\sin\alpha(a)}\left(\mu + \nu\frac{\cos\alpha}{a}\right)\right]} = -1\,.$$

From here

$$\mu = [2\pi p(a^2 - r_w^{\,2}) - \omega^2\rho(a)\, a^3]\sin\alpha(a) - \nu\,\frac{\cos\alpha(a)}{a}\,.$$

This and the Equation (4.2) give

$$\sin\theta(r) = -\frac{2\pi p(r^2 - r_w^2)}{\left[\omega^2\rho(r)\, r^3 + \frac{1}{\sin\alpha(r)}\left(\mu + \nu\frac{\cos\alpha}{r}\right)\right]} = -\frac{2\pi p(r^2 - r_w^2)\sin\alpha(r)}{\left[\omega^2\rho(r)\, r^3 \sin\alpha(r) + \left(\mu + \nu\frac{\cos\alpha}{r}\right)\right]}$$

$$= -\frac{2\pi p(r^2 - r_w^2)\sin\alpha(r)}{\left[\omega^2\rho(r)r^3\sin\alpha(r) + \left([2\pi p(a^2 - r_w^2) - \omega^2\rho(a)a^3]\sin\alpha(a) - \nu\frac{\cos\alpha(a)}{a} + \nu\frac{\cos\alpha}{r}\right)\right]}$$

$$= \frac{-2\pi p(r^2 - r_w^2)\sin\alpha(r)}{\omega^2[\rho(r)r^3\sin\alpha(r) - \rho(a)a^3\sin\alpha(a)] + 2\pi p(a^2 - r_w^2)\sin\alpha(a) + \nu\left(\frac{\cos\alpha(r)}{r} - \frac{\cos\alpha(a)}{a}\right)}. \tag{4.3}$$

This general formula includes several important cases. The cosine (pantographic) expansion rule (Section 3.3) eliminates the constant ν due to its multiplication by 0, i.e. it makes the conditions (4.1) dependent ($\Phi[f] = L[f]\cos\alpha(a)/a$). If in this case $\omega = 0$ (static condition), the influence of mass distribution is annulled and one obtains the well known formula (e.g. Hofferberth [2], Biderman [3,25])

$$\sin\theta(r) = -\frac{(r^2 - r_w^2)\sin\alpha(r)}{(a^2 - r_w^2)\sin\alpha(a)} .$$

Knowledge of the function $\sin\theta(r)$ enables calculating the function f by means of numerical integration,

$$f(r) = f(r_B) + \int_{r_B}^{r} \frac{\sin\theta(u)}{\sqrt{1-\sin^2\theta(u)}}\,\mathrm{d}u$$

or, more generally,

$$f(r) = f(r_0) + \operatorname{sign}(r - r_0)\int_{r_0}^{r} \frac{\sin\theta(u)}{\sqrt{1-\sin^2\theta(u)}}\,\mathrm{d}u ,$$

where the free integration variable (radius) is denoted by u to prevent ambiguity.

Since $\sin\theta(a) = -1$, the square root $\sqrt{1-\sin^2\theta(u)}$ tends to 0 for $u \to a-$. Thus, the integral $\int_{r_0}^{r}$ becomes singular and a special treatment is needed to compute it. The derivative $\frac{\mathrm{d}}{\mathrm{d}r}\sin\theta(r)$ is the curvature of the planar curve $z = f(r)$ [9],

$${}^1\kappa(r) = \frac{\mathrm{d}}{\mathrm{d}r}\sin\theta(r) = \frac{\mathrm{d}}{\mathrm{d}r}\frac{f'}{\sqrt{1+f'^2}} = \frac{f''\sqrt{1+f'^2} - f'\dfrac{f'f''}{\sqrt{1+f'^2}}}{1+f'^2} = \frac{f''}{(1+f'^2)^{3/2}} .$$

The curvature is final and different from zero. Hence, near the point $r = a$ the function f can be approximated by the arc of its osculation circle, $(a-R)^2 + z^2 = R^2$, where

$$R(a) = \left|\frac{1}{{}^1\kappa(a)}\right| .$$

The meridian curve can be computed in the two following steps:

§ First a small number ε (precision) is chosen, e.g. $\varepsilon=10^{-4}$, and the osculating arc $z(r)=\sqrt{(2R-a+r)(a-r)}$ over the interval $[(1-\varepsilon)a,\ a]$ is constructed.

§ A decreasing sequence $(1-\varepsilon)a = r_0 > r_1 > r_2 > \ldots > r_n = r_B$ is chosen and coordinates

$$z_i = z(r_i) = z_{i-1} + \int_{r_{i-1}}^{r_i} \frac{\sin\theta(u)}{\sqrt{1-\sin^2\theta(u)}}\,\mathrm{d}u$$

are computed numerically (by Gauss' 3node formula, [10]).

The distances between points should be chosen dependently on changes of $f'(r)$, e.g. $|(r_i - r_{i-1})\, f'(r_{i-1})| \approx$ const for big $|f'(r_{i-1})|$. More details concerning preciseness, partitioning the interval $[r_B, a]$ etc. can be found in [10, 26-30].

4.2 Designing Problems

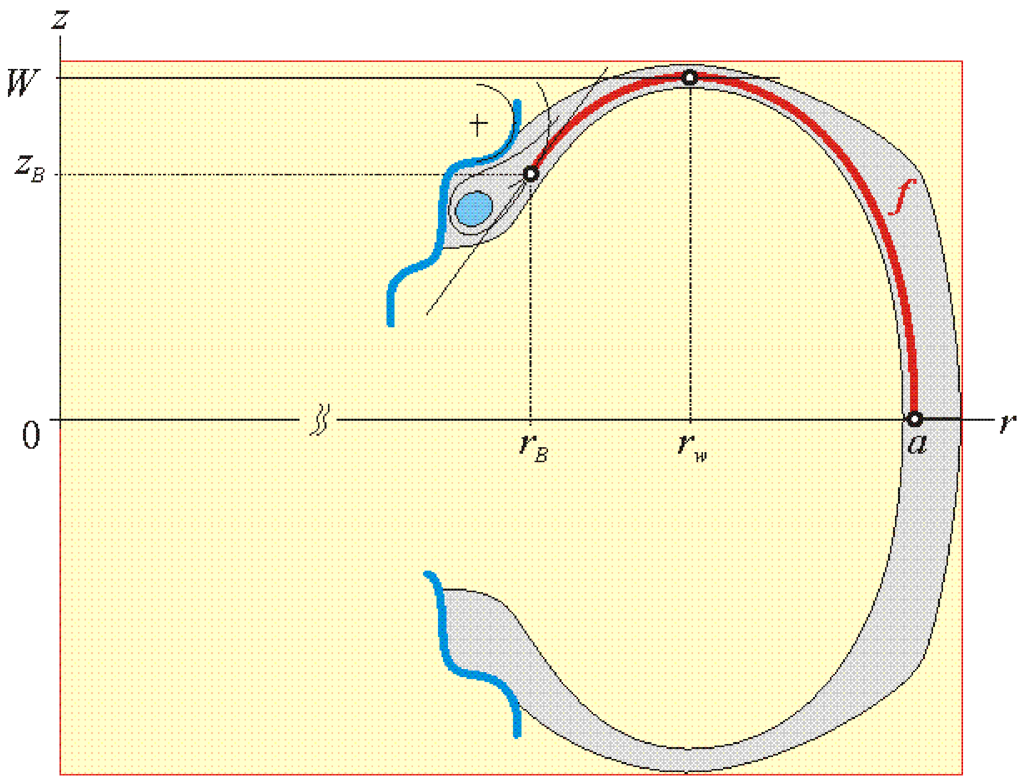

Figure 4.2 – A sketch of the problem (A) *for a diagonal tire given through its main dimensions.*

Static case plays a fundamental role in attaining the given (standard) dimensions of a tire on a prescribed rim because the declared tire width and diameter are measured on inflated and unloaded tire in static condition. Subtraction of thicknesses on equator, sidewall and beads gives a, W and an arc concentric with the arc of rim shoulder on which the bead point (r_B, z_B) is to be put. Figures 4.1, 4.2 show that the sought function shall satisfy the following conditions:

$$\left.\begin{aligned} f(r_B) &= \int_{r_B}^{a} \frac{\sin\theta(u)}{\sqrt{1-\sin^2\theta(u)}}\,\mathrm{d}u = z_B, \\ f(r_w) &= \int_{r_w}^{a} \frac{\sin\theta(u)}{\sqrt{1-\sin^2\theta(u)}}\,\mathrm{d}u = W. \end{aligned}\right\} \qquad (a, W, r_B, z_B)\ \ \mathbf{a}\ \ (r_w, \alpha(a)) \qquad \textbf{(A)}$$

There are no other conditions. Thus, if the cosine rule (cos) does not hold there may be infinitely many solutions of the equations (A) depending on the parameter $\nu/(2\pi p)$. If the cosine rule does hold and the solution of (A) exists, it is determined uniquely.

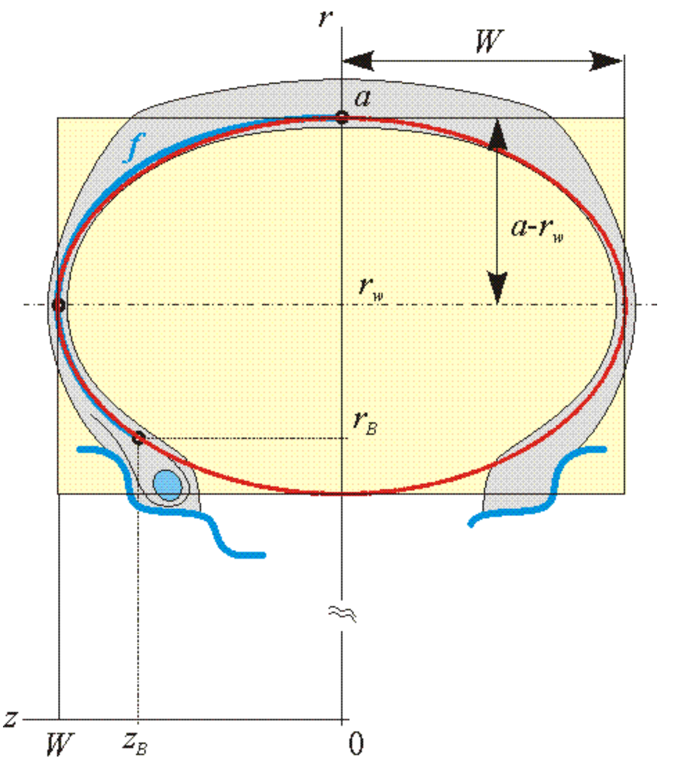

Figure 4.3 – Approximation of the meridian curve with the ellipse inscribed into rectangle given by main tire dimensions.

A good initial estimate may be obtained when the meridian curve is approximated by the ellipse inscribed into the $2W\times 2(a-r_B)$ rectangle and running through the bead point (r_B, z_B) (Figure 4.3). It yields

$$\frac{r_w}{a} \approx \frac{\dfrac{r_B}{a} + \sqrt{1-\left(\dfrac{z_B}{W}\right)^2}}{1+\sqrt{1-\left(\dfrac{z_B}{W}\right)^2}}\,.$$

Figure 4.4 shows a nomograph for an approximate solution of the problem (A). In this nomograph the parameter r_w/a determines a curve. Its intersection point with the abscissa line W/a determines the angle $\alpha(a)$.

In [29] there is also an application of the Gauss' method described in a more detailed way. This method is a two-dimensional analogue of the secant method in the case of a system of two nonlinear equations [10]. Another method can be found in [31].

Remark. One could use also other kinds of curves to approximate the meridian curve, e.g. some kind of spirals.

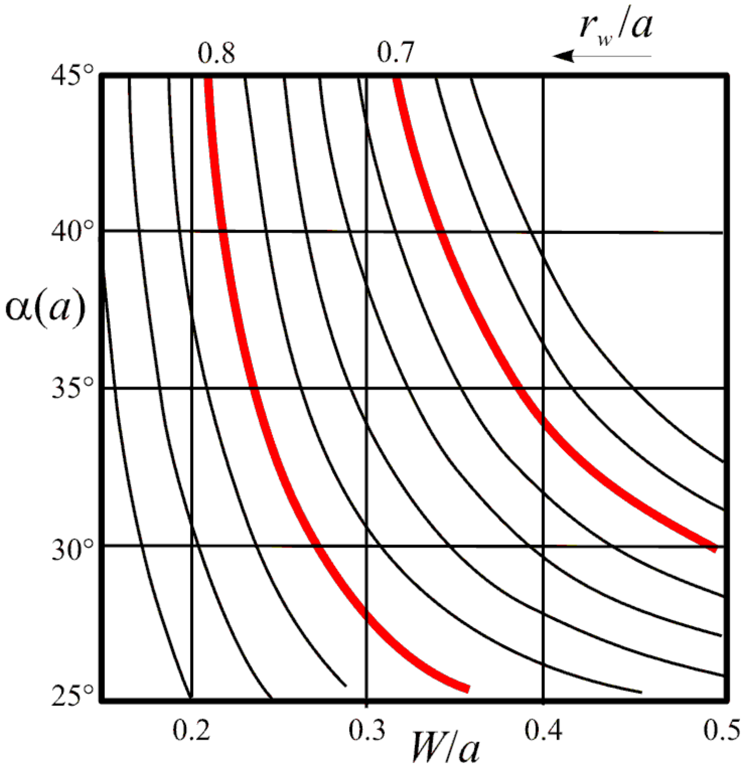

Figure 4.4 – Nomograph for approximate determining r_w and $\alpha(a)$ in inflated diagonal tire.

If the second condition in the system (A) is substituted by two isoperimetric conditions (4.1) the following system of equations arises

$$\left.\begin{aligned} f(r_B) &= \int_{r_B}^{a} \frac{\sin\theta(r)}{\sqrt{1-\sin^2\theta(r)}}\,\mathrm{d}r = z_B, \\ L[f] &= \int_{r_B}^{a} \frac{\sqrt{1+f'^2(r)}}{\sin\alpha(r)}\,\mathrm{d}r = l_{AB}, \\ \Phi[f] &= \int_{r_B}^{a} \frac{\sqrt{1+f'^2(r)}}{r\tan\alpha(r)}\,\mathrm{d}r = \phi_{AB} \end{aligned}\right\} (L, \Phi, r_B, z_B)\ \mathbf{a}\ (a, r_w, \nu) \qquad \textbf{(B)}$$

that represents the so called problem (B). This system of three nonlinear equations should warrant unique determination of the three unknown parameters a, $\nu/(2\pi p)$ and r_w. The problem (B) may be viewed as a transcription of the original problem of the search for the equilibrium meridian curve of the diagonal carcass (the word diagonal relates to $\alpha(r)<\pi/2$ while radial means $\alpha(r)=\pi/2$).

Solution of the system (B) for a chosen equator radius $\tilde{a}$ and a fictive eligible function $\tilde{\alpha}(r)$ may be used to design the mold for the developed tire [30].

As soon as the polar angle between both the cord ends in beads, $2\phi_{AB}$, is once set up on the building drum, it remains practically preserved during the next production steps and in exploitation as well. Conversely, the cord length, $2l_{AB}$, especially in nylon or polyester materials, may change due to tension induced by inflation pressure, elasticity and creep. This must be taken into account and the carcass meridian curve in mold may be computed according to the assumed reduced cord length, $2\tilde{l}_{AB}$, and possible axial bead displacement, $z_B \rightarrow \tilde{z}_B$ (Figure 4.5). The fixed angle ϕ_{AB} can be attained naturally by reduced values of the function $\alpha(r)$. The radius of carcass equator remains eligible, but it is usually chosen $\tilde{a} \leq a$. Thus, for a given expansion rule an angle α_D must be found that substitutes the unknown a in (B).

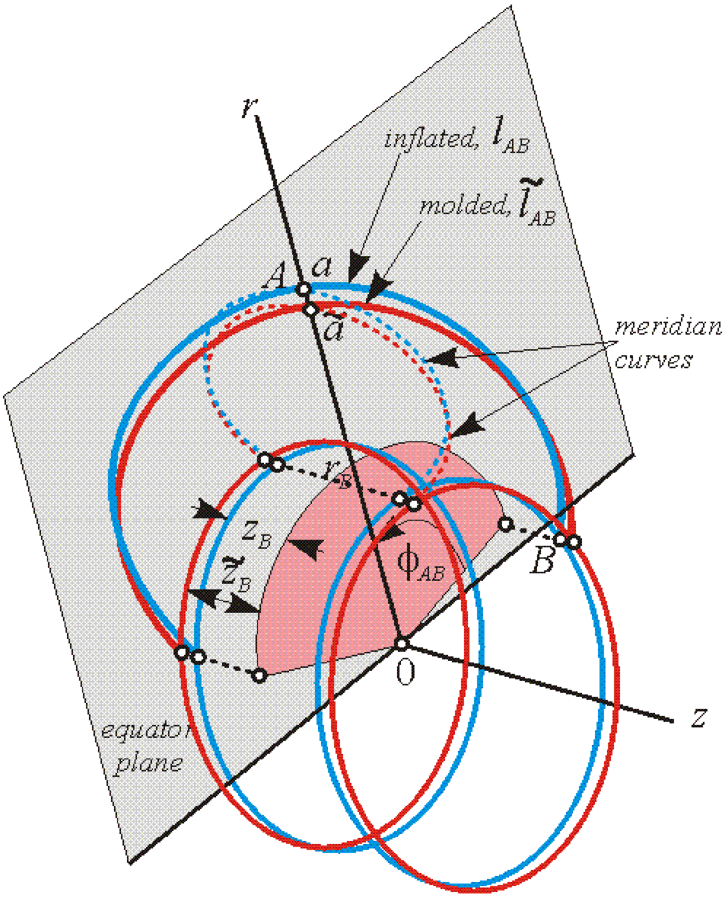

Figure 4.5 – Paths of the same carcass cord in mold and in inflated tire.

Solution of problems (A) and (B) does not exist whenever one likes. Also practical computation is relatively difficult. Those problems are discussed in more detail e.g. in [29,30]. In [30] the influence of rotating velocity on the tire shape, e.g. that of mass distribution is discussed.

Nevertheless, diagonal tires have turned to be rather a specialized sort of tires today. So we can abandon this topic.

4.3 Special Cases

4.3.1 Tubular Tire

Tubular tire is a toroidal pressure vessel with a closed meridian curve (Figure 4.6). Minimizing negative consequences of hysteretic losses leads to small thickness of carcass composite and tubeless construction [32].

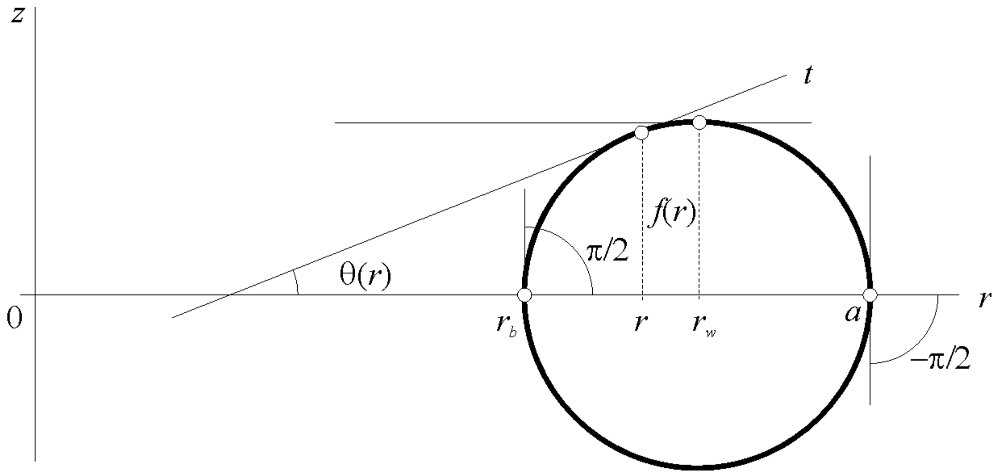

Figure 4.6 – A schematic of the tubular tire meridian.

Due to small expansion ratios of carcass (not exceeding 1.1) one could use any of expansion rules of the section 3.3. With respect to tradition, however, the usual cosine rule and the basic formula are preferable

$$\sin\theta(r) = -\frac{(r^2 - r_w^2)\sin\alpha(r)}{(a^2 - r_w^2)\sin\alpha(a)} .$$

The closeness of the meridian curve implies the following boundary conditions at the endpoints r_b, a of the meridian function f :

$$f(r_b) = 0, \quad \sin\theta(r_b) = 1,$$
$$f(a) = 0, \quad \sin\theta(a) = -1.$$

Let us define r_w by the equation $\sin\theta(r_w) = 0$. The cosine rule and introducing $t_b = r_b/a$, $t_w = r_w/a$ yield immediately

$$\cos\alpha(a) = \sqrt{\frac{1 - 2t_w^2 + t_b^2}{(1 + t_b^2)(1 - 2t_w^2) + t_b^4 + t_w^4}} .$$

This enables to solve the boundary problem by means of one parameter t_w.

Solutions of several boundary problems for r_b/a = 0.1, 0.3, 0.5, 0.7, 0.9 are shown in Figure 4.7.

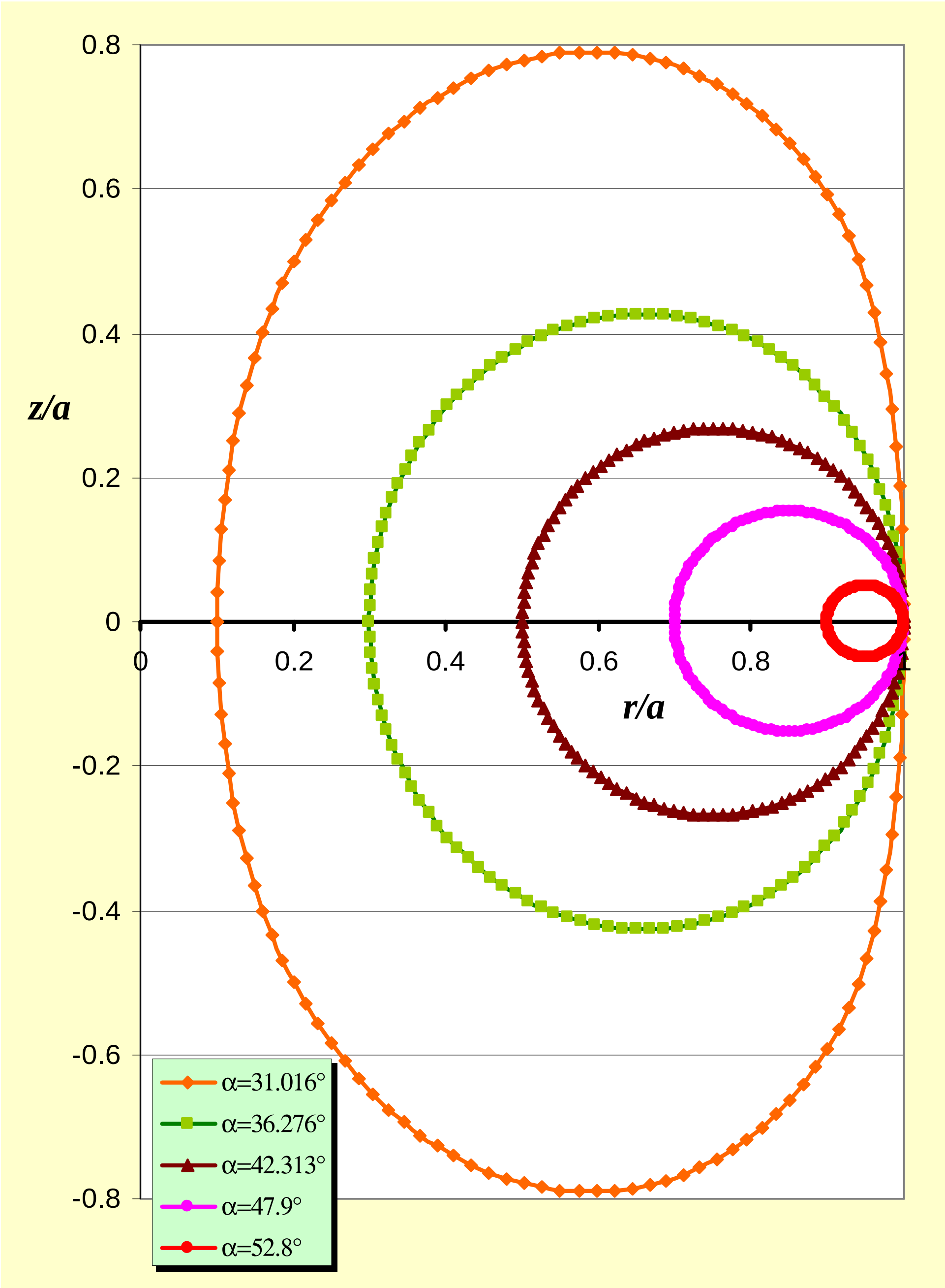

Figure 4.7 – Meridians of closed toroidal cord-rubber composite membrane related to the equator radius a and several bottom radii r_b.

If such a meridian curve is taken as mold profile and the angle α_{cord} between cord and equator is chosen arbitrarily, then the equation

$$g(R) \equiv \alpha(R) - \arccos\left(\frac{R}{a}\cos\alpha_{\text{cord}}\right) = 0$$

defines the corresponding equator radius R after inflation. This equation must be solved numerically [10]. $R_0 = \dfrac{a\cos\alpha(a)}{\cos\alpha_{cord}}$ gives a good estimate of R.

Example. Let us choose a = 330mm, r_b = 305mm. The corresponding meridian curve shown in Figure 4.8 is chosen for the meridian of molded carcass. Solving the boundary problems gives: t_w = 0.962135, $\alpha(a)$ = 53.41646°, L = 47.96014mm, Φ = 0.08662rad., V = 0.979448dm^3. The cord angle for building the tubular tire is chosen α_{cord} = 50°. Then the corresponding cord length is

$$L_{cord} = \int_{r_b}^{a} \frac{\sqrt{1+f'^2(r)}}{\sin\alpha_{cord}(r)}\,\mathrm{d}r = \int_{r_b}^{a} \frac{\sin\alpha(r)}{\sin\alpha_{cord}(r)} \frac{\sqrt{1+f'^2(r)}}{\sin\alpha(r)}\,\mathrm{d}r \approx \frac{\sin\alpha(a)}{\sin\alpha_{cord}} L$$

$$= \frac{\sin 53.41646°}{\sin 50°} 47.96014\text{mm} = 50.27313\text{mm}.$$

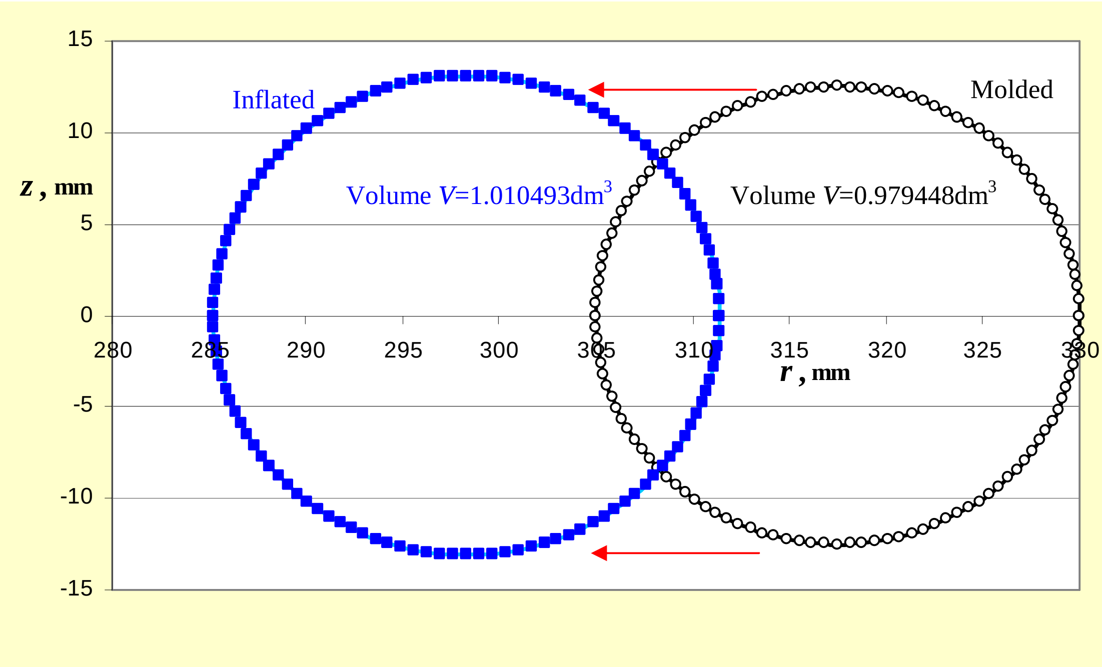

Figure 4.8 – Meridian curves of molded and inflated cord-rubber composite membrane with α_{cord} = 50° < 53.4° = $\alpha(a)$.

Now the new equilibrium equator radius R is to be found. It may be expected in the neighborhood of $\dfrac{a\cos 53°}{\cos 50°} \approx 310$. A simple program in DELPHI was set up to find the equilibrium meridian curve for the couple (L, R). It gives:

$$R_0 = 310\text{mm} \longrightarrow \alpha_0 = 53.199405°, \quad g_0 = -0.30091,$$

$$R_1 = 315\text{mm} \longrightarrow \alpha_1 = 53.232299°, \quad g_1 = +0.418857.$$

The inverse interpolation yields

$$R_{01} = \frac{1}{g_1 - g_0}\begin{vmatrix} 0-g_0 & R_0 \\ 0-g_1 & R_1 \end{vmatrix} = 312.09\text{mm}, \qquad g(R_{01}) = 0.00068.$$

Another iteration step may be performed with R_0 = 312mm and $R_1 = R_{01}$. One obtains R = 311.4323mm, which yields the angle $\alpha(R)$ = 53.304177° and $g(R) = -1.8\times10^{-7}$. Thus, it can be taken as the solution of the problem. Repeating the computation with this new value of R gives the meridian curve shown on the left side of Figure 4.8.

This computation can be fully automated, of course.

Integrity of the wheel/tire system on the road requires the tubular tire to diminish its diameter when inflated in the free condition, i.e. its behavior must be similar to that shown in Figure 4.8.

Figure 4.9 shows general trend of equator and meridian changes with increasing the carcass cord angle. If the mold meridian curve determined by the couple of a and $\alpha(a)$ remains the same then due to the inflation the free tubular tire radius R increases or decreases according to the difference $\alpha_{cord} - \alpha(a)$ while the volume V of the tire increases in any case.

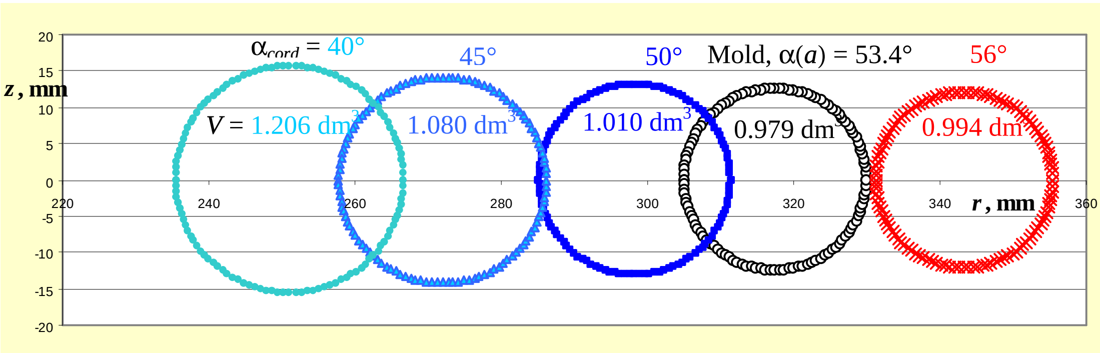

Figure 4.9 – Meridian curves of molded and inflated cord-rubber composite membrane with different cord angles α_{cord}.

Considerable changes in cord carcass angle α_{cord} produce but small changes in the resulting equilibrium angle $\alpha(R)$ as shown in Figure 4.10. The equilibrium meridian curves are therefore similar and almost circular ones.

These considerations represent an approximation of the real behavior of tubular tires because they neglect the stress-strain behavior of cords, which is not negligible at usual high inflation pressures in tubular tires (up to 1.2MPa and more). Nevertheless they are very realistic in the range of the cord angles α_{cord} between 40° and 60°.

The radius R is strictly limited from above by the cosine rule that gives

$$R \leq \frac{a}{\cos\alpha_{cord}}.$$

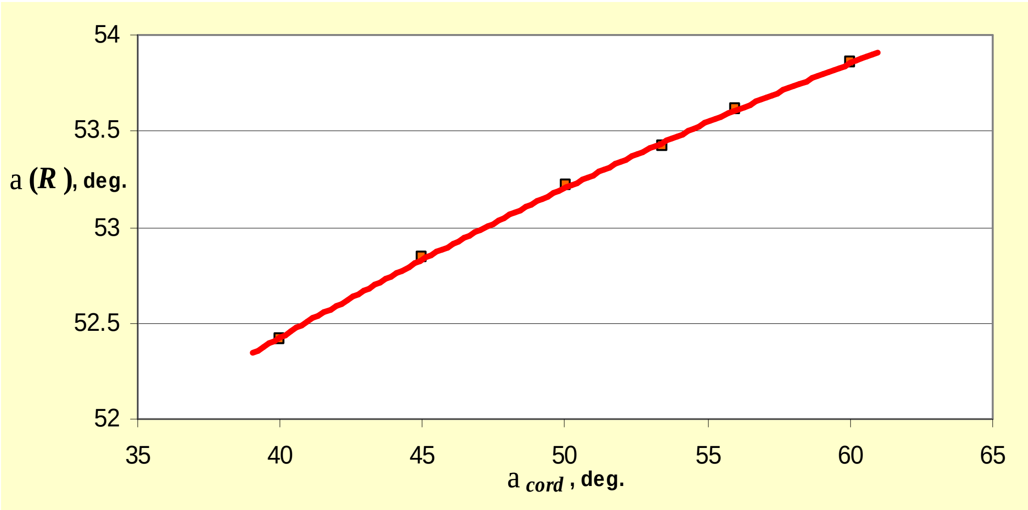

Figure 4.10 – The resulting equilibrium angle $\alpha(R)$ *depends only weakly on the cord angle* α_{cord} *in building the carcass.*

4.3.2 Radial Carcass

Radial carcass is characterized by identity

$$\alpha(r) = \frac{\pi}{2}$$

that reduces the Equation 4.3 as follows

$$\sin\theta(r) = \frac{-(r^2 - r_w^2)}{\frac{\omega^2}{2\pi p}\left[\rho(r)\,r^3 - \rho(a)\,a^3\right] + (a^2 - r_w^2)}. \tag{4.4}$$

The fraction $\frac{\omega^2}{2\pi p}$ reflects the antagonistic influence of the velocity and inflation pressure on the shape of the rotating radial carcass.

In static case the formula (4.4) is simplified to

$$\sin\theta(r) = \frac{-(r^2 - r_w^2)}{a^2 - r_w^2} = \frac{-(r^2 - a^2 + a^2 - r_w^2)}{a^2 - r_w^2} = \frac{1-\left(\frac{r}{a}\right)^2}{1-\left(\frac{r_w}{a}\right)^2} - 1.$$

Introducing the dimensionless parameter

$$\lambda = \frac{1-\left(\frac{r_w}{a}\right)^2}{2} \tag{4.5}$$

brings the following simplification

$$\sin\theta(r) = \frac{1-\left(\frac{r}{a}\right)^2}{2\lambda} - 1. \tag{4.6}$$

Then

$$f(r;\,a,\,\lambda) - f(a) = \begin{cases} a[E-(1-2\lambda)F] & \lambda < \frac{1}{4}, \\ a[S + \frac{1}{2}\ln\frac{a(1-S)}{r}] \quad \text{for} & \lambda = \frac{1}{4}, \\ a\frac{2E-F}{2k} & \lambda > \frac{1}{4}, \end{cases} \tag{4.7}$$

where

$$F = F(k,\,\phi(r)) = \int_0^{\phi(r)} \frac{d\phi}{\sqrt{1-k^2\sin^2\phi}} \;,$$

$$E = E(k,\,\phi(r)) = \int_0^{\phi(r)} \sqrt{1-k^2\sin^2\phi}\; d\phi \;,$$

are elliptic integrals of the 1st and 2nd kind in Legendre's normal form,

$$S = S(r) = \sqrt{1-\frac{r^2}{a^2}}\,,$$

$$k^2 = 4\lambda \quad \text{and} \quad \phi(r) = \arcsin\frac{S(r)}{k} \quad \text{for} \quad \lambda < \frac{1}{4},$$

$$k^2 = \frac{1}{4\lambda} \quad \text{and} \quad \phi(r) = \arccos\frac{r}{a} \quad \text{for} \quad \lambda > \frac{1}{4}.$$

Several examples can be seen in Figure 4.11.

The length l of an arc of the meridian curve over an interval $[r,\,a]$ may be computed as follows [33]

$$l(r;\,a,\,\lambda) - l(a) = \begin{cases} 2a\lambda F & \lambda < \frac{1}{4}, \\ a\ln\frac{(1-S)}{4} \quad \text{for} & \lambda = \frac{1}{4}, \\ \frac{aF}{\sqrt{\lambda}} & \lambda > \frac{1}{4}. \end{cases}$$

Similarly, the volume V of the corresponding cavity

$$V(r;\,a,\,\lambda) = 4\pi\int_r^a r\,f(r;\,a)\,dr = 2\pi\,[a^2 f(a) - r^2 f(r;\,a) - I(r)]\;.$$

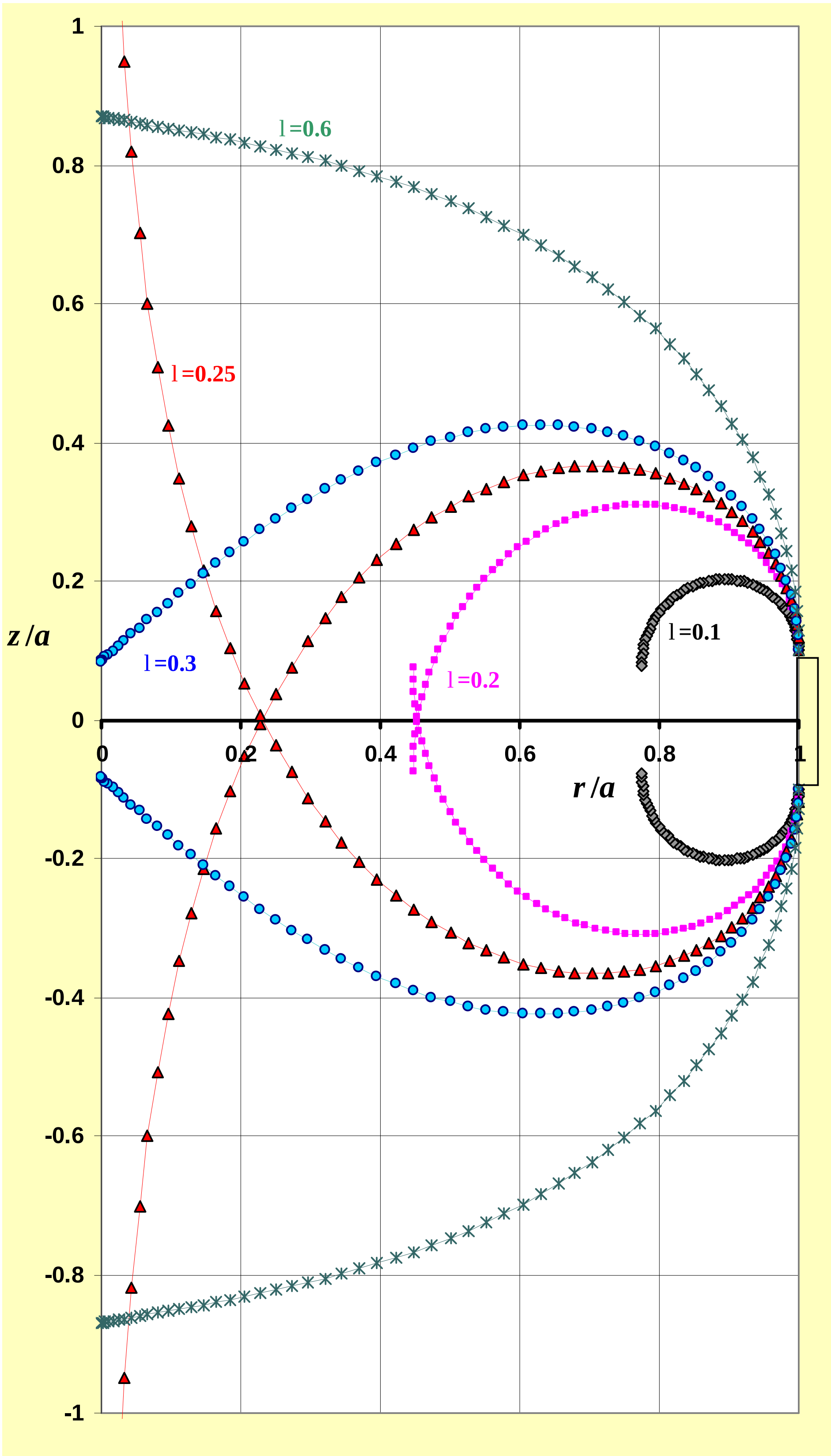

Figure 4.11 – Functions f(r; λ, a)/a for f(a)/a = 0.1 and several λ.

Here, on the right side,

$$I(r) = \int_r^a r^2 \tan\theta(r)\,\mathrm{d}r = a^3 \int_{r/a}^{1} \frac{t^2(1-2\lambda-t^2)}{\sqrt{(1-t^2)(4\lambda-1+t^2)}}\,\mathrm{d}t$$

$$= \begin{cases} a^3(1+2r^2/a^2)\,S(r)/6 & \text{for } \lambda = \frac{1}{4}, \\ a^3[H(\phi(r)) - H(\phi(a))]/6 & \phantom{\text{for }} \lambda \neq \frac{1}{4} \end{cases}$$

where

$$H(\phi(r)) = \begin{cases} 2F(k^2-1)+(2-k^2)E+J(\phi(r)) & \text{for } \lambda < \frac{1}{4} \\ [F(1-k^2)+(2k^2-1)E+J(\phi(r))]/k^3 & \phantom{\text{for }} \lambda > \frac{1}{4} \end{cases}$$

and

$$J(\phi(r)) = k^2 \sin(2\phi(r)) \sqrt{1-k^2\sin^2\phi(r)} \ .$$

Figure 4.12 shows that the theory presented here can be almost immediately used in overpressure expansion of the radial carcass in the second stage of radial tire building [34]. The basic task is to minimize the energy E needed for joining together the belt and the carcass. The shape of carcass is controlled by the distance d_B between its beads, $E(d_B) = g(f(a;\ d_B))$. Obviously, a = const. and $\partial f(a;\ d_B)/\partial d_B = 0$ implies $\mathrm{d}E(d_B)/\mathrm{d}d_B = 0$, so the width of contact area 2 $f(a;\ d_B)$ is to be maximized.

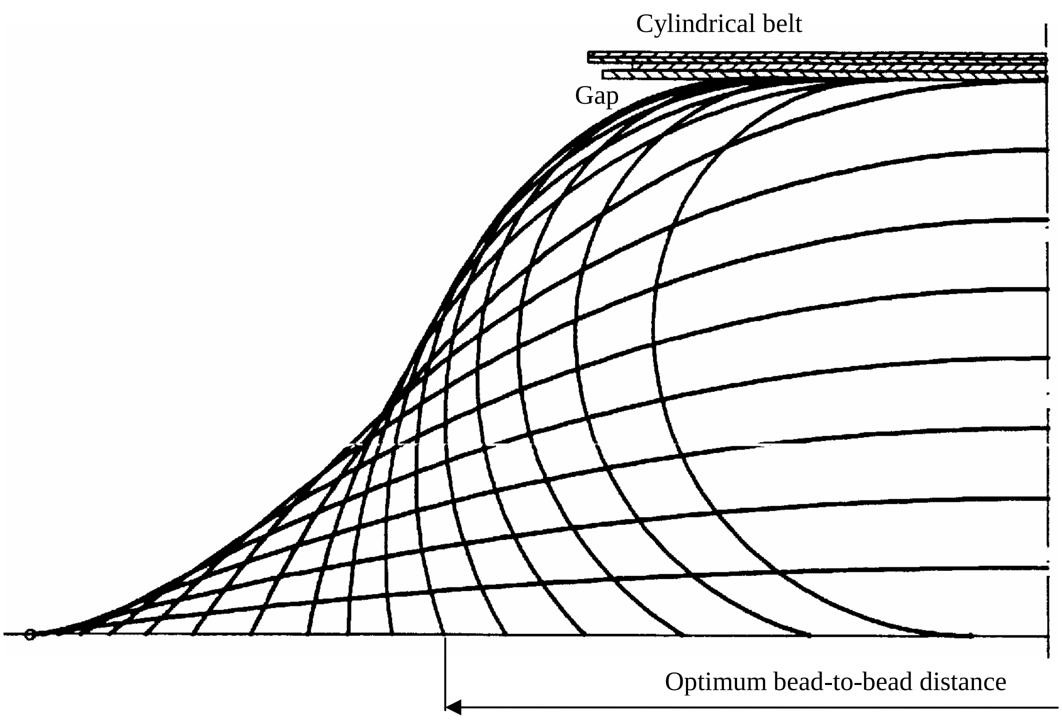

Figure 4.12 – Radial carcass expansion.

4.3.3 Isotropic Axisymmetric Linearly Elastic Membrane

The meridian curve of a linearly elastic isotropic membrane can be found when solving the problem

$$p\left[\frac{V_0}{2\pi}-\int_{r_B}^{a} rf(r)\,\mathrm{d}r\right]+\frac{E}{2}\left[\int_{r_B}^{a} h(r)\,r\sqrt{1+f'^2(r)}\,\mathrm{d}r-h_0A_0\right]\longrightarrow \min.$$

where V_0 is an initial volume bounded by the non-extended membrane, E is the elasticity constant in Nm^{-2}, A_0 is the initial area and h is the thickness of the membrane. The membrane is supposed to expand in all directions uniformly. The additive constants do not influence the extreme behavior of the energy sum on the left side. Thus, one can introduce an energy function

$$F(r, f, f') = -2pr\,f(r) + Eh(r)r\sqrt{1+f'^2(r)}\,.$$

The corresponding Euler-Lagrange equation [13]

$$\frac{\mathrm{d}}{\mathrm{d}r}\left(\frac{\partial F}{\partial f'}\right)-\frac{\partial F}{\partial f} = \frac{\mathrm{d}}{\mathrm{d}r}\Big(Ehr\,\frac{f'}{\sqrt{1+f'^2}}\Big) + 2pr = 0$$

can be easily integrated (as usual we put $\dfrac{f'}{\sqrt{1+f'^2}} = \sin\theta$)

$$E\,h(r)\,r\sin\theta + p\,r^2 = C = \text{const.}$$

The parameter a denotes the radius at which $\theta(a) = -\pi/2$ ($\sin\theta(a) = -1$). Thus,

$$C = pa^2 - Eha = a(pa - Eh(a))$$

and

$$\sin\theta(r) = \frac{a(pa-E\,h(a))-pr^2}{E\,h(r)\,r} = p\,\frac{a^2-r^2}{E\,h(r)\,r}-\frac{a\,h(a)}{r\,h(r)}\,.$$

Let us consider the simplified case when the thickness $h(r)$ is constant (independent of r), i.e. $h(r) = h_0$. Then

$$\sin\theta(r) = \frac{p}{Eh_0}\,\frac{a^2-r^2}{r}-\frac{1}{r/a} = \frac{pa^2}{Eah_0}\,\frac{1-(r/a)^2}{r/a}-\frac{1}{r/a}\,.$$

If a new variable $t = r/a$ is introduced and $K = \dfrac{pa}{Eh_0} > 0$ is a new constant, then

$$\sin\theta(t) = \frac{K(1-t^2)-1}{t}\,.$$

Obviously, $t = 1$ determines the upper end of the domain of f, $\sin\theta(1) = -1$. The lower boundary of the domain of f, $t = t_b$, is defined by $\sin\theta(t_b) = 1$ for $K \geq 1$ and $\sin\theta(t_b) = -1$ for $0 < K < 1$, i.e.

$$t_b = \begin{cases} 1-1/K & \text{for } K\geq 1 \\ 1/K-1 & \phantom{\text{for }} K<1 \end{cases}.$$

The role of the parameter K in case of fixed boundary is illustrated in Figure 4.13.

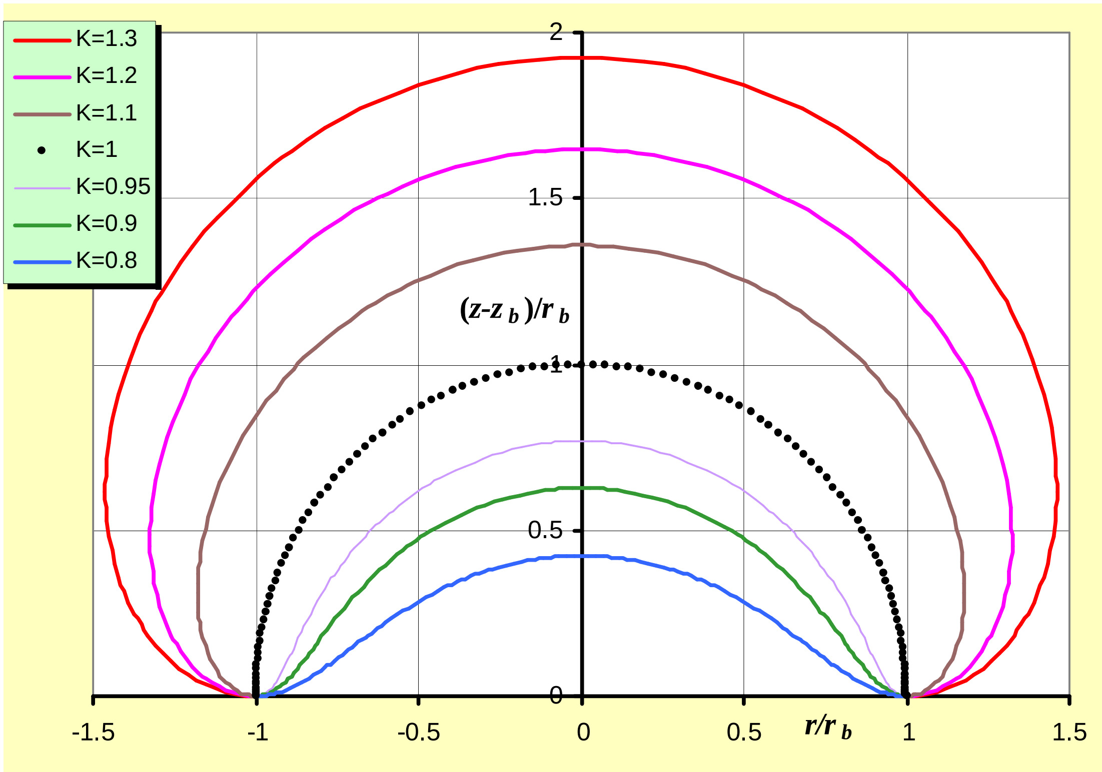

Figure 4.13 – Meridian curves of axisymmetric, isotropic and linearly elastic membrane.

After several simple arrangements the meridian curve can be expressed by means of elliptic integrals in the following way:

$$f(r) = a \int_{r/a}^{1} \frac{\sin\theta(t)}{\sqrt{1-\sin^2\theta(t)}}\,\mathrm{d}t = a \int_{r/a}^{1} \frac{\dfrac{K(1-t^2)-1}{t}}{\sqrt{1-\left(\dfrac{K(1-t^2)-1}{t}\right)^2}}\,\mathrm{d}t$$

$$= a \int_{r/a}^{1} \frac{K(1-t^2)-1}{\sqrt{t^2-\left(K(1-t^2)-1\right)^2}}\,\mathrm{d}t = a \int_{r/a}^{1} \frac{(1-1/K)-t^2}{\sqrt{(1-t^2)(t^2-(1-1/K)^2)}}\,\mathrm{d}t.$$

In the important case of $K > 1$ (Figure 4.14) one obtains

$$f(r) = a\,[E(k,\phi) - (1-1/K)\,F(k,\phi)]\,,$$

where

$$k = \sqrt{1-(1-1/K)^2} = \frac{\sqrt{2K-1}}{K} \quad \text{and} \quad \phi = \arcsin\left(K\sqrt{\frac{1-t^2}{2K-1}}\right).$$

The special case of $K = 1$ yields $k = 1$, $\phi = \arcsin\sqrt{1-t^2}$, i.e.

$$f(r) = a\,E(1, \phi) = \int_0^{\phi(r)} \sqrt{1-\sin^2\phi}\;\, d\phi \;= a \int_0^{\phi(r)} \cos\phi\;\, d\phi \;= \sin\left(\arcsin\sqrt{1-t^2}\,\right)$$

$$= a\sqrt{1-t^2}\,.$$

In other words, $K = 1$ gives $f^2(r) = a^2(1 - t^2) = a^2 - (at)^2$, i.e. a circle

$$f^2(r) + r^2 = a^2.$$

This result can be obtained directly considering the curvature of the meridian curve [9]

$$\kappa(t) = \frac{1}{a}\left|\frac{d}{dt}\sin\theta(t)\right| = \frac{1}{a}\left|\frac{\mathrm{d}}{\mathrm{d}t}\left(-Kt + \frac{K-1}{t}\right)\right| = \frac{1}{a}\left|-K - \frac{K-1}{t^2}\right|,$$

where K=1 implies $\kappa(t) = \dfrac{1}{a}$.

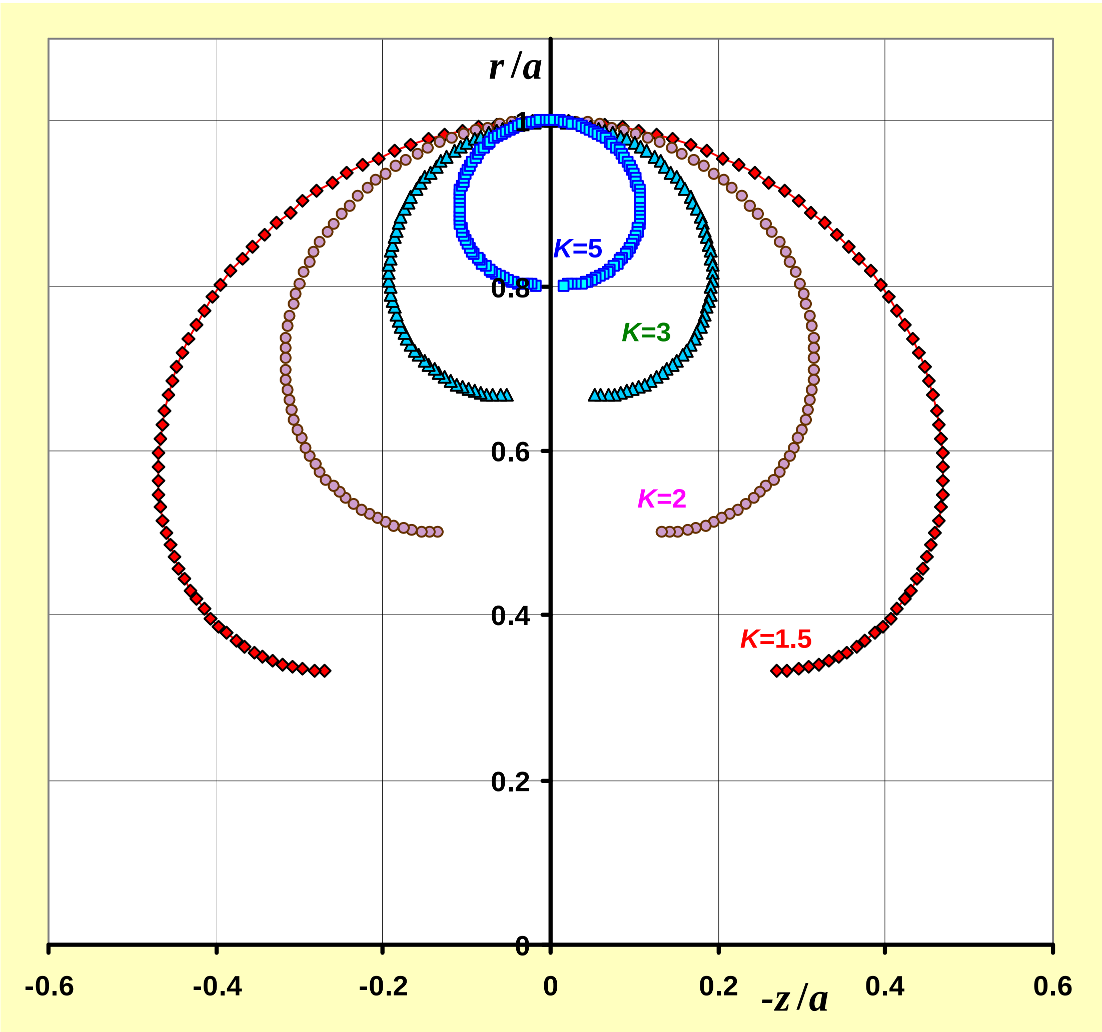

Figure 4.14 – Meridian curves of axisymmetric, isotropic and linearly elastic membranes for several K>1.

The behavior of the meridian curve near the lower boundary of its domain ($r = at_b$) signalizes a loss of stability – a phenomenon that is manifested by corrugating the surface of the internal part (i.e. facing towards the axis of revolution) of free tubes when they are inflated.

Another approach to the search for the shape of isotropic (flexible but inextensible) membrane or tire can be found in [35].

Remark. Considering r as a function of z, $r(0) = r_b$, $r(H) = 0$ leads to the following expression of volume $V = \pi \int_0^H r^2 \,\mathrm{d}z$. Integration by parts gives

$$\pi \int_0^H r^2 \,\mathrm{d}z = \pi r^2 z \Big|_{z=0}^{z=H,\, r=0} - 2\pi \int_0^H rz \,\mathrm{d}z = -2\pi \int_0^H rz \,\mathrm{d}z \,.$$

The variable z is the internal one and may therefore be denoted by r while the original r may be denoted otherwise arbitrarily. In this way we get the problem of maximizing the standard volume integral $\int_{r_0}^{r_1} r f \,\mathrm{d}r$.

4.4 Radial Tire

A schematic cross-section of the radial tire was presented in Figure 1.1 and a 3D picture of carcass expansion is shown in Figure 4.15. The belt of cord-rubber composite is a substantial element of radial tire. Its circumferential stiffness is very high while its radial bending stiffness is quite low so it behaves like a usual girdle. The belt constricts the radial expansion of tire carcass as indicated in Figure 2.11.

The presence of belt as well as that of rim brings restriction conditions on the carcass meridian. They represent impenetrable areas and carcass comes in smooth contact with them, i.e. tangents of the carcass meridian and those of belt and bead area surface are identical at the borders of the contact areas [9, Section 6.4]. In first approximation the meridians of both the contact surfaces can be simply approximated by circles (Figure 4.16).

Let R_N be the radius of the belt circle

$$(r - (R_A - R_N))^2 + z^2 = R_N^2 \,,$$

ϑ the absolute value of angle between the common tangent and the positive direction of the r-axis and (r_ϑ, z_ϑ) the boundary point of the contact area. Because the point (r_ϑ, z_ϑ) is unknown it is advantageous to take the angle ϑ for a new parameter. The inverse value of the product of radius r_ϑ and the curvature ${}^1\kappa$ at (r_ϑ, z_ϑ) may be taken for the second parameter Λ (Figure 4.16)

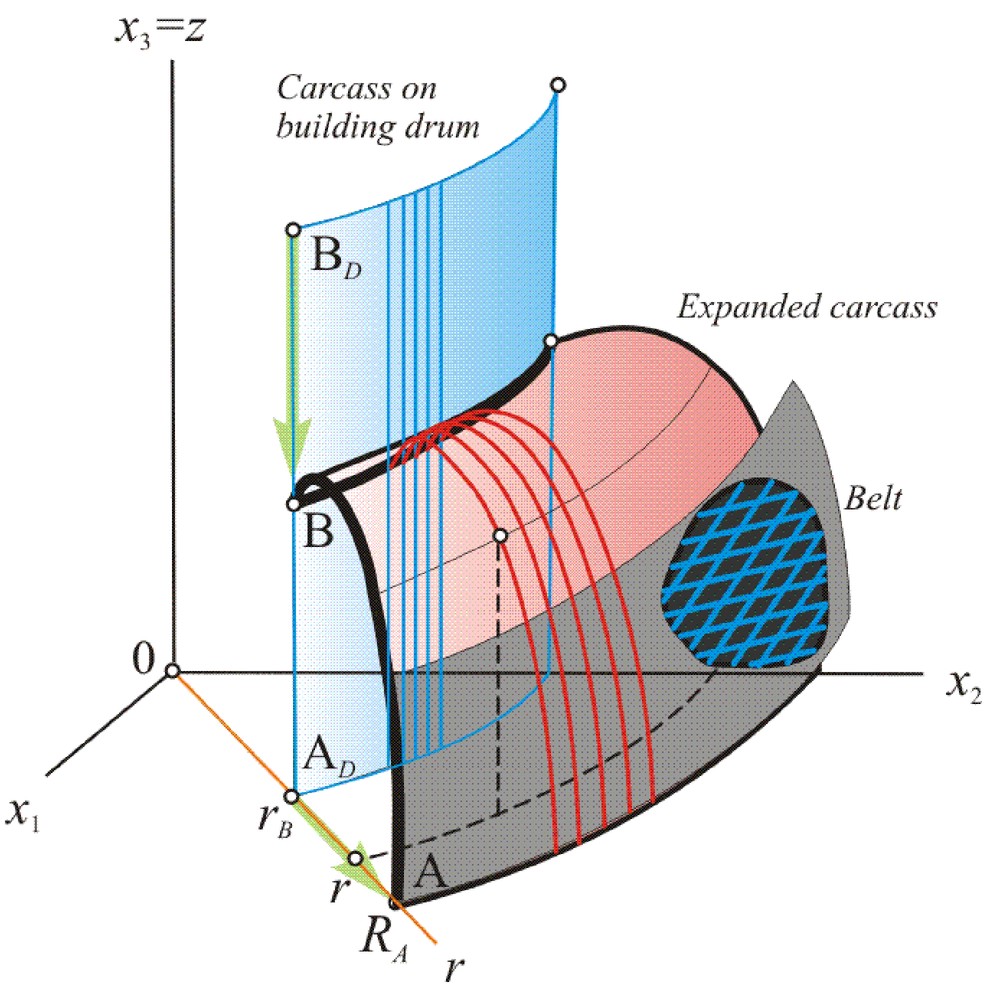

Fig. 4.15 – Schematic of radial carcass expansion.

$$\Lambda = \left| \frac{1}{r_\vartheta{}^1\kappa(r_\vartheta)} \right| = \frac{1}{r_\vartheta \left| \frac{\mathrm{d}}{\mathrm{d}r} \sin\theta(r_\vartheta) \right|} = \frac{1}{r_\vartheta \left| \frac{-2r_\vartheta}{a^2 - r_w^2} \right|} = \frac{a^2 - r_w^2}{2r_\vartheta^2} \ .$$

Now one obtains

$$\sin\vartheta = \left| \frac{r_\vartheta^2 - r_w^2}{a^2 - r_w^2} \right| = \frac{r_\vartheta^2 - r_w^2}{2\Lambda r_\vartheta^2} \ .$$

From here it follows

$$r_w = r_\vartheta \sqrt{1 - 2\Lambda \sin\vartheta} \ ,$$

$$a = r_\vartheta \sqrt{1 + 2\Lambda(1 - \sin\vartheta)} \ ,$$

$$\lambda = \frac{\Lambda}{1 + 2\Lambda(1 - \sin\vartheta)} \ .$$

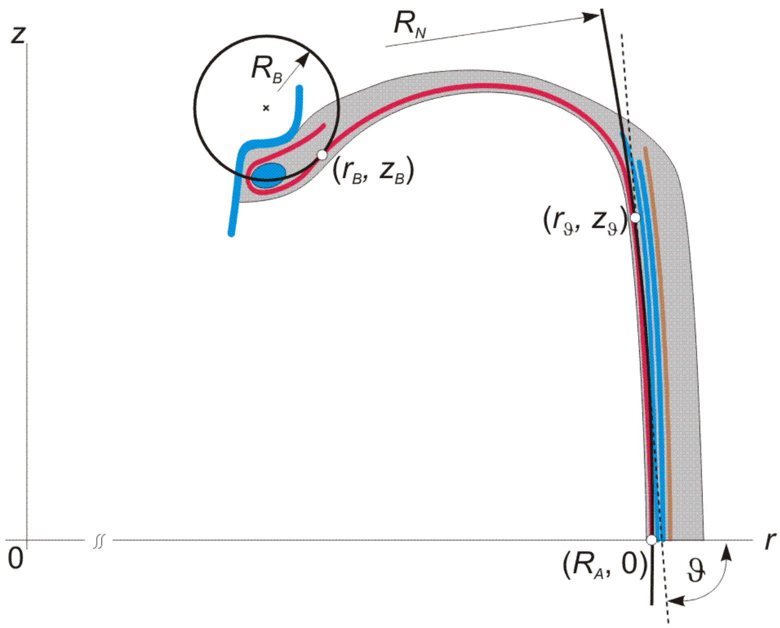

Figure 4.16 – Some parameters determining the geometry of radial tire carcass.

In this way the classification (4.7) is preserved and an apparatus for solving static boundary problems concerning the meridian curve of radial carcass is prepared. The simplest and most transparent method is the shooting method based on interpolation among solutions of corresponding initial problems [10]. More details can be found e.g. in [24].

This theory was presented in form of nomographs [36] enabling manual solving technical problems (A) and (B) from Section 4.2 also in radial tires [24,28]. Let us remark that the problem (A) remains unchanged but the problem (B) due to the identity $\Phi[f] \equiv 0$ is simplified as follows:

$$\left.\begin{aligned} f(r_B) &= \int_{r_B}^{a} \frac{\sin\theta(r)}{\sqrt{1-\sin^2\theta(r)}}\,\mathrm{d}r = z_B, \\ L[f] &= \int_{r_B}^{a} \sqrt{1+f'^2(r)}\,\mathrm{d}r = l_{AB}, \end{aligned}\right\} \quad (R_A, l_{AB}, R_N, r_B, z_B) \to (\Lambda, \vartheta) \qquad \textbf{(B)}$$

Both the problems (A), (B) as well as mold design require special computer codes, of course.

When designing mold the distance between beads is increased as usual to eliminate assembly problems (compressed air leaking between beads and rim especially in truck tires). The angular velocity ω can be employed to reduce the stress in tire wall. Also the carcass meridian length should be adapted to cord release in beads due to high temperature and plasticizing rubber matrix at the start of vulcanization process.

4.4 Strength Calculations

Material integrity is a necessary condition for performance capability of pneumatic tire running on the road or off the road. When a crack appears in the tire structure then the stress on its surface drops to zero and must be taken over by the material in the crack vicinity. This may lead to a very fast stress increase in that region which ends in total tire failure. Variability and especially impact components are characteristics of the tire load and their randomness makes it more difficult to estimate the stresses in conditions of usual traffic. Materials change their properties during the tire life as well. Thus, to assure sufficient safety the ratio of material strength versus its static load must be chosen relatively large.

Tire structure calculations may be based on various physical principles. In Section 2.3 there was shown a possibility of determining cord tension by general means of air volume changes. The air energy corresponding to the volume difference arisen by the restricting action of an external load is equal to the energy consumed in elongation of the considered component – the set of carcass cords. This idea can be used in calculating tension of belt and beads in radial as well as in diagonal tires [24,37,38]. This requires:

(i) possession of a code to compute the tire volume,

(ii) convenient displacement models to grasp changes caused by loading of considered elements (cord, belt, bead) – like those shown in Figure 4.17.

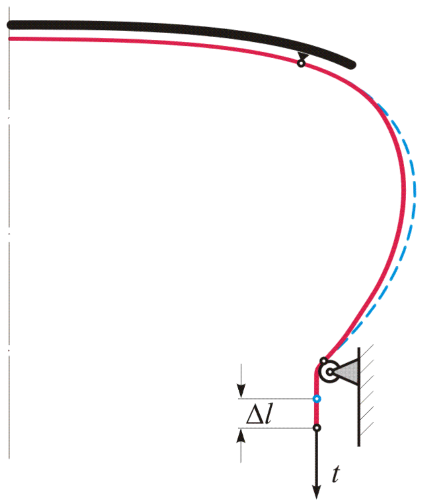

(a) Radial carcass cord tension

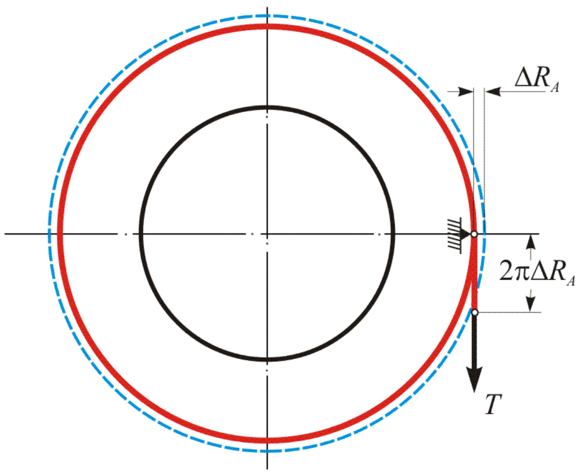

(b) Belt tension

Figure 4.17 – Models for evaluating volume changes due to: (a) radial carcass cord tension and (b) belt tension.

In radial carcass the law of conservation of energy (the first law of thermodynamics) yields

$$N\,t\,\Delta l/2 \approx W_{cord}(x) = W_{air}(x) = -\int_{V(l)}^{V(l-\Delta l)} p(V)\,\mathrm{d}V \ ,$$

where p denotes the internal air overpressure (inflation pressure) and N is the total number of carcass cords. The Boyle law implies

$$- \int_{V(l)}^{V(l-\Delta l)} p(V)\, \mathrm{d}V = -\, p(V(l))\, V(l) \int_{V(l)}^{V(l-\Delta l)} \frac{\mathrm{d}V}{V} = -\, p(V(l))\, V(l) \ln \frac{V(l-\Delta l)}{V(l)}$$

$$= -\, p(V(l))\, V(l) \ln\left(1 + \frac{V(l-\Delta l) - V(l)}{V(l)}\right) \approx p(V(l))\, V(l) \frac{V(l) - V(l-\Delta l)}{V(l)}$$

$$= p(V(l))\, (V(l) - V(l-\Delta l))\ .$$

Therefore, if N denotes the total number of carcass cords,

$$t = \lim_{\Delta l \to 0} p(V(l)) \frac{V(l) - V(l-\Delta l)}{\Delta l} = \frac{2}{N}\, p(V(l)) \frac{\mathrm{d}V}{\mathrm{d}l}(l)\ .$$

The belt tension can be derived similarly [37,38] :

$$T(R) = \lim_{\Delta R \to 0} p(V(R)) \frac{V(R+\Delta R) - V(R)}{2\pi\, \Delta R} = \frac{1}{2\pi}\, p(V(R)) \frac{\mathrm{d}V}{\mathrm{d}R}(R)\ .$$

This idea may be generalized to any external force $F(x)$ whose point of action moves by a longitudinal segment $g(x)$, where x is a parameter [37]. Then

$$W_{mech}(x) = \int_{g(x_0)}^{g(x)} F(t)\, \mathrm{d}t = - \int_{V(x_0)}^{V(x)} p(V)\, \mathrm{d}V = W_{air}(x)$$

and differentiation with respect to x gives

$$F(g(x)) \frac{\mathrm{d}}{\mathrm{d}x} g(x) = p(V(x)) \frac{\mathrm{d}}{\mathrm{d}x} V(x)\ .$$

For example: $x = \Delta l$, $g(x) = 2x$ in the cord tension and $x = \Delta R_A$, $g(x) = 2\pi x$ in the belt tension.

•

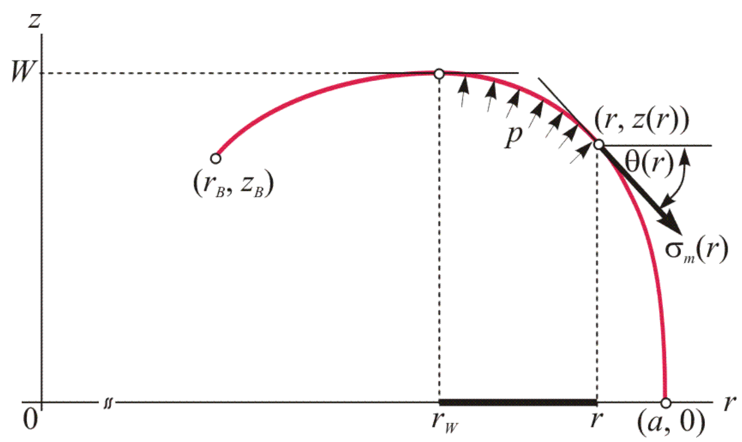

Figure 4.18 – A schematic to compute the meridian stress s_m.

Safe performance of tires seems to be the most probable cause of the search for the static equilibrium shape of tires as a well substantiated base for strength considerations. Figure 4.18 shows a basic schematic for computing the meridional stress σ_m. The z-projection of the resulting force acting on the surface area determined by parallels of radii r_W and r is

$$F_z(r) = \int_{S(r_W,r)} (\mathbf{i_z}.\, p\mathbf{n})\, \mathrm{d}S = p \int_{S(r_W,r)} \sin(\pi/2 - \theta(t))\, \mathrm{d}S$$

$$= p \int_{(r_W,r)\times(0,2\pi)} \cos\theta(t)\, t\sqrt{1+f'^2(t)}\, \mathrm{d}t\, \mathrm{d}\phi = 2\pi \int_{r_w}^{r} t\, \mathrm{d}t = p\pi(r^2 - r_w^{\,2}),$$

where $\mathbf{i_z}$ is the unit vector in the z-direction and $\mathbf{n}$ is the unit vector of the external normal. Because $\sin\theta(r_w) = 0$ the force $F_z(r)$ is equalized merely by the projection of total force acting on the parallel of radius r, $F_z(r) = 2\pi r\, \sigma_m(r) \sin\theta(r)$. Thus,

$$\sigma_m(r) = \frac{p(r^2 - r_w^2)}{2r\sin\theta(r)}.$$

On the other hand, in uniform radial carcass, obviously, $\sigma_m(r) = n(r)\, t(r)$, where $n(r)$ is the number of cords per unit length segment of the r-parallel. Hence,

$$t(r) = \frac{p(r^2 - r_w^2)}{2r\; n(r)\sin\theta(r)} = \frac{2\pi\; p(r^2 - r_w^2)}{2N\dfrac{r^2 - r_w^2}{a^2 - r_w^2}} = \frac{\pi\; p(a^2 - r_w^2)}{N} = \text{const.}$$

The relation (4.5) gives

$$t(r) = 2\pi p\frac{\lambda a^2}{N} = 2\pi p\frac{\Lambda r_\vartheta^2}{N}.$$

●

The computation of belt tension T seems to be derived in the easiest way by reproducing main ideas of F. Frank [31]. The projection of pressure force acting on the contact area of belt and carcass into a meridional plane is shown in Figure 4.19. It is reduced by the meridional stress at the boundary parallel of radius r_ϑ. Therefore,

$$T = 2\, p\, A_F - 2\, r_\vartheta\, \sigma_m(r_\vartheta) \cos\vartheta.$$

The magnitude of the contact area projection A_F can be estimated by Simpson's formula [10],

$$2A_F = \int_{-z_\vartheta}^{z_\vartheta} r\, \mathrm{d}z \approx \frac{2z_\vartheta}{6}\,[r(-z_\vartheta) + 4r(0) + r(z_\vartheta)] = \frac{2z_\vartheta}{3}\,[2r(0) + r(z_\vartheta)].$$

Hence,

$$T \approx 2p\,[(2R_A + r_\vartheta)\, z_\vartheta/3 - \Lambda\, r_\vartheta^{\,2} \cos\vartheta]\,.$$

This total circumferential force is distributed onto individual cords corresponding to their density and angles with the circumferential direction.

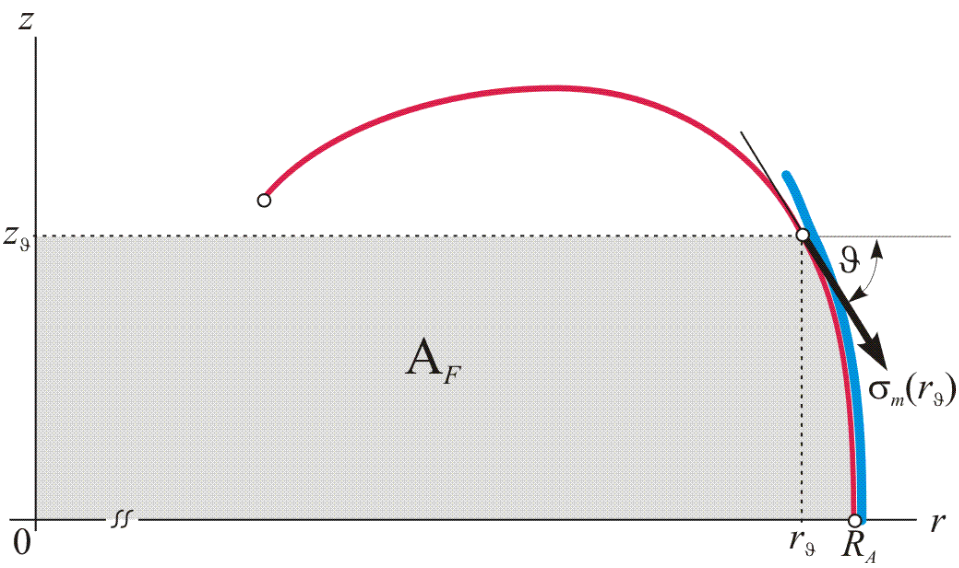

Figure 4.19 – Computing the total belt tension in radial tire.

●

Example. In 235/40R18 tire the carcass meridian curve is given as solution of the following simplified problem (A) (in mm)

$$(R_A, W, R_N, r_B, z_B) = (309.5, 115.5, 3000, 249.8, 104.4) \rightarrow (\Lambda, \vartheta) .$$

This yields $\Lambda = 0.1000949$, $\vartheta = 1.542534$, $r_\vartheta = 308.30$mm, $z_\vartheta = 84.85$mm and the meridional length $l = l_{AB} = 163.4$mm. Let us approximate the derivative $\mathrm{d}V(l)/\mathrm{d}l$ by the ratio of symmetric differences [10]

$$\frac{\mathrm{d}V}{\mathrm{d}l}(l) \approx \frac{V(l+\Delta l) - V(l-\Delta l)}{2\,\Delta l},$$

where $\Delta l = 0.2$mm. Solving the corresponding problems (B),

$$(309.5, 163.4 \pm 0.2, 3000, 249.8, 104.4) \rightarrow (\Lambda, \vartheta),$$

one obtains $V(l+\Delta l) = 22.870251\text{dm}^3$, $V(l-\Delta l) = 22.822429\text{dm}^3$. If the inflation pressure is $p = 200$kPa and the total number of radial cords in carcass is $N = 4000$, then the individual cord tension is

$$t = \frac{2}{N} p(V(l)) \frac{\mathrm{d}V}{\mathrm{d}l}(l) \approx \frac{2}{4000} 200\,000 \frac{0.022\,870\,251 - 0.022\,822\,429}{0.0004}$$
$$= 2.988875\text{N}.$$

On the other hand,

$$t = 2\pi\, p \frac{\Lambda r_\vartheta^2}{N} \approx \frac{2\pi}{4000} 200\,000 \times 0.1000949 \times 0.3083^2 = 2.988883\text{N}.$$

Thus, the difference between the two results is negligible and caused by numerical inaccuracy.

Let us remark that the real carcass is never uniform perfectly. Also cord strength is a random quantity whose distribution may be well approximated by B-distribution. More details can be found in [39].

In a similar way one obtains for the belt tension

$$T = \frac{1}{2\pi}\, p(V(R))\, \frac{\mathrm{d}V}{\mathrm{d}R}(R) \approx \frac{p}{2\pi}\, \frac{V(R+\Delta R) - V(R-\Delta R)}{2\,\Delta R}$$

$$= \frac{200\ 000}{2\pi}\, \frac{0.022911526 - 0.022781049}{0.0004} = 10\ 383.03\mathrm{N}$$

and

$$T \approx 2p\, [(2R_A + r_\vartheta)\, z_\vartheta/3 - \Lambda\, r_\vartheta^2 \cos\vartheta]$$

$$= 2{\times}200\ 000\ [(2{\times}0.3095 + 0.3083)\ 0.08485/3 - 0.1000949{\times}0.3083^2{\times} \cos 1.542534]$$

$$= 10\ 383.314\mathrm{N}.$$

Again, both the results are practically the same and the small difference 0.31N is a consequence of rounding errors.

Remark 1. In uniform diagonal carcass the meridional stress

$$\sigma_m(r) = n(r)\, t(r) \sin \alpha(r),$$

where r denotes the distance from the axis of revolution, $n(r)$ is the total number of cords per unit length of r-parallel (Figures 3.3, 3.4),

$$n(r) = \frac{r_D n_D}{r \sin \alpha_D}\,.$$

Here n_D is the number of cords per unit length perpendicularly and α_D is the cord angle on building drum (radius r_D). Thus, for the usual cosine rule, $\cos \alpha(r) = (r/r_D) \cos \alpha_D$,

$$t(r) = \frac{\sigma_m(r)}{n(r) \sin \alpha(r)} = p\, \frac{(a^2 - r_w^2) \sin \alpha(a)}{2\, r_D n_D \sin \alpha_D}\, \frac{1}{\sin^2 \alpha(r)} = \text{const.} \times \frac{1}{\sin^2 \alpha(r)}\,.$$

This means: in diagonal carcass the cord tension is increasing with radius r.

Remark 2. If the bead area can be supposed stiff, the tension in wires of bead bundle may be estimated by tire volume changes due to increase of bead radius and bead displacement controlled by the shape of rim contour. Another way is using the projection of the meridional stress on radius $\sigma_m(r_B)$ into the bead plane under the angle $\vartheta_C = \arctan \dfrac{z_B - z_C}{r_B - r_C}$, where $(r_C,\ z_C)$ denotes the bead bundle(s) center in rim with small conicity (5°). The total tension in bead is approximately

$$T_C \approx r_C\, \sigma_m(r_B) \cos \vartheta_C = r_C\, \sigma_m(r_B)\, \frac{r_B - r_C}{\sqrt{(r_B - r_C)^2 + (z_B - z_C)^2}}\,.$$

If the friction between individual wires may be supposed high enough then the force T_C can be thought distributed uniformly onto individual wires and their tension confronted with their strength.

P

5 RESPONSE OF RADIAL TIRE TO EXTERNAL LOAD

The pneumatic tire is the first dynamical element between the road and vehicle, i.e. a car, truck, aircraft, bicycle, etc. When designing a vehicle the designer needs to have some estimates of tire response to the external force signals so that he could create a tuned project. External loads in tire exploitation are non-axisymmetric which brings another complexity into tire analysis. Though the belt in radial tires restricts the carcass in radial direction it, on the other hand, has the advantage in its high circumferential stiffness. Considering negligible circumferential elongation allowed an approximation of the ´equator´ of the vertically loaded radial tire by a smooth combination of four circular arcs [12]. This model appears to be rather an artificial geometrical construction. Radial flexibility and circumferential inextensibility of the belt together with our experimental knowledge [40,41] led later to development of the so called belt model of radial tire [42]. The belt model is much more general and besides radial forces it enables to compute also lateral forces and moments in cornering tires etc. [43]. It is still relatively simple and works with analytical solutions, which provides its numerical efficiency and easy use. Also in the today’s FEM era the belt model may serve as an independent source of predictions of tire stiffness in main directions. Many experimental results have confirmed its consistency and closeness to reality.

The pneumatic tire within the dynamical system of vehicle works as a spring in the first place. If m denotes the mass of the wheel (unsprung mass), t the time and x the displacement of the wheel center from its equilibrium position then according to the second law of motion (e.g. [44]) the following force F is connected with the acceleration of mass m (if m is assumed constant)

$$F(t) = m\,\frac{\mathrm{d}^2 x}{\mathrm{d}t^2}(t).$$

In linear spring (oscillator) this force is proportional to the displacement,

$$F(t) = -k\,x(t),$$

where the ratio (stiffness)

$$k = \left|\frac{F}{x}\right| .$$

is constant for any couple (x, F). However, the occurrence of such an ideal spring is very rare. To preserve this transparent linear model the real elastic behavior is approximated by various substitutions of the stiffness, e.g. by a local stiffness,

$$k(x) = \left|\frac{\mathrm{d}F(x)}{\mathrm{d}x}\right|.$$

Even an elementary knowledge on tire materials (Chapter 2) leads to expectation that the tire elasticity does also depend on temperature, velocity of deflection etc. In search for logical connections one has – with some arbitrariness, of course – to summarize the important features into several clearly formulated simplifying assumptions and set up a convenient mathematical model on this basis.

Dynamical behavior of the pneumatic tire is represented by the following scalar differential equation of the second order (it can be generalized to vector case easily)

$$\frac{d^2x(t)}{dt^2} = f(t, x(t), \frac{dx(t)}{dt}),$$

where f is a suitable function (from the standpoint of the existence and uniqueness of solution [9,10,45]).

The time dependence connected e.g. with temperature changes is ignored as usual, thus, thermodynamic equilibrium is supposed. Then the last equation may be rewritten as follows

$$\frac{d^2x}{dt^2} = \frac{1}{m}(F(x) + G(x, \frac{dx}{dt})),$$

where the functions F, G may be simplified (linearized). The ratio G/F is very small in rolling tire. This was experimentally verified in radial oscillations in car tires [40,41]. The elastic component $\frac{F(x)}{m}$ plays then a dominant role.

5.1 Static Radial Deflection

Our first model that fitted experimental load–deflection curves quite well is described in [12]. The "equator" of the deflected tire is approximated by a smooth curve of the same length as the original equator of the inflated unloaded tire. This spline curve [10] is composed of four sections: the straight segment of the contact area, the large arc concentric with the original unloaded equator but with a greater radius and two equal transient arcs of smaller radius enabling a smooth joining the contact area to the free, unloaded arc. This way the radius R_A is given, "bead point" (r_B, z_B) is kept fixed and the meridian length l_{AB} as well as belt radius R_N can be fixed or slightly changed. Thus, to any polar angle ϕ the following problem (B) is assigned:

$$(R_A, l_{AB}, R_N, r_B, z_B)_\phi \to (\Lambda, \vartheta)_\phi .$$

Its solution yields principally the volume $V_A(\phi)$ of the corresponding axisymmetric body.

The total volume of the model that belongs to the radial deflection u is then

$$V(u) = \frac{1}{2\pi}\int_{-\pi}^{\pi} V_A(\phi)\, d\phi = \frac{1}{\pi}\int_{0}^{\pi} V_A(\phi)\, d\phi .$$

The last integral over the area $[0, \psi]$ of variable radius $R_A(\phi)$ is computed numerically (by the 3-node Gauss formula [10]).

The volume change enables to compute the energy increase of the air filling in the tire $U(u)$. Doing this for $n>3$ values of u_i one gets a set of points $(u_i, U(u_i))$, $i = 1, \ldots, n$. It can be fitted by the following regression polynomial

$$P(u) = b_1u^2 + b_2u^3 .$$

The external deflecting force F (vertical load) is then found by differentiation of P with respect to u,

$$F(u) = 2b_1u + 3b_2u^2 .$$

Direct measurement of air pressure increments in the 185SR14 radial tire at various deflections is described in [12]. There is also mentioned their comparison with corresponding predicting curve determined from volume changes of model. In this case the ratio of the air energy represents 92-95 percent of the total deflection energy. This corresponds excellently with the vertical stiffness regression published in [13] recently (as mentioned in Chapter 1).

5.2 Belt Model

The ring on elastic foundations belongs to the models that are permanently used in the mechanics of tires. However, the elastic foundation created by linearly elastic spring does not describe the behavior of tires faithfully and must be improved in various ways.

The belt model (Figures 1.1 and 5.1) is consistently based on the air volume work and uses the consequent theory of meridional curve (Chapter 4). Volume changes derived this way imply nonlinearity of the foundation in dependence of radial deflection. The basic theory was published in [42,43]. Here only a short survey will be given with some supplements.

Figure 1.1 shows the basic partitioning the radial tire into:

- low stiffness (modulus) tread area consisted of thick rubber layer equipped with tread pattern (grooves, sipes etc.),
- reinforced area of carcass, belt and beads with high stiffness in specific directions.

Equilibrium shape of the reinforced part was the theme of Chapter 4. In the foregoing Section 5.1 the volume of axisymmetric cavity swept by the meridional curve was used to compute the volume of non-axisymmetric cavity of vertically deflected tire model. The same principle creates a basis for using the elastic support that may be characterized by three coefficients of stiffness connected with axes of natural cylindrical system of coordinates $0r\phi z$:

- u = radial coordinate, k_u = coefficient of radial stiffness,
- v = circumferential coordinate, k_v = coefficient of circumferential stiffness,
- w = axial, lateral coordinate, k_w = coefficient of axial, lateral stiffness.

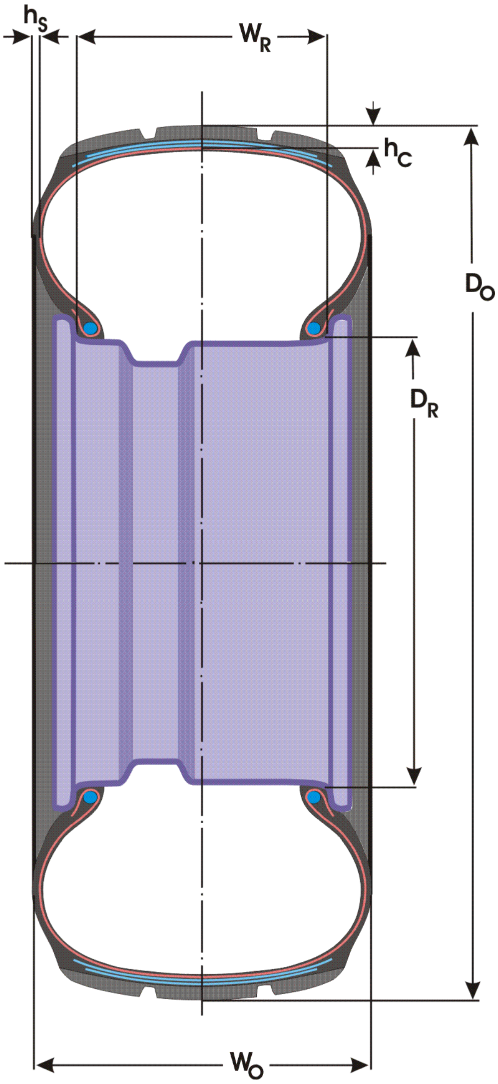

Figure 5.1 – Main geometrical parameters to set up the belt model of radial tire.

The stiffness coefficients k are computed by means of axisymmetric displacements of belt. If X is such displacement (radial, circumferential, lateral) and $W(X)$ denotes the corresponding energy change computed by the air volume changes including estimated stress-strain energy of tire wall, then in linear support

$$W(X) = \int_0^{2\pi}\int_0^{X} k_X\, X\, dX\, R_A\, d\phi = \pi R_A\, k_X\, X^2.$$

Thus,

$$k_X = \frac{1}{2\pi R_A}\,\frac{d^2 W(X)}{dX^2}\,.$$

The second derivative is computed numerically [10] , of course,

$$\frac{d^2 W(X)}{dX^2} \approx \frac{W(X+\Delta X) - 2W(X) + W(X-\Delta X)}{\Delta X^2}\,.$$

Originally the stiffness coefficients were calculated for $X = 0$. But to include nonlinearity, they may be considered as functions of X. In the case of radial stiffness coefficient k_u the use of belt tension is advantageous (Section 4.4):

$$k_u(R_A) \approx \frac{-p}{2\pi R_A}\,\frac{(V(R_A+\Delta R_A) - V(R_A)) - (V(R_A) - V(R_A-\Delta R_A))}{\Delta R_A{}^2}$$

$$\approx \frac{1}{R_A}\,\frac{T(R_A) - T(R_A-\Delta R_A)}{\Delta R_A} \xrightarrow[\Delta R_A \to 0]{} \frac{1}{R_A}\,\frac{dT(R_A)}{dR_A}\,.$$

Then taking different R_A enables to construct $k_u(R_A)$ as a quadratic function, for example.

In belt model also centrifugal acceleration can be taken into account very simply. If m is the mass of the entire belt block and ω the angular velocity the belt tension is increased by $\dfrac{m\omega^2}{2\pi R_A} R_A = \dfrac{m\omega^2}{2\pi}$. Tread pattern disturbs the constancy of mass density in circumferential direction and small variability in belt tension along circumference certainly contributes to tire vibrations at high speeds. Hence, transversal grooves also if distributed irregularly in tread pattern [46] may turn to a source of tire noise emissions.

As mentioned above, high circumferential stiffness is a characteristic property of belt of radial tire. So, in a simplified way, the belt may be considered to be inextensible longitudinally. The circumferential component of the strain tensor [47] is then

$$\varepsilon_{\phi\phi} = \frac{1}{r}\left(\frac{\partial v}{\partial \phi} + u\right) = 0$$

and, because $r>0$, one gets a very important relationship between the radial and circumferential components of belt displacement [42]:

$$u = -\frac{\partial v}{\partial \phi}.$$

Thus, the variable u is eliminated and the belt model can be described by two components of deflection, v and w.

We will shortly write v' instead of $\frac{\partial v}{\partial \phi}$, v'' instead of $\frac{\partial^2 v}{\partial \phi^2}$, etc.

If energy losses are negligible, loading a radial tire rotating with angular velocity ω induces a deflection for which, according to the Hamilton's principle [44], the functional

$$S = \int_{t_0}^{t_1} (E_{kin} - E_{pot})\, \mathrm{d}t$$

attains its stationary value. Here E_{kin} is the kinetic energy,

$$E_{kin} = \frac{m\omega^2}{4\pi} \int_{-\pi}^{\pi} [(R_A - v')^2 + (v'')^2 + (w'')^2]\, \mathrm{d}\phi\,.$$

The potential energy

$$E_{pot} = \frac{R_A}{2} \int_{-\pi}^{\pi} [Q_v(v, v', v'') + Q_w(w, w', w'')]\, \mathrm{d}\phi\,,$$

where

$$Q_v(v, v', v'') = T\left(\frac{v''}{R_A}\right)^2 + k_u(v')^2 + k_v\, v^2,$$

$$Q_w(w, w', w'') = D\left(\frac{w''}{R_A^2}\right)^2 + T\left(\frac{w'}{R_A}\right)^2 + k_w\, w^2,$$

and D is the transversal (axial) stiffness of the belt [42].

Obviously, S may be decomposed into two independent summands,

$$S = S_v + S_w,$$

where

$$S_v = \int_{-\pi}^{\pi} \Big(\frac{m\omega^2}{4\pi} \, [(R_A - v')^2 + (v'')^2] - \frac{R_A}{2} \, Q_v(v, v', v'') \Big) \, \mathrm{d}\phi,$$

$$S_w = \int_{-\pi}^{\pi} \Big(\frac{m\omega^2}{4\pi} (w'')^2 - \frac{R_A}{2} \, Q_w(w, w', w'') \Big) \, \mathrm{d}\phi \, .$$

Both the functionals S_v and S_w are of the same type

$$\int_a^b F(x, y(x), y'(x), y''(x)) \, \mathrm{d}x \, .$$

The corresponding Euler-Poisson equation sounds [9]

$$\frac{\mathrm{d}^2}{\mathrm{d}x^2}\left(\frac{\partial F}{\partial y''}\right) - \frac{\mathrm{d}}{\mathrm{d}x}\left(\frac{\partial F}{\partial y'}\right) + \left(\frac{\partial F}{\partial y}\right) = 0 \, .$$

Putting $F = S_v$ and $F = S_w$ successively yields two linear differential equations of the fourth order of the same type (basic equation of belt model)

$$y'''' + A\, y'' + By = 0 \, .$$

The coefficients A and B are displayed in the following table.

	v	w
A	$\dfrac{2\pi R_A^2 k_u - m\omega^2 R_A}{2\pi T - m\omega^2 R_A}$	$-\dfrac{2\pi R_A^2 T}{2\pi D - m\omega^2 R_A^3}$
B	$-\dfrac{2\pi R_A^2 k_v}{2\pi T - m\omega^2 R_A}$	$\dfrac{2\pi R_A^4 k_w}{2\pi D - m\omega^2 R_A^3}$

In static or quasistatic deflections $\omega = 0$, obviously, and A, B become simpler.

General solution of homogeneous equation

$$y'''' + A\, y'' + By = 0$$

may be presented as a linear combination of its four linearly independent fundamental solutions [9,45]

$$y_k(\phi) = \mathrm{e}^{\,a_k \phi}, \quad k = 1, \ldots, 4,$$

where a_k are roots of the corresponding characteristic equation [9,45]

$$a^4 + Aa^2 + B = 0.$$

The numbers a_k are real or complex, dependent on A and B. Thus, the general solution may also be written as a linear combination of hyperbolic functions sinh $\alpha\phi$, cosh $\alpha\phi$, trigonometric functions sin $\alpha\phi$, cos $\alpha\phi$, and their products

$$y_k(\phi) = C_1\, y_1(\phi) + C_2\, y_2(\phi) + C_3\, y_3(\phi) + C_4\, y_4(\phi) \,.$$

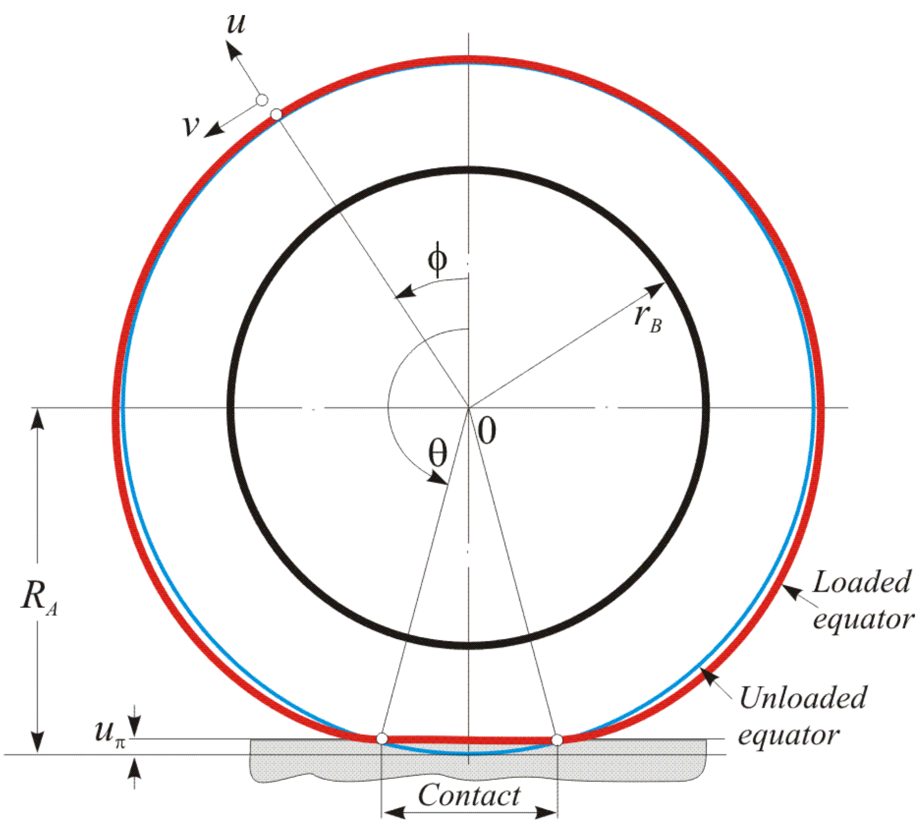

Figure 5.2 – A sketch of boundary conditions in vertical loading.

The four unknown constants are to be found from boundary conditions in the considered case of loading. The case of vertically loaded radial tire is illustrated in Figure 5.2, others are more schematically shown in Figure 5.3.

Solutions with respect to the inflation pressure and tire geometry (belt tension and stiffness coefficients of the belt support) are mostly set up from the functions as follows:

Even solutions:	cosh $\alpha\phi$ cos $\beta\phi$	and	sinh $\alpha\phi$ sin $\beta\phi$,
Odd solutions:	cosh $\alpha\phi$ sin $\beta\phi$	and	sinh $\alpha\phi$ cos $\beta\phi$.

For more details on computing α and β from A and B see [42].

Boundary conditions in the mentioned main types of loading are summarized up in the following table.

Remark. The conditions below can be adopted to a more general case of the cylindrical support coaxial with the tire. The plane corresponds then to the infinite radius of cylinder.

Loading	Solution	Boundary and length conditions
Radial (Vertical)	Even	$-v'(\theta) + R_A - \dfrac{R_A - u_\pi}{\cos\theta} = 0\,,$ $-v''(\theta) - \dfrac{(R_A - u_\pi)\sin\theta}{\cos^2\theta} = 0\,,$ $-\pi R_A - (R_A - u_\pi)\tan\theta + \int_0^\theta \sqrt{(R_A - v')^2 + (v'')^2}\, d\theta = 0\,.$
Circumferential	---	$v(\theta - v_\pi/R_A) = v(-\theta - v_\pi/R_A) = v_\pi\,,$ $v'(\theta - v_\pi/R_A) = v'(-\theta - v_\pi/R_A) = 0\,.$
Lateral (Axial)	Even	$w(\pi) = w_\pi\,,$ $w'(\pi) = 0\,.$
Torsional	Odd	$w(\pi) = 0\,,$ $w'(\pi) = (R_A - u_\pi)\sin\delta,$ where δ is the torsion angle.

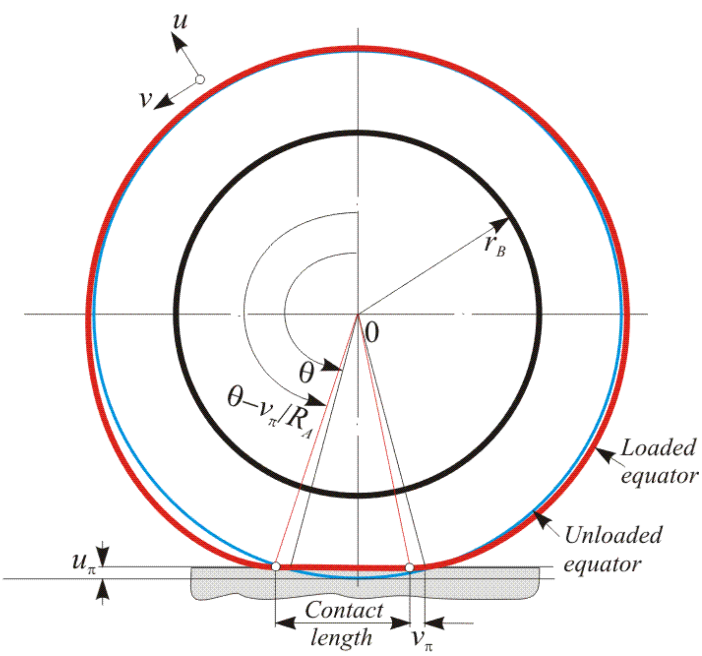

Circumferential deflection

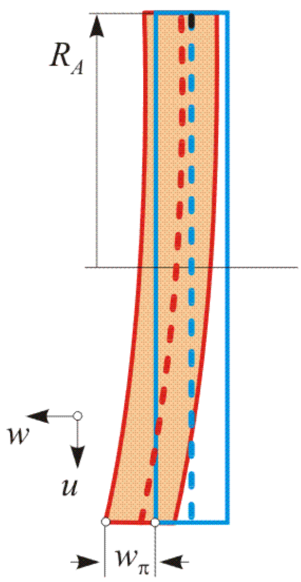

Axial deflection of the belt

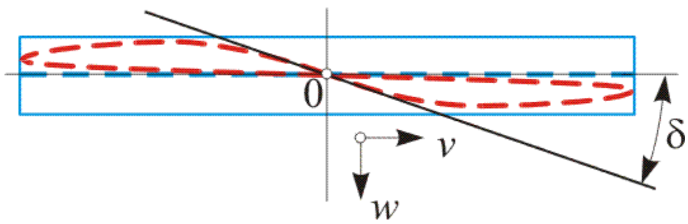

Ground projection of tire equator in torsional deflection.

Figure 5.3 – Illustrations of boundary conditions in static circumferential, axial and torsional deflections.

If the solution $v_k(\phi)$, $w_k(\phi)$ is found for given deflections x_k, $k = 1, \ldots, n$, the corresponding energy $E(x_k)$ can be obtained by integration. Fitting the points $(x_k, E(x_k))$ by a simple function facilitates computing the load. It is advantageous, of course, to choose the regression function (regression polynomial P) as simple as possible. We have used the following polynomial of the 4th order

$$P(x) = x^2(a_1 + a_2x + a_3x^2).$$

Principally, three fitting polynomials P_u, P_v, P_w would be constructed for a general deflection $\mathbf{x} = \begin{pmatrix} u \\ v \\ w \end{pmatrix}$. The force is then

$$\mathbf{F}(\mathbf{x}) = \begin{pmatrix} F_u(u,v,w) \\ F_v(u,v,w) \\ F_w(u,v,w) \end{pmatrix} = \begin{pmatrix} \partial P_u(u,v,w)/\partial u \\ \partial P_v(u,v,w)/\partial v \\ \partial P_w(u,v,w)/\partial w \end{pmatrix}.$$

The belt model of the reinforced part alone (without tread layer) gives a very good approximation of vertical load-deflection curve of real radial tire. The tread layer is namely much stiffer in radial direction than the pneumatic part of tire, so the influence of tread in its serial connection to the reinforced part is small (Figure 5.4). But in tangential loadings the shear contribution of the tread to the tangential deflections is considerable.

We will prefer writing (F_R, F_C, F_z) instead of (F_u, F_v, F_w) as a rule.

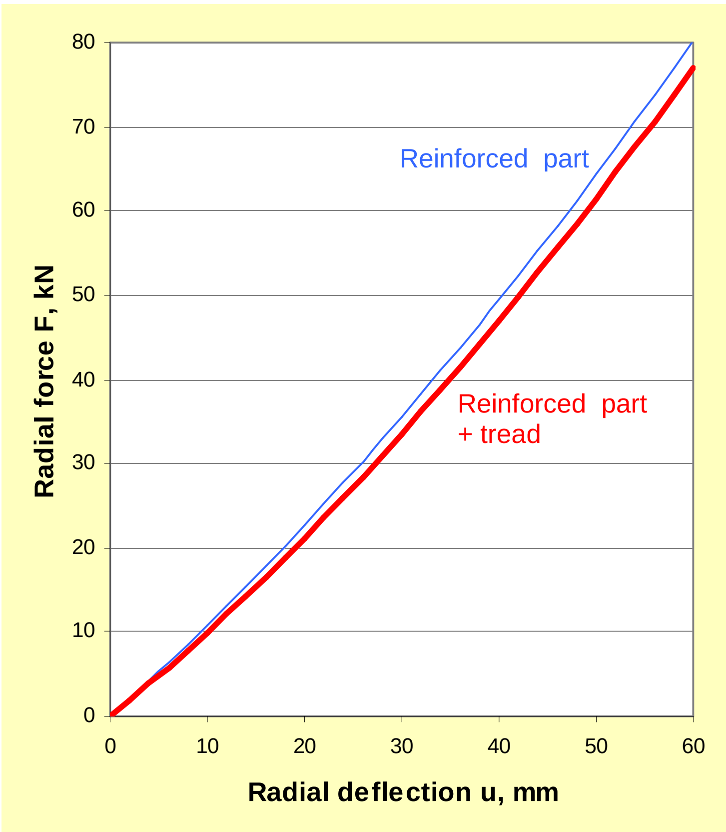

Figure 5.4 – Radial load-deflection curves in 445/65R22.5 truck tire (infl. pressure p = 800kPa).

5.3 Tangential Loadings

Tangential forces are transmitted by friction. So the tire can transfer tangential loadings only if it is loaded vertically (radially). Values of tangential forces are limited by the coefficient of friction in due direction.

The coefficient of friction depends, besides the interface of interfacing bodies, i.e. tread compound and road surface, on real dimensions of real contact area and contact pressure. In microscopic view the interfacing surfaces are of fractal nature [48]. Their contact behavior depends on temperature, skid velocity etc. Concisely, friction is a very complex phenomenon connected always with a lot of uncertainty [49].

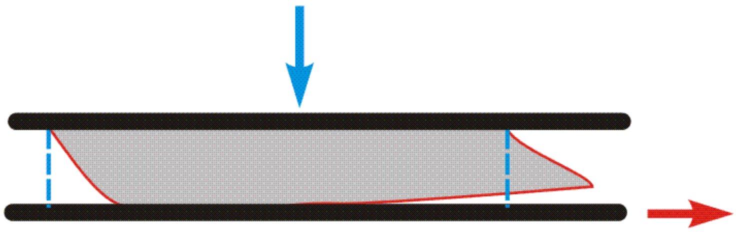

Figure 5.5 – Rubber plate under vertical and lateral loading.

As well known (see e.g. [7]) the coefficient of friction is a decreasing function of normal pressure. We verified it experimentally with a low parallelepiped (plate) of tread rubber vulcanized onto a steel plate fixed in a jig on static tire tester. Its base size corresponded to a common car tire patch. First a vertical load was applied and then the supporting steel plate was hauled horizontally. In spite of its small height the rubber plate was deformed considerably in the way shown in Figure 5.5. The ratios μ of tangential vs. vertical force are presented in Figure 5.6.

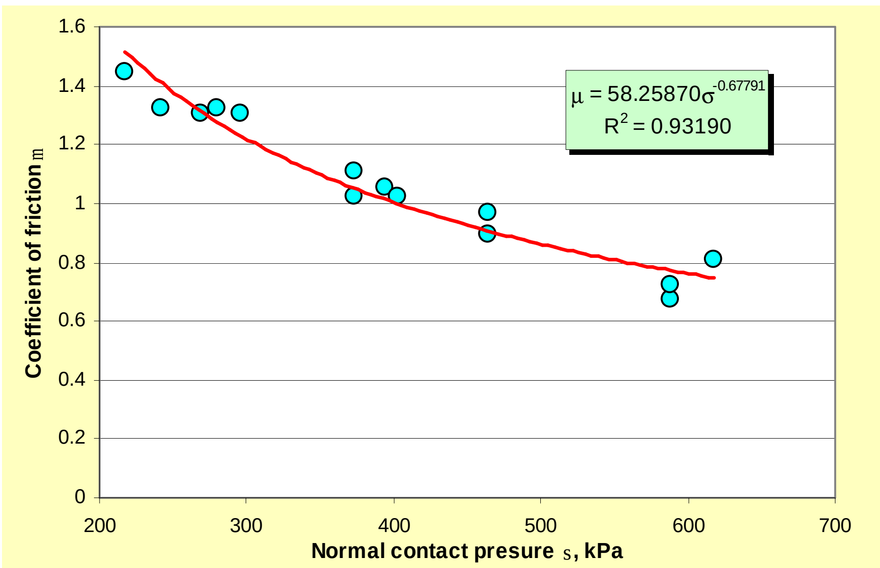

Figure 5.6 – Drop of the rubber/steel coefficient of friction with increasing normal pressure .

The tread pattern is a source of anisotropy in tire tread layer. Tread blocks may be compressed and bent so much that the vertical load is transmitted just by frontal edges of the tread pattern blocks. This way the normal pressure σ in contact area increases significantly while the coefficient of friction μ drops. When the shear tangential stress in contact exceeds the value corresponding $\mu\sigma$, the tread block starts to slip. Thus, the contact area is in a simplified way decomposed in adhesion and sliding zone. In the adhesion zone there are no tangential movements of tread surface due to the condition

$$\tau < \mu\sigma \,.$$

The boundary of the adhesion zone is determined by the equality $\tau = \mu\sigma$. The remainder of contact area is called slip zone and, in a hypothetically ideal case, it would hold there $\tau = \mu\sigma$. But, as well known, to start the movement of a weighty body on a support needs a greater force than to keep on its movement. This phenomenon is used in ABS systems in daily practice. Therefore, in the slip zone it is $\tau < \mu\sigma$ as well.

An example of static lateral load-deflection curve is shown in Figure 5.7. Lateral displacements of the surface of tread layer become substantially greater than those in radial directions due to considerable bending and stretching tread blocks.

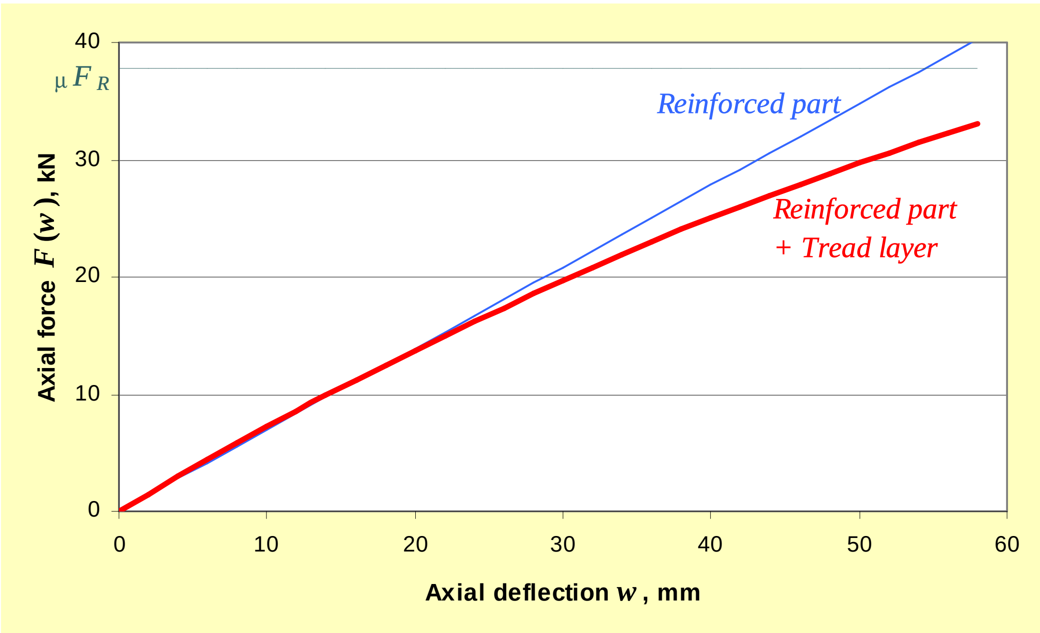

Figure 5.7 – Static lateral load-deflection curve of 445/65R22.5 truck tire
(p = 800kPa, F_R = 54kN, μ = 0.7).

The case of circumferential load can be analyzed in an analogous way [42].

Lateral forces on tires of a vehicle arise due to the support (road) transversal slope, due to lateral wind, cornering etc. Axial forces on tire are compensated by angular deviation of the wheel plane from the direction of movement, i.e. by cornering. Cornering radial tire was dealt with in [43].

If the plane of wheel deviates from the instant direction of wheel movement by an angle δ (slip angle) an axial force $F_z(\delta)$, i.e. in the direction of tire revolution axis *z*, arises as a resultant of axial stresses τ in contact area A. The distance *t* between its point of action and geometric center of contact s_0 of vertically loaded tire is called the pneumatic trail. Those quantities are given by the following equations

$$F_z = \iint_A \tau(s, w; F_z, t)\, dA(s, w),$$

$$t = \frac{1}{F_z} \iint_A (s - s_0)\, \tau(s, w; F_z, t)\, dA(s, w),$$

where *s* is the circumferential and *w* the axial coordinate in the contact area A.

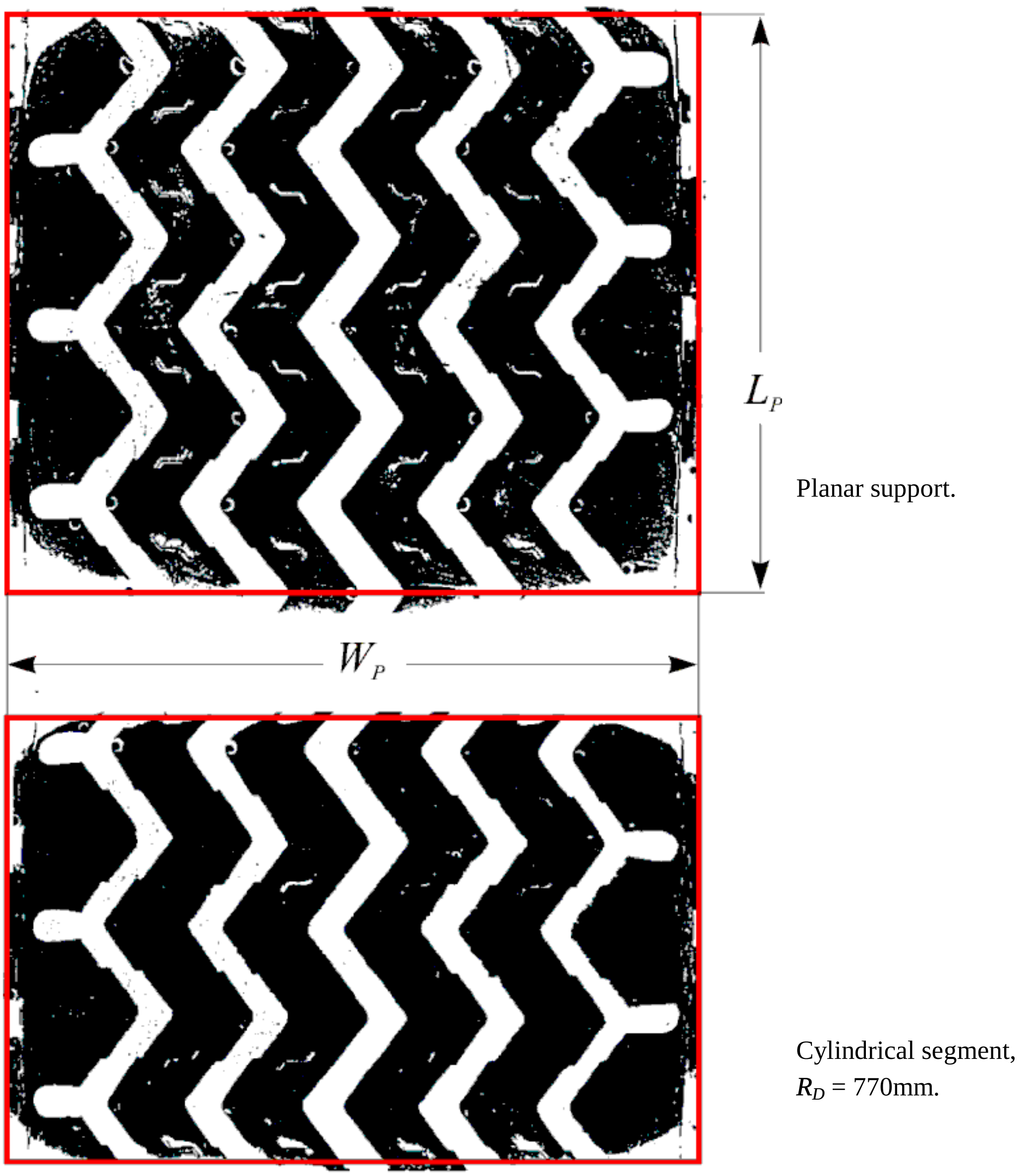

Figure 5.8 – Contact areas in 15R22.5 tire. Inflation pressure p = 800kPa, vertical load 49kN.

In radial tires the contact area is almost rectangular, A = $W_P \times L_P$ (Figure 5.8). Supposing τ constant in axial direction (or substituting it by the mean value across the contact area) the double integration over the area A can be reduced to the single one [9]. Then the following system of two nonlinear equations is obtained:

$$\left.\begin{aligned} F_1(F_z,t) &\equiv F_z - W_P \int_0^{L_P} \tau(s;F_z,t)\,\mathrm{d}s = 0 \\ F_2(F_z,t) &\equiv t - \frac{W_P}{F_z} \int_0^{L_P} (s-s_0)\,\tau(s;F_z,t)\,\mathrm{d}s = 0 \end{aligned}\right\} \qquad \text{(S)}$$

An example of solution this system is presented in Figure 5.10.

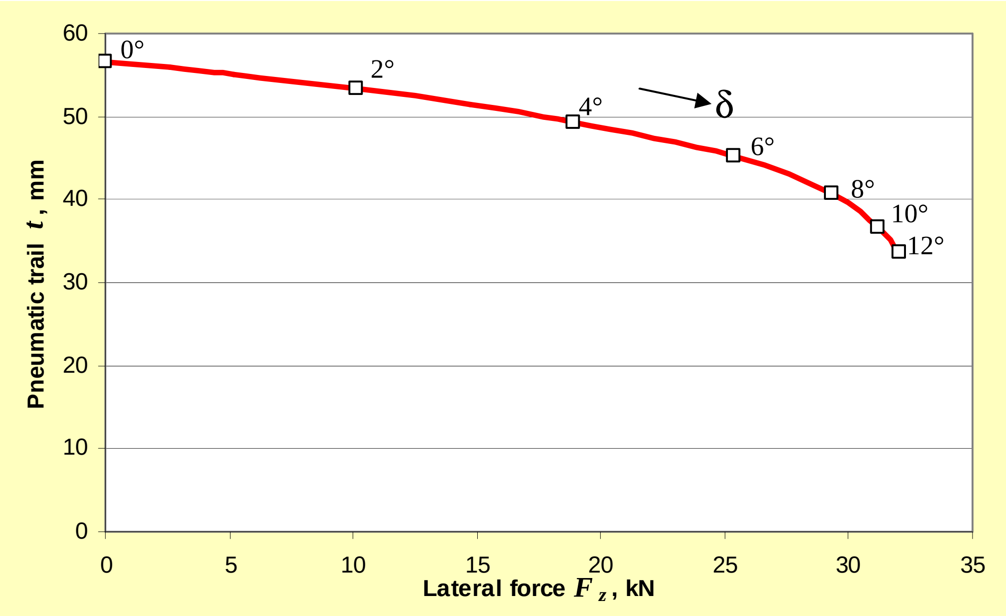

Figure 5.9 – Solution of the system (S) in 445/65R22.5 truck tire for coefficient of friction m = 0.7, inflation pressure p = 800kPa and radial load F_R = 54kN.

The lateral force F_z acting in the direction of tire revolution axis z is the first main characteristics of cornering, the self-aligning torque, $M_z = F_z.t$, is the second one. Substituting t by M_z in Figure 5.9 gives the so called Gough's plot [7,8].

Most frequently, however, the functions $F_z(\delta)$ and $M_z(\delta)$ are plotted separately, like in Figures 5.10, 5.11. The derivative $\frac{\mathrm{d}}{\mathrm{d}\delta}F_z(0)$ defines initial cornering stiffness. Also $\frac{\mathrm{d}}{\mathrm{d}\delta}M_z(0)$ is important because the slip angle δ in usual traffic conditions on highway is small. More details can be found in [42,43].

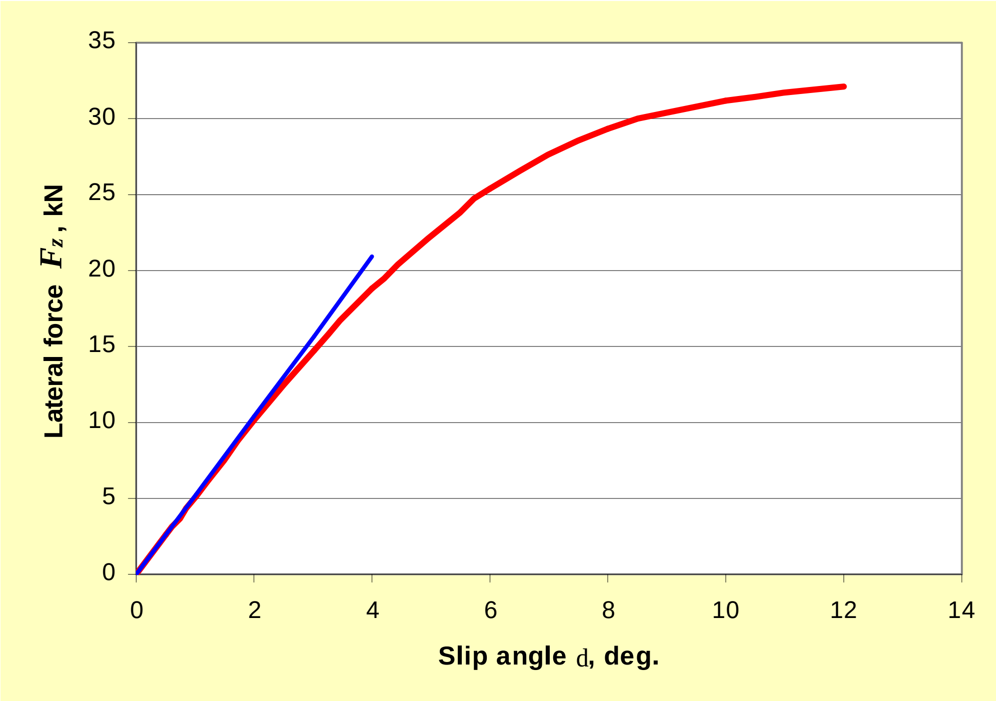

Figure 5.10 – Lateral force in dependence on slip angle in 445/65R22.5 tire (p = 800kPa, F_R = 54kN, m = 0.7).

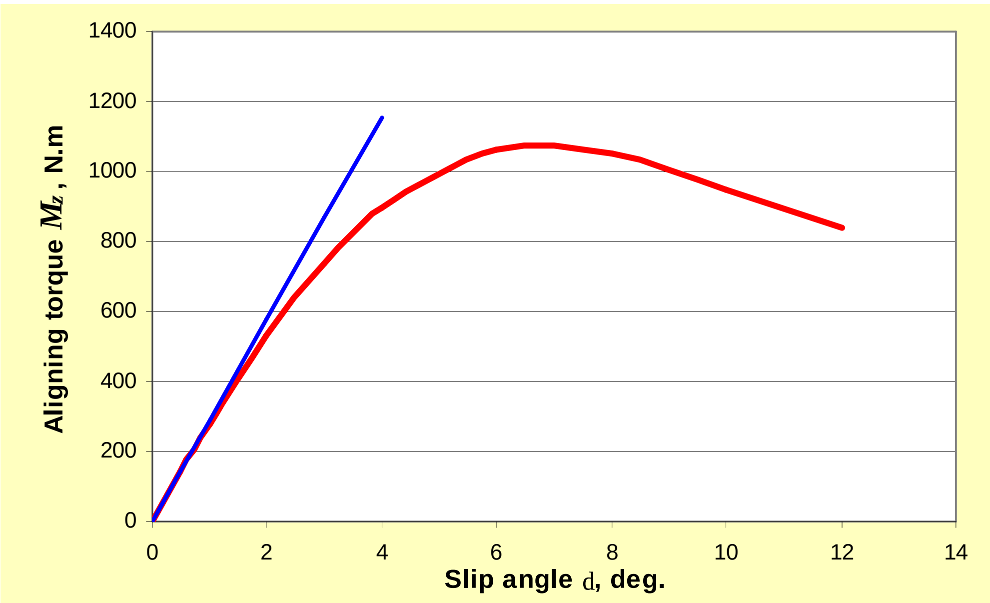

Figure 5.11 – Self-aligning torque in dependence on slip angle in 445/65R22.5 tire (p = 800kPa, F_R = 54kN, m = 0.7).

5.4 Verification of the Belt Model

Confrontation of theoretical predictions with experimental results is a necessary part of each theoretical work connected with reality. During several years enough experimental data were collected and parts of them were published in quoted papers, e.g. [42,43,50]. Here several other results are presented while tires for measurements were taken rather occasionally.

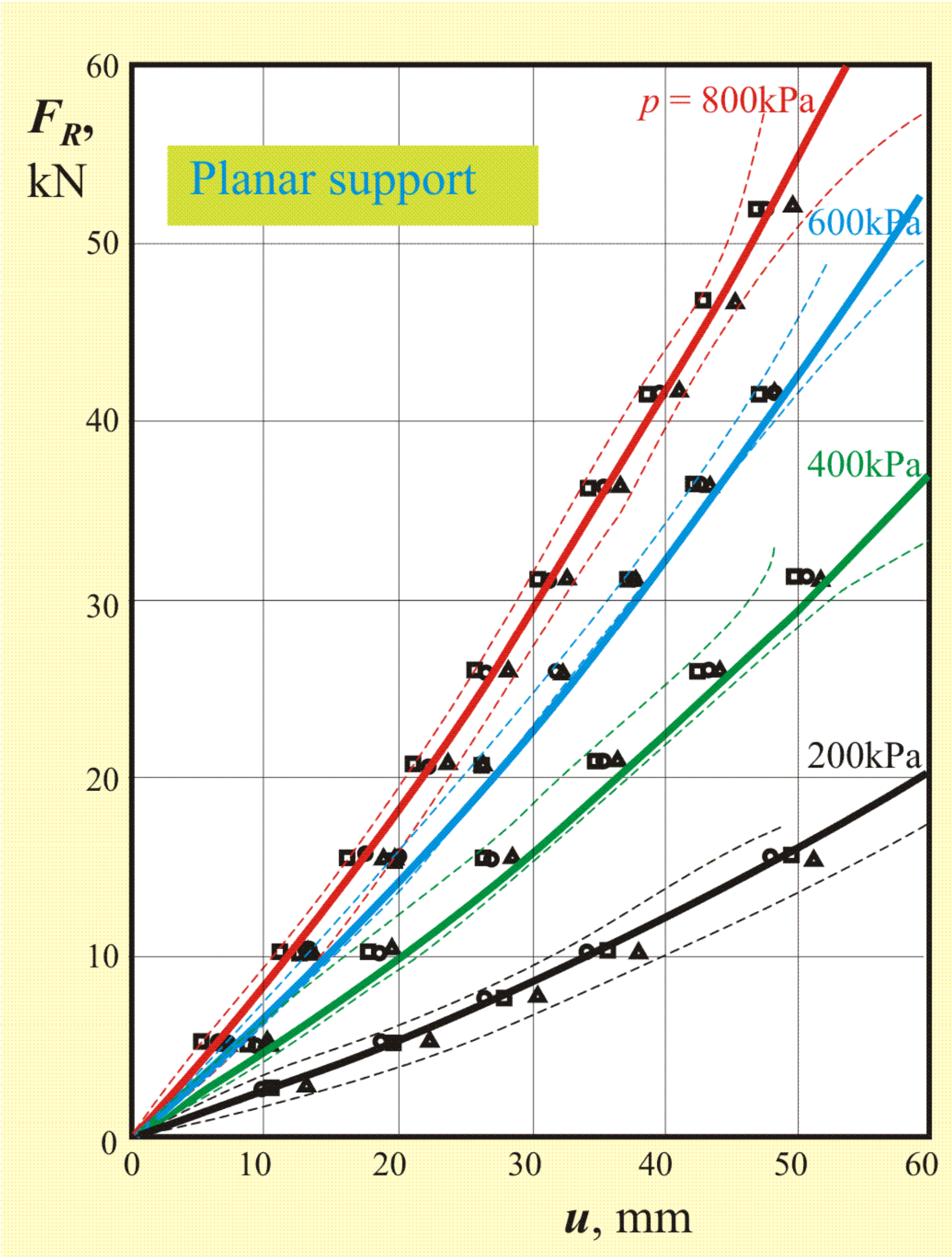

Figure 5.12 – Static radial load-deflection curves of belt model at various inflation pressures vs. corresponding experimental points in 15R22.5 tire on flat support. The predicted curves are drawn as continuous thick lines, the dotted lines show 95% confidence limits.

For detailed testing radial load-deflection curves on flat support and a cylindrical segment with radius 770mm the 15R22.5 super low profile truck tire (with aspect ratio 0.65) was chosen. Figure 5.12 shows the case of planar support, the model curves computed for cylindrical surface confronted with measurement on cylindrical segment of 770mm radius are in Figure 5.13.

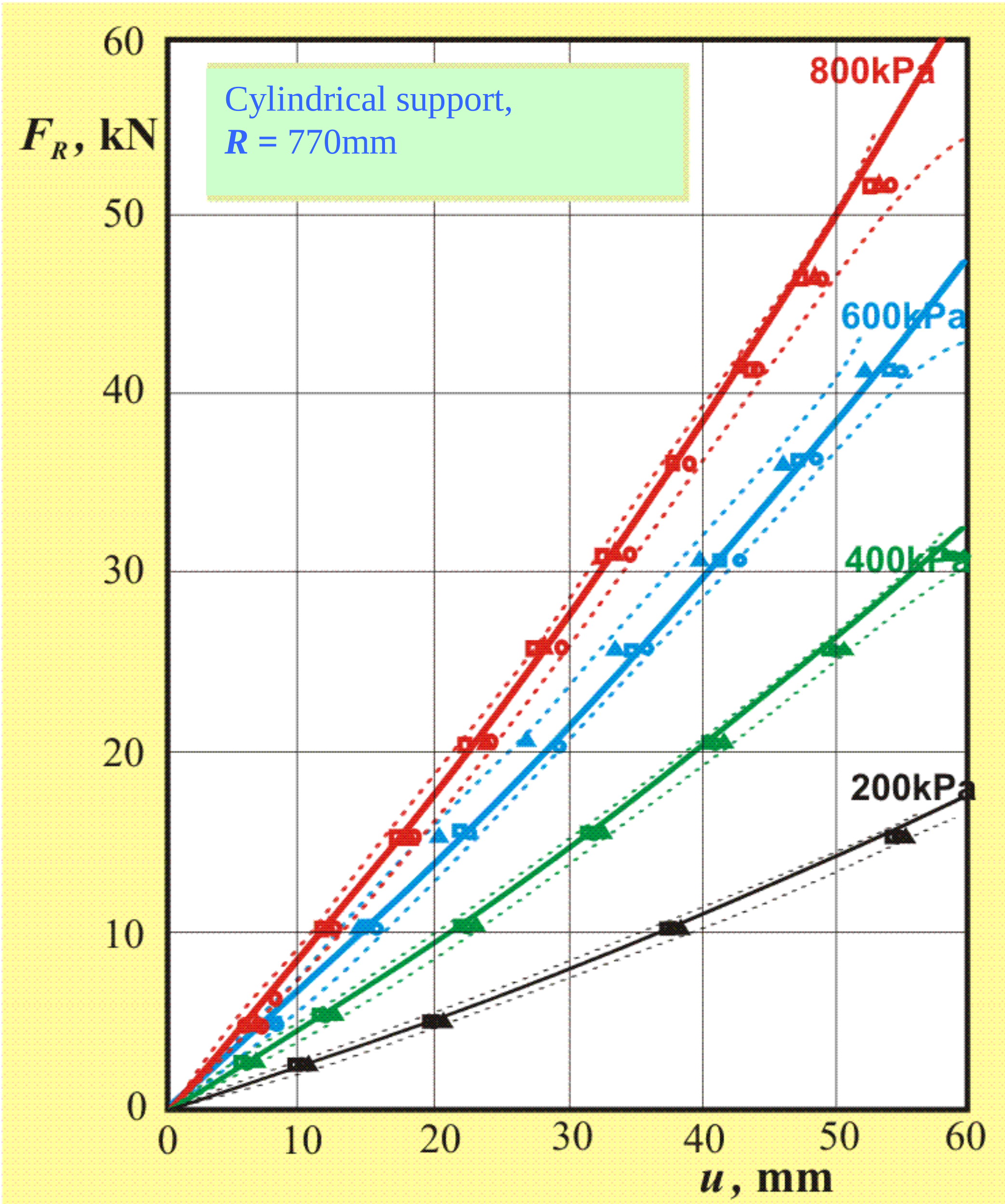

Figure 5.13 – Static radial load-deflection curves of belt model at various inflation pressures vs. corresponding experimental points in 15R22.5 tire on cylindrical segment of 770mm radius. The continuous thick lines belong to predicted curves, the dotted lines are borders of 95% confidence band.

In a smaller truck tire, 295/80R22.5, the static load-deflection curves on planar support and those on the roadwheel (*D* = 2m) at the speed of 100km/h are shown in Figure 5.14. The centrifugal acceleration changes the carcass meridian and reduces radial stiffness of the belt support (k_u) but on the other hand the belt tension (*T*) is increased. At the same time the stiffness of the tread rubber decreases due to the temperature increase. These antinomy moderates the expected changes of tire stiffness at higher speeds.

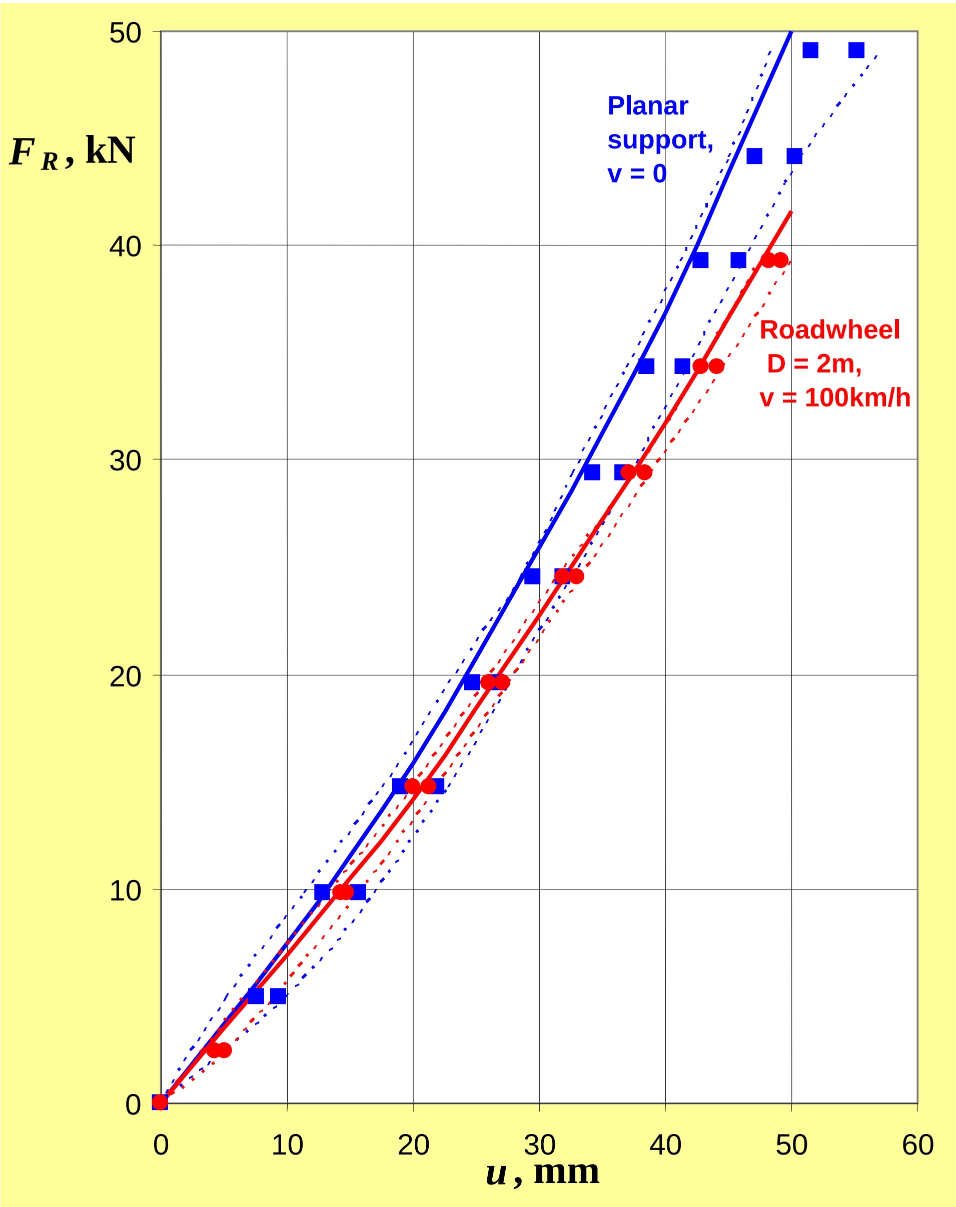

Figure 5.14 – Radial load-deflection curves of belt model vs. corresponding experimental points in 295/80R22.5 tire. The predicted curves are drawn as continuous thick lines, the dotted lines belong to 95% confidence limits.

The following Table presents laboratory measurements in 295/80R22.5 on a 2m-roadwheel at several speeds. Small variability disables to compare the results graphically.

F, kN	*v* = 50km/h			*v* = 100km/h			*v* = 150km/h		
	experiment		model	experiment		*model*	experiment		*model*
3	5.0	4.4	**4.63**	4.7	4.0	**4.53**	4.1	3.4	**4.31**
10	14.9	14.5	**14.44**	14.3	13.9	**14.17**	13.7	13.1	**13.56**
15	21.4	21.0	**20.92**	20.6	20.3	**20.59**	19.9	19.5	**19.78**
20	27.1	26.8	**27.06**	26.2	26.1	**26.70**	25.4	25.1	**25.73**
25	32.8	32.6	**32.91**	32.0	31.9	**32.53**	31.1	30.9	**31.44**
30	38.4	38.2	**38.49**	37.5	37.3	**38.12**	36.5	36.3	**36.93**
35	44.0	44.0	**43.84**	43.2	43.1	**43.48**	41.9	42.0	**42.23**
40	49.4	49.2	**48.97**	48.6	48.4	**48.64**	47.4	47.2	**47.34**

•

In computing tangential forces one needs to know the contact length quite exactly. The comparison of predicted contact lengths to the measured ones is shown in the following Figures 5.15 and 5.16.

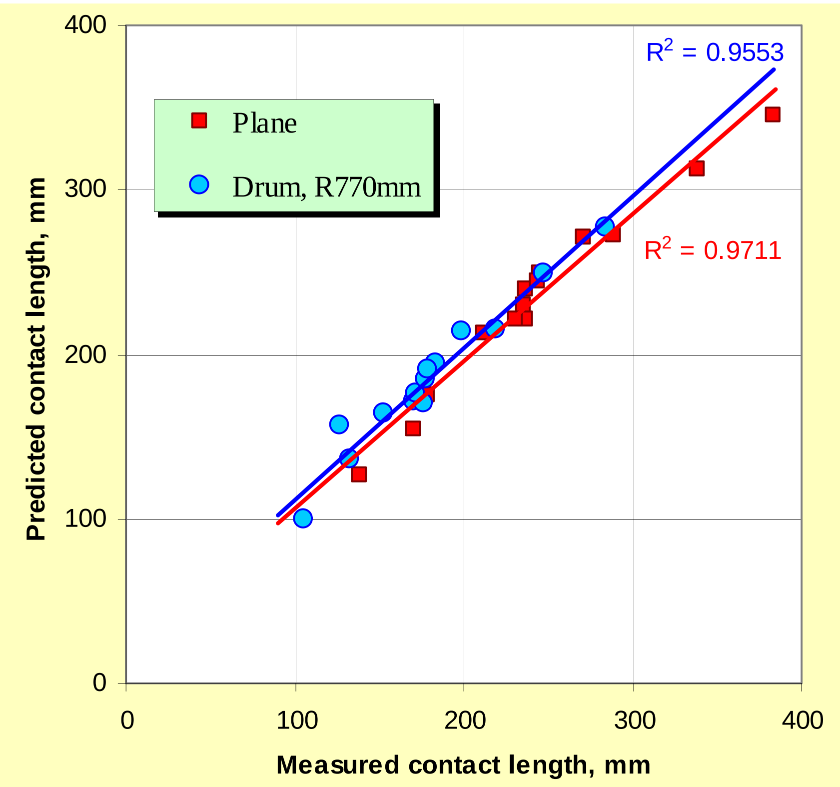

Figure 5.15 – Contact lengths in 15R22.5 tire in radial loading.

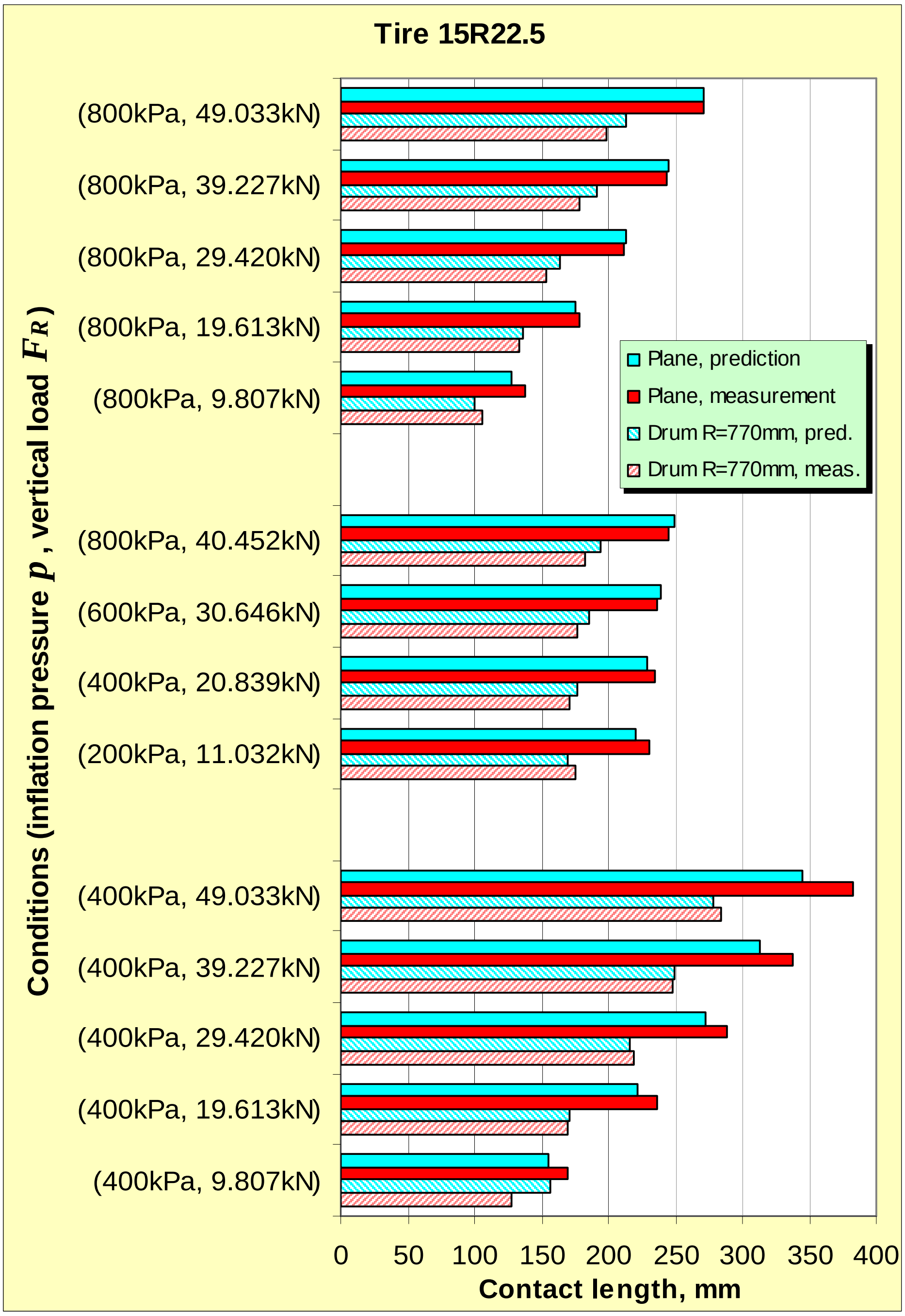

Figure 5.16 – Comparison of contact lengths in 15R22.5 tire in radial loading.

Some comparison of computed results with experimental data for circumferential and lateral loadings can be found in [42]. It is necessary to say that the measuring methods of that time were not very perfect from today's point of view. The same could be said on cornering measurements. But this matter cannot be discussed here.

Figure 5.17 illustrates dependence of lateral force and self-aligning torque on the slip angle in three car tires.

Lateral force

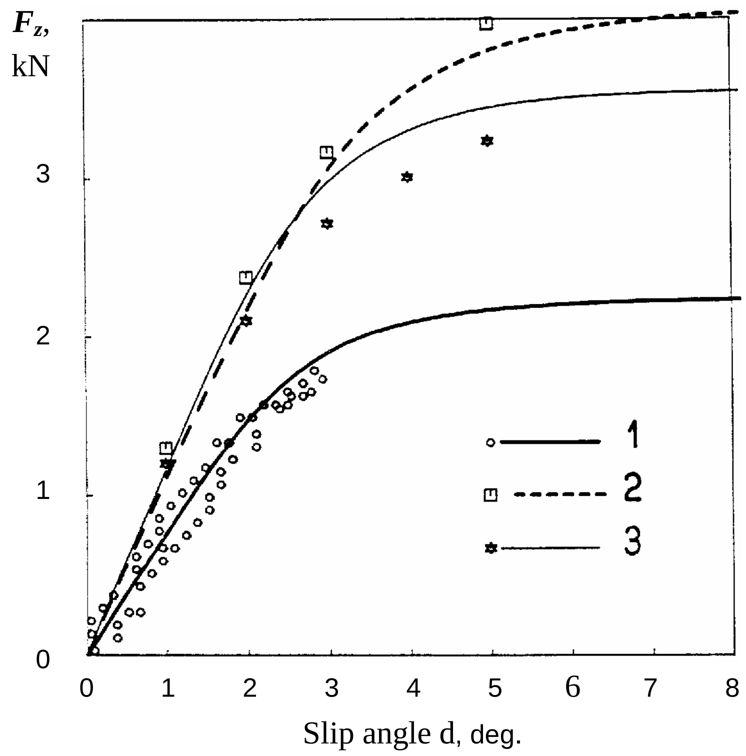

Self-aligning torque

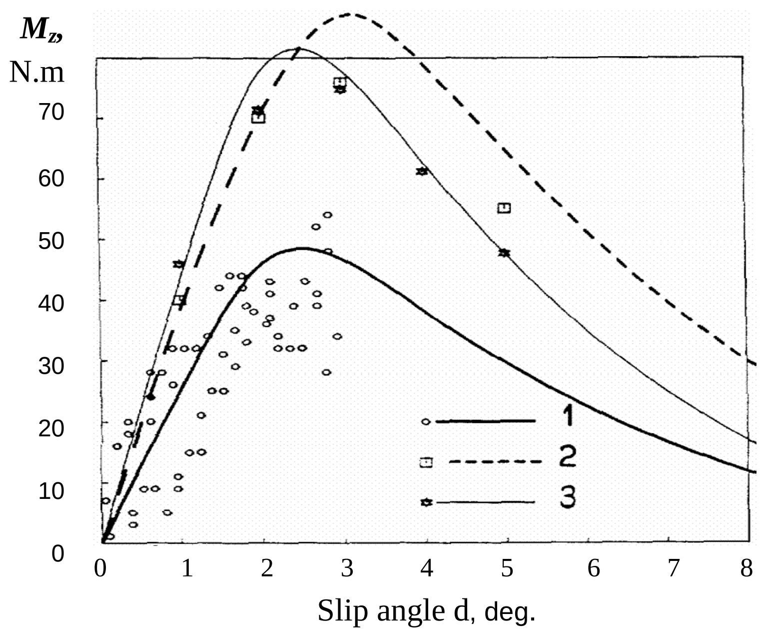

Figure 5.17 – Measurement vs. prediction in lateral force F_z and self-aligning torque M_z in car tires.
1. 165/70R13, p=200kPa, F_R = 3.53kN, speed v = 50km/h,
2. 175/70HR13, p=230kPa, F_R = 5.0kN, speed v =100km/h (exp. data from Prof. F. Vlk, Brno),
3. 185/70R14, p=200kPa, F_R = 4.0kN, speed v = 50km/h (exp. data from Prof. F. Vlk, Brno).

P

6 SOME APPLICATIONS OF THE BELT MODEL

Pneumatic tire is a dynamical system not only in respect to external forces and torques but also itself due to its structure. The tensioned belt on elastic foundation and stressed carcass represent analogues of beams, strings and membranes. Moreover, the tire cavity is a resonator. All this is very important in attempts to reduce vibrations connected to tires. The belt model, however, is too simple to give complete answers to such complex questions. Nevertheless, there are some cases, in which it can be applied successfully.

6.1 Wheel Oscillations

a) Radial Oscillations

Chapter 5 started with the equation

$$\frac{d^2 x}{dt^2} = \frac{1}{m}\,(F(x) + G(x, \frac{dx}{dt}))$$

to describe vertical motion of the wheel. Now the elastic force $F(u)$ can be supposed known, so it remains necessary to say something about the loss function G. Figure 6.1 shows, however, that oscillations of revolving wheel are damped negligibly [41]. Thus, $G(u, \frac{du}{dt}) \approx 0$.

In the neighborhood of the equilibrium position u_0 corresponding to the static force F_0 the function F may be linearized,

$$F(u) = F_0 - k\,(u - u_0), \quad k = dF(u_0)/du \approx [F(u_0{+}h) - F(u_0{-}h)]/(2h).$$

Then one obtains the harmonic oscillator

$$\frac{d^2 u}{dt^2} + \frac{k}{m}\,u = \frac{1}{m}\,(F_0 + k\,u_0) = \text{const.}$$

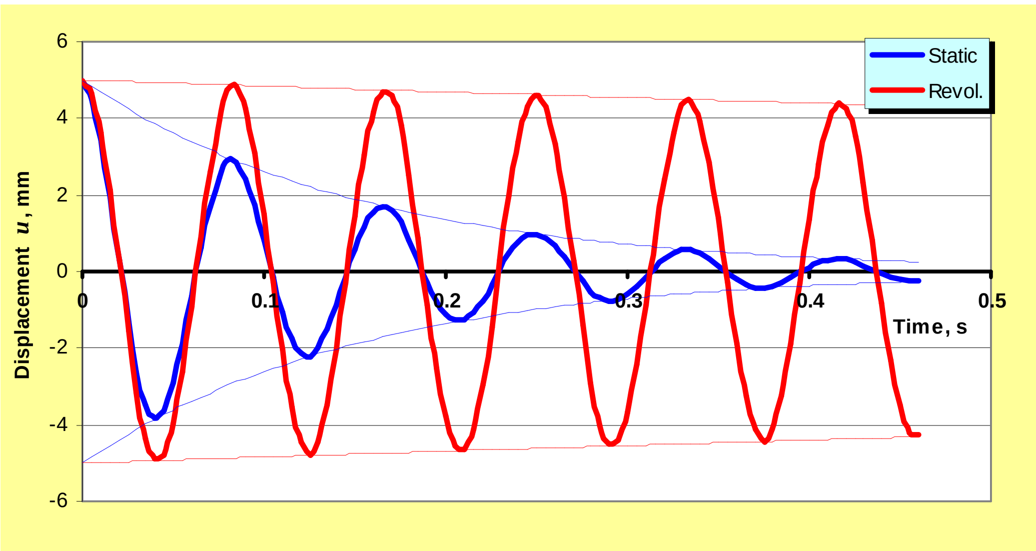

Figure 6.1 – Radial wheel oscillations in static case and revolving.

The frequency of its oscillations is

$$f = \frac{1}{2\pi}\sqrt{\frac{k}{m}}.$$

Similar relation served for experimental establishing the “dynamical” stiffness of tires by frequency of convenient experimental system oscillations [40,41]. Predictions of corresponding slopes $\frac{\mathrm{d}F}{\mathrm{d}u}$ of the belt model vs. experimental results are shown in Figure 6.2.

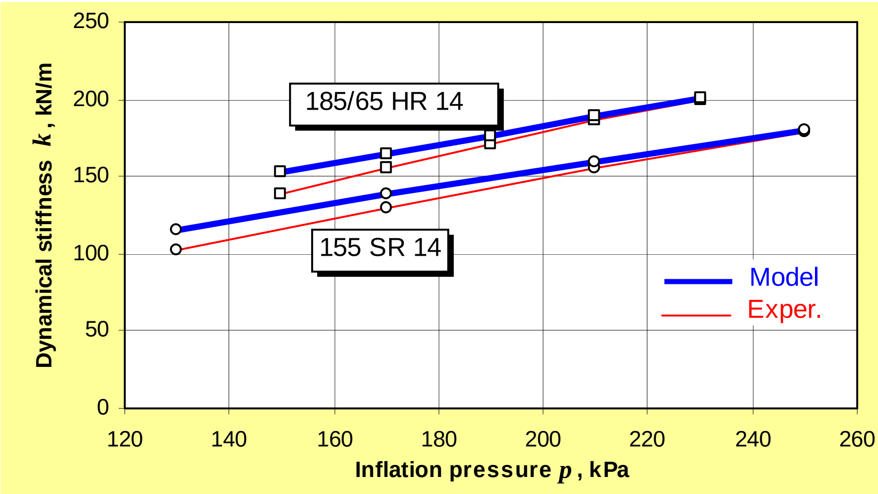

Figure 6.2 – Radial dynamical stiffness in two car tires.

If C denotes the effective rolling circumference $C = 2\pi R_{eff}$ of the tire then

$$f = \frac{v}{C}$$

is the frequency of tire revolution (Hz). This may become the source of resonance vibrations caused by jth harmonic of uniformity disturbance, if $f = f_j$, i.e. at the speed

$$v_j = C\frac{1}{2j\pi}\sqrt{\frac{k}{m}} = \frac{R_{eff}}{j}\sqrt{\frac{k}{m}}, \qquad j = 1, 2, \ldots$$

The most important is the highest speed. It belongs to the first harmonic

$$v_1 = R_{eff}\sqrt{\frac{k}{m}}.$$

Example. Figure 6.2 for the inflation pressure p = 200kPa gives the following estimates:

Tire	k, kN/m	m, kg	R_{eff}, m	v_1, km/h
155R14	155	13	0.28	110
185/65R14	180	15	0.31	122

Remark. When a tractor runs fast on the plane road low resonance speed due to low inflation pressure and thereby low stiffness of tires may cause problems.

b) Torsional (Directional) Oscillations

Let us reduce the wheel with pneumatic tire to a homogeneous disk of the same radius R_A and moment of inertia with respect to its radial axis $J \approx \frac{m}{4} R_A{}^2$, where m is the mass of the wheel.

The equation of movement is

$$J \frac{\mathrm{d}^2\delta}{\mathrm{d}t^2} = -M_z(\delta) \approx -\frac{\mathrm{d}M_z(0)}{\mathrm{d}\delta}\delta ,$$

i.e.

$$J \frac{\mathrm{d}^2\delta}{\mathrm{d}t^2} + \frac{\mathrm{d}M_z(0)}{\mathrm{d}\delta}\delta \approx 0 .$$

From this it follows that the frequency of directional vibrations of the wheel is

$$f_{dir} \approx \frac{1}{2\pi}\sqrt{\frac{\frac{\mathrm{d}M_z(0)}{\mathrm{d}\delta}}{J}} \quad \text{(Hz)} .$$

The critical speed is approximately

$$v_1 = R_A \sqrt{\frac{1}{J}\frac{\mathrm{d}M_z(0)}{\mathrm{d}\delta}} = 2\pi R_A\, f_{dir} .$$

Example. For the tires from the end of the foregoing section one obtains

Tire	$\frac{\mathrm{d}M_z(0)}{\mathrm{d}\delta}$, N.m	m, kg	R_A, m	J, kgm^2	f_{dir}, Hz	v_1, km/h
155R14	2120	13	0.29	0.27	14.0	92
185/65R14	2728	15	0.31	0.36	13.9	97

Remark. The parts connected to the wheel may represent much larger mass. However, a more detailed analysis belongs rather to mechanics of vehicle.

6.2 Stiff Belt Oscillations

The belt and tread belt block is a relatively autonomous massive part of the radial tire that may be excited to its own oscillations in several directions. For the sake of simplicity the belt is supposed stiff and oscillating as a cylindrical ring. Further, it will be written a instead of R_A [33,51].

a) Radial Oscillations

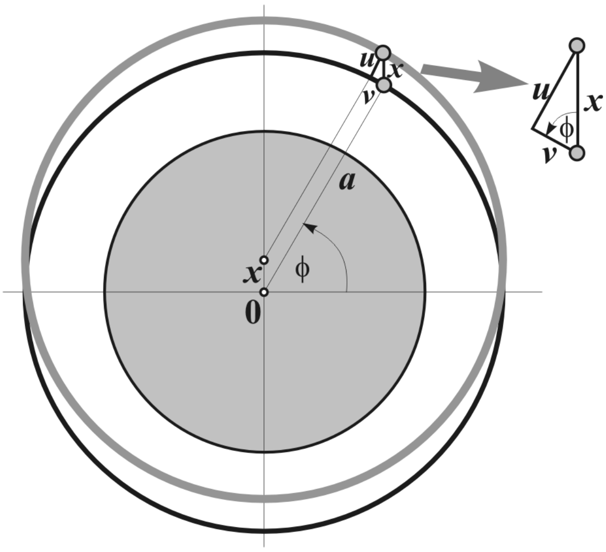

Figure 6.3 – Radial displacement of the stiff belt.

It is seen in Figure 6.3 that the radial and circumferential displacements u and v with respect to the fixed rim are

$$u(x, \phi) \approx x \sin \phi,$$

$$v(x, \phi) \approx x \cos \phi.$$

Potential energy corresponding to the displacement x is then

$$E_{pot} \approx \frac{1}{2} \int_0^{2\pi} [k_u u^2 + k_v v^2]\, a \, \mathrm{d}\phi$$

$$= ax^2 \int_{-\pi/2}^{\pi/2} [k_u \sin^2\phi + k_v \cos^2\phi] \, .$$

Because

$$\int_{-\pi/2}^{\pi/2} \sin^2\phi \, \mathrm{d}\phi = \int_{-\pi/2}^{\pi/2} \cos^2\phi \, \mathrm{d}\phi = \frac{\pi}{2},$$

one obtains

$$E_{pot} \approx \frac{\pi}{2} a (k_u + k_v) x^2.$$

The mass of sidewalls can be neglected. If m is the mass of the belt block, then the kinetic energy of the block is

$$E_{kin} = \frac{m}{2} \left(\frac{\mathrm{d}x}{\mathrm{d}t} \right)^2 .$$

Considering the belt system conservative enables to use the Hamilton's principle: the displacement $x(t)$ gives the functional

$$\int_0^t L(x, \frac{\mathrm{d}x}{\mathrm{d}t})\, \mathrm{d}t = \int_0^t (E_{kin} - E_{pot})\, \mathrm{d}t = \frac{1}{2} \int_0^t \left[m \left(\frac{\mathrm{d}x}{\mathrm{d}t} \right)^2 - \pi\, a\, x^2 (k_u + k_v) \right] \mathrm{d}t$$

a stationary value. The Euler-Lagrange equation [9] in this simple case yields

$$-\frac{\partial L}{\partial x} + \frac{\mathrm{d}}{\mathrm{d}t} \frac{\partial L}{\partial \left(\frac{\mathrm{d}x}{\mathrm{d}t} \right)} = 0 = \pi a (k_u + k_v)\, x + m \frac{\mathrm{d}^2 x}{\mathrm{d}t^2} .$$

The frequency corresponding to this linear harmonic oscillator is

$$f_{rad} = \frac{1}{2} \sqrt{\frac{a(k_u + k_v)}{\pi\, m}} \ \text{(Hz)} .$$

b) Torsional (Circumferential) Oscillations

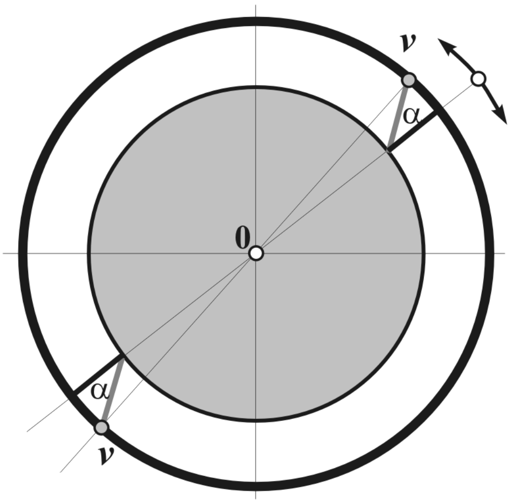

Figure 6.4 – Circumferential displacement of the stiff belt.

Figure 6.4 shows that circumferential displacements v are the same along the whole circumference

$$v(\phi, t) = v(t).$$

Corresponding potential energy is

$$E_{pot} = \frac{1}{2}\int_0^{2\pi} k_v\, v^2\, a\, \mathrm{d}\phi = \pi a\, k_v\, v^2 ,$$

kinetic energy

$$E_{kin} = \frac{m}{2}\left(\frac{\mathrm{d}v}{\mathrm{d}t}\right)^2 .$$

Considering the belt system conservative enables to use the Lagrange function

$$L(v, \frac{\mathrm{d}v}{\mathrm{d}t}) = \frac{m}{2}\left(\frac{\mathrm{d}v}{\mathrm{d}t}\right)^2 - \pi a\, k_v\, v^2$$

and equation

$$-\frac{\partial L}{\partial v} + \frac{\mathrm{d}}{\mathrm{d}t}\frac{\partial L}{\partial\left(\frac{\mathrm{d}v}{\mathrm{d}t}\right)} = 0 = \pi a\, k_v\, v + m\frac{\mathrm{d}^2 v}{\mathrm{d}t^2} .$$

This yields the eigenfrequency of circumferential vibrations

$$f_{circ} = \frac{1}{2\pi}\sqrt{\frac{2\pi a k_v}{m}} = \sqrt{\frac{a k_v}{2\pi m}}\ \text{(Hz)} .$$

c) Lateral (Axial) Oscillations

Axisymmetric Oscillations

Like in the case b) it is $w(\phi, t) = w(t)$ and $E_{pot} = \pi a\, k_w\, w^2$, $E_{kin} = \frac{m}{2}\left(\frac{\mathrm{d}w}{\mathrm{d}t}\right)^2$ and

$$E_{sym} = E_{pot} + E_{kin} = \pi a\, k_w\, w^2 + \frac{m}{2}\left(\frac{\mathrm{d}w}{\mathrm{d}t}\right)^2 = \text{const.}$$

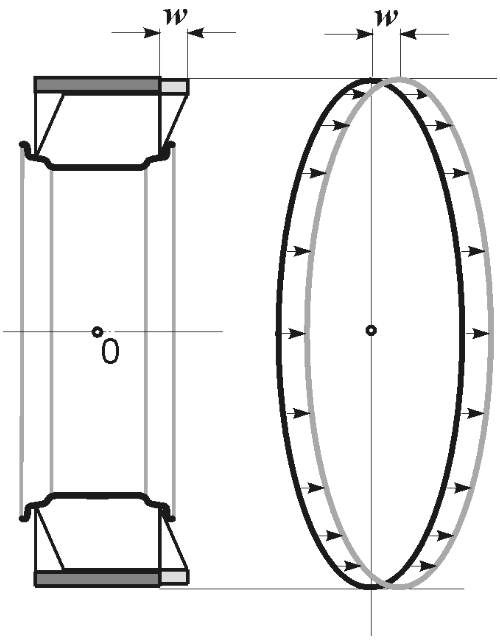

Figure 6.5 – Axisymmetric displacement

Differentiation of this equation with respect to time t gives

$$[\, 2\pi a\, k_w w + m \frac{d^2 w}{dt^2} \,]\, \frac{dw}{dt} = 0\,,$$

i.e. either $\frac{dw}{dt} = 0$ and then w = const. is a static displacement or

$$2\pi a\, k_w w + m \frac{d^2 w}{dt^2} = 0\,,$$

which yields

$$f_{lat} = \frac{1}{2\pi}\sqrt{\frac{2\pi a k_w}{m}} = \sqrt{\frac{a k_w}{2\pi m}}\ \text{(Hz)}\,.$$

Antisymmetric Oscillations

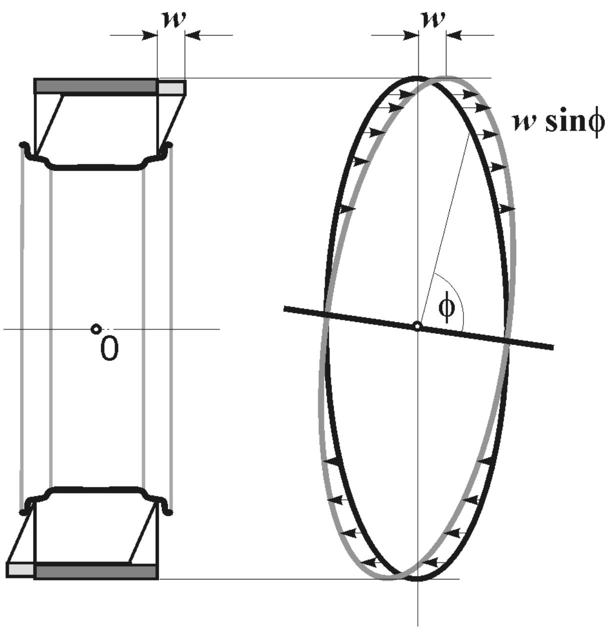

Figure 6.6 – Antisymmetric displacement

In this case (Figure 6.6)

$$E_{pot} = \frac{1}{2}\int_0^{2\pi} k_w\, w^2(t)\sin^2\phi\; a\, d\phi$$

$$= \pi a\, k_w\, w^2(t)/2,$$

$$E_{kin} = \frac{1}{2}\int_0^{2\pi} \frac{m}{2\pi a}\left(\frac{dw}{dt}\right)^2 a\, d\phi$$

$$= \frac{m}{2\pi}\int_0^{\pi} [\frac{d}{dt}(w(t)]^2 \sin^2\phi)\, d\phi$$

$$= \frac{m}{4}\left(\frac{dw(t)}{dt}\right)^2.$$

Now

$$E_{pot} + E_{kin} = \frac{1}{2} E_{sym}$$

and the equation of movement as well as the frequency remain the same as in the axisymmetric case (Figure 6.5). But the antisymmetric oscillations (Figure 6.6) are preferable due to lower total energy.

Examples. In 165/70R13 tire we have a = 0.2685m, m = 2kg, p = 200kPa. The coefficients of stiffness and frequencies of different vibration modes are as follows:

	v = 0km/h	v = 100km/h
k_u, Pa	474 845	378 675
k_v, Pa	322 523	318 536
k_w, Pa	77 662	82 581
f_{rad}, Hz	92.3	86.3
f_{circ}, Hz	83.0	82.6
f_{lat}, Hz	40.7	42.0

In 235/40R18 tire a = 0.3095m, m = 5.7kg, p = 200kPa. The coefficients of stiffness and frequencies of different vibration modes are listed in the following table:

	v = 0km/h	v = 120km/h
k_u, Pa	493 020	460 834
k_v, Pa	484 999	480 155
k_w, Pa	116 309	124 849
f_{rad}, Hz	65.0	63.8
f_{circ}, Hz	64.7	64.4
f_{lat}, Hz	31.7	32.9

6.3 Incompatibility of Conditions on Road and Roadwheel

Ignoring the obvious difference between road conditions and laboratory conditions concerning the heat transfer and energy dissipation one could reduce the problem of equivalent conditions to setting up equal radial deflection, contact pressure and contact length. Radial deflection is namely connected to carcass and belt deflections, contact pressure is joined with tread rubber compression and hysteresis, contact length mainly to shear stress and slips in circumferential direction. The following example shows that equivalent load and inflation pressure do not exist generally. Thus, any simulation of road regime through testing on a wheel road is necessarily unrealistic.

Let us consider the 295/80R22.5 tire, for example, with inflation pressure p = 850kPa. In static condition on planar support the vertical load F_R = 35kN produces radial deflection u_∞ = 35.8mm, contact length $L_{P,\infty}$ = 232mm (Figure 5.9) and average contact pressure $p_{m,\infty}$ = 948kPa. Preserving those tree quantities u, L_P, p_m also on a roadwheel would require that the following three planar curves

$$u(p, F_R) = u_\infty, \quad L_P(p, F_R) = L_{P,\infty}, \quad p_m(p, F_R) = p_{m,\infty}$$

intersect in one single point. Figure 6.7 shows these curves in the case of the considered 295/80R22.5 tire on the 2m roadwheel.

An analogous picture for the 165/70R13 car tire was published in [52]. It is possible to consider more quantities, e.g. the maximum circumferential change of belt curvature represented by the carcass equator curvature at the ends of contact area.

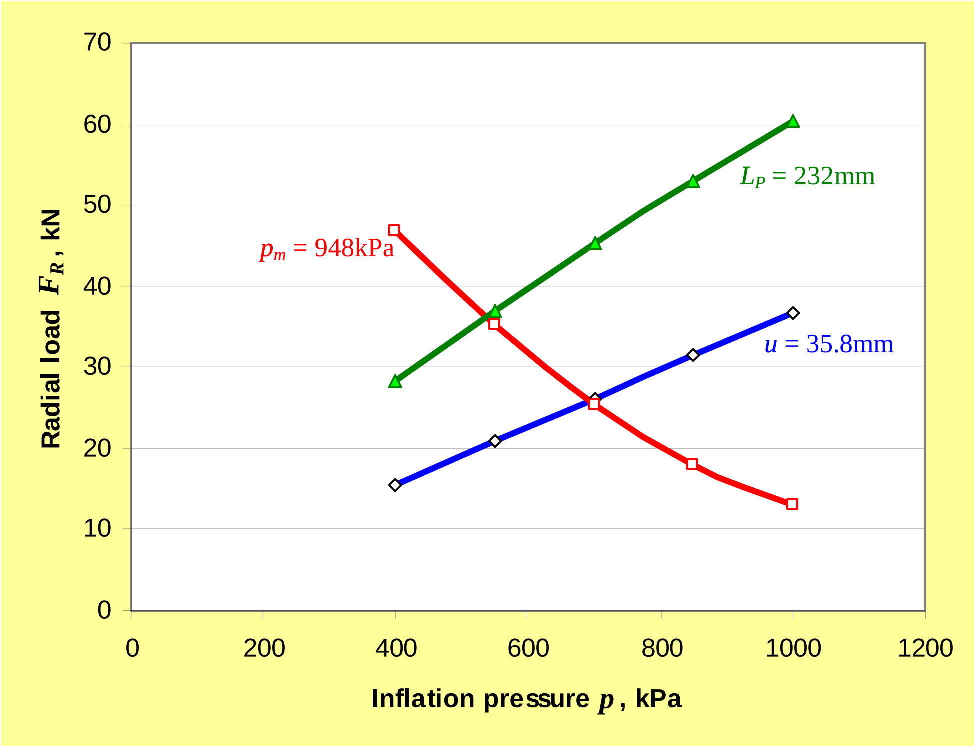

Figure 6.7 – Three conditions of planar contact transferred onto 2m roadwheel in 295/80R22.5 tire.

Remark. A correct formulation of the problem should be like this: what conditions in laboratory testing on drums are minimizing the differences in tire response simultaneously. So far namely only the most obvious radial deflection has been respected.

6.4 Optimization Problems

First applications of mathematical models are usually connected with attempts for improvements and finding more suitable solutions of various problems in design and technology. The possibility to predict radial deflections of radial tires led to considerations on optimization (based on the theory of games) even before the belt model had been developed [53]. Some optimization examples were published also in [42,43].

Tire production necessarily follows economical interest, which, in a very simplified view, means attaining the maximum profit from a set of available raw materials. If a tire is run on highways exclusively one may suppose the tire will be exposed to smaller irregularities and deflections than somewhere off the road. So it may be designed as it would almost never be deflected more than, say, 50mm. This condition may be well fulfilled also with a tire whose total profile is just a bit higher, e.g. 100mm. Higher cross sections supply higher ride comfort and damping capacity but on the other side they can need higher material consumption.

Such conclusions, however, collide with the necessity to amortize the existing machinery in a maximum measure and in shortest time. Implementations of new ideas require investments and always bring problems. Moreover the tire and rim create one unit that must fit the system of suspension etc. Nevertheless, wide cylindrical tires with low aspect ratios on today's vehicles show that the rational view has found its place.

The influence of tire geometry on some of tire properties will be shown on the case of preserving the carcass cord length and equator radius. The diameter and width of the rim will be increased while the bead area profile will remain the same. Such changes of the main rim dimensions will then be constricted by the condition that the tangent angle $\theta(r_B)$ in the bead point (Figure 4.16) is approximately 46°.

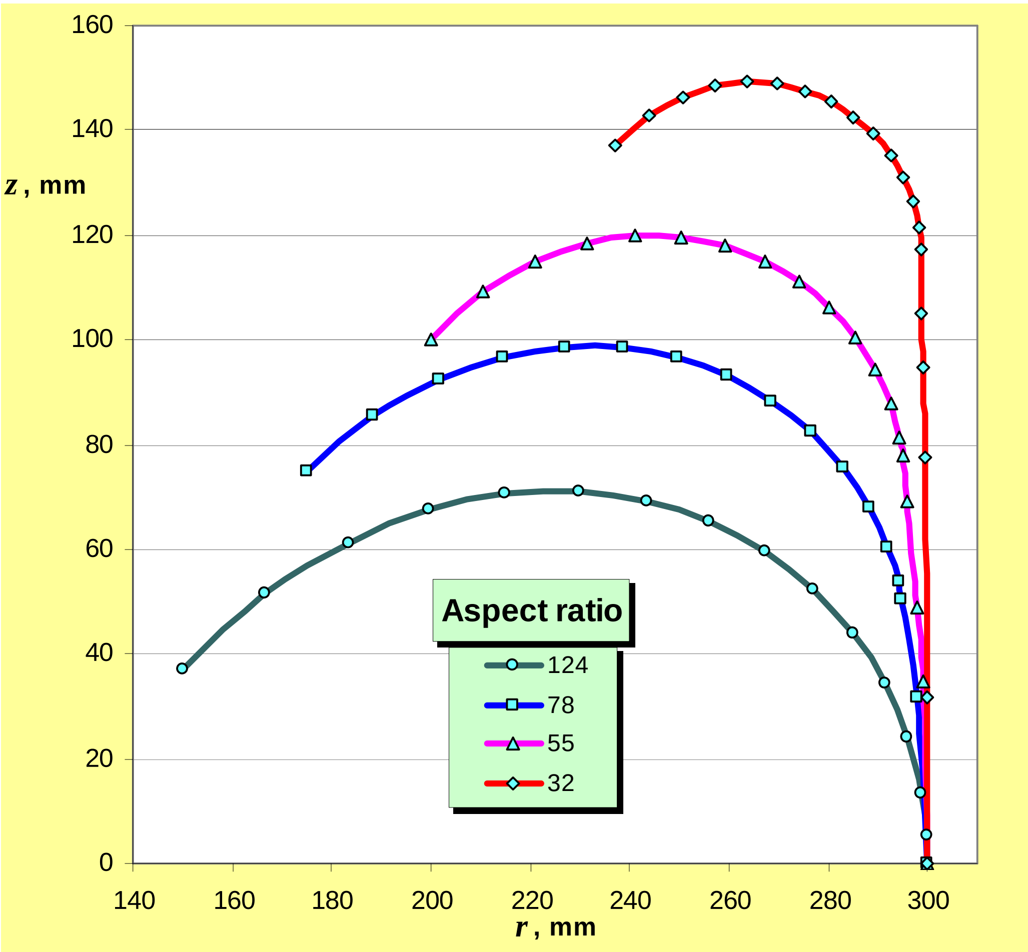

Figure 6.8 – Several meridional curves for fixed equator radius and meridional length.

The meridian curve parameters are chosen as follows:

- equator radius R_A =300mm,
- meridian length l_{AB} = 200mm,
- bead area height $r_B - D_{rim}/2 \approx$ 42mm.

Other parameters are listed in the following table.

´Rim´, in	r_B, mm	z_B, mm	R_N, mm	$\theta(r_B)$, °	W, mm	*Aspect ratio*, %	$R_A–r_B$, mm	Volume V, dm^3
3x10	150	37	100	45.7	71.0	124	150	24.5
6x12	175	75	250	43.3	98.7	78	125	31.9
7x13	187	87	400	44.8	108.9	66	113	33.3
8x14	200	100	600	46.5	119.8	55	100	33.9
9x15	213	113	900	48.0	130.6	46	87	33.4
10x16	225	125	1300	49.2	140.4	38	75	32.1
11x17	237	137	5000	46.7	149.2	32	63	30.2

Table 6.4.1 – Geometric parameters of different cross-sections.

Force parameters of the corresponding belt models at the same inflation pressure p = 200kPa and static vertical load F_R = 5884N (600kgf) are summarized up in Table 6.4.2.

´rim´, in	T, kN	k_u, MPa	k_v, MPa	k_w, MPa	u, mm	L_P, mm	Radial load-deflection curves $F_R(u)$, N
3x10	0.284	0.610	0.190	0.112	39.81	266	$–0.02073u^3 + 3.53773u^2 + 39.826u$
6x12	5.828	0.676	0.218	0.133	27.66	155	$–0.00536u^3 + 2.59443u^2 + 145.028u$
7x13	8.173	0.610	0.224	0.129	26.34	138	$–0.00254u^3 + 2.12361u^2 + 169.209u$
8x14	10.728	0.555	0.234	0.124	24.86	124	$–0.00111u^3 + 1.80099u^2 + 192.566u$
9x15	13.233	0.506	0.249	0.121	23.54	113	$–0.00037u^3 + 1.56089u^2 + 213.431u$
10x16	15.533	0.468	0.294	0.117	22.16	105	$–0.00058u^3 + 1.44423u^2 + 233.851u$
11x17	17.435	0.436	0.291	0.136	21.40	99	$–0.00340u^3 + 1.45014u^2 + 245.441u$

Table 6.4.2 – Static force parameters in cross-section variants of Table 6.4.1.

As soon as radial load-deflection curves (several of them are shown in Figure 6.9) and corresponding contact lengths are determined (Figure 6.10) computations of tangential forces and cornering can be performed. Some results are shown in Figure 6.10.

Figure 6.11 demonstrates that tires with low aspect ratios have shorter contact length. This is advantageous in respect to circumferential displacements in contact area and wear rate. However, it is disadvantageous on wet road due to short time needed for running the distance between front and rear edge of contact length and consequentially lower critical speed for hydroplaning (Chapter 9).

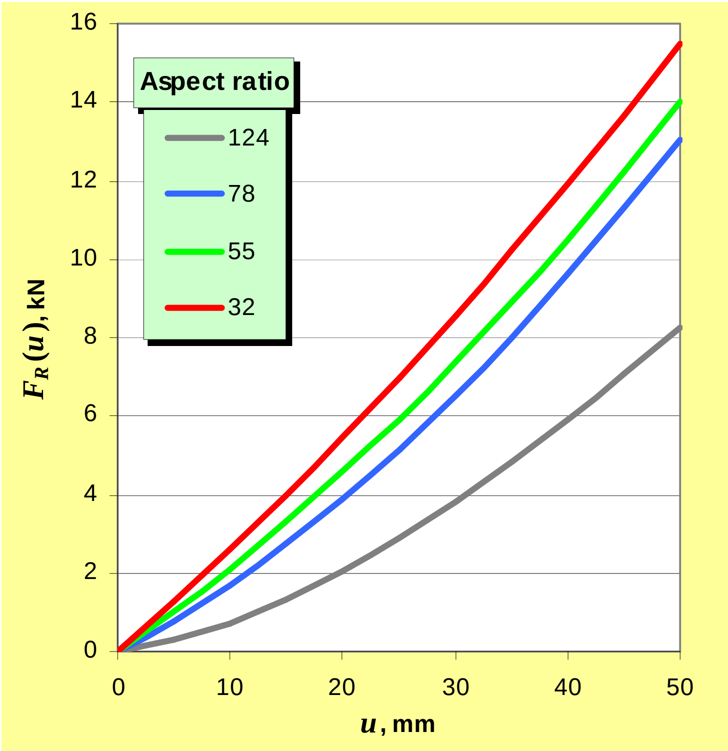

Figure 6.9 – Some of radial load-deflection curves from Table 6.4.2.

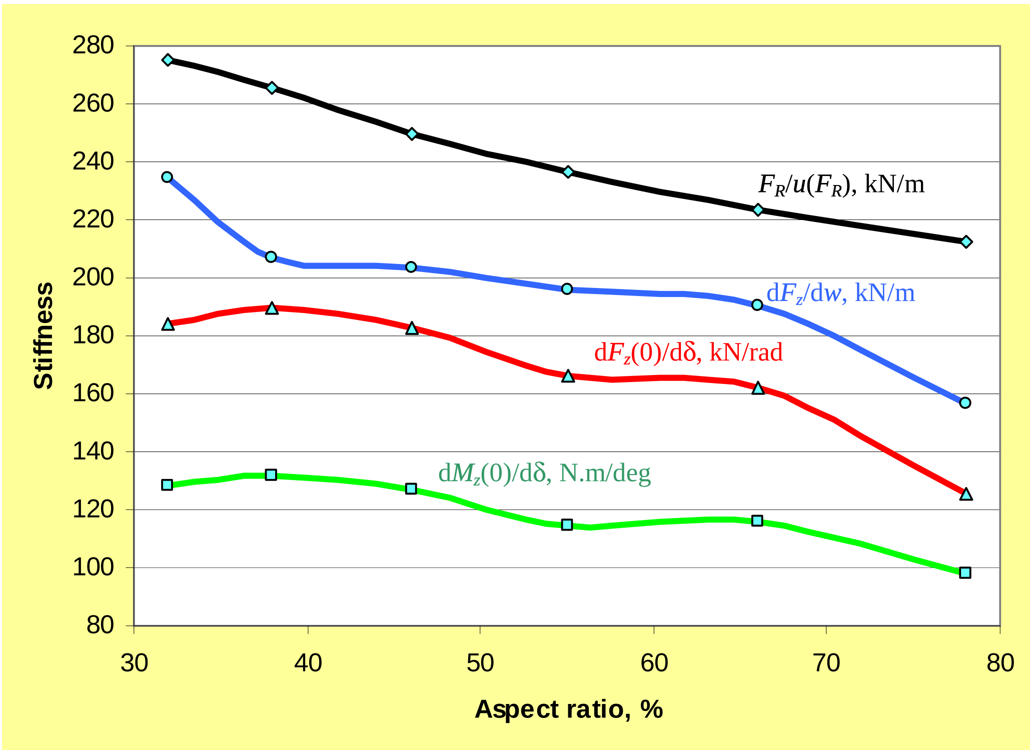

Figure 6.10 – Changes of radial, lateral and cornering stiffness in tire variants from Table 6.4.1.

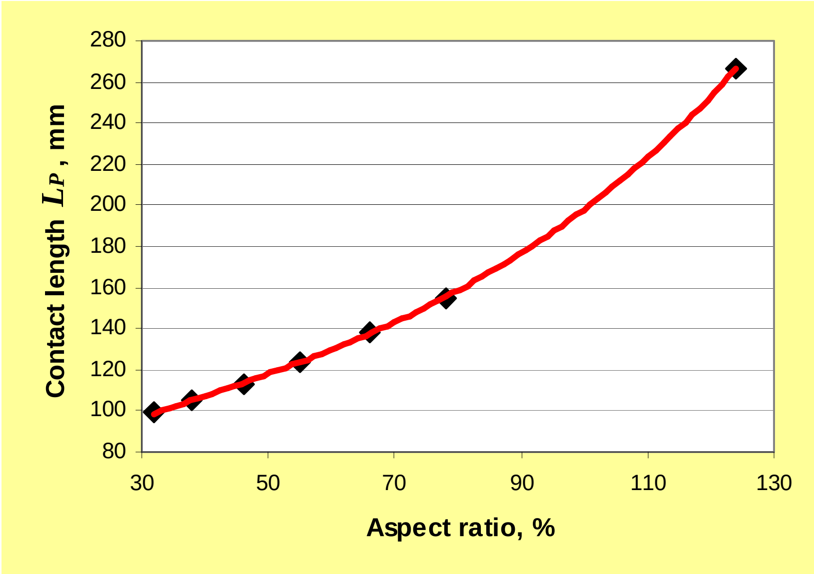

Figure 6.11 – Contact lengths under the same vertical load F_R = 5.887kN.

In connection with the contact length and energy losses it is also very interesting to consider radial displacements of the carcass equator along the circumference. Figure 6.12 shows the functions $u(\phi)$ for some of variants of Table 6.4.1. It can be seen that the decreasing aspect ratio smoothes the equator curve, i.e. reduces its curvature and local bending in the free part of the belt. This can reduce the bending hysteresis but, on the other hand, Table 6.4.1 shows increase of the total belt tension and, due to wider belt plies, greater interlaminar shear stress too.

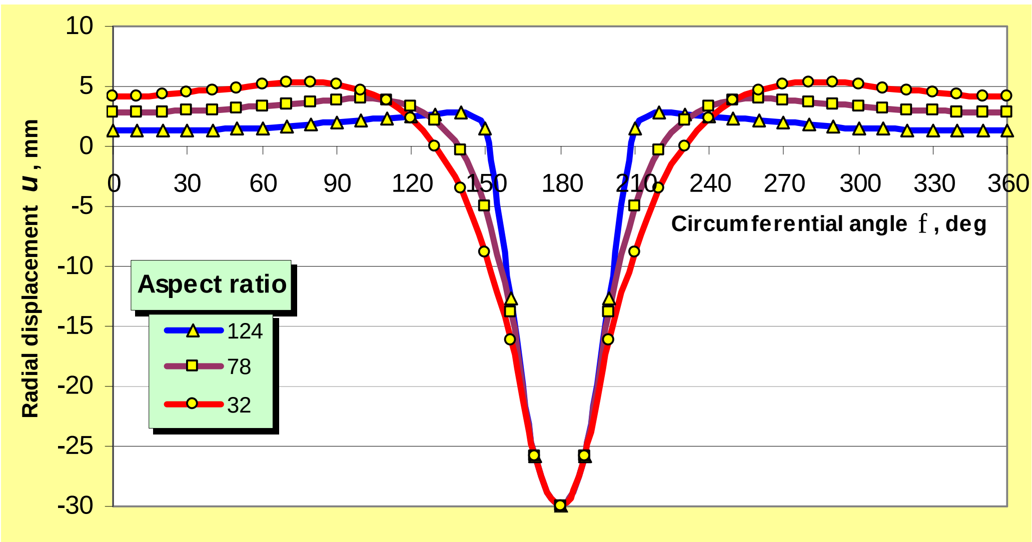

Figure 6.12 – Radial displacements of equator in three tire variants with different aspect ratios for the same radial deflection of 30mm.

Also the following very simplified economical reasoning speaks in favor of low profile tires. Let us take the sum

$$S = l_{AB}\,(R_A + D_{rim}/2) + W\,R_A$$

as a representative of material consumption. The vertical load corresponding to a fixed radial deflection, e.g. u_e = 22mm (Table 6.4.2), be an indicator of exploitation. The fraction (specific loading capacity)

$$e = \frac{F_R(u_e)}{S}$$

is then a measure for the material efficiency (Figure 6.13).

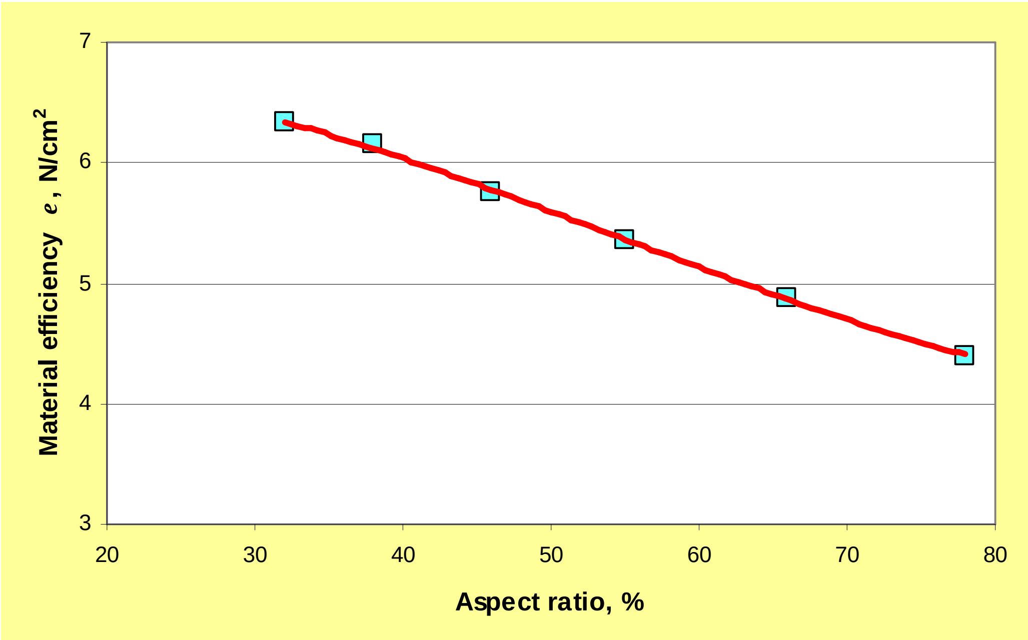

Figure 6.13 – Material loading efficiency increases with decreasing aspect ratio.

This very superficial consideration would require many improvements in various directions to be taken as serious and relevant. Namely, the unit N/cm^2 says little about real material consumption and should be substituted by something more convenient.

Nevertheless, even such consideration indicates that positive impacts may overwhelm negative ones. Worse damping, increased harshness or inclination to hydroplaning must be kept on acceptable levels by other means – rubber properties.

6.5 Tread Thickness and Modulus in Cornering

Tread pattern provides flexibility to tread rubber blocks and plays a very important role in tire response to tangential loading. Rubber modulus under the same conditions depends on rubber blend composition. It changes during the tire life and its instant values depend on temperature (Chapter 2). Groove depths decrease due to tread wear. Higher modulus E and smaller groove depth h_g reduce tangential mobility of tread blocks. Their influence on cornering characteristics is illustrated in the following Figures 6.14, 6.15. Interestingly, almost the same cornering force and torque are produced in E = 5MPa, h_g = 7mm and E = 3MPa, h_g = 2mm. As a rule, however, E is increased in tread rubber aging.

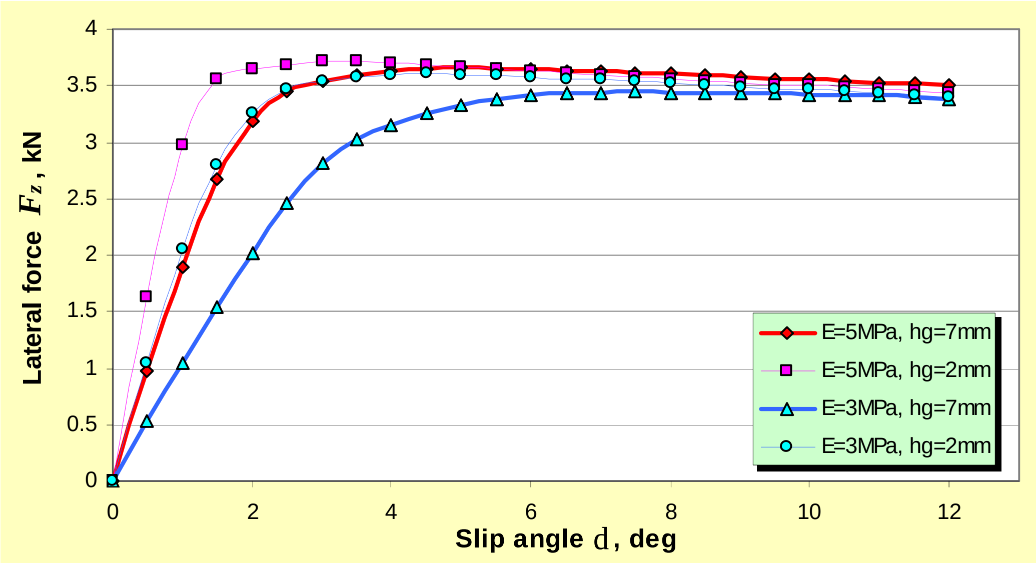

Figure 6.14 – Computed lateral force in 235/40R18 tire for two different tread rubber moduli and groove depths. Planar support, v = 90 km/h, p = 200kPa, F_R = 4.5kN.

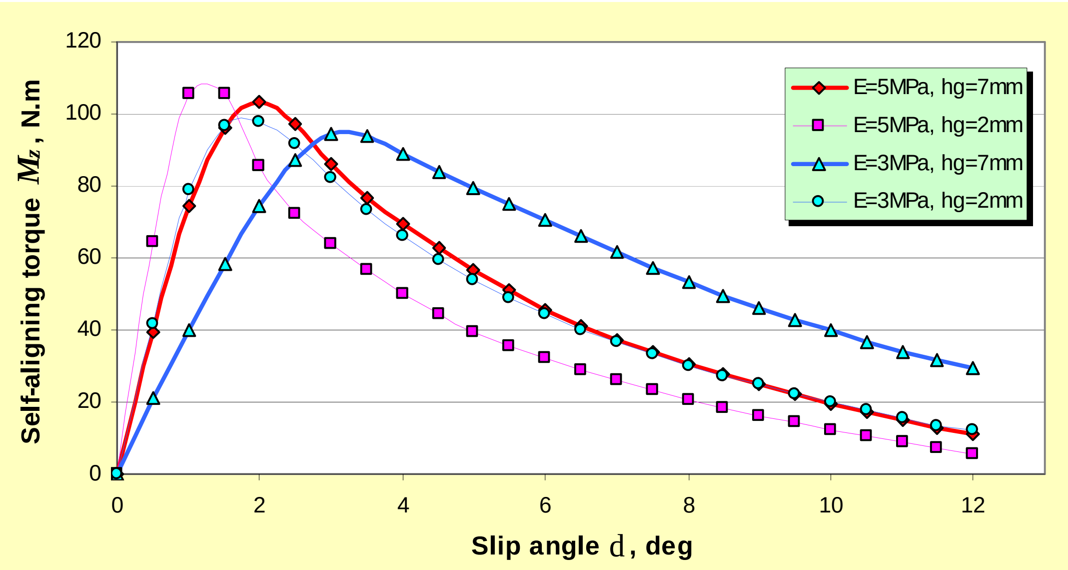

Figure 6.15 – Computed aligning torque in 235/40R18 tire for two different tread rubber moduli and groove depths. Planar support, v = 90 km/h, p = 200kPa, F_R = 4.5kN.

P

7 ROLLING RESISTANCE

Every body interacts with its environment in such a way that some local energy equilibrium is approached. In rolling loaded tire a part of its “ordered energy“ is transferred into local acceleration of the surrounding mass. Dissipative mechanisms produce heat, noise, turbulence of air or displacements of the mass covering the ground such as water, mud, snow, dust, stones etc. But through friction, material hysteresis and heat transfer also internal energy represented by temperature is changed. The choice of materials and the construction of the tire wall and tread pattern are the only areas, where tire producers can assert their effort to reduce energy losses in rolling tire.

If the tire is rolling with minimum transfer of its kinetic energy to its neighborhood, for example on planar, smooth highway or even better on a test machine in laboratory, its energy loss is practically equal to the heat produced due to stress/strain changes and hysteresis in its wall and tangential slips of tread. Hysteresis in linear materials is proportional to the square of the strain or stress amplitude. Having estimated elastic and hysteresis parameters of tire materials, one can try to solve the problem of determining the strain energy loss in tire wall at given external load of tire. Nowadays the use of some FEM software is the most common way to solve this problem.

When tire material or construction is changed and a new tire is made, it is necessary to examine the expected effect experimentally. The simplest way for determining rolling losses is to measure the rolling resistance of the tire directly. Tire rolling resistance on the background of reduction of total energy losses of tires is excellently summarized in [8] or the paper of SCHURING, D. J. – FUTAMURA, S., Rubber Chem. Technol., Vol. **63**, (*1990*), p. 315. After a significant reduction of rolling resistance due to radial construction and material improvements the need of tools for evaluation and distinguishing small differences in measured data appeared. The goal of the following sections is to show proper analytical expressions for the rolling resistance coefficient as functions of test condition parameters.

Friction

Friction is a very complex way of interaction of bodies or fluids and no definitive, generally valid conclusions on it have been formulated so far. It is influenced by many factors, e.g. by smoothness of the interfacing surfaces of bodies, by temperature, normal pressure, by vibrations and thus by the velocity of movement, etc.

Most frequently the Coulomb friction model is used. It claims that the resistance **R** against movement is proportional to the load component parallel with the normal of the supporting surface and its direction is opposite to the relative velocity $\boldsymbol{v}$, i.e.

$$\mathbf{R} = -\mu F \boldsymbol{v}/|\boldsymbol{v}| \;.$$

Thus, in one-dimensional or scalar case,

$$R = -\,\mathrm{sign}(v)\,\mu F \;\geq\; 0$$

The quantity

$$\mu = \frac{|\mathbf{R}|}{F} \geq 0$$

is called coefficient of friction. Let us consider a simple example for illustration.

An axisymmetric body, such as cylinder or disk, characterized by the outer radius a and moment of inertia J, revolving with a circumferential velocity v is slowed down by friction which can be represented by a circumferential brake. The movement of the body in relation to its fixed axis of rotation can be described by one generalized variable, namely the angle ϕ between a fixed direction, e.g. the vertical one, and radius vector of a fixed point on the circumference. Let the initial value at the instant $t = 0$ be zero, $\phi(0) = 0$. Kinetic energy of the body at the time t is

$$E_{kin}(t) = \frac{J}{2}\left(\frac{\mathrm{d}\phi(t)}{\mathrm{d}t}\right)^2 = \frac{J}{2}\ \omega^2(t)\ ,$$

where ω is the angular velocity.

The dissipated energy is equal to the work of the friction force during the time t

$$W(t) = \int_0^t \mathbf{R.v}\ \mathrm{d}t = \int_0^t \mu F a \frac{\mathrm{d}\phi}{\mathrm{d}t}\mathrm{d}t = \mu F a \phi(t).$$

Due to law of conservation of energy

$$E_{kin}(t) + W(t) = E_{kin}(0) = \frac{J}{2}\ \omega^2(0) = \frac{J}{2}\left(\frac{v(0)}{a}\right)^2 .$$

Substitution in the left side and differentiation with respect to t give

$$J\frac{\mathrm{d}^2\phi}{\mathrm{d}t^2} + \mu F a = 0. \tag{7.1}$$

This equation can be immediately used in tire rolling resistance measurements.

7.1 Basic Principles of Rolling Resistance Measurements

1. *Standard dynamometric measurements*. To keep the velocity $v = a\omega(t)$ constant the torque $M = \mu F a$ eliminating the rolling resistance moment must be supplied. For constant angular velocity $\omega(t)$ the equation (7.1) gives $\mu = \dfrac{M}{F \times a}$.
2. *Recording* $\phi(t)$ *or* $\mathrm{d}\phi(t)/\mathrm{d}t$. For convenient number and distribution of points $(t_i, \phi(t_i))$ or $(t_i, \mathrm{d}\phi(t_i)/\mathrm{d}t)$, $i = 1, 2, ..., n$ the angle $\phi(t)$ or angular velocity $\mathrm{d}\phi(t_i)/\mathrm{d}t$ can be approximated by a regression function, e.g. by a polynomial, which can easily be differentiated. This method in combination with up-to-date electronics can be used in improvised facilities for estimating rolling losses in tires (e.g. uncustomary, very small or extremely big ones).
3. *Direct monitoring the tension* on a haul device equipped with the measured tire.

4. *Coast-down tests*. No special device is required but, on the other hand, only an average coefficient $\bar{\mu}$ over an time interval can be obtained. Conservation of energy gives at the instant t_s of stop

$$W(t_s) = E_{kin}(0) - E_{kin}(t_s).$$

From this and the above expressions one yields with $v_0 = v(0)$, $s = a\,\phi(t_s)$

$$\bar{\mu} = \frac{Jv_0}{a^2 F t_s} = \frac{Jv_0^2}{2a^2 F s}$$

or, in $n > 1$ steps,

$$\bar{\mu}_{k,\,k+1} = \frac{J}{a^2 F}\,\frac{v_k - v_{k+1}}{t_{k+1} - t_k}, \qquad k = 0, 1, \ldots, n-1.$$

Remark. Practically the same equations hold also for free rolling tires mounted on massive rims in laboratory tests or in measurements on vehicles. Extensions of moving systems only increase the number of terms in total kinetic energy expressions. Energy losses in all real dynamical systems are influenced by friction in bearings, aerodynamic turbulence etc. Hence, elimination of these external losses constitutes the basic problem in processing rolling resistance data.

Variability of rolling resistance can be demonstrated on the 295/80R22.5 tire run on the 2m road wheel [51]. The initial inflation pressure was 850kPa and the air content in the tire was fixed. Vertical load was kept on 34.83kN. The velocity changed stepwise every five minutes by ±10km/h as shown in Figure 7.1.

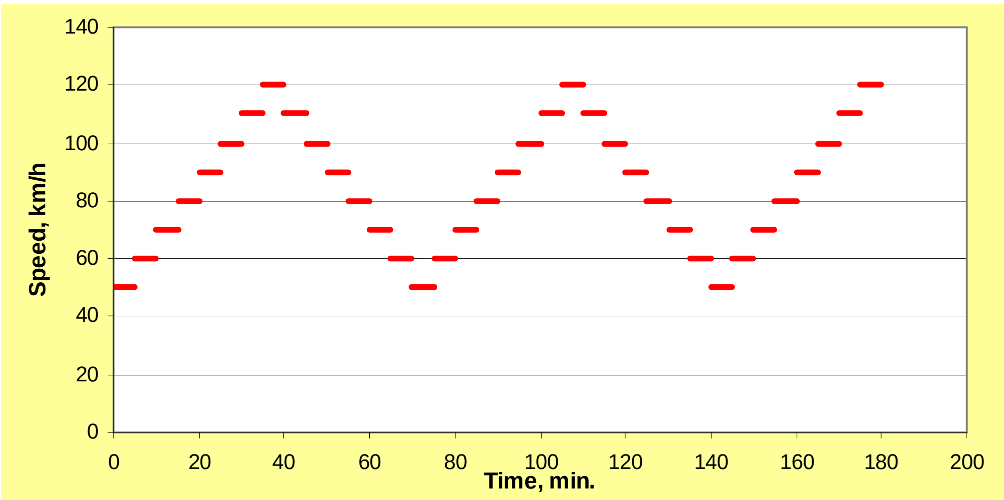

Figure 7.1 – Cyclic changes of speed in 295/80R22.5 tire.

The rolling resistance was measured at the end of each 5-minute-time interval. Corresponding results are recorded in Figure 7.2. The steep decrease of rolling resistance coefficient in the beginning of the test is caused by fast increase of both the tread temperature and inflation pressure. The last branch of the test is marked by triangles. A tendency to creation of a slim equilibrium loop is obvious.

Figure 7.3 shows results in two tires 295/80R22.5 for speeds chosen independently as $v = 10i$ (km/h), where i is a random number from the set {5, 6, …, 11, 12}.

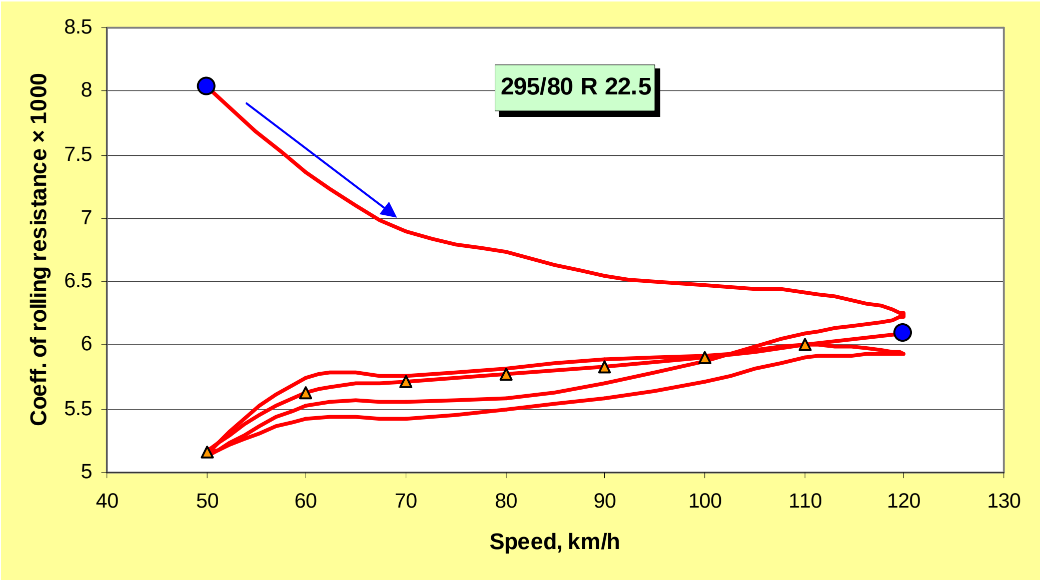

Figure 7.2 – Changes of rolling resistance in cyclic setting up the speed shown in Figure 7.1.

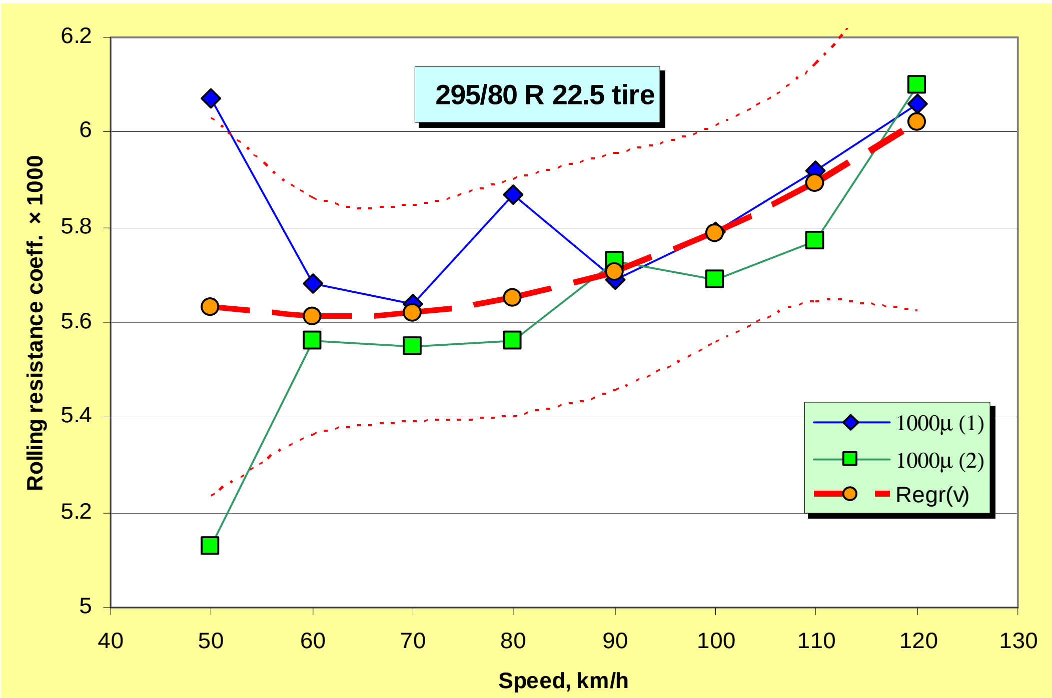

Figure 7.3 – Rolling resistance measured at speeds randomly chosen between 50 and 120km/h.

In order to attain some degree of objectivity in measuring the tire rolling resistance coefficients μ it was necessary to settle obligatory standards like ISO 9948 or J1269 that should assure reproducibility and comparability of results.

7.2 Dependence of m on Velocity

A fixed cross-section on the rolling tire circumference is periodically deflected. During a revolution a strain cycle is performed in each meridional section. Depending on temperature gradient the heat generated due to hysteresis and friction is transferred from the location of its rise to its neighborhood causing temperature changes. Hysteresis at constant deflection velocity and the heat rate decrease with temperature (Chapter 2). The local or average temperature ϑ due to a step increment of speed can be well approximated by the exponential function

$$\vartheta(t) = \vartheta_0 + (\vartheta_e - \vartheta_0)(1 - e^{-a(t-t_0)}),\ a > 0,$$

Here the index e relates to an equilibrium state, $\vartheta(t) \rightarrow \vartheta_e$ for $t \rightarrow \infty$. In this transition process the rolling resistance coefficient drops which can be described roughly as follows

$$\mu(t) = \mu_e + (\mu(t_0) - \mu_e)\ e^{-b(t-t_0)}, \quad b > 0,$$

where $\mu(t) \rightarrow \mu_e$ for $t \rightarrow \infty$ and μ_e is an equilibrium value.

The equilibrium rolling resistance of radial tires changes very little in the common performance speed range. The approximate constancy of μ would imply proportionality between the energy lost in tires and the distance run.

However, hysteresis depends on strain rate (speed of deflection). At low velocities the dominant influence belongs to temperature increase, i.e. μ is a decreasing function of velocity. But at high speeds vibration phenomena occur (demonstrated e.g. by the noise level), the number of strain cycles is multiplied and the stress-strain intensity in tire wall is increased. This prevails the drop of material hysteresis.

Because no power is needed to keep a body in rest in stable condition, one could put $\mu(0) = 0$. On the other hand, however, a relatively great power is needed to bring a body from the state of stable rest to movement. Omitting details we simply assume that

(i) $\mu(v) \rightarrow a_0 > 0$ for $v \rightarrow 0$ and

(ii) $\mu(v)$ is a smooth function of rolling velocity v in the region of $v > 0$.

Thus, $\mu(v)$ can be approximated by a polynomial

$$\mu(v) \approx a_0 + a_1 v + a_2 v^2 + \ldots + a_n v^n, \quad a_0 > 0.$$

The initial decrease of μ and its rapid increase at higher speeds due to vibrations requires at least two other non-zero coefficients.

Linear Regression

Regression is the most common way for finding the coefficients a_i on the right hand side of the approximation of $\mu(v)$ [11]. To maximize degrees of freedom and refine statistical considerations it is desirable to reduce the number of a_i to minimum.

Let us suppose that the mean value of μ at a given velocity v can be expressed more generally as linear combination of three independent functions $(f_1(v) = 1, f_2(v), f_3(v))$,

$$\mu(v) \approx \beta_1 .1 + \beta_2 f_2(v) + \beta_3 f_3(v) . \tag{7.2}$$

Let us further assume that some homogeneous values of μ are obtained in a series of *m* tires according a test plan given as a sequence of pairs of speeds and times $\{(v_1, t_1), ..., (v_n, t_n)\}$. Thus the function (7.2) shall fit a set

$$\{\mu_{ij} : i = 1, ..., n; j = 1, ..., m\}.$$

Remark. To assure independence in measurement, the indices *i* and *j*, i.e. speed and time, should be chosen independently. Evidently, such an experiment would be more complicated. As a rule, times t_i are chosen as approximately quasi-equilibrium ones. If time instants t_i were random, the variance in the corresponding experiment would increase considerably. Though this variance would represent the real performance conditions much better than the quasi-equilibrium conditions do, the sensitivity of such testing would drop dramatically. Moreover, the time and money consumption would increase. To reveal small differences in different tire series it is necessary to reduce the experimental variance as much as possible. This is achieved in praxis by a fixed, computer controlled testing regime $\{(t_i, v_i): i = 1, \ldots, n\}$.

●

Considering values μ_{ij} obtained at *n* velocities v_i in *m* tires with random errors ε_{ij} in equation (7.2) one gets the following linear regression model

$$\mu_{ij} = \beta_1 + \beta_2 f_2(v_i) + \beta_3 f_3(v_i) + \varepsilon_{ij}, \quad i = 1, ..., n; \; j = 1, ..., m$$

or, in matrix form,

$$\mathrm{m} = \mathbf{X}\mathrm{b} + \mathrm{e} , \tag{7.3}$$

$$\mathrm{b} = \begin{pmatrix} \beta_1 \\ \beta_2 \\ \beta_3 \end{pmatrix}, \qquad \mathrm{m} = \begin{pmatrix} \mu_{11} \\ \vdots \\ \mu_{1n} \\ \vdots \\ \mu_{m1} \\ \vdots \\ \mu_{mn} \end{pmatrix}, \qquad \mathrm{e} = \begin{pmatrix} \varepsilon_{11} \\ \vdots \\ \varepsilon_{1n} \\ \vdots \\ \varepsilon_{m1} \\ \vdots \\ \varepsilon_{mn} \end{pmatrix}.$$

Here **X** is an *nm* × 3 matrix consisting of *m* blocks

$$\mathbf{X}_j = \begin{pmatrix} 1 & f_2(v_1) & f_3(v_1) \\ \ldots & \ldots & \ldots \\ 1 & f_2(v_n) & f_3(v_n) \end{pmatrix}, \quad j = 1, ..., m ,$$

each of which corresponds to an individual tire and the design of experiment, b is the vector of regression coefficients, m is the vector of measured values and e denotes the vector of errors.

The assumption that all components of the error vector e belong to the same normal distribution $N(0, \sigma^2)$ (homoscedasticity) represents the simplest case.

Multiplying the equation (7.3) by the transposed matrix $\mathbf{X}^T$ yields the so called normal equations [11]

$$\mathbf{X}^T \mathbf{X}\, \mathrm{b} + \mathbf{X}^T \mathrm{e} = \mathbf{X}^T \mathbf{X}\, \mathbf{b} = \mathbf{X}^T \mathrm{m} \quad ,$$

where **b** is an estimate of the unknown vector b of coefficients. The design of experiment assures regularity of the matrix $\mathbf{X}^T\mathbf{X}$. Its inverse $\mathbf{V} = (\mathbf{X}^T\ \mathbf{X})^{-1}$ is called covariance matrix. Then

$$\mathbf{b} = \mathbf{V}\,\mathbf{X}^T \mathrm{m}\,.$$

The variance σ^2 is estimated by $s^2 = S^2 / (n-3)$, where

$$S^2 = (\mathbf{Xb} - \mathrm{m})^T . (\mathbf{Xb} - \mathrm{m})$$

is the sum of squares of residuals, *SSR*. It can be proved that under the assumptions concerning e the vector **b** belongs to the multivariate normal distribution, i.e. b_i belongs to $\mathrm{N}(\beta_i, V_{ii}\,\sigma^2)$ and its variance can be estimated by $V_{ii}\, s^2$ [11].

The matrix **V** also defines the confidence belts for individual values of $\mu(v)$ and for the whole regression polynomial at a chosen significance level α [11].

For $m > 1$ adequacy of the regression function can be tested. The experimental variance is estimated by

$$s_E^2 = \frac{1}{n}\sum_i s_{Ei}^2 \quad \text{with} \quad s_{Ei}^2 = \frac{1}{m-1}\sum_j (\mu_{ij} - \bar{\mu}_i)^2 \text{ and } \bar{\mu}_i = \frac{1}{m}\sum_i \mu_{ij}\,.$$

The sum of squares of residuals can be decomposed as follows

$$S^2 = \sum_{i,j}\left[(\mu_{ij} - \bar{\mu}_i) + (\bar{\mu}_i - b_1 - b_2 f_2(v_i) - b_3 f_3(v_i))\right]^2 = n\, s_E^2 + S_L^2\,.$$

The contribution to variance caused by lack of fit and estimated by $s_L^2 = S_L^2/(n-3)$ is compared with the experimental variance estimated by s_E^2. If

$$F = s_L^2 / s_E^2 \geq F_\alpha(n-3, N-n),$$

where F_α denotes the critical value for the significance level α, the adequacy of regression must be rejected.

•

After having obtained adequate regression polynomials in two series of tires, *I* and *II*, their statistical identity can be tested within their common variance limits [54].
For k parameters $\beta_1, \ldots, \beta_k$ in regression function (7.2) and different numbers of tires in both series the following criterion is to be used

$$Z = \frac{N_I + N_{II} - 2k}{2(S_I^2 + S_{II}^2)} (\mathbf{b}_{II} - \mathbf{b}_I)^T (\mathbf{V}_I + \mathbf{V}_{II})^{-1} (\mathbf{b}_{II} - \mathbf{b}_I)\ ,$$

which belongs to the distribution $F(k, N_I + N_{II} - 2k)$.

In the most frequent case, when the same test design is run, i.e. $N_I = N_{II} = N = mn$ and $\mathbf{V}_I = \mathbf{V}_{II} = \mathbf{V}$, the quantity

$$Z = \frac{N-3}{S_I^2 + S_{II}^2} (\mathbf{b}_{II} - \mathbf{b}_I)^T (2\mathbf{V})^{-1} (\mathbf{b}_{II} - \mathbf{b}_I) = \frac{N-3}{S_I^2 + S_{II}^2} (\mathbf{b}_{II} - \mathbf{b}_I)^T \mathbf{A}^T\mathbf{A}\, (\mathbf{b}_{II} - \mathbf{b}_I) \frac{1}{2}$$

belongs to the distribution $F(k, 2(N-k))$. Thus, if $Z \geq F_\alpha(k, 2(N-k))$, the identity of rolling resistance polynomials in both series must be rejected at the significance level α.

Choice of f_2, f_3

The functions f_2, f_3 in Equation (7.2) must be linearly independent. If a fixed design of rolling resistance tests is kept, one could use orthogonal polynomials, i.e. polynomials orthogonal on a fixed set of discrete values of velocity. Unfortunately, their adaptation to individual plans would just complicate the problem without any contribution to its causal or physical substance. So, in an easier way, simply two different powers of v will be taken: $f_2(v) = v^r$, $f_3(v) = v^s$, where r, s are integers, $0 < r < s$.

A set of pairs $\{(r, s) : 0 < r < s < 10\}$ was examined in 61 various series of radial tires. Results are shown in Table 7.2.1. The right upper part (above diagonal) of the Table contains total sums of squares of residuals, the left lower part shows the transposed matrix whose entries are the corresponding numbers of non-adequacy cases.

s ®

s	1	2	3	4	5	6	7	8	9	r
1	X	10.48	6.68	4.10	2.57	1.87	1.75	2.05	2.63	1
2	27	X	4.77	3.12	2.16	1.73	1.68	1.88	2.26	2
3	25	18	X	2.39	1.86	1.64	1.64	1.77	2.00	3
4	16	15	10	X	1.69	1.60	1.62	1.71	1.83	4
5	15	9	7	4	X	1.60	1.62	1.67	1.73	5
6	5	3	4	3	2	X	1.63	1.66	1.68	6
7	4	2	2	3	1	2	X	1.65	1.66	7
8	4	2	2	2	2	2	5	X	1.66	8
9	4	3	3	3	3	4	6	8	X	9
	1	2	3	4	5	6	7	8	9	

r ®

Table 7.2.1 – Sums of squares of residuals, $S^2(r, s)x10^{-4}$ (above diagonal) and numbers of non-adequacy cases n(s, r) (below diagonal) in 61 series of radial tires in dependence on power exponents r, s.

Hence, with regard to minimum r and s the regression polynomial

$$P(v) = \beta_1 + \beta_2 v^2 + \beta_3 v^4$$

is quite acceptable (and recommendable) for the speed range from 50 to 170km/h.

In different tires and other speed ranges another regression polynomial may prove most appropriate, of course. Figure 7.3 shows an example, where using a polynomial of degree greater than 2 would be of no use.

Let us consider rolling resistance data of the 165/70R13 tire obtained in laboratory on a 2m-roadwheel (Table 7.2.2).

i	1	2	3	4	5
speed v_i, km/h	50	90	120	150	170
$10^3\ \mu_{i1}$	12.29	13.09	13.95	16.14	18.01
$10^3\ \mu_{i2}$	12.46	12.93	13.92	16.05	17.87

Table 7.2.2 - Values of rolling resistance coefficients μ in 165/70 R 13 tire.
Initial inflation pressure p = 250 kPa, load F_R = 5100 N.

Figure 7.4 shows the regression polynomials for several *r*, *s*. Exponents (*r*, *s*) from the matrix

$$\begin{pmatrix} (1,2) & (1,3) & (1,4) & (1,5) & (1,6) \\ & (2,3) & (2,4) & (2,5) & (2,6) \\ & & (3,4) & (3,5) & (3,6) \\ & & & (4,5) & (4,6) \end{pmatrix}$$

give *SSR* shown in Figure 7.5. Minimal *SSR* are near the diagonal. Larger *r* may fail in extrapolations. Thus, it is difficult to give a general recommendation. E.g. one can start with *r* = 1 and try *s* = 2, 3, … until adequacy is reached. Then *r* = 2, *s* = 3, 4, … can be tested etc. Finally, the pair (*r*, *s*) minimizing *r* + *s* can be taken as the result.

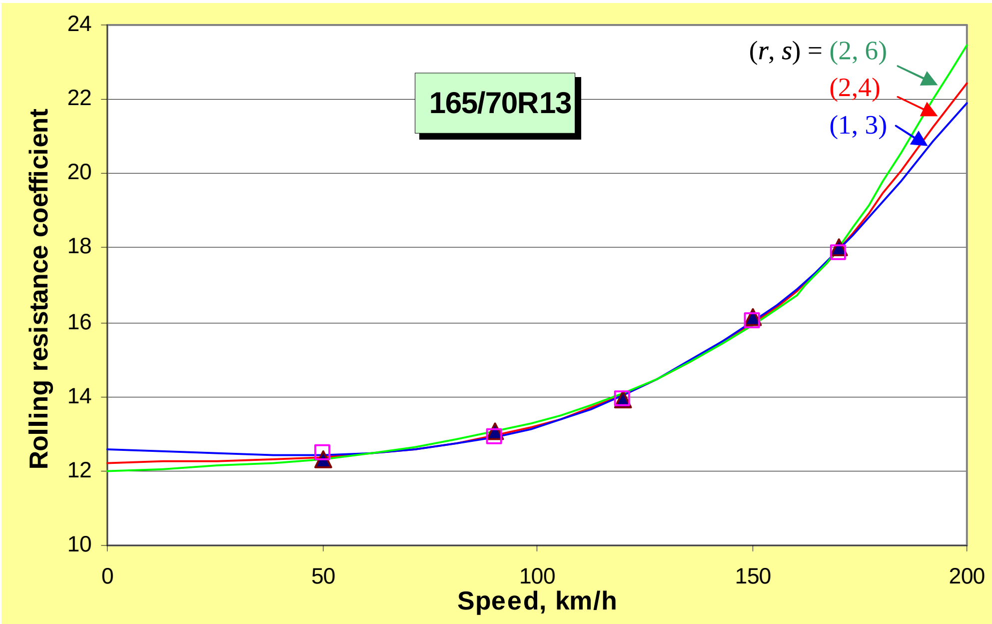

Figure 7.4 – Several regression polynomials for the data in Table 7.2.

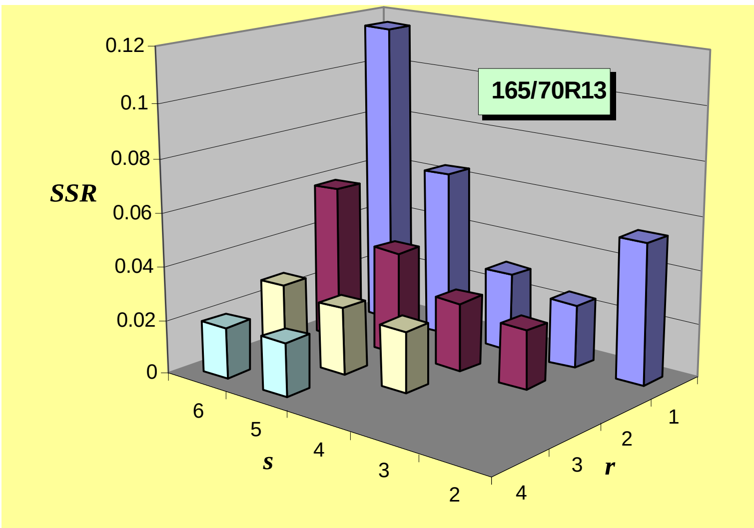

Figure 7.5 – Sums of squares of residuals (SSR) for different (r, s).

Influence of Some Construction Factors on Rolling Resistance

The linear regression methods were used to evaluate effects of wider rim and some construction changes in tire belt. Dotted lines denote the corresponding 95-percent confidence limits around regression polynomials.

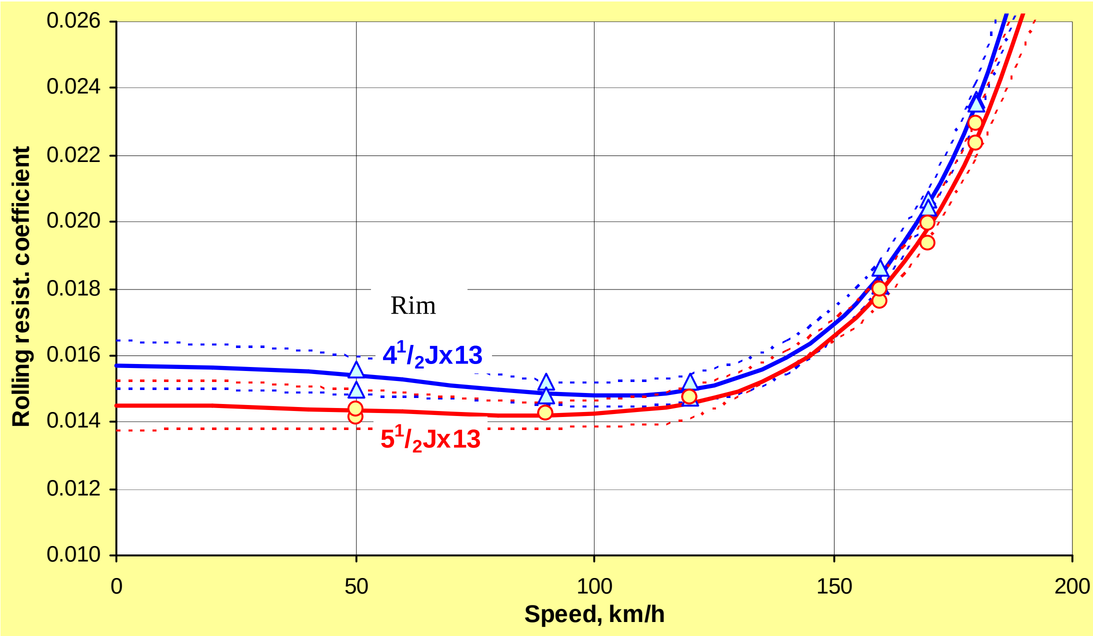

Figure 7.6 – Influence of the rim width on rolling resistance in 165/70 R 13 tires.

Both data series in Figure 7.6 are very close each other, so let us test the hypothesis H_0: they are statistically indistinguishable. Let be r = 2, s = 4 and $\mathbf{b}_1$, $\mathbf{b}_2$ be vectors of regression coefficients belonging to the 4½", 5½" rims

$$\mathbf{b}_1 = \begin{pmatrix} 0.016395 \\ -0.003603 \\ 0.001768 \end{pmatrix}, \quad \mathbf{b}_2 = \begin{pmatrix} 0.016115 \\ -0.003658 \\ 0.001802 \end{pmatrix}, \quad \mathbf{b}_2 - \mathbf{b}_1 = \begin{pmatrix} 2.55\times10^{-3} \\ -5.47\times10^{-5} \\ 3.35\times10^{-5} \end{pmatrix}.$$

Further,

$$\mathbf{A}^T\mathbf{A} = \begin{pmatrix} 12 & 22.38 & 56.391 \\ 22.38 & 56.391 & 156.9201 \\ 56.391 & 156.9201 & 455.2821 \end{pmatrix},$$

$$N = 12, \quad S_I^2 = 1.9134\times10^{-7}, \quad S_{II}^2 = 2.2829\times10^{-7},$$

so

$$Z = \frac{N-3}{S_I^2 + S_{II}^2}(\mathbf{b}_{II} - \mathbf{b}_I)^T\, \mathbf{A}^T\mathbf{A}\, (\mathbf{b}_{II} - \mathbf{b}_I)\,/2 = 5.807113 > 3.1599076 = F_{0.05}(3, 18).$$

Thus, the hypothesis H_0 must be rejected. In other words: the change of rolling resistance due to one inch change in rim width is statistically significant.

The next two examples show how the belt width and cord angle in steel belt plies influence the rolling resistance. Results are presented without further comments in the following figures.

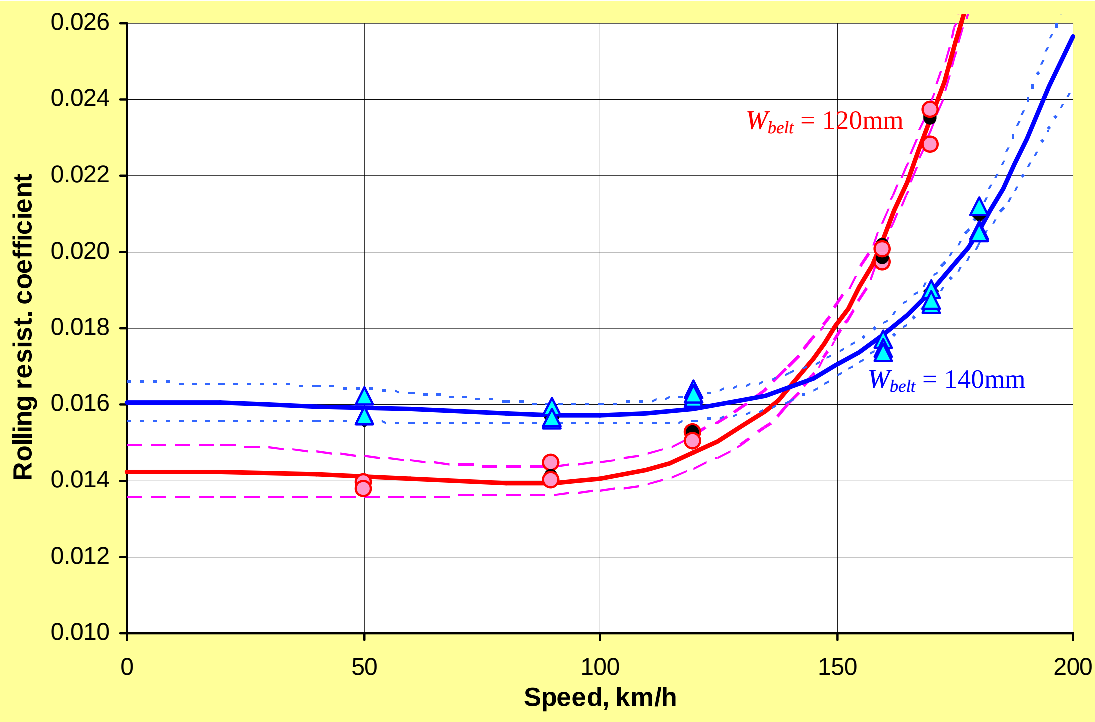

Figure 7.7 – Influence of the belt width on rolling resistance in a 165/70R13 tire.

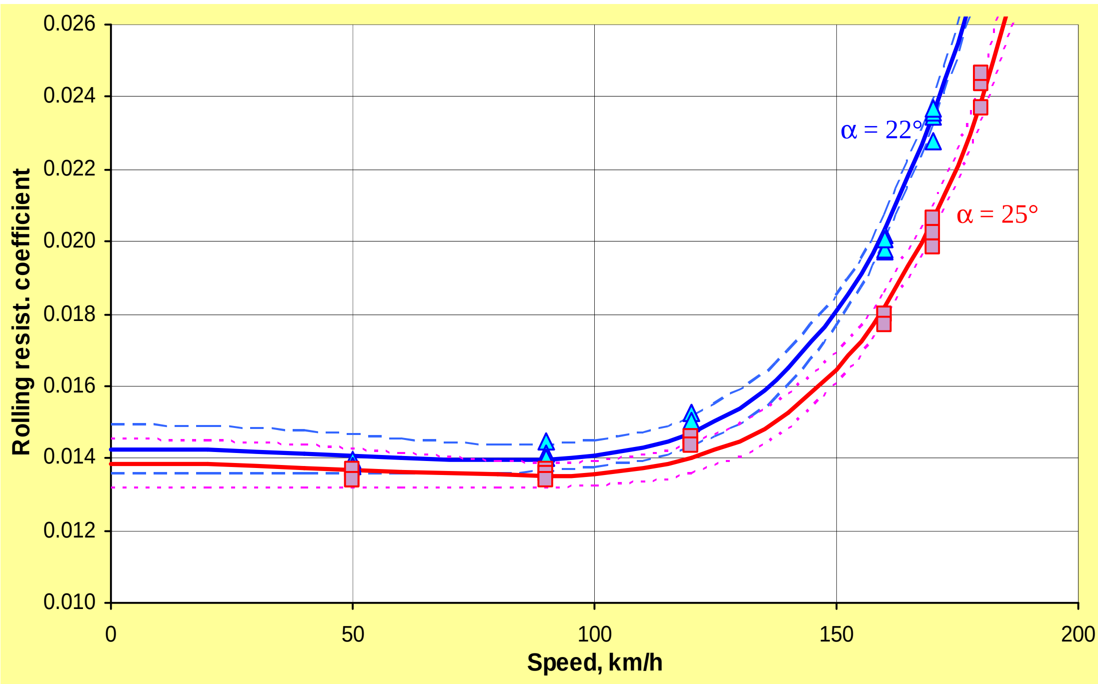

Figure 7.8 – Impact of the belt angle on rolling resistance in a 165/70R13 tire.

7.3 Dependence of m on Inflation Pressure and Load

Tire rolling resistance plays a very important role in highway traffic. Tires in daily use do not run always in optimal conditions. Although their speed is bounded from above by legal limits they may be overloaded e.g. by low inflation pressure or high load. Then the question arises how the load and inflation pressure influence the rolling resistance at a given speed.

As well known, rolling resistance depends substantially on two factors connected with tread/belt block: radial deflection u and contact pressure p_{mc}, i.e.

$$R(p, F_R) \approx a_0 + a_1\, u + a_2\, p_{mc}.$$

The following Figures 7.9, 7.10 show these quantities as functions of the inflation pressure p and vertical load F_R in 295/80R22.5 tire on the road wheel with diameter 2m computed by means of belt model.

The functions $u(p, F_R)$, $p_{mc}(p, F_R)$ appear quite simple and smooth. The variables p, F_R may be chosen independently in a convenient range. Then the coefficient of rolling resistance may be approximately represented by the following function

$$1000\, \mu(p, F_R) \approx \beta_0 + \beta_1\, F_R + \beta_2\, \frac{1}{p}.$$

In order to find the estimates b_0, b_1, b_2 of coefficients β_0, β_1, β_2 in 295/80R22.5 tires a statistically designed experiment was carried out [51,55].

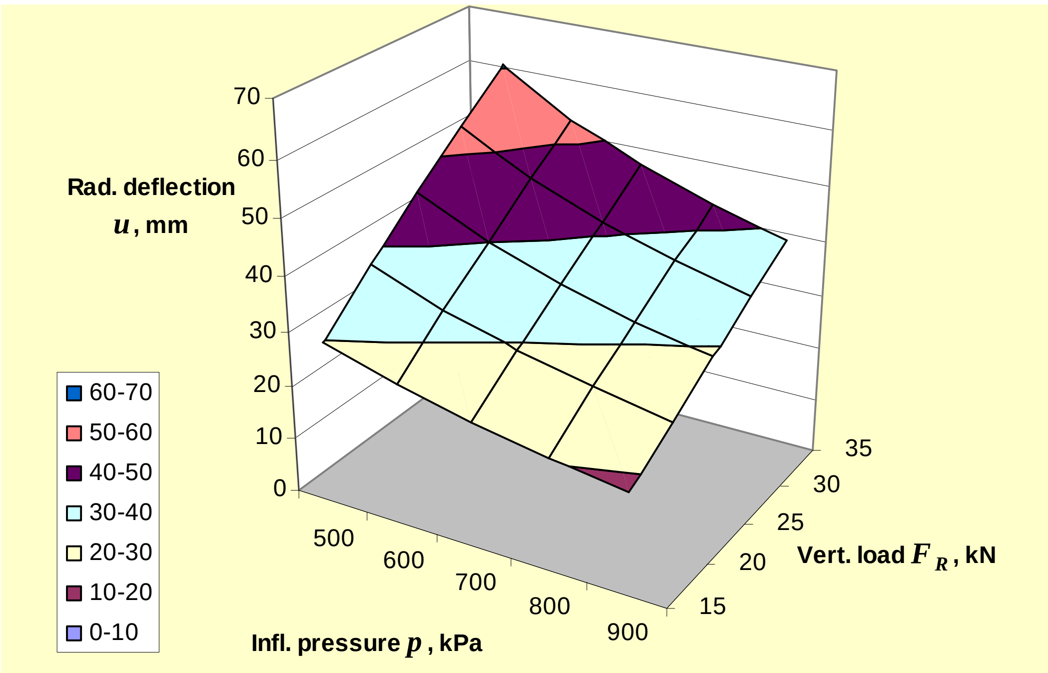

Figure 7.9 – Radial deflection u of the 295/80R22.5 tire on 2m-drum computed by belt model.

An acceptable and sufficiently large area for load F_R and inflation pressure p at constant speed 70km/h was determined by the belt model so that tire destruction during testing was avoided. The radial deflection was limited by 50mm and the maximum contact pressure by 1.2MPa. Experimental points were designed in the corresponding area as shown in Figure 7.11. Two tires were tested independently at randomly chosen points of design.

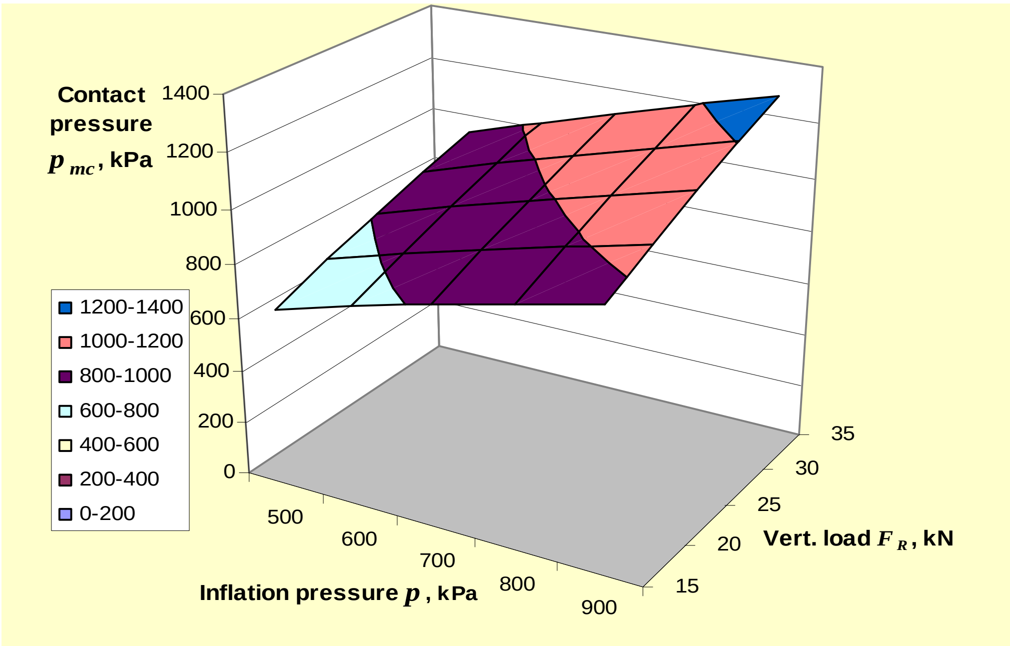

Figure 7.10 – Contact pressure p_{mc} of the 295/80R22.5 tire on 2m-drum computed by belt model.

The regression coefficients were

$$b = \begin{pmatrix} 6.344 \pm 0.883 \\ -0.030 \pm 0.020 \\ 0.494 \pm 0.429 \end{pmatrix},$$

the residual variance estimate $s_{res}^2 = S^2/(n\text{–}3) = 0.03345$ and the estimate of experimental variance was $s_{ex}^2 = 0.01757$. Because

$$F = \frac{s_{res}^2}{s_{ex}^2} = 1.90349 < 3.37375 = F_{0.05}(6, 9),$$

the function (F_R is given in kN, p in kPa)

$$\mu(p, F_R) = (6.344 - 0.030\, F_R + 0.494\, \frac{1}{p}) \times 10^{-3}$$

represents adequately the rolling resistance coefficient of the 295/80R22.5 tire on the 2m roadwheel at velocity 70km/h for the inflation pressure from 550 to 850kPa and vertical load from 15 to 35kN. Figure 7.12 shows the resulting response surface.

Similar results with the same type of regression function were obtained also in car tires 155R13 in the experimental range [150kPa, 250kPa]×[3kN, 5kN] [56]:

$$\mu(p, F_R) = (9.160 - 0.443\, F_R + 1.492\, \frac{1}{p}) \times 10^{-3}$$

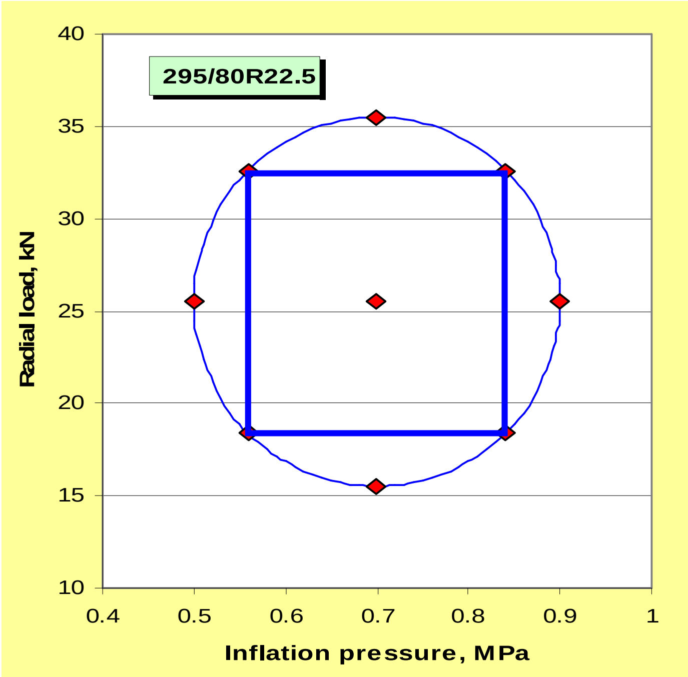

Figure 7.11 – Design of experiment to determine the function $\mu(p, F_R)$ *in 295/80R22.5 tire.*

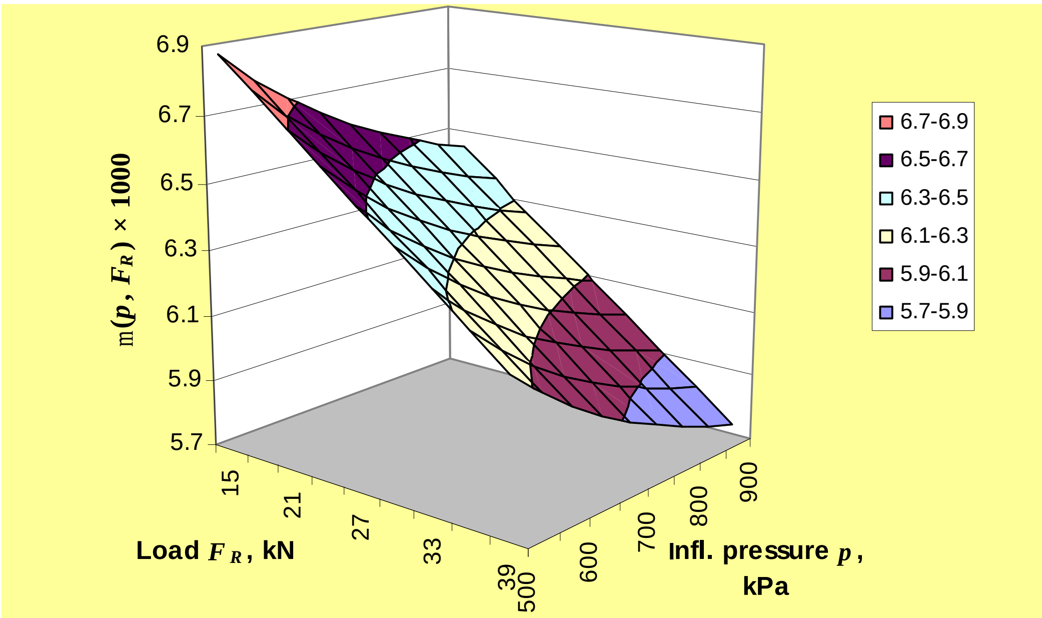

Figure 7.12 – The regression approximation of the surface $\mu(p, F_R)$ *in the 295/80R22.5 tire.*

Remark. In a bounded region of conditions the rolling resistance coefficient can be approximated by the product $1000\,\mu(v, p, F_R) = (\beta_0 + \beta_1 v^r + \beta_2 v^s)(\beta_3 + \beta_4 F_R + \beta_5/p)$.

P

8 TIRE UNIFORMITY

Tire uniformity is a necessary condition for comfort ride at high velocities. Tire cannot be perfectly uniform due to its heterogeneous structure, tread pattern and ways of tire production. Nevertheless, uniformity disturbances are always a nuisance worsening the comfort, so there is a permanent pressure on tire manufacturers to reduce them.

Vehicle is considered as a dynamical system composed of relatively stiff parts joined together with deformable parts like springs and shock absorbers. The behavior of such a complex mechanical system leads to systems of many differential equations with nonlinearities. As a rule the dynamical system of vehicle is substantially simplified to reach its principal transparency and enable its mathematical solvability.

Today such dynamical systems can be modeled as multibody systems by means of various software packages like MSC/ADAMS, MSC/AUTOSIM etc.

8.1 Two-Mass Model of Vehicle

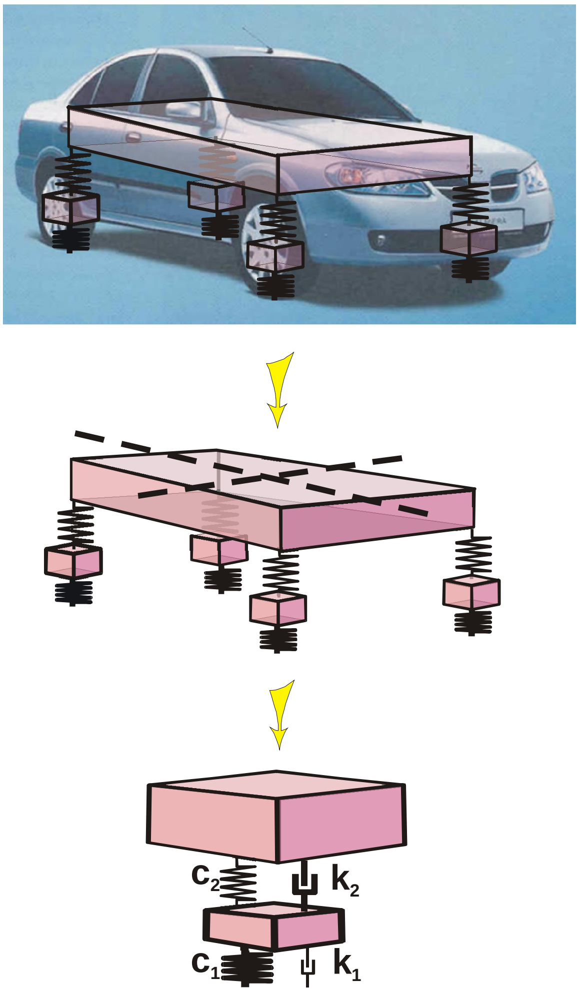

Figure 8.1 – Reduction a car to a two-mass system to describe its vertical oscillations.

The big parallelepiped in Figure 8.1 represents the car body, the four smaller bodies with springs and shock absorbers the suspension (chassis). Radial deflections of tires are small related to wheel distances. Thus, the first approximation of vertical vibrations may be obtained by a quarter of the original model, the two-mass system (Figure 8.2).

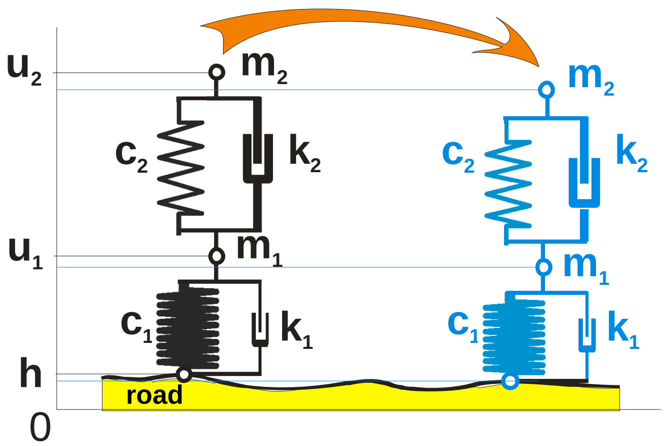

Figure 8.2 – Dynamical two-mass system, vertical coordinates and their changes in displacement on a bumped surface of the road.

The mass of the wheel, hub, axle shaft etc. is m_1 (unsprung mass), that of a quarter of the car body m_2 (sprung mass). Tire stiffness c_1 in usual condition is much higher than the stiffness c_2 of body spring. Damping k_1 of radial oscillations in tires (Figure 6.1) is substantially smaller than that of body shock absorbers k_2. Real springs are nonlinear (Figures 5.4, 5.13-5.15, 6.8) but in small oscillations they may be linearized.

In the first spring (tire) the change of its length is equal to the displacement of the mass m_1 (concentrated in the wheel center) in relation to the road surface $h = h(x, t)$,

$$\Delta_1 = u_1 - h.$$

The change of length of the second spring is

$$\Delta_2 = u_2 - u_1.$$

Total potential energy is the sum of potential energies of both springs,

$$U = U_1 + U_2 = -\frac{1}{2}[c_1(u_1 - h)^2 + c_2(u_2 - u_1)^2)]\ .$$

Similarly, the kinetic energy is the sum of kinetic energies of both masses

$$T = (T_1 + T_2) = \frac{1}{2}(m_1 \dot{u}_1^{\,2} + m_2 \dot{u}_2^{\,2})\ ,$$

where the dot denotes the derivative with respect to time, $\dot{u}_1 = \dfrac{\mathrm{d}u_1}{\mathrm{d}t}$ etc.

The dissipated energy F is taken in a simplified manner as the loss due the viscosity in both damping members

$$F = F_1 + F_2 = -\frac{1}{2}[k_1(\dot{u}_1 - h)^2 + k_2(\dot{u}_2 - \dot{u}_1)^2].$$

The motion of the system from Figure 8.2 is described by two Langrange's equations of the second kind [44]

$$\frac{\mathrm{d}}{\mathrm{d}t}\left(\frac{\partial}{\partial \dot{u}_k}(T-U)\right)-\frac{\partial}{\partial u_k}(T-U) = \frac{\partial}{\partial \dot{u}_k}F \;+F_k\,, \qquad k = 1, 2,$$

where F_k are external forces. Substituting T, U, F by corresponding expressions yields

$$m_1\ddot{u}_1 + c_1(u_1-h) - c_2(u_2-u_1) = -k_1(\dot{u}_1-\dot{h}) + k_2(\dot{u}_2-\dot{u}_1) + F_1,$$

$$m_2\ddot{u}_2 + c_2(u_2-u_1) = -k_2(\dot{u}_2-\dot{u}_1) + F_2\,.$$

When initial conditions are given this system of equations can be solved e.g. numerically [10]. But concrete solutions in time do not supply general view on the system behavior. Transfer functions or, more precisely, frequency characteristics are much more eloquent. The Laplace transform [9] gives for F_1=F_2=0 [51,57]

$$U_1(p) = \frac{(m_2p^2+k_2p+c_2)(c_1+k_1p)}{[m_1p^2+(k_1+k_2)p+(c_1+c_2)][m_2p^2+k_2p+c_2]-[k_2p+c_2]^2}\,H(p),$$

$$U_2(p) = \frac{(c_1+k_1p)(k_2p+c_2)}{[m_1p^2+(k_1+k_2)p+(c_1+c_2)][m_2p^2+k_2p+c_2]-[k_2p+c_2]^2}\,H(p)\,,$$

where $H(p)$, $U_1(p)$, $U_2(p)$ are Laplace's images of $h(t)$, $u_1(t)$, $u_2(t)$.

Putting $p = \mathrm{i}\omega$ gives formally Fourier's images ($\mathrm{i} = \sqrt{-1}$).

Let the denominator be written as the sum of real and imaginary parts,

$$D(\mathrm{i}\omega) = R(\omega) + \mathrm{i}\, I(\omega),$$

where

$$R(\omega) = \mathrm{Re}\, D(\mathrm{i}\omega) = m_1m_2\,\omega^4 - [m_1c_2+(c_1+c_2)m_2+k_1k_2]\,\omega^2 + c_1c_2\,,$$

$$I(\omega) = \mathrm{Im}\, D(\mathrm{i}\omega) = (k_1c_1+c_1k_2)\,\omega - [m_2k_1+(m_1+m_2)k_2]\,\omega^3\,.$$

Then the amplitude-frequency characteristics of the car body is

$$A(\omega) = \frac{|(c_1+\mathrm{i}\omega k_1)(c_2+\mathrm{i}\omega k_2)|}{|D(\mathrm{i}\omega)|} = \frac{\sqrt{(c_1c_2-k_1k_2\omega^2)^2+\omega^2(c_1k_2+c_2k_1)^2}}{\sqrt{R^2(\omega)+I^2(\omega)}}\,.$$

The discomfort of the ride on the road surface is physiologically perceived through the body acceleration. Integral transforms of car body acceleration $\dfrac{\mathrm{d}^2u_2(t)}{\mathrm{d}t^2}$ are simply $p^2U_2(p)$, $\omega^2A(\omega)$, respectively.

Example. Let us consider the following parameters:

c_1 = 250 000 N/m (radial stiffness of tire),
c_2 = 30 000 N/m (stiffness of body springs),
k_1 = 3 kg/s (damping coefficient of tire),
k_2 = 2 000 kg/s (damping coefficient of body shock absorber),
m_1 = 50 kg (wheel + hub + axle),
m_2 = 400 kg (a quarter of sprung mass, i.e. body + passengers + load) .

Figure 8.3 shows the amplitude-frequency characteristics of the sprung mass for different radial stiffness of tire as practically proportional to the inflation pressure.

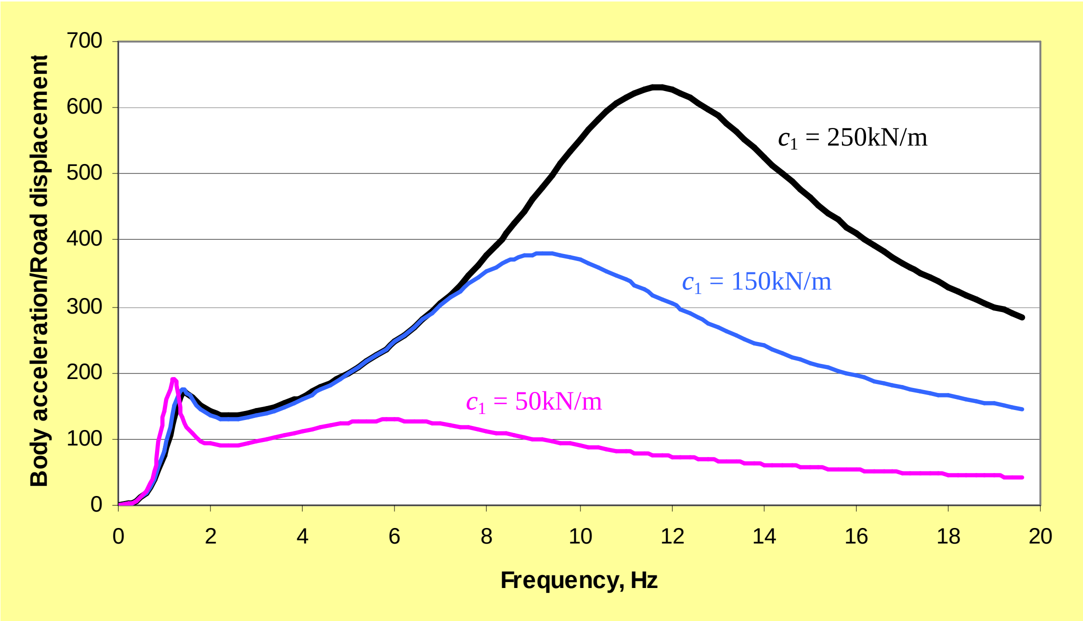

Figure 8.3 – Amplitude-frequency characteristics of sprung mass acceleration for variable radial stiffness of tire.

Because real dynamic systems of automobiles are nonlinear in the first place and incomparably complex in comparison to the two-mass model more realistic estimates of transfer functions are obtained by means of spectral densities $S(\omega)$ of accelerations measured in convenient places of the automobiles and the spectral density $S_0(\omega)$ of road displacements,

$$\left|A(\omega)\right| = \sqrt{\frac{S(\omega)}{S_0(\omega)}} .$$

But the corresponding measurements are complicated, very particular and expensive. On the other hand, the computer modeling offers much cheaper possibilities. Their results, however, must be verified by measurements at several pilot points at least.

8.2 Disturbances of Radial Uniformity

Generally, tires transmit spatial forces and are required to have sufficient adhesion to the support in all weather conditions. Tread pattern enhances the adhesion but at the same time it is a source of uniformity disturbances and noise emissions of the tire. Slices of tread, sidewalls, carcass and belt plies in building process are another source of such disturbances [52]. Variability of steel cord circumferential density in radial carcass of truck tire and other irregularities were discussed in [58,59].

The mentioned irregularities cause variability of force on rolling tire which can be tracked in a relatively easy way on special testers of uniformity. The principle of measuring the radial force is shown in Figure 8.4.

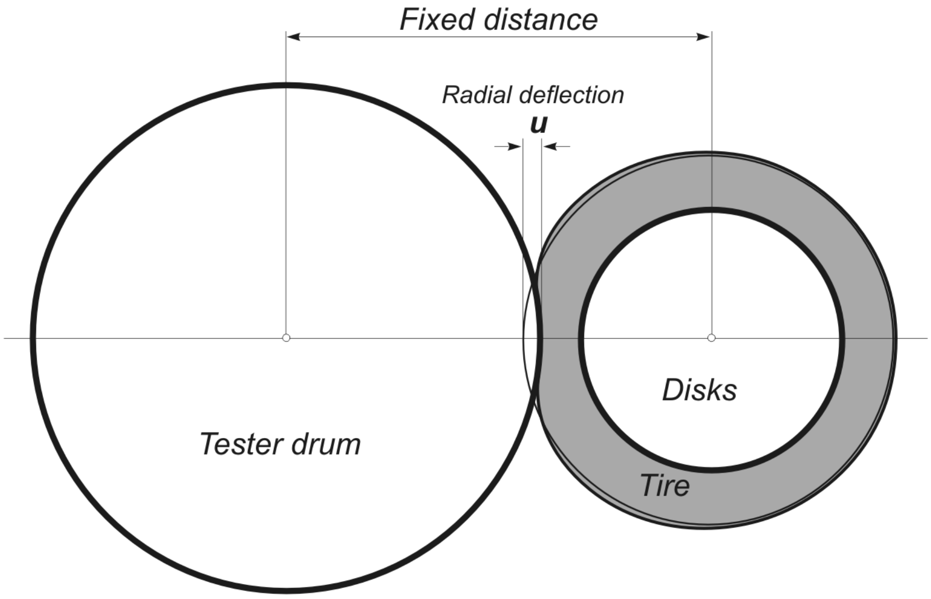

Figure 8.4 – Sketch of tire uniformity measurement.

The tire is placed between two massive disks whose distance is set up to the width of the simulated rim in the next step. The tire is inflated to the nominal air pressure. The drum is pressed against the tire until the radial force attains the required value. From that moment the distance between the parallel axes of the drum and the tire (disks) is kept fixed. Then the tire rolls several times in one direction (e.g. counter-clockwise one) and then in the opposite direction. During this process irregularities in forces and geometry are measured, recorded and evaluated.

The arrangement of uniformity testing (Figure 8.4) suggests the idea of dominant role of the tread outer surface and a smoothing effect of the contact area in the way of moving averages of the order corresponding to the contact length [51,60].

Effects of long-wave geometric disturbances on radial force variations can be estimated relatively well by the belt model. Let the 295/80R22.5 tire be considered as an example. Its carcass geometry is given by the following 5-tuple (Chapter 4)

$$(R_A, W, R_N, r_B, z_B) = (492, 139, 400, 318.9, 93.8).$$

Solution of the corresponding problem (A) yields the parameters Λ = 0.1580705, ϑ = 1.3854194 and meridian length L_{AB} = 287.17mm.

The belt tension T is considered constant due to general tendency of belt to occupy the circular shape [52]. Thus, a change of one parameter may induce changes in other ones making the total effect milder. The total thickness of tread and belt block (i.e. the difference of the outer tire radius and the carcass equator radius) is h_{TB} = 16+13 = 29mm, the belt tension at the inflation pressure 850kPa and velocity 10km/h is T = 49 015.87N.

Example. If the tire is assumed to be vulcanized in a perfectly axisymmetric mold a long-wave disturbance of ±1mm of tread thickness produces decreasing and increasing the carcass equator radius of 491 and 493mm, while the tire width as well as the beads remain unchanged. The changes of meridian length can be estimated in a simplified way by solving the following two problems (A)

$$((R_A^*, W, R_N, r_B, z_B) \to (\Lambda, \vartheta),$$

where R_A^* = 491 and 493mm. One obtains

R_A, mm	Λ	ϑ, rad.	L_{AB}, mm	T, N
491	0.1573085	1.3839069	286.42	49 391.56
493	0.1588227	1.3869022	287.94	48 653.44

The constant belt tension may be supposed to be the original value T = 49 015.87N. Changes of T at different meridional lengths are eliminated by changing the carcass equator radius (found by interpolation):

h_{TB}	R_A, mm
17 + 13	491.391
15 + 13	492.625

Hence, the carcass run-out caused by the 2mm-difference in tread thickness is

$$\Delta R = 1.234\text{mm}.$$

The belt model gives also radial load-deflection curves corresponding to different tread thicknesses:

h_{TB}	$R_A(h_{TB})$, mm	$F(u)$, N
30	491.391	$-0.00940\, u^3 + 5.26867\, u^2 + 669.803\, u$
29	492.000	$-0.00933\, u^3 + 5.25550\, u^2 + 670.142\, u$
28	492.625	$-0.00925\, u^3 + 5.24225\, u^2 + 670.478\, u$

The perfect tire with the outer radius 492 + 29 = 521mm at 850kPa and radial deflection 37mm corresponding to radial load 31.5kN on uniformity tester drum with radius 800mm determines the distance between the axes of revolution of both tire and drum

$$d = 800 + 492 + 29 - 37 = 1284\text{mm} .$$

Let this distance be fixed, $d = 800 + R(h_{TB})_A + h_{TB} - u = 1284$mm. Then the radial deflection of the tire in a place with another tread thickness h_{TB} *is*

$$u(h_{TB}) = -\,d\, + 800 + R_A(h_{TB}) + h_{TB}\, = R_A(h_{TB}) + h_{TB}\, - 484 .$$

Now the corresponding radial loads, $F(u(h_{TB}))$, can be computed from the formulas written above:

h_{TB}, mm	$u(h_{TB})$, mm	$F(u)$, N
30	37.391	31 919.27
29	37.000	31 519.38
28	36.625	31 137.07

Thus, the rate caused by a long wave variability of the tread-belt thickness is

$$\frac{\mathrm{d}F(h_{TB})}{\mathrm{d}h_{TB}} \approx \frac{31\,919.27-31\,137.07}{2} \approx 391\mathrm{N/mm}\,,$$

the rate of tread radial run-out

$$\frac{\mathrm{d}R(h_{TB})}{\mathrm{d}h_{TB}} = \frac{\mathrm{d}(R_{\mathrm{A}}(h_{TB})+h_{TB})}{\mathrm{d}h_{TB}} \approx 1 + \frac{491.391 - 492.625}{2} \approx 0.383$$

and the rate of carcass radial run-out

$$\frac{\mathrm{d}R_{\mathrm{A}}(h_{TB})}{\mathrm{d}h_{TB}} \approx \frac{491.391-492.625}{2} \approx -0.617\,.$$

The ideal relationship between radial force variation and tread or carcass run-out is

$$\left|\frac{\mathrm{d}F(h_{TB})}{\mathrm{d}R(h_{TB})}\right| \approx \frac{391}{0.383} \approx 1020.9\mathrm{N/mm} \quad \text{or} \quad \left|\frac{\mathrm{d}F(h_{TB})}{\mathrm{d}R_A(h_{TB})}\right| \approx \frac{391}{0.617} \approx 633.7\mathrm{N/mm}.$$

In a series of 4 273 of the 285/80R22.5 tires the average ratio Q_R of radial force variation and radial run-out was 605.2N/mm with the sample standard deviation 131.2N/mm, in another series of 4021 of those tires the average ratio of radial force variation and radial run-out was 628.5N/mm with the sample standard deviation 234.2N/mm. Hence, $\left|\mathrm{d}F(h_{TB})/\mathrm{d}R_A(h_{TB})\right|$ appears to be a quite acceptable approximation of Q_R.

Impact of the sidewall or bead apex thickness variability, bead bundle eccentricity etc. on radial uniformity can be estimated in a similar way.

●

Any serious measurement must be repeatable. Repeatability was verified by detailed measurements along the circumference of the 295/80R22.5 tire carried out one after another four times [51,60].

In regular regime of measurement the following seven quantities are recorded in 128 equidistant positions $\{\phi_k = 2\pi k/128\colon k = 0, 1, \ldots, 127\}$ of the circumferential angle.

1. radial force deviation in the clockwise direction,
2. lateral force deviation in the clockwise direction,
3. radial force deviation in the counterclockwise direction,
4. lateral force deviation in the counterclockwise direction,
5. radial run out on the tire equator,
6. axial run out on the sidewall from the bottom part of the vulcanization mold,
7. axial run out on the sidewall from the upper part of the vulcanization mold.

Evident periodicity of forces and run outs leads to their decomposition in harmonic components. E.g. the radial force can be written as the following trigonometric polynomial in the phasor form [10]

$$S_n(\phi) = r_0 + \sum_{k=1}^{n} r_k \sin(k\phi + \phi_k),$$

where $r_k = \sqrt{a_k^2 + b_k^2}$ is the amplitude and ϕ_k the phase of the kth harmonic,

$$\phi_k = \begin{cases} -\arctan(b_k / a_k) & \\ -\operatorname{sign}(b_k) + \arctan(b_k / a_k) & \text{for} \\ -\operatorname{sign}(b_k)\,\pi/2 & \end{cases} \begin{matrix} a_k > 0 \\ a_k < 0 \\ a_k = 0 \end{matrix},$$

$$a_k = \frac{1+\operatorname{sign}(k)}{2\pi} \int_0^{2\pi} F(\phi)\cos(k\phi)\,d\phi, \qquad b_k = \frac{1+\operatorname{sign}(k)}{2\pi} \int_0^{2\pi} F(\phi)\sin(k\phi)\,d\phi,$$

$k = 0, 1, \ldots, n.$

Figure 8.5 – Average of 4 measurements of radial force variation and radial run out in a new rejected 295/80R22.5 truck tire for tuned phases.

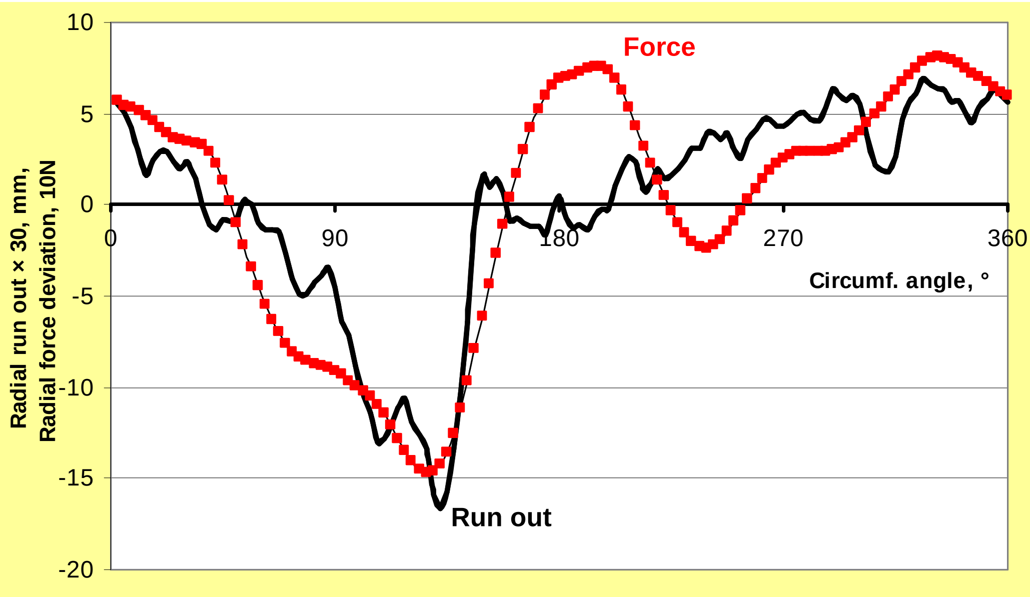

Figure 8.6 – Radial force deviation and run out in the 295/80R22.5 tire from Fig. 8.5 after grinding.

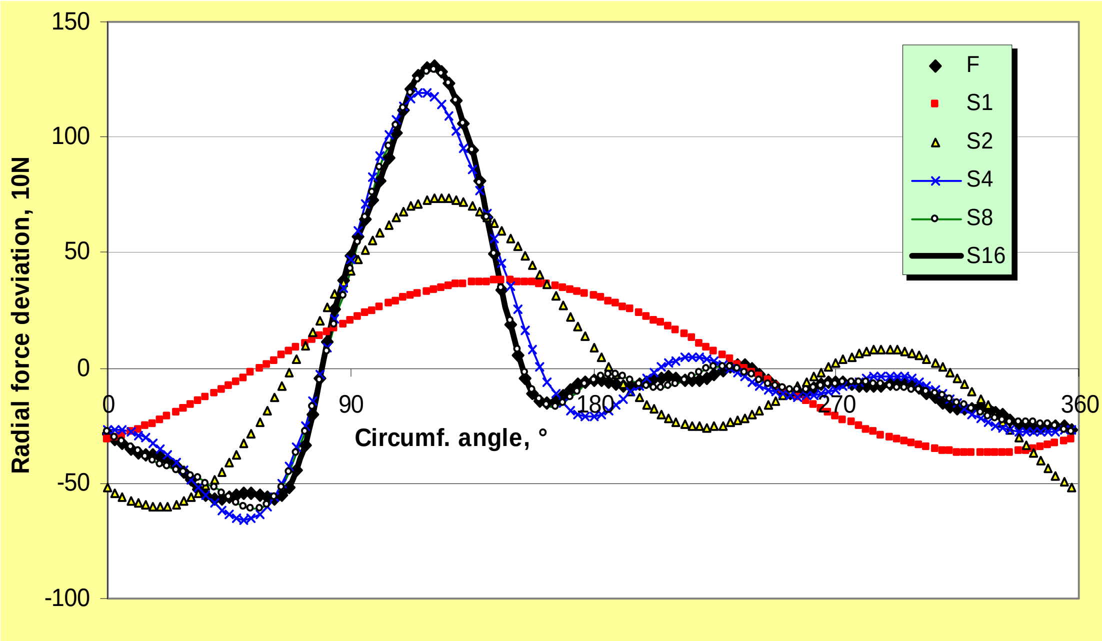

Figure 8.7 – Approximation of the average radial force from Figure 8.5 by several trigonometric polynomials S_n.

The fitness of trigonometric polynomial may be evaluated by the standard deviation

$$\delta_n = \sqrt{\frac{\sum_{i=1}^{128}\left[S_n(x_i) - F(x_i)\right]^2}{127}} .$$

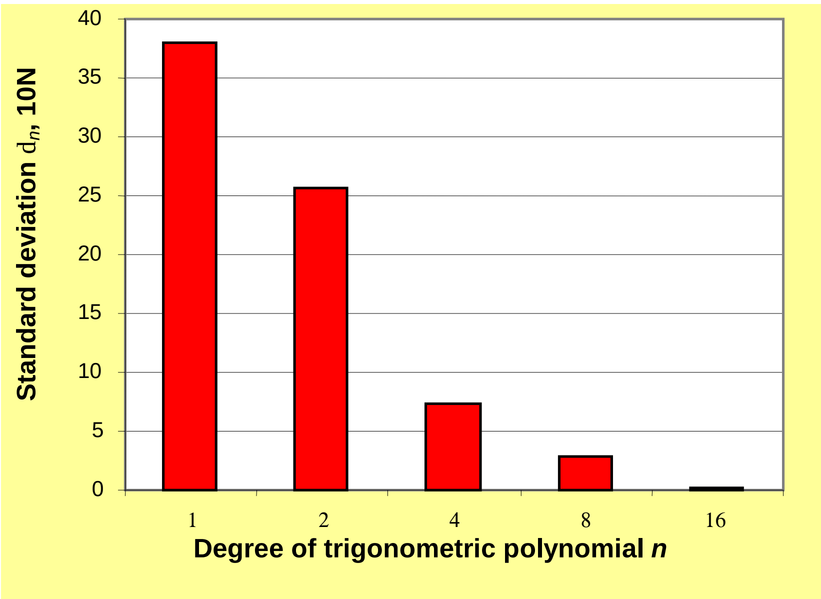

Figure 8.8 – Approximation quality of trigonometric polynomials.

The variable radial force can be viewed as a random process [11] that can be decomposed into infinite harmonic components. Fisher's test [11] reveals, which of the components in the corresponding finite amplitude specter $\{r_k: k = 0, 1, \ldots, n\}$ are statistically significant, i.e. stand out from the random noise.

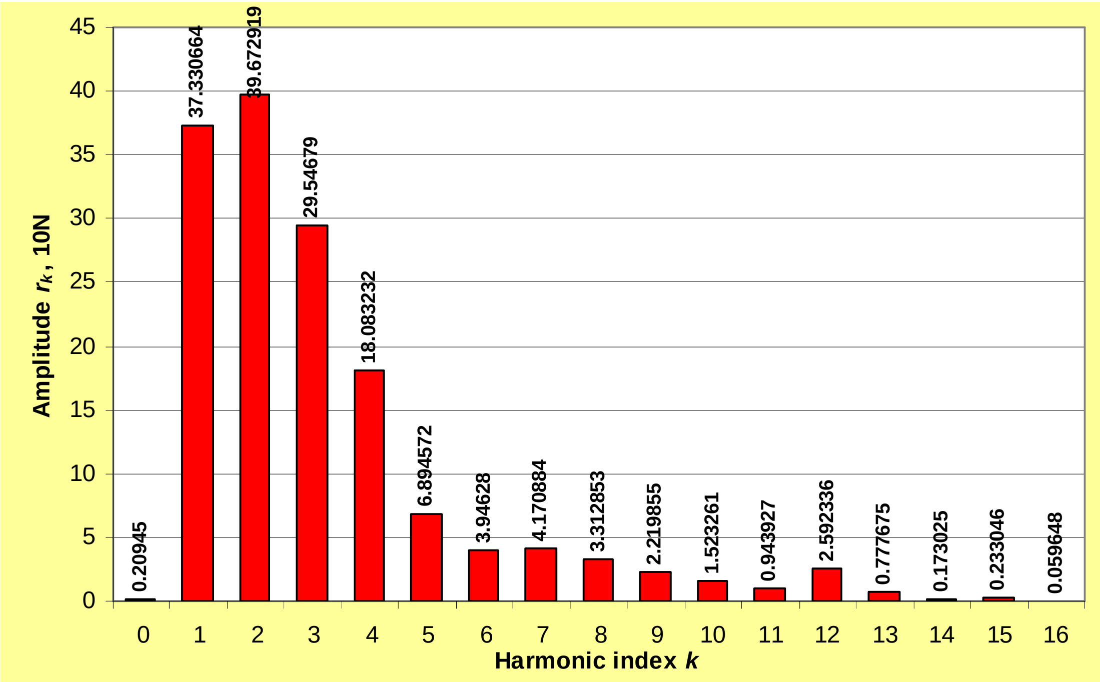

Figure 8.9 – Amplitude specter of the average radial force displacement from Figure 8.5

Amplitudes are ordered in the decreasing series, $r_1 > r_2 > \ldots$, and its squares are summed up, e.g. $S_1 = \sum_{j=1}^{16} r_j^2$. Then $S_2 = S_1 - r_1^2$, $S_3 = S_2 - r_2^2$, … The Fisher's test in specter of Figure 8.9 is summarized in the following Table ($W_{0.05}$ are critical values) [11].

j	(k)	r_j	r_j^2	S_j	r_j^2/S_j	$W_{0.05}$ (17–j)
1	(2)	39.67292	1573.941	4274.566	**0.368211**	0.337691
2	(1)	37.33066	1393.578	2700.626	**0.516021**	0.355160
3	(3)	29.54679	873.013	1307.047	**0.667927**	0.374726
4	(4)	18.08323	327.003	434.035	**0.753404**	0.396806
5	(5)	6.89457	47.535	107.031	**0.444123**	0.421932
6	(7)	4.17088	17.396	59.496	0.292393	0.450800
7	(6)	3.94628	15.573	42.100	0.369908	0.484331
8	(8)	3.31285	10.975	26.527	0.413731	0.523768

Thus, only the first five harmonics are statistically significant in this case.

8.3 Distribution of Low-Speed Uniformity Disturbances

Standard tire uniformity measurements are carried out at very low speeds of 1 revolution/s, i.e. less than 10km/h in car tires. The measurement result is a vector

$$\mathbf{x} = \begin{pmatrix} x_1 \\ \vdots \\ x_m \end{pmatrix},$$

whose components are:

x_1 = *RFV* (Radial Force Variation peak to peak),
$x_2 = r_1$ = *H1* (Amplitude of the first harmonic in radial force),
x_3 = *LFV* (Lateral Force Variation peak to peak),
x_4 = *CON* (Conicity),
x_5 = *TRO* (Top Run Out of the upper sidewall (in mold)),
x_6 = *BRO* (Bottom Run Out of the lower sidewall (in mold)),
x_7 = *RRO* (Radial Run Out on equator).

This list may be extended by further items, e.g. ply steer *PS*, further harmonics in radial (*H2*, …) and lateral (*LH1*, *LH2*, …) forces, run out in different positions on tread or sidewall etc. The rolling direction may be respected as well.

Components $x_1, \ldots, x_m$ are random variables bounded from above and from below, similarly like strength of materials [39]. For example, radial or lateral force disturbances cannot be negative and cannot be greater than e.g. nominal load of tire. This is valid also for conicity although it may be of both signs, positive or negative.

Thus, a component of uniformity disturbance is a random variable from some final interval I = $[b_1, b_2]$. As a rule, its relative frequency (probability density) f increases from $f(b_1) = 0$ to a maximum $f(x_{max}) > 0$ (modus), $b_1 < x_{max} < b_2$, and then decreases to $f(b_2) = 0$. The following product is one of such simple and smooth functions

$$A(x-b_1)^{b_3}\,(b_2-x)^{b_4}\,,\quad A, b_3, b_4 > 0.$$

This function defines a probability density only if it is normed, i.e.

$$A\int_{b_1}^{b_2}(x-b_1)^{b_3}\,(b_2-x)^{b_4}\,\mathrm{d}x = 1\,.$$

The function

$$t(x) = \frac{x-b_1}{b_2-b_1}$$

is one-to-one mapping $[b_1, b_2] \to [0, 1]$. Hence

$$\int_{b_1}^{b_2}(x-b_1)^{b_3}\,(b_2-x)^{b_4}\,\mathrm{d}x = (b_2-b_1)^{b_3+b_4+1}\int_0^1 t^{b_3}(1-t)^{b_4}\,\mathrm{d}t = (b_2-b_1)^{b_3+b_4+1}\mathrm{B}(b_3+1, b_4+1)\,,$$

where B is the well known Euler's Beta function [39]. Between this and more frequently used Gamma function [9, 39] is the following connection

$$\mathrm{B}(b_3+1,\, b_4+1) = \frac{\Gamma(b_3+1)\,\Gamma(b_4+1)}{\Gamma(b_3+b_4+2)}\,.$$

The corresponding (cumulative) distribution function is then

$$F(x,\mathbf{b}) = \frac{\Gamma(b_3+b_4+2)}{\Gamma(b_3+1)\,\Gamma(b_4+1)} \int_0^{\frac{x-b_1}{b_2-b_1}} t^{b_3}(1-t)^{b_4}\,\mathrm{d}t\,,$$

where $\mathbf{b} = (b_1, \ldots, b_4)^{\mathrm{T}}$ is the unknown vector of parameters. It may be defined by minimization of the function

$$X^2(\mathbf{b}) = \sum_{i=1}^{K} \frac{(n_i - np_i)^2}{np_i}\,.$$

Here n is the total number of elements in the considered series of tires. The interval of measurement $\mathrm{I} = [b_1, b_2]$ is decomposed into K subintervals I_i (classes), n_i are frequencies (numbers of elements in I_i) and np_i are ´theoretical´ frequencies,

$$p_i = \int_{I_i} \mathrm{d}\,F(x,\mathbf{b})\,.$$

Parameters $b_1, \ldots, b_4$ are found by direct minimization of $X^2(\mathbf{b})$ based on genetic algorithm [10,39].

For great n the quantity $X^2(\mathbf{b})$ belongs to $\chi^2(K{-}1)$ distribution. This enables testing the goodness of fit [11,54] by comparing $X^2(\mathbf{b})$ to the critical value $\chi^2_\alpha(K{-}1{-}4)$. In other words, the fraction $X^2(\mathbf{b})/\chi^2_\alpha(K{-}1{-}4)$ must be < 1.

Example. A series of the 385/55R22.5 tires of range n = 786 was decomposed into K = 16 classes with respect to lateral force variation (*LFV*). The search for minimum of $X^2(\mathbf{b})$ gave the following results (Δ_α denotes confidence limit for probability level α under the assumption of normality of b_k, $\Delta_\alpha = u_{1-\alpha/2}\, s/\sqrt{r}$, where $u_{1-\alpha/2}$ is the quantile of N(0, 1), s is standard deviation and r = 5 is number of calculation repetitions)

	Run 1	Run 2	Run 3	**Run 4**	Run 5	$\Delta_{0.05}$
b_1	1.494	2.016	1.822	**1.771**	1.358	0.061
b_2	35.435	32.580	34.996	**35.672**	35.664	1.502
b_3	5.533	4.581	4.999	**5.121**	5.759	0.187
b_4	19.180	15.358	17.967	**18.748**	19.718	2.564
X^2	2.086	2.499	2.125	**2.046**	2.164	
$X^2/\chi^2_{0.05}$	0.106	0.127	0.108	**0.104**	0.110	

The minimum $X^2(\mathbf{b})$ was obtained in the 4th run (shadowed column) and is taken as the parameter vector estimate $\mathbf{b}$. Thus,

$$\mathbf{b}^{min} = {}^{4}\mathbf{b} \pm D_{005} = \begin{pmatrix} 1.771 \pm 0.061 \\ 35.672 \pm 1.502 \\ 5.121 \pm 0.181 \\ 18.748 \pm 2.564 \end{pmatrix}.$$

Figure 8.10 shows the comparison of real frequencies n_i with those predicted by Beta distribution, np_i.

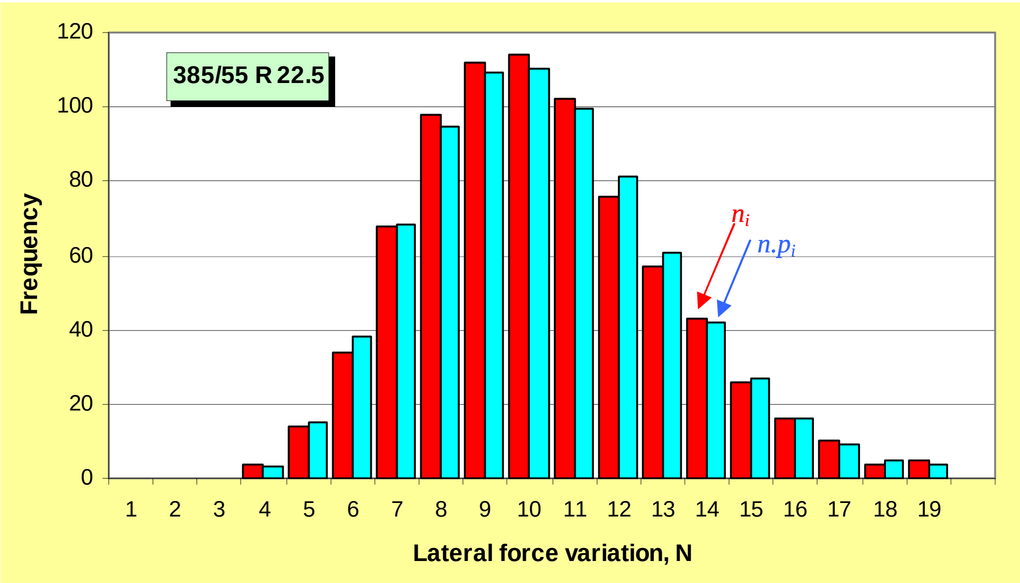

Figure 8.10 – Empirical and theoretical frequencies in a series of 786 tires 385/55R22.5.

•

Similar results were obtained also in other components of uniformity disturbances. E.g. Figure 8.11 presents the conicity.

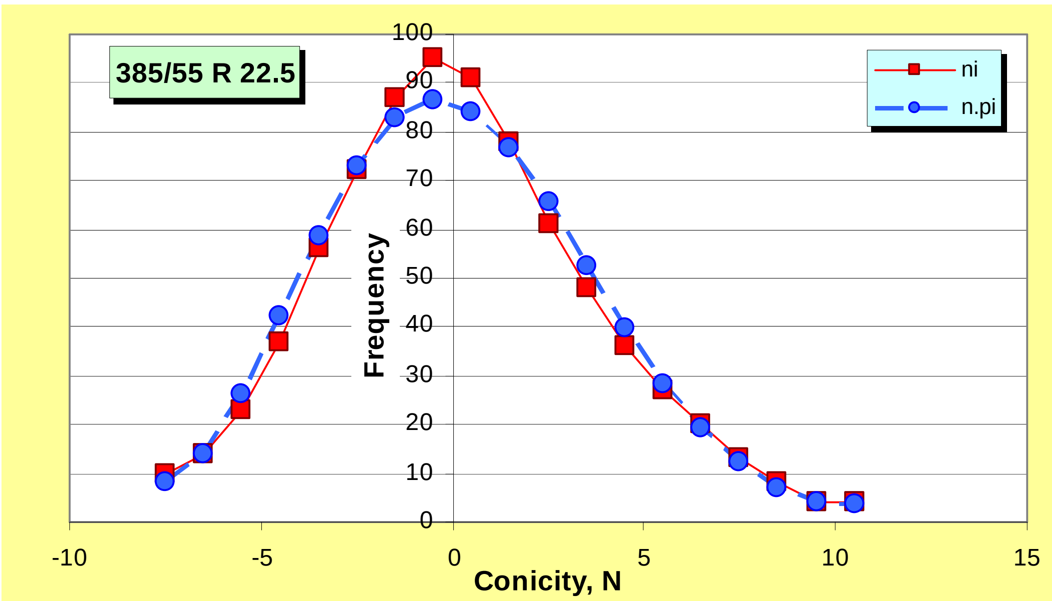

Figure 8.11 – Empirical n_i and theoretical np_i frequencies of conicity in a series of 786 tires 385/55R22.5.

The choice of probability distribution is free. Other distributions are suggested in [39], e.g. the double–branch normal distribution DN(b_1, b_2, b_3). Its density,

$$f_{DN}(x;\, b_1, b_2, b_3) = \begin{cases} \dfrac{\sqrt{2/\pi}}{b_2 + b_3} \exp\left[-\left(\dfrac{x-b_1}{b_2\sqrt{2}}\right)^2\right] & \text{for } x \le b_1 \\[2ex] \dfrac{\sqrt{2/\pi}}{b_2 + b_3} \exp\left[-\left(\dfrac{x-b_1}{b_3\sqrt{2}}\right)^2\right] & \text{for } x > b_1 \end{cases},$$

is positive in the whole real axis R^1. This, of course, contradicts the requirement of boundedness of measured quantities. The same fault appears in correspondingly generalized Weibull distribution that could be considered for some positive quantities.

The following Table presents ratios $X^2(\mathbf{b})/\ \chi^2_\alpha(K-1-p)$ for different probability distributions (p = 2 in normal distribution, p = 3 in D-normal distribution and p = 4 in beta distribution) and speaks in favor of beta distribution.

Tire size	*n*	*X*	*Normal d.*	*D-normal d.*	*Beta distr.*
385/55 R 22.5	786	RFV	1.020	**0.202**	**0.204**
		H1	**0.924**	**0.379**	**0.378**
		LFV	1.552	**0.140**	**0.104**
		CON	**0.539**	**0.128**	**0.193**
		PS	**0.410**	**0.529**	**0.354**
		TRO	**0.940**	**0.143**	**0.103**
		BRO	2.335	**0.058**	**0.183**
		RRO	**0.781**	**0.068**	**0.065**
385/65 R 22.5	1 842	RFV	3.880	**0.821**	**0.721**
		H1	2.568	**0.400**	**0.397**
		LFV	3.011	**0.532**	**0.373**
315/80 R 22.5	4 517	RFV	3.753	**0.860**	**0.438**
		H1	6.630	**0.486**	**0.247**
		LFV	6.500	**0.545**	**0.472**
295/80 R 22.5	4 273	RFV	5.541	**0.560**	**0.703**
		H1	7.078	**0.580**	**0.815**
		LFV	10.907	**0.931**	**0.738**
		CON	7.218	**0.975**	**0.449**
		TRO	8.048	**0.864**	**0.541**
		BRO	4.302	**0.754**	**0.281**
		RRO	7.605	**0.846**	**0.695**
295/80 R 22.5	4 022	RFV	2.383	**0.238**	**0.252**
		H1	2.825	**0.985**	**0.718**
		LFV	8924	**0.513**	**0.732**
		RRO	6.384	**0.515**	**0.770**
275/70 R 22.5	1 178	RFV	2.091	**0.328**	**0.284**
		H1	2.275	**0.921**	**0.370**
		LFV	3.023	**0.229**	**0.211**
		CON	**0.326**	**0.509**	**0.578**
		TRO	2.137	**0.251**	**0.348**
		BRO	3.501	**0.351**	**0.524**
		RRO	2.200	**0.261**	**0.338**
Sum of testing ratios			**121.611**	**15.902**	**13.579**

8.4 Correlation among Uniformity Components

Individual quantities registered in tire uniformity testing may appear independent or joined mutually. The correlation coefficient shows a quantitative evaluation of the dependence degree between two simple quantities. In vector quantities it is substituted by correlation matrix whose entries are the customary correlation coefficients [11].

Results of uniformity testing in a series of tires can be written as an $n\times m$ matrix, where n is the number of tires in the series and m is the number of measured quantities,

$$\mathbf{X} = \begin{pmatrix} x_{11} & x_{12} & \dots & x_{1m} \\ x_{21} & x_{22} & \dots & x_{2m} \\ \dots & \dots & \dots & \dots \\ x_{n-1,1} & x_{n-1,2} & \dots & x_{n-1,m} \\ x_{n,1} & x_{n,2} & \dots & x_{n,m} \end{pmatrix} = (\mathbf{x}_1, \dots, \mathbf{x}_m) .$$

Columns $\mathbf{x}_1, \dots, \mathbf{x}_m$ represent the measured quantities. The sample correlation coefficient of vectors $\mathbf{x}_j$, $\mathbf{x}_k$ is the number

$$r_{jk} = \frac{\sum_{i=1}^{n}(x_{ij}-\overline{x_j})(x_{ij}-\overline{x_k})}{\sqrt{\sum_{i=1}^{n}(x_{ij}-\overline{x_j})^2}\sqrt{\sum_{i=1}^{n}(x_{ij}-\overline{x_k})^2}} ,$$

where $\overline{x_j} = \frac{1}{n}\sum_{i=1}^{n} x_{ij}$, $\overline{x_k} = \frac{1}{n}\sum_{i=1}^{n} x_{ik}$ are the column averages. The numbers r_{jk} are entries of the $m\times m$ symmetric matrix $\mathbf{R}$. Obviously, $r_{jj} = 1$, $j = 1, \dots, m$. Critical value of the correlation coefficient for the n-dimensional vectors (n>2) and the significance level α is [11,54]

$$r_\alpha(n) = \left(1+\frac{n-2}{t_\alpha^2(n-2)}\right)^{-\frac{1}{2}} ,$$

where $t_\alpha(n–2)$ is the corresponding critical value of t-distribution.

Here is an example of the correlation matrix in a series of tires 385/55R22.5 in which eight components of uniformity were registered (n = 786, $r_{0.05}(784) = 0.06994$). Entries above the diagonal need to be written only, due to symmetry.

	H1	LFV	CON	PS	TRO	BRO	RRO
RFV	**0.9037**	0.0220	0.0577	-0.0108	-0.0183	0.0301	**0.8397**
H1		-0.0048	**0.0866**	0.0002	-0.0015	0.0166	**0.7687**
LFV			0.0136	0.0556	-0.0201	-0.0506	0.0528
CON				**-0.1316**	0.0196	**0.0722**	0.0699
PS					-0.0639	-0.0238	-0.0020
TRO						**0.1926**	-0.0309
BRO							0.0048

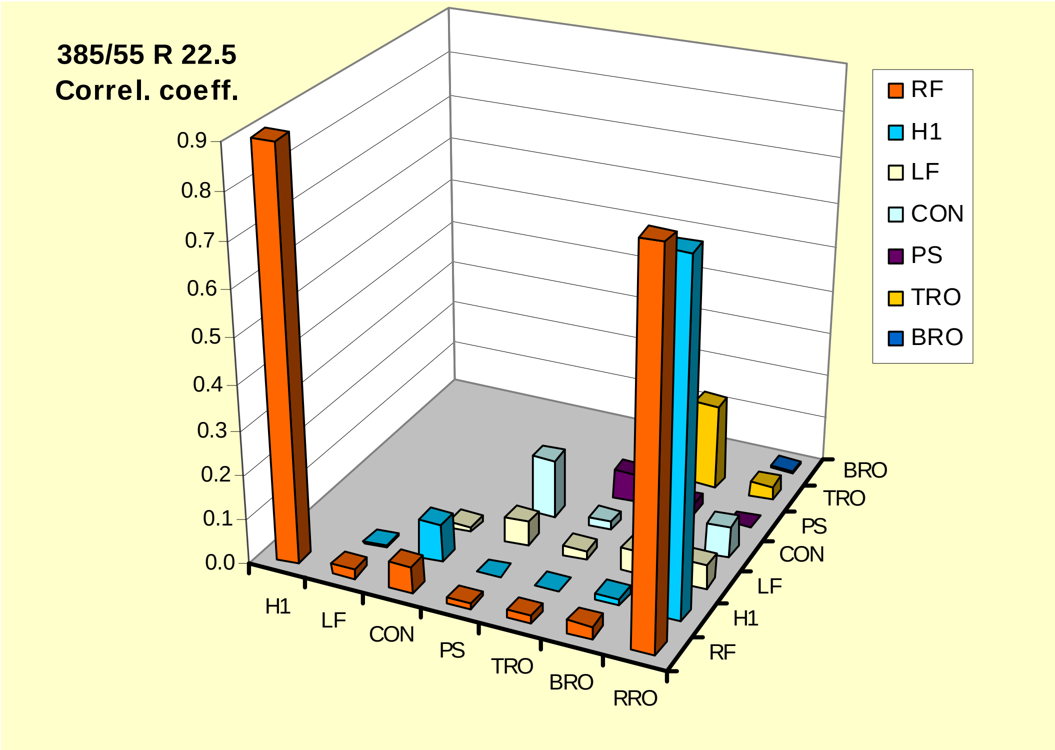

Figure 8.12 – Visualization of the above correlation matrix obtained in 786 tires 385/55R22.5.

The relationship between two components $\mathbf{x}_j$, $\mathbf{x}_k$ of uniformity may also be shown by graphical presentation of pairs (x_{ij}, x_{ik}) like in Figures 8.13, 8.14.

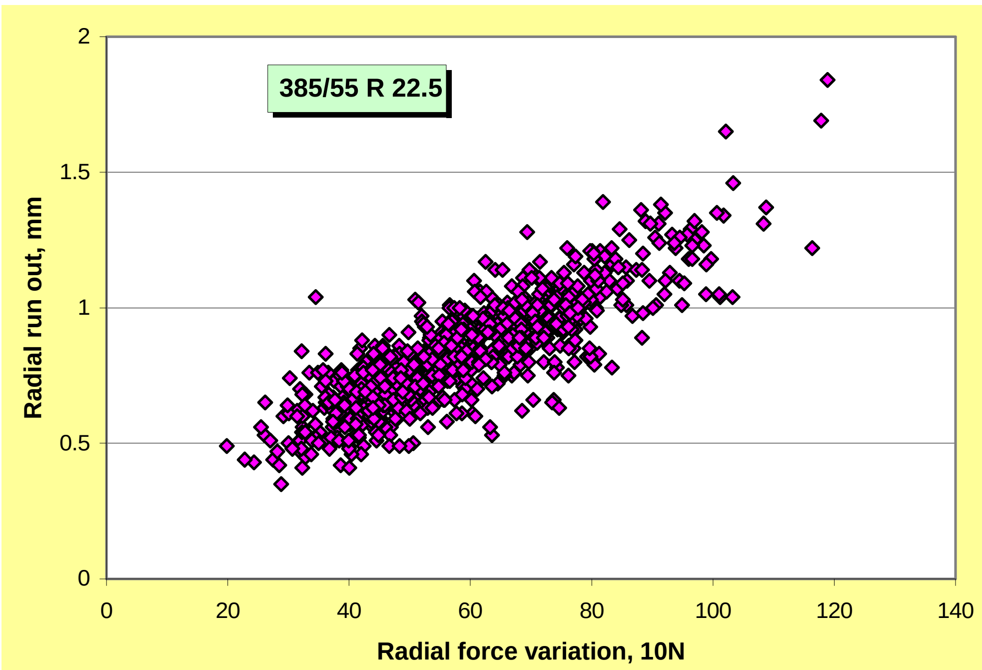

Figure 8.13 – Pairs of radial force variation and radial run out in 786 tires 385/55R22.5.

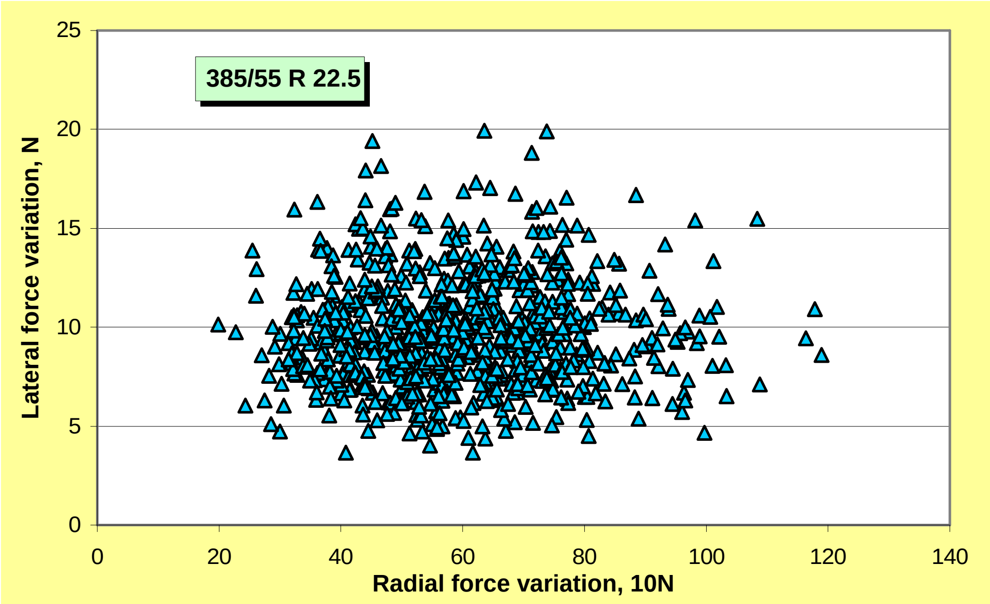

Figure 8.14 – Pairs of radial force variation and lateral force variation in 786 tires 385/55R22.5.

The correlation matrix shows that the significantly correlated components are joined to disturbances of radial uniformity, i.e. radial force variation, first harmonic, radial run out. In other uniformity characteristics the correlation is substantially weaker, even statistically non significant as a rule.

Similar results were obtained in many other truck and car tire series of different sizes [51,59,61].

8.5 High Speed Uniformity

In car tires higher speeds and smaller rolling radii must be taken into account. Very low aspect ratio and high centrifugal acceleration increase the total belt tension and the tire behavior might be expected a bit closer to that of stiff eccentric model [52].

In the mentioned work [52] general tending to circular (cylindrical) belt was experimentally shown on a radial tire whose belt consisted of two circumferential sections of very different stiffness. There are two consequences of it:

- the model of eccentric represents the first harmonic in radial uniformity disturbance and may be the first approximation in analysis of uniformity,
- higher harmonics can be assigned to imperfectly prepared parts, slicing, bead bundle placing in tire building and the following production steps.

Revolving the wheel round an eccentric axis is shown in Figure 8.15. There is a visible difference in the lengths of the upper and lower parts of the wave path of the axis of revolution. It necessarily produces acceleration and deceleration in the horizontal direction, thus, a periodic circumferential force.

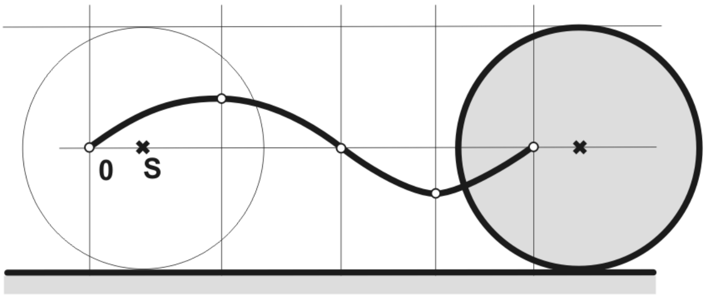

Figure 8.15 – Stiff cylindrical eccentric as the simplest model for radial uniformity disturbances.

Deformability and elasticity are inherent properties of tire reducing significantly negative consequences of radial uniformity disturbances. Their effect could be represented by diminishing the eccentricity, i.e. the distance between the geometric center S and the axis of revolution O in Figure 8.15.

Radial run out changes the rolling radius of the tire. Consequently, angular acceleration dω/dt is arisen, the same in the entire wheel. The mass m of the wheel produces the torque

$$M = \int_m r \frac{\mathrm{d}v}{\mathrm{d}t} \mathrm{d}m = \int_m r \frac{r\,\mathrm{d}\omega}{\mathrm{d}t} \mathrm{d}m = \frac{\mathrm{d}\omega}{\mathrm{d}t} \int_m r^2 \mathrm{d}m = J \frac{\mathrm{d}\omega}{\mathrm{d}t} ,$$

where J is the moment of inertia. The torque can be assigned to a circumferential force F_C (also called tangential force) acting on the arm equal to the wheel radius R, i.e.

$$M = RF_C .$$

The mass of the wheel is small in comparison to the total mass of vehicle. If no slip is supposed then the translational velocity of automobile is constant. This implies

$$0 = \frac{\mathrm{d}v}{\mathrm{d}t} = \frac{\mathrm{d}(\omega R)}{\mathrm{d}t} = R\frac{\mathrm{d}\omega}{\mathrm{d}t} + \omega\frac{\mathrm{d}R}{\mathrm{d}t}$$

and

$$\frac{\mathrm{d}\omega}{\mathrm{d}t} = -\frac{\omega}{R}\frac{\mathrm{d}R}{\mathrm{d}t} .$$

The rolling radius may be substituted by the initial part of its Fourier expansion [10]

$$R(\phi) = A\,(r_0 + \sum_{k=1}^{N} r_k \sin(k\phi + \phi_k)) ,$$

where $A \approx 1$, r_0 is the average rolling radius of tire, r_k and ϕ_k are amplitudes and phases of radial run out harmonics. Then

$$\frac{\mathrm{d}R(\phi)}{\mathrm{d}t} = \frac{\mathrm{d}R(\phi)}{\mathrm{d}\phi}\,\omega = A\omega \sum_{k=1}^{N} k r_k \cos(k\phi + \phi_k).$$

The circumferential force

$$F_C = \frac{M}{R} = \frac{J}{R}\left(-\frac{\omega}{R}\frac{\mathrm{d}R}{\mathrm{d}t}\right) = -A\frac{J}{R^2}\,\omega^2 \sum_{k=1}^{N} k r_k \cos(k\phi + \phi_k) \approx \frac{Jv^2}{R^4} \sum_{k=1}^{N} k r_k \cos(k\phi + \phi_k).$$

Thus, F_C is increasing with the square of velocity.

●

To illustrate the high speed uniformity two series of tires were chosen:

- 235/40R18 tires, $n = 518$ and
- 235/60R18 tires, $n = 1\,216$.

Main parameters of those tires are as follows:

Tire	*235/40R18*	*235/60R18*
Overall diameter, mm	645	739
Overall width, mm	241	240
Rim	8.5×18	7.5×18
Belt model parameters:		
Carcass equator radius R_A, mm	309.5	356.5
A half of carcass ´width´ W, mm	115.5	115.0
Carcass curvature radius in belt area R_{AN}, mm	3000.0	1000.0
Bead point radial coordinate r_B, mm	249.8	250.3
Bead point axial coordinate z_B, mm	104.4	92.3

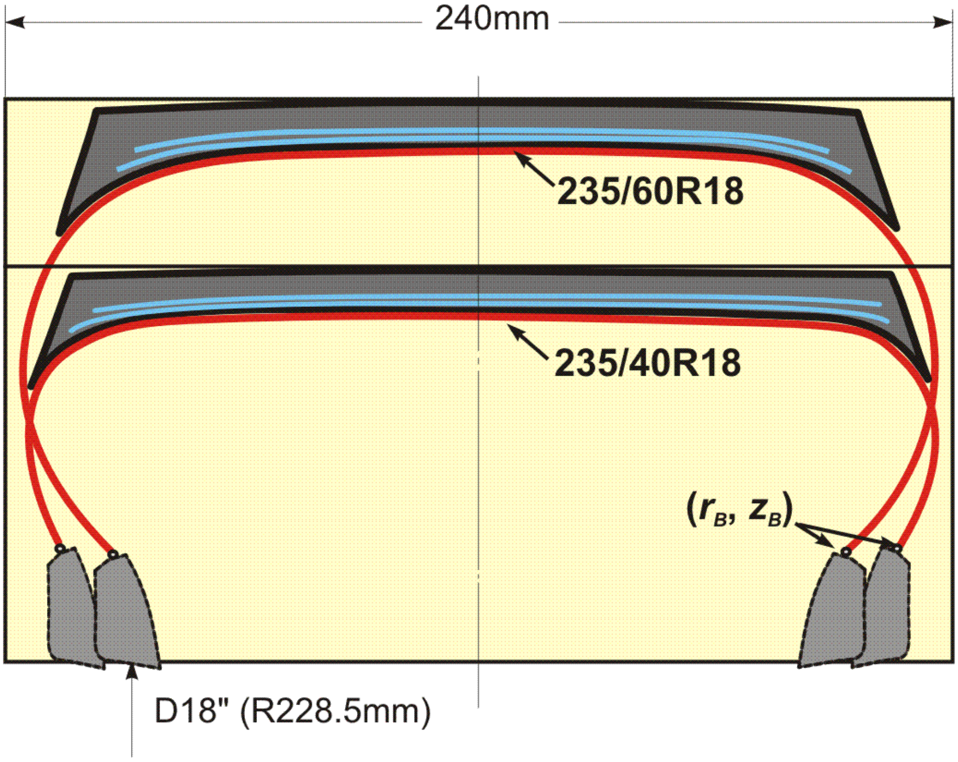

Figure 8.16 – Sketches of belt models for the 235/40R18 and 235/60R18 tires.

Distribution of low speed radial force variation is presented in Figure 8.17. Squares represent real frequencies n_i in total n tires, while continuous lines and small circles belong to Beta distribution and theoretical frequencies np_i.

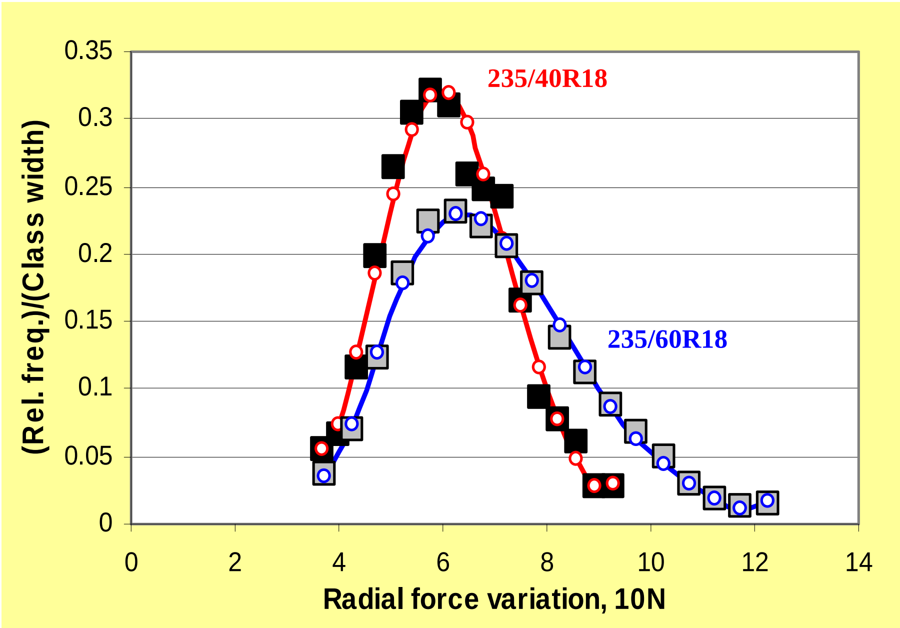

Figure 8.17 – Distribution of radial force variation in two series of car tires at low speed (v = 8km/h).

The distribution of uniformity disturbances is changed dramatically at high speeds. This is illustrated in the following two figures.

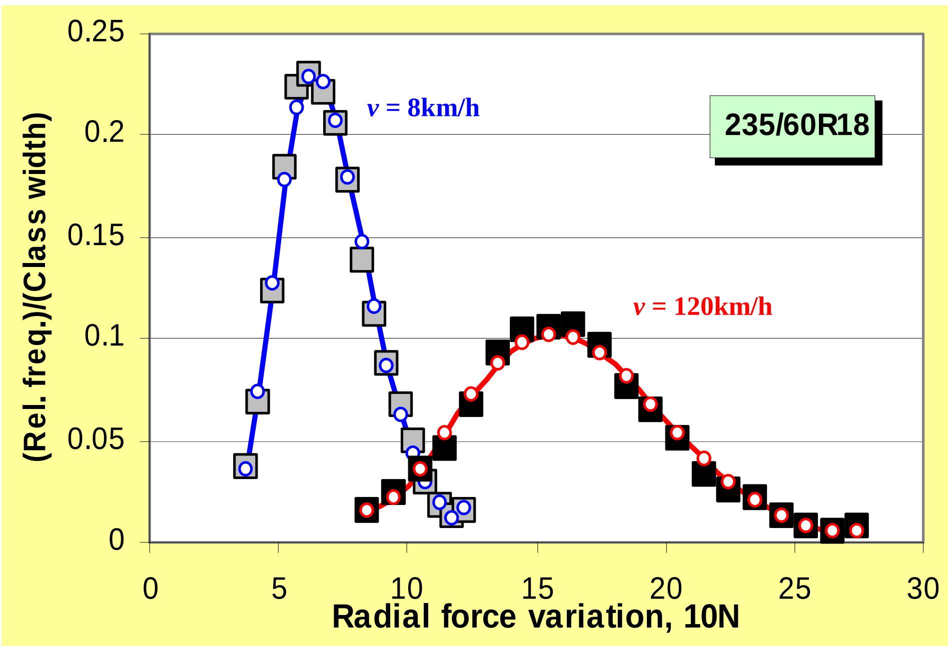

Figure 8.18 – Distribution of radial force variation in 235/60R18 tires at speeds 8km/h and 120km/h.

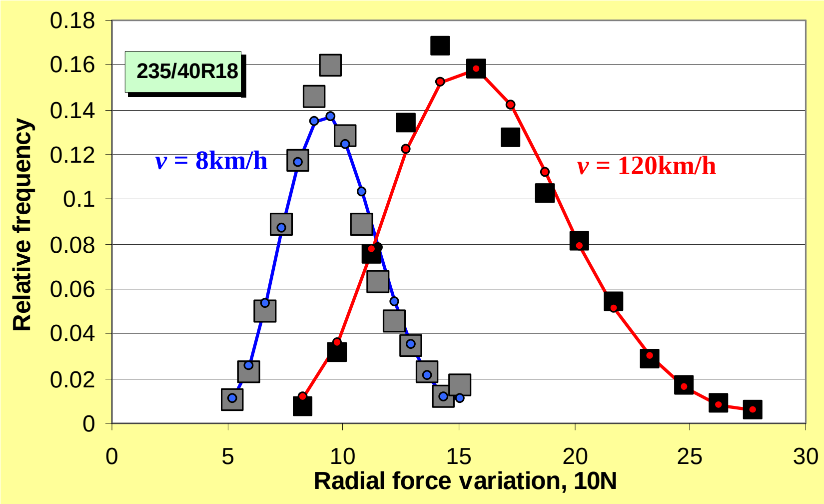

Figure 8.19 – Distribution of radial force variation in 235/40R18 tires at speeds 8km/h and 120km/h.

The influence of the changes of velocity on lateral force variability is shown in Figure 8.20.

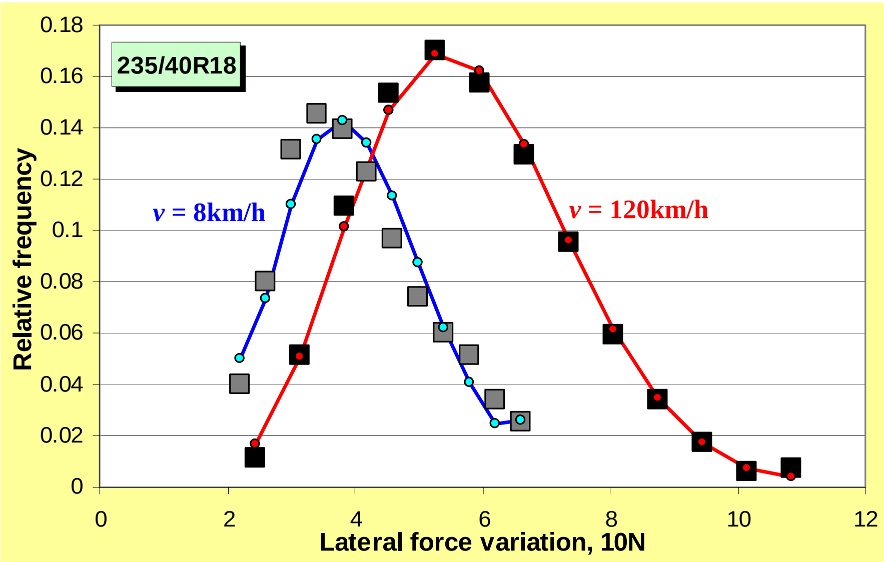

Figure 8.20 – Distribution of lateral force variation in 235/40R18 tires at speeds 8km/h and 120km/h.

It can be said generally that the correlations among different uniformity parameters (components) illustrated in Section 8.3 on several samples of truck tires preserve its validity also in car tires.

But high speeds give rise to the question concerning the relation between low speed parameters and high speed parameters. If the real tires behaved like a stiff eccentric there would be a very strong correlation between uniformity parameters at velocities v = 8km/h and v = 120km/h. The following figure shows, however, that the connection between radial force variations at low and high speeds can be unexpectedly weak.

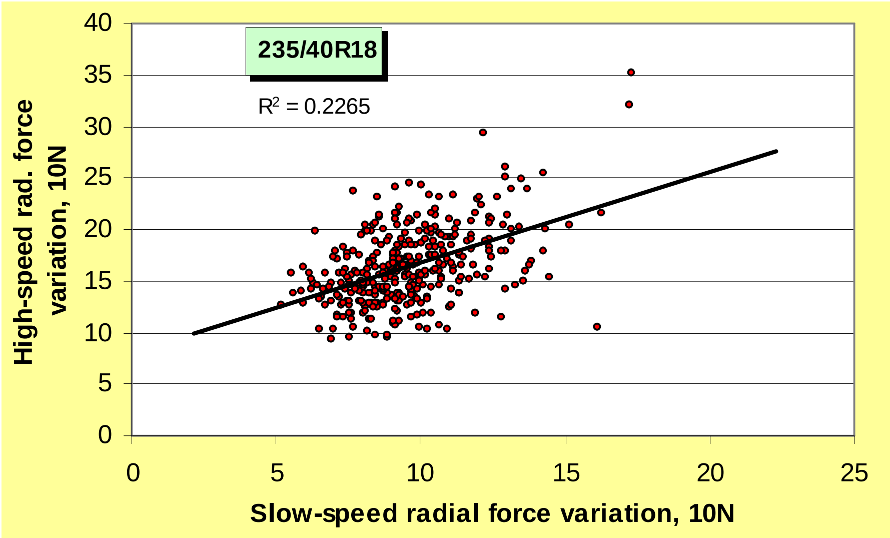

Figure 8.21 – Weak relationship between radial force variations at speeds of 8 and 120km/h.

This fact does not sound very encouragingly because tires perform regularly at high speeds while standard uniformity tests are performed at very low speeds. This way the value of standard low speed uniformity tests is reduced. It should also be taken into account that the shorter contact length on drum significantly diminishes the smoothing effect of contact area making the force uniformity tests more severe [51,60].

The model of stiff eccentric predicts a strong coupling of circumferential forces with radial run out at high speeds but this is not always true in real tires (Figure 8.22).

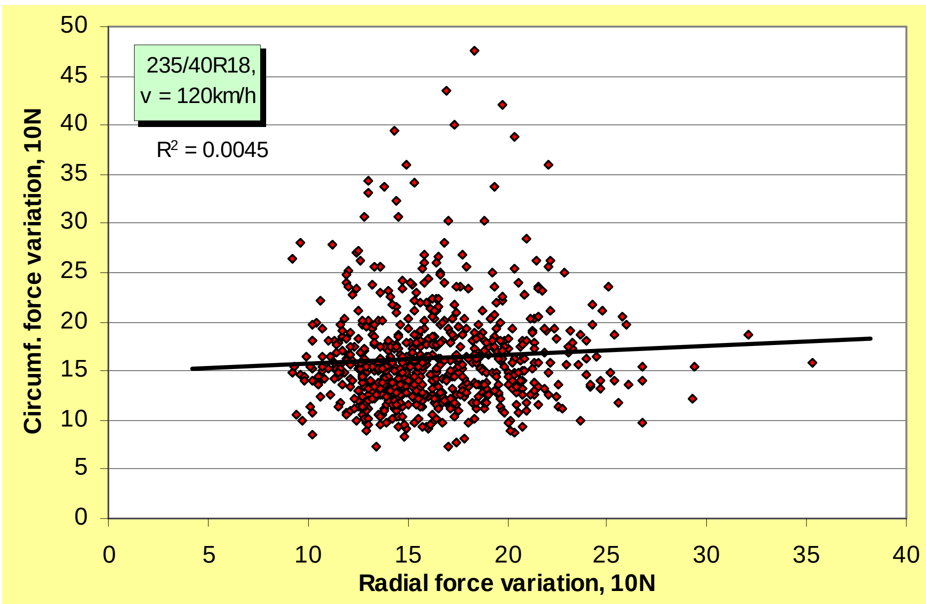

Figure 8.22 – Weak correlation between radial and circumferential force variations at 120km/h.

●

8.6 – Concluding remarks

Tire testing could be viewed as a comprehensive autonomous science that uses special tools of mechanics and thermodynamics, electronics, informatics, statistics. The inherent variability of almost all parameters and characteristics of tire contribute significantly to the complexity of mathematical modeling of tire behavior. The following Figures 8.23 and 8.24 show examples of radial force and run out variance in a new tire and the same tire after its rolling on the roadwheel for several hours.

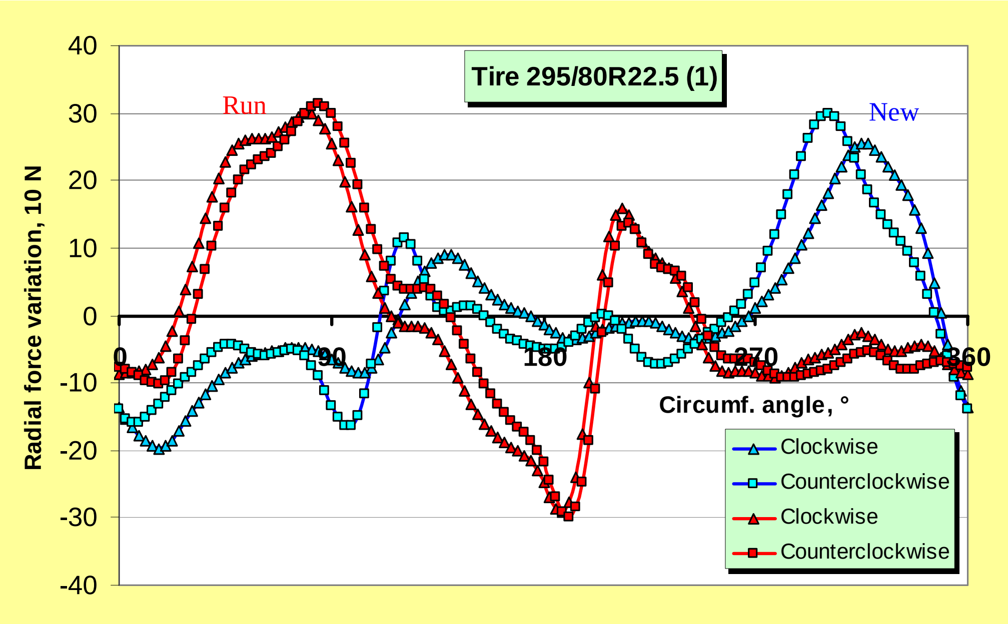

Figure 8.23 – Change of radial force variation due to several hours of rolling the loaded tire on the roadwheel.

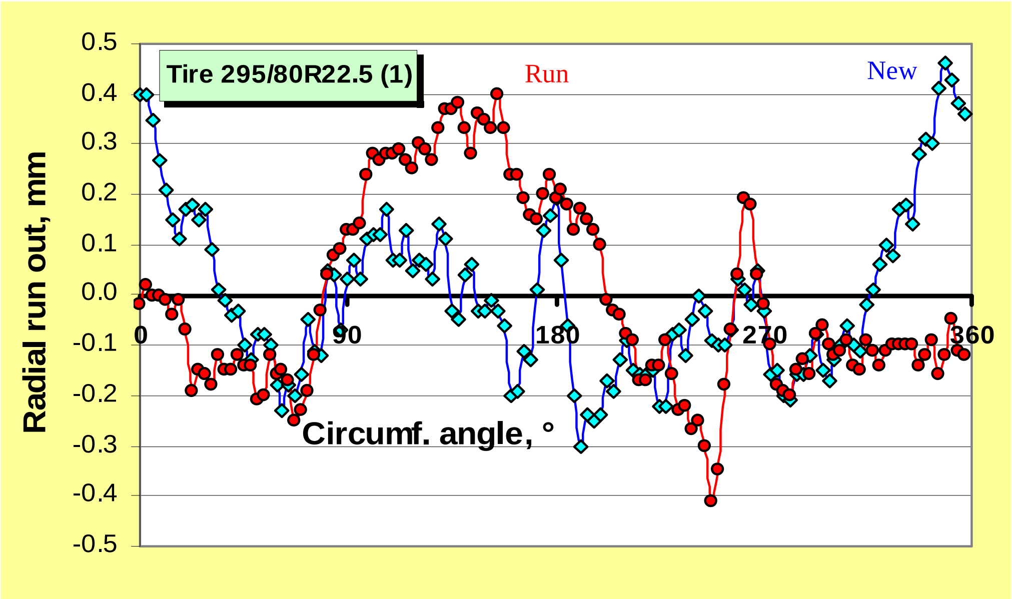

Figure 8.24 – Change of radial run out due to several hours of rolling the loaded tire on the roadwheel.

Similar variability can be found in high-speed uniformity. With another series of the 235/40R18 tires a high degree of correlation was obtained (Figure 8.25).

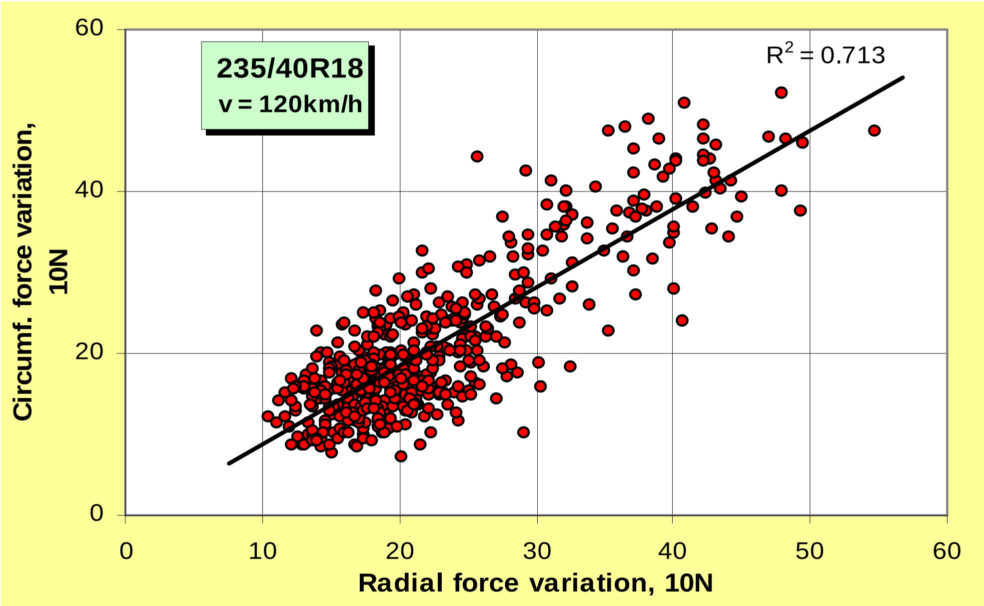

Figure 8.25 – Correlation between radial and circumferential force variations at 120km/h in another series of the 235/40R18 tires.

Thus, results and conclusions obtained by processing measured data samples are always obtained only within some statistical confidence.

Generally, the tire uniformity, especially the high speed uniformity, still remains an open and challenging theme.

P

9 SUPPLEMENTARY THEMES

9.1 Hydroplaning

Hydroplaning is slipping the tire on the layer of water at high speeds similar to ice skating or skiing. In slips on the ice or snow a thin layer of water arises due to contact pressure and friction and the skate, ski, etc. moves almost without any resistance on that lubricating layer. A similar behavior can occur in tire on flooded road in torrential rain.

The older literature says that critical speed, i.e. the speed at which the friction on the tire/road interface drops practically to zero, is proportional to the square root of the average contact pressure. This, however, is a too general conclusion.

Recently many attempts were made to model the hydroplaning directly as a problem of hydrodynamics using modern numerical methods of flow mechanics. Several decades ago H. Bathelt published a simple model based on sinking a plate into water layer [62].

We popularized and simplified his approach in the simplest case of the rectangular plate sinking in the ideal incompressible fluid [63].

●

The descent of a rectangular plate is sketched in Figure 9.1. The potential energy of compressed liquid equals the work of the external vertical load F when the plate sinks from the height $h_0 = h(0)$ to $h(t)$, i.e.

$$W(t) = F(h_0 - h(t)) \ .$$

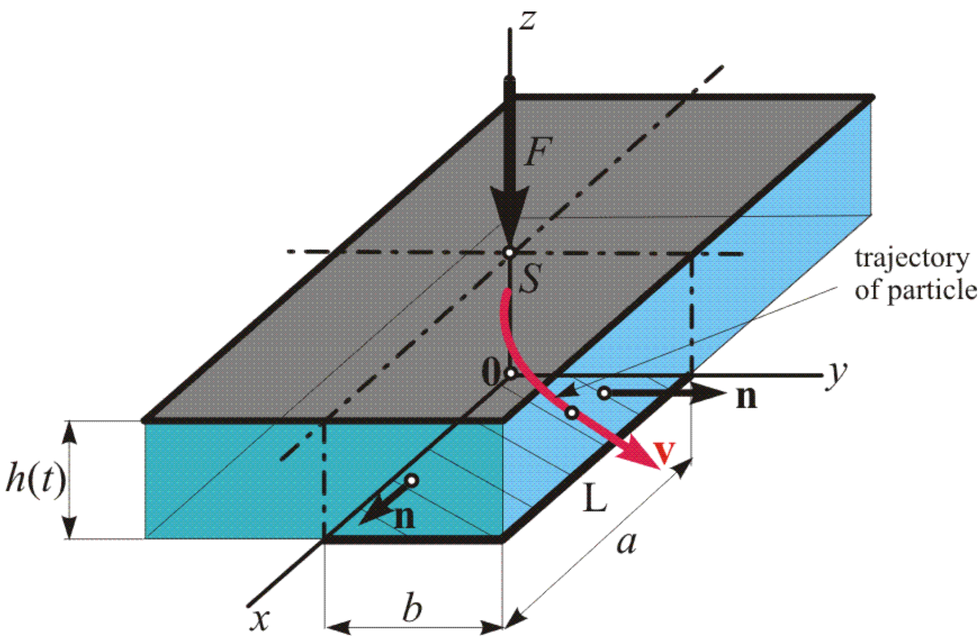

Figure 9.1 – Descent of a rectangular plate in water layer.

The kinetic energy of incompressible liquid (ρ = const) in the volume V between the plate R = $[-a, a]\times[-b, b]$ and the ground (Figure 9.1) is the sum

$$T(t) = \frac{\rho}{2}\Big[\int\limits_{V(t)} v^2\,\mathrm{dV} + \int\limits_0^t \int\limits_{\partial V(t)} v^2\,\mathbf{v.n}\,\mathrm{dS}\Big]$$

$$= \frac{\rho}{2}\Big[\int\limits_0^{h(t)} \Big(\int\limits_{-a}^{a}\int\limits_{-b}^{b} v^2\,\mathrm{d}x\,\mathrm{d}y\Big)\,\mathrm{d}z + \int\limits_0^t \Big(\int\limits_0^{h(t)} \Big(4\int\limits_L v^2\,\mathbf{v.n}\,\mathrm{d}s\Big)\,\mathrm{d}z\Big)\,\mathrm{d}t\Big],$$

where $\mathbf{v}$ denotes the instant velocity of liquid particle, $\mathbf{n}$ is the unit normal vector of the surface ∂V and $\mathbf{v.n}$ is scalar product. Let the flow in the volume V be potential and the instant velocity of liquid particles be assumed independent of the vertical coordinate z. Then the components of velocity can be supposed to be

$$v_x(x, y, z, t) = f_x(t)\,x,$$
$$v_y(x, y, z, t) = f_y(t)\,y.$$

where the time functions f_x, f_y are arbitrary, thus, they can be chosen so that

$$f_x(0) = f_y(0) = 0,$$
$$f_x(t) + f_y(t) = -\frac{1}{h(t)}\frac{\mathrm{d}h(t)}{\mathrm{d}t}.$$

Then

$$\int\limits_{-a}^{a}\int\limits_{-b}^{b} v^2\,\mathrm{d}x\,\mathrm{d}y = \int\limits_{-a}^{a}\Big(\int\limits_{-b}^{b} (f_x^2 x^2 + f_y^2 y^2)\,\mathrm{d}y\Big)\,\mathrm{d}x = \frac{2ab}{3}(a^2 f_x^2 + b^2 f_y^2),$$

$$\int\limits_L v^2\,\mathbf{v.n}\,\mathrm{d}s = \int\limits_0^a (f_x^2 x^2 + f_y^2 y^2)\,f_y\,b\,\mathrm{d}x + \int\limits_0^b (f_x^2 x^2 + f_y^2 y^2)\,f_x\,a\,\mathrm{d}y$$

$$= \frac{ab}{3}(f_x^2 f_y a^2 + 3 f_y^3 b^2 + 3 f_x^3 a^2 + f_x f_y^2 b^2)$$

and

$$T(t) = \frac{2ab\rho}{3}\Big[h(t)(a^2 f_x^2 + b^2 f_y^2) + \int\limits_0^t h\,(f_x^2 f_y a^2 + 3 f_y^3 b^2 + 3 f_x^3 a^2 + f_x f_y^2 b^2)\,\mathrm{d}t\Big].$$

The law of conservation of energy yields $T(t) = W(t)$, i.e. $\dfrac{\mathrm{d}T(t)}{\mathrm{d}t} = \dfrac{\mathrm{d}W(t)}{\mathrm{d}t}$. After substitution of the corresponding expressions one obtains

$$\frac{2ab\rho}{3}\Big[\frac{\mathrm{d}h(t)}{\mathrm{d}t}(a^2 f_x^2 + b^2 f_y^2) + 2h(t)\Big(a^2 f_x \frac{\mathrm{d}f_x(t)}{\mathrm{d}t} + b^2 f_y \frac{\mathrm{d}f_y(t)}{\mathrm{d}t}\Big)$$
$$+ h(t)(f_x^2 f_y a^2 + 3 f_y^3 b^2 + 3 f_x^3 a^2 + f_x f_y^2 b^2)\Big] = -F\frac{\mathrm{d}h(t)}{\mathrm{d}t}.$$

Division by $h(t)$, substitution $\dfrac{1}{h(t)}\dfrac{\mathrm{d}h(t)}{\mathrm{d}t} = -(f_x(t) + f_y(t))$, introducing $p_m = \dfrac{F}{4ab}$ as an average pressure and several simple arrangements give

$$2\,f_x\left(\frac{\mathrm{d}f_x/\mathrm{d}t}{b^2}+\frac{f_x^2}{b^2}-\frac{3p_m}{\rho a^2b^2}\right)+2\,f_y\left(\frac{\mathrm{d}f_y/\mathrm{d}t}{a^2}+\frac{f_y^2}{a^2}-\frac{3p_m}{\rho a^2b^2}\right)=0\,.$$

Since the functions $f_x(t)$, $f_y(t)$ are considered independent, the expressions in parentheses must vanish. This leads to the following two simple differential equations

$$\frac{\mathrm{d}\,f_x(t)}{\mathrm{d}t}+f_x^2(t)=\frac{3p_m}{\rho a^2}=A^2>0,$$

$$\frac{\mathrm{d}\,f_y(t)}{\mathrm{d}t}+f_y^2(t)=\frac{3p_m}{\rho b^2}=B^2>0$$

of the same type

$$\frac{\mathrm{d}y}{\mathrm{d}t}+y^2=C^2.$$

The solution of the last equation for the initial condition $y(0) = 0$ is as follows

$$t=\frac{1}{2C}\ln\frac{C+y}{C-y}\quad\text{or}\quad y(t)=C\frac{\mathrm{e}^{2Ct}-1}{\mathrm{e}^{2Ct}+1}=C\frac{\mathrm{e}^{Ct}-\mathrm{e}^{-Ct}}{\mathrm{e}^{Ct}+\mathrm{e}^{-Ct}}=C\tanh Ct\,.$$

Therefore,

$$f_x(t)=\sqrt{\frac{3p_m}{\rho a^2}}\tanh\left(t\sqrt{\frac{3p_m}{\rho a^2}}\right),\qquad f_y(t)=\sqrt{\frac{3p_m}{\rho b^2}}\tanh\left(t\sqrt{\frac{3p_m}{\rho b^2}}\right).$$

Then

$$\frac{1}{h(t)}\frac{\mathrm{d}h(t)}{\mathrm{d}t}=\frac{\mathrm{d}\ln h(t)}{\mathrm{d}t}=-\left(f_x(t)+f_y(t)\right)$$

$$=-\sqrt{\frac{3p_m}{\rho a^2}}\tanh\left(t\sqrt{\frac{3p_m}{\rho a^2}}\right)-\sqrt{\frac{3p_m}{\rho b^2}}\tanh\left(t\sqrt{\frac{3p_m}{\rho b^2}}\right),$$

which can be integrated very easily

$$-\ln\frac{h_0}{h(t)}=-\left[\ln\cosh\left(t\sqrt{\frac{3p_m}{\rho a^2}}\right)+\ln\cosh\left(t\sqrt{\frac{3p_m}{\rho b^2}}\right)\right].$$

Hence,

$$\boxed{h(t)=\frac{h_0}{\cosh\left(\frac{t}{a}\sqrt{\frac{3p_m}{\rho}}\right)\cosh\left(\frac{t}{b}\sqrt{\frac{3p_m}{\rho}}\right)}}\,. \tag{9.1}$$

The time t_s needed for the plate descent from h_0 to h_1, $t_s = h^{-1}(h_0)$, is found by numerical solution of the equation

$$h(t) = h_1.$$

●

The slick tire or the tire with completely worn pattern behaves like the sinking plate whose base is equal to the contact patch. The contact area in radial tires is rectangular approximately (Figure 5.9). The supporting road surface has ever some roughness $h_R > 0$ that is added to the initial water layer height h_0 (Figure 9.2). The time needed for descent from $h_R + h_0$ to h_R is $t_s = h^{-1}(h_R)$. If v_{tr} is the translation velocity of the wheel and L_P the contact length, then in case $t_s < L_P/v_{tr}$ the tread reaches the road asperities and a "dry" contact still exists. If $t_s \geq L_P/v_{tr}$ the tire slips on the water film with almost zero friction. This phenomenon is called hydroplaning. The critical speed is

$$v_{crit} = \frac{L_P}{t_s}.$$

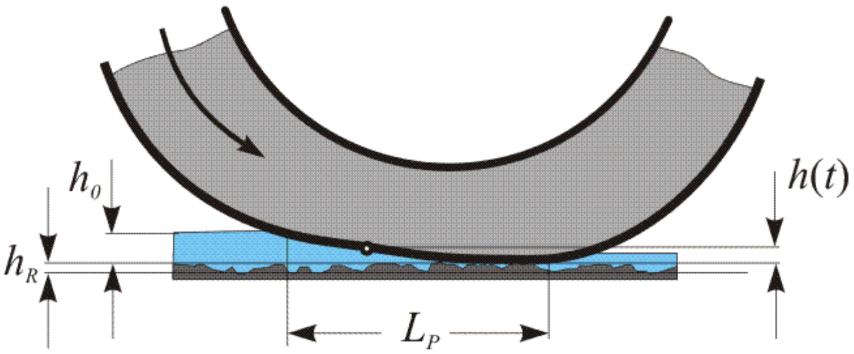

Figure 9.2 – Descent of the tire in water layer on rough road.

In tires without tread pattern the time t_s is relatively long and v_{crit} is low. Let us consider some slick variants from the Tables 6.4.1 and 6.4.2 shown in Figure 6.8. Their vertical load is $F_R = 5.884$kN. Corresponding results are shown in Figure 9.3.

Tread pattern increases the critical speed in dependence on groove cross-section and depths h_G. In smooth tread ($h_G = 0$) the function $h(t)$ is also smooth (differentiable). When the grooved tread sinks the grooves are filled with water first. Then, in the second stage, the tire sinks like the rectangular plate while the open grooves take part in draining water out of contact area.

If ψ is the ratio of the real contact area to the whole area insides its external rectangular contour then the volume occupied by grooves is $L_P \times W_P \times (1-\psi) \times h_G$ approximately. Thus, the uniformly patterned plate sinks in the first stage like a smaller tread block plate from $h_0 + h_R$ onto the level $h_P = h_0 + h_R - (1-\psi) \times h_G$. When $h_P < 0$ and therefore $h_0 < (1-\psi) \times h_G - h_R$, the entire water layer is "absorbed" in tread pattern and the danger of hydroplaning would arise only in extremely high speeds (Figure 9.4). As soon as the grooves are flooded the second stage of tire descent starts, in which the tread pattern drains off water through open grooves. The depth $(1-\psi) \times h_G$ is simply added to the road roughness and the time t_s is determined by attaining the level of

h_R + $(1-\psi)\times h_G$. There must some time elapse to turn the local flow around individual tread blocks into the flow in the global contact area.

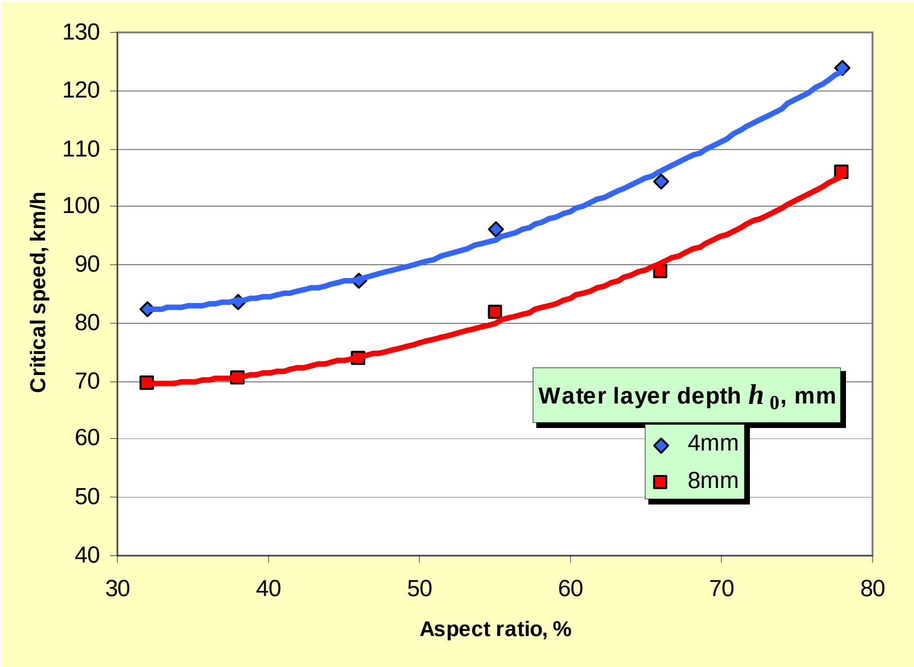

Figure 9.3 – Critical speeds for slick variants of the Section 6.4 in water layers of 4 and 8mm. The road roughness h_R = 0.8mm, tire inflation pressure 250kPa, vertical load 5884N

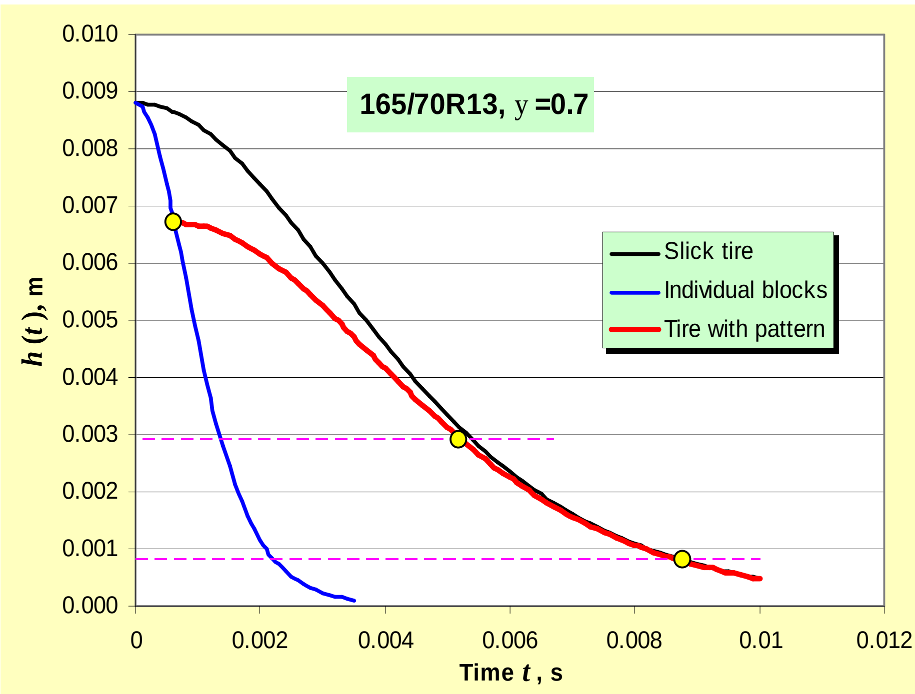

Figure 9.4 – Time needed to contact the road asperities. The water layer h_0=8mm; the 165/70R13 tire.

The impact of tread pattern grooves on the critical speed $v_{crit} = L_P/t_s$ is shown in more detailed way in Figure 9.5.

The formula (9.1) for $h(t)$ reflects the influence of liquid density too. As the rain starts, the dust on highway turns into mud which has higher density than water. Figure 9.5 shows on a slick tire that the time needed for tire/road contact is increased and, consequently, the critical speed may decrease substantially.

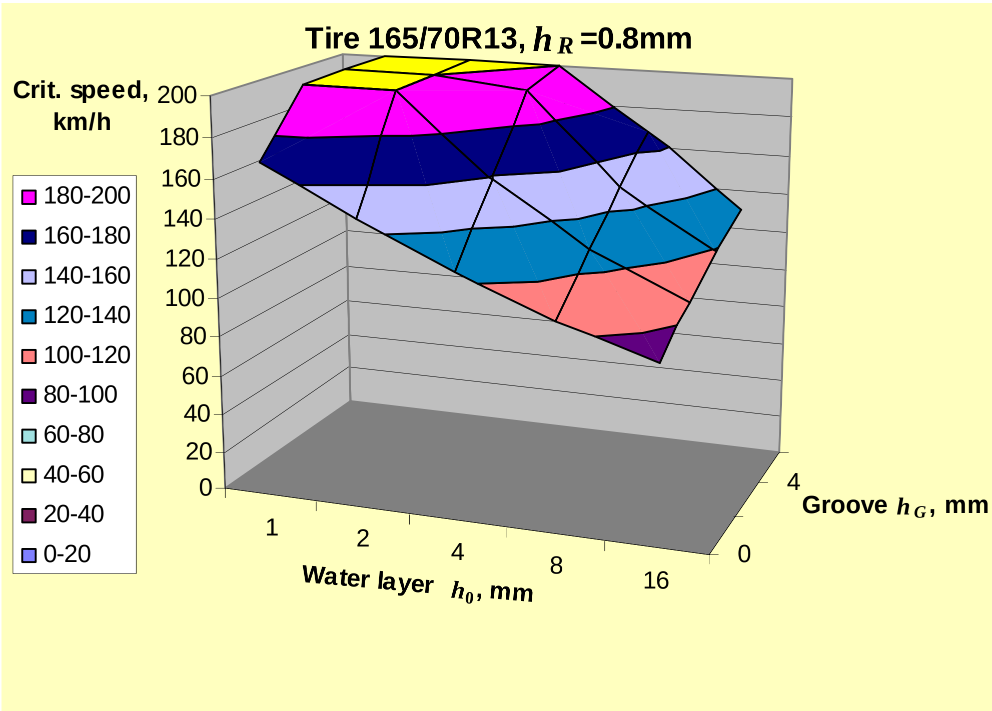

Figure 9.5 – Critical speeds for the 165/70R13 tire. Conditions p = 200kPa, *F*=3.15kN, ψ=0.7.

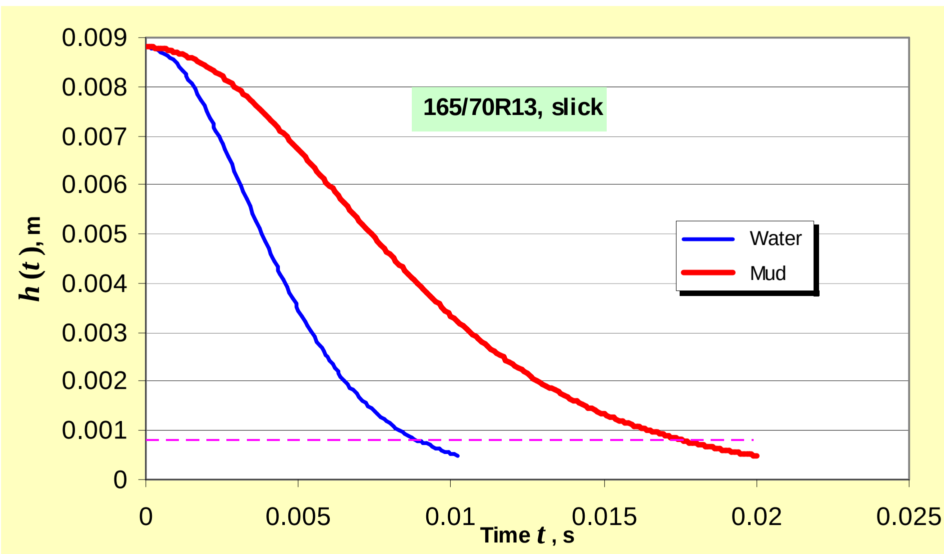

Figure 9.6 – Time needed to contact the road asperities; p = 200kPa, *F*=3.15kN.
Mud is assumed to have 4times higher density than water.

Remark. The model shown here operates with the ideal liquid and is just a static one. Therefore, it must be taken as a qualitative approximation or a vivid illustration only. Bathelt considered viscose liquid too [62]. Tire wet traction solved by Reynolds equation used in the theory of bearings (μ = coefficient of dynamic viscosity)

$$\frac{\partial^2 p}{\partial x^2} + \frac{\partial^2 p}{\partial y^2} = \frac{12\mu}{h^3}\,\frac{\mathrm{d}h}{\mathrm{d}t}$$

was published in [5]. It is obvious, however, that static models must stay far beyond reality. To describe the movement of tire running in the water layer requires methods of flow dynamics and adequate numerical means.

9.2 Stochastic Model for Tread Wear

The most significant factors in tire wear are: the sum of tangential slips and the local temperature (friction) in the tire/road interface. Both of them are closely associated with instant meteorological conditions on the road.

The simplest way to ascertain the reduction of the tread thickness is to measure the groove depth y. Let x be the total distance run in a regular wear test when vehicles run the same course repeatedly to maintain the tangential forces and slips on the same level approximately.

Wear rate

$$\frac{\mathrm{d}y}{\mathrm{d}x}$$

depends on friction conditions in contact area and on mobility of tread figures as well. In a simplified way the influence of both those factors may be assumed separated as follows

$$\frac{\mathrm{d}y}{\mathrm{d}x} = -\,a\,f(x)\,g(y)\,,$$

where $a > 0$ is a constant, f is an integrable function and g is an increasing continuous function, $g(y) > d > 0$. The physical meaning of x, y implies that $x, y \geq 0$.

If (x_0, y_0) denotes the initial point, $y(x_0) = y_0$, and

$$F(x) = \int_0^x f(u)du, \quad G(y) = \int_0^y \frac{du}{g(u)},$$

the integration of the above differential equation yields

$$G(y) - G(y_0) = -\,a\,[F(x) - F(x_0)\,]\,.$$

The solution $y(x)$ can be written as follows

$$y(x) = G^{-1}\,\{\mathrm{G}(y_0) - a\,[F(x) - F(x_0)]\}\,.$$

Obviously, the tangential mobility of tread pattern blocks or ribs increases with y increasing. Hence, g should be a non-decreasing function. If y is reduced slanted groove walls increase the tread pattern stiffness as well as the real tire/road contact interface. The simplest choice of g is then a polynomial of the second degree. Moreover, it must be expected that g tends to a constant if y is small, thus

$$\frac{d^2 g(0)}{dy^2} = 0 .$$

Then $g(y) = b_0 + by^2$, $b \geq 0$. Let it be simply put $b_0 = 1$, i.e.

$$g(y) = 1 + by^2 .$$

Substituting this in the above equations gives

$$G(y) = \int_0^y \frac{du}{1+(\sqrt{b}\,u)^2} = \frac{1}{\sqrt{b}} \arctan(\sqrt{b}\,y) \quad \text{for} \quad b > 0,$$

$$G(y) = y \quad \text{for} \quad b = 0$$

and

$$y(x; a, b) = \begin{cases} \dfrac{1}{\sqrt{b}} \tan\left\{\arctan(\sqrt{b}\,y_0) - a\sqrt{b}\,[F(x) - F(x_0)]\right\} & b > 0 \\ & \text{for} \\ y_0 - a[F(x) - F(x_0)] & b = 0 \end{cases} .$$

The function F is connected with the external conditions, especially those of weather. Its choice is a more delicate matter.

Temperature and humidity are the most obvious characteristics of weather. Analysis of meteorological data records unveiled a considerable correlation between relative humidity and temperature of the air (in the Middle Europe area at least [64]). Both the quantities may be decomposed into periodic components determined by the instant position of the Earth on its orbit around the Sun and the stochastic ones, which can be considered to be normally distributed [11]. Autocorrelation functions showed that the stochastic component u at the sampling period of a day may be considered as a Markov process (autoregressive process AR(1))

$$u(k) = q\,u(k-1) + e(k), \qquad 0 < q < 1, \quad k = 1, 2, \ldots$$

The random quantity e belongs to the normal distribution, $e \in \mathrm{N}(0, (1 - q^2) \operatorname{var} u)$ [11].

Using the process u for determining the values $F(x)$ requires a convenient choice of its parameters. Data analysis led to values

$$q = 0.78, \qquad s_u \approx \sqrt{\operatorname{var} u} \approx 0.19.$$

If v is the average distance run each day,

$$v = \frac{x}{N} ,$$

then

$$\operatorname{var} \left|F(x) - F(x_0)\right| = v^2 \operatorname{var} \sum_{i=1}^{N} u(i) ,$$

where N is the number of steps (days). It can be shown [64] that

$$\operatorname{var}\left|F(x)-F(x_0)\right| \;=\; \operatorname{var} u \;\frac{v^2}{(1-q)^2}\left[N(1-q^2)-2q(1-q^N)\right],$$

i.e. the variance is an increasing function of N.

The relation

$$\left|F(x)-F(x_0)-\int_{t_0}^{t_0+N} f(u)\,du\right| \;=\; 1.96\,\sqrt{\operatorname{var}\left|F(x)-F(x_0)\right|}\;,$$

can be used in modeling the wear process. Here $1.96 = u_{0.975}$ is the critical value of normal distribution on the significance level of 0.05 [11]. The function f representing the weather (temperature) is [64]

$$f(t) \;=\; 1-0.14\cos\left(\frac{2\pi t}{365.24}+0.019\right) \;+\; u(\operatorname{trunc}(t))\,,$$

where trunc(t) denotes the entire part of t (e.g. trunc(π) = 3).

Summarized up, the function y depends on two parameters a, b. But there is an obstacle in finding their estimates by regression: heteroscedasticity. On the other hand the minimization of the sum of equal powers of residuals is always a well defined problem and its solution may be found using direct methods [10].

In praxis tread wear tests are performed on homogenous sets of tires mounted with designed exchanges in a vehicle convoy that runs along a constant route. The depths of pattern grooves are measured and recorded periodically. This way a data set

$$\{(x_i, y_{ij}) : i = 1, \ldots, N;\, j = 1, .., J_i\}$$

is obtained, where N is the number of distances at which the measurement was performed and J_i is the number of tires in ith measurement (J_i is usually the same for all i, nevertheless also the possibility of tire failure needs to be respected).

Let

$$S(a, b; p) \;=\; \sum_{i=1}^{N} w_i \sum_{j=1}^{J_i}\left|y(x_i;a,b)-y_{ij}\right|^p ,$$

where $p > 0$ and w_i are weights that shall express the importance of ith measurement, e.g.

$$w_i = \left(\frac{x_i}{x_N}\right)^r, \quad r > 0,$$

to emphasize the last ones.

The function S may be geometrically interpreted as a distance of the measurement point ($y_{11}, \ldots, y_{1J_1}, \ldots, y_{N1}, \ldots, y_{NJ_1}$) from the hypersurface

$$\mathrm{H} = \{y(x_k;\, a, b) : k = 1, \ldots, J_1, J_1{+}1, \ldots, J_1{+}J_2, \ldots, J_1{+} \ldots {+}J_{N-1}, \ldots, n;\; -\infty < a, b < \infty\}$$

in the Euclidean space R^n, where $n = \sum_{i=1}^{N} J_i$ is the total number of measurements [9,64,65]. Direct search methods have proved to be most reliable for finding the parameters a, b.

Example. In a specific tread wear test in car tires 165/70R13 run from late November to early January of the next year the following data set was obtained in one of several tread pattern and tread profile variants.

Measurement index i	Distance x_i, 1000km	Minimum groove depth y_{ij}, mm	
0	0.00	7.05	7.09
1	4.05	5.57	5.43
2	8.80	4.80	4.46
3	12.16	3.98	3.65
4	16.21	3.37	3.12

The exponents were chosen $p = r = 1$, i.e. the weights were $w_i = x_i/x_N$. The corresponding computer code yielded $a = 0.13188 \pm 0.10945$, $b = 0.04438 \pm 0.06758$, the coefficient of determination $R^2 = 0.948$ and the adequacy of the model was confirmed by the F-test ($F = SSR/SSE = 2.029 < 6.39 = F_{0.95}(2, 4)$). Modeling the tread wear with contribution of the Markov process $u(k)$ characterized through parameter $q = 0.78$ and $u \in \mathrm{N}(0, 0.19^2)$ including the confidence limits is shown in Figure 9.7. The confidence limits for the significance level $\alpha = 0.05$ [11] are drawn as dotted lines. For the minimum groove depth $y_{min} = 1.6$mm one obtains the predicted tread life

$$23\,300\text{km} < x_{1.6} < 30\,700\text{km}.$$

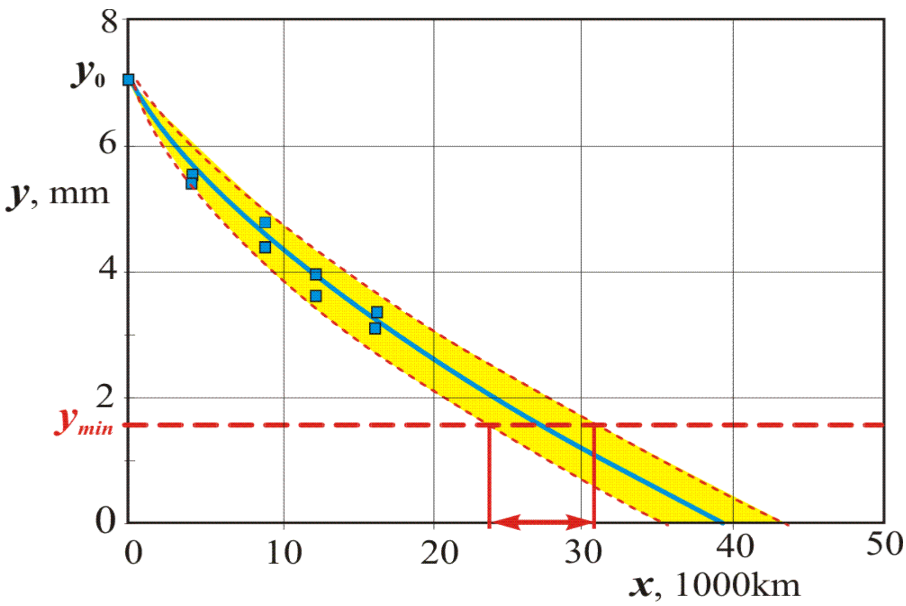

Figure 9.7 – Tread wear modeling in two 165/70R13 tires made with a special tread variant.

Comparison of the model prediction vs. experimental results, discussion on seasonality influence, suggestions for simplifications and other details can be found in [64].

9.3 Experiments in Cord/Rubber Composite Stiffness

In the first stage of research rectangular test pieces were prepared of rubberized steel cord and vulcanized in laboratory presses. They could be made with various angles, widths and ply numbers. When they were strained they changed their cross-section profile, the relationship between their elongation and the corresponding tensile force was nonlinear and there were problems to define their stiffness [66,67]. Changes of width were mentioned in Section 3.3 and are visualized in Figure 9.8.

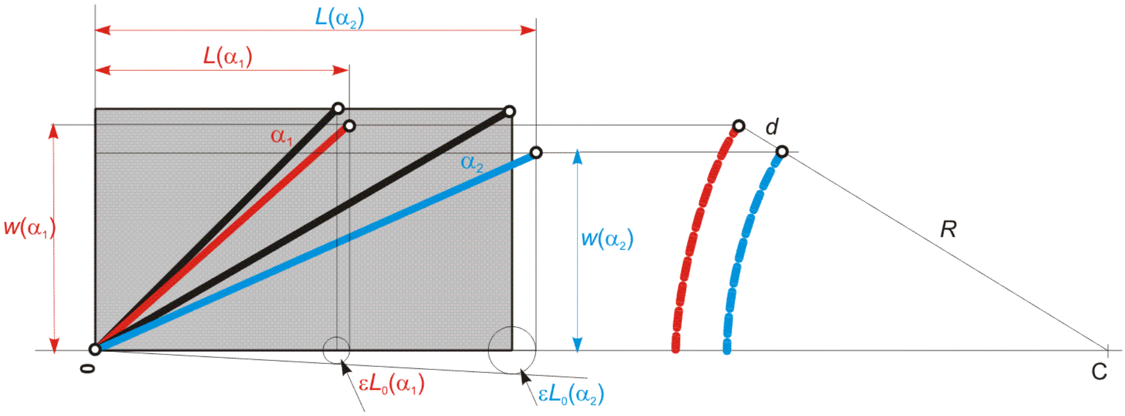

Figure 9.8 – Cross-section bending in two layer cord/rubber composite with different cord angles.

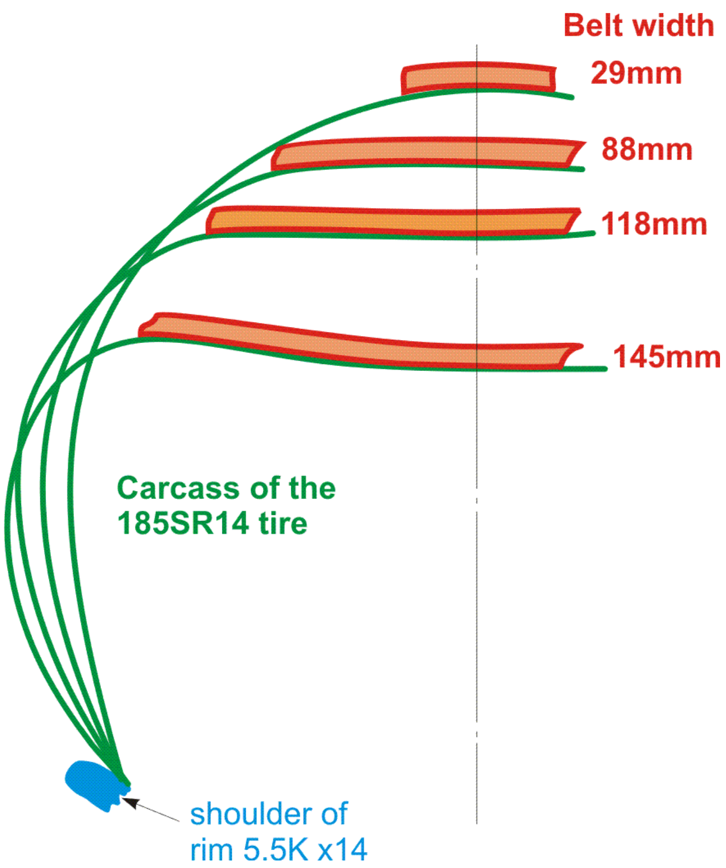

Figure 9.9 – Meridian curves of the same radial carcass surface with various belt radii and widths.

To avoid problems with clamping test pieces in jaws of tensile testing machines an especially prepared carcass of the 185/65R14 tire was used to strain the cylindrical belts. The belt widths were computed as the contact zone widths between belt and radial carcass for different belt radii [68]. The cross-sections of different belt combinations with the carcass of the 185SR14 tire are shown in Figure 9.9.

The belt stiffness in the circumferential direction is

$$K = \frac{T(\varepsilon)}{\varepsilon},$$

where $\varepsilon = \Delta C/C$ is the belt strain due to carcass inflation, C is belt circumference and ΔC is the increase of circumference caused by the belt tension $T(\varepsilon)$. The belt stiffness increases with the belt width nonlinearly (Figure 9.10). It might be a broken line.

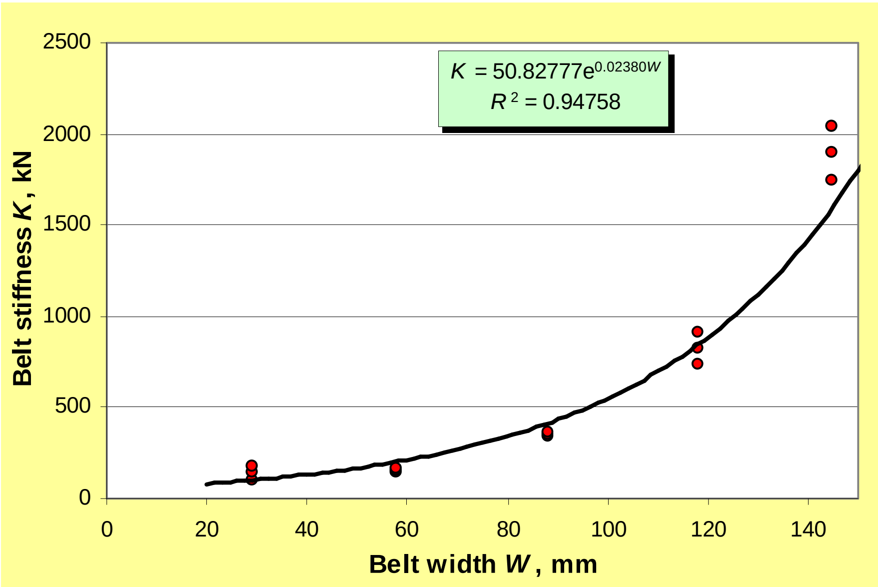

Figure 9.10 – Nonlinear dependence of belt stiffness on belt width.

9.4 Cord Bending

The radial carcass cords are exposed to periodic tension and bending wave during each revolution of loaded tire. This is important especially in steel cords because their internal friction may produce wear of primary filaments (fretting). As shown in work [69] this problem becomes relevant when sidewall meridional length is decreased. The producers of steel cord are developing new cord constructions and steel composition to reduce internal cord wear. Concerning cord bending cords with smaller diameters and, consequently, increased numbers of carcass cords are preferable.

P

REFERENCES

Note: All papers published in Plasty a kaučuk *are in Czech*.

[1] TOMKINS, E.: "The History of the Pneumatic Tyre". Eastland Press, London *1981*.

[2] HOFFERBERTH, W., "Zur Statik des Luftreifens", Kautschuk u. Gummi, **9**, *1956*, S. 225.

[3] BIDERMAN, V. L. in: "Trudy NIIŠP", sb. 3, Moscow *1957*.

[4] FRANK, F. – HOFFERBERTH, W., Rubber Chemistry and Technology, **40**, *1967*, p. 271.

[5] BIDERMAN, V. L. – BUKHIN, B. L. et al.: "Mechanics of Pneumatic Tires I" (Russian), Moscow *1974*.

[6] BUKHIN, B. L. et al.: "Mechanics of Pneumatic Tires II" (Russian), Moscow *1976*.

[7] "Mechanics of Pneumatic Tires", editor S. K. CLARK, U.S. Government Printing Office, Washington, D. C. *1981*.

[8] GENT, A. N. – WALTER, J. D. et al.: "The Pneumatic Tire". NHTSA Washington *2005*.

[9] www.koutny-math.com (Courses | Mathematical Base for Applications).

[10] www.koutny-math.com (Courses | Numerical Methods & Fourier Analysis).

[11] www.koutny-math.com (Courses | Prelude to Probability and Statistics).

[12] KOUTNY, F., "A Method for Computing the Radial Deformation Characteristics of Radial Tires", Tire Science and Technology, **4**, *1976*, p. 190.

[13] RHYNE, T. B., Tire Science and Technology, **33**, *2005*, pp. 136-155.

[14] MEISSNER, B. – ZILVAR, V.: "Physics of Polymers". SNTL, Prague *1987*.

[15] KOUTNÝ, F. – KUSÁK, K., "Nonlinearity of Rubber Shear Strain ", Yearbook VÚGPT ´82, *1982*, p. 46.

[16] KOUTNÝ, F. – KUSÁK, K., "On Small Strains in Rubber", Plasty a kaučuk, **21**, *1984*, p. 296.

[17] KOUTNÝ, F. – SYCHA, A., "Notes on Radial Tires Rubber Proprieties ", Plasty a kaučuk, **25**, *1988*, p. 292.

[18] KOUTNÝ, F., "Viscoelastic Properties of Nylon Cords", Plasty a kaučuk, **27**, *1990*, p. 139.

[19] KOUTNÝ, F., "Water-Filled Tire", Plasty a kaučuk, **19**, *1982*, p. 311.

[20] KOUTNÝ, F., "Simpson's Formula in Computing Building Drum Width", Plasty a kaučuk, **3**, *1966*, p. 208.

[21] LEIBEE, J. B. – SCHAFFERS, W. J., "A New Tire Expansion Rule and its Use in Tire Design Computations", Rubber Chemistry and Technology, **42**, *1969*, p. 1079.

[22] KOUTNY, F., "Mathematische Untersuchung der Beziehungen zwischen den Konfektionsgrößen eines Autoreifens I", Plaste u. Kautschuk, **14**, *1967*, S. 327.

[23] KOUTNY, F., " Mathematische Analyse der Beziehungen zwischen den Konfektionsgrößen von Kraftfahrzeugen II", Plaste u. Kautschuk, **16**, *1969*, S. 353.

[24] KOUTNY, F.: "Air Volume Energy Method in Theory of Tires". International Polymer Science and Technology, **5**, *1978*, No. 8/T100.

[25] BIDERMAN, V. L. et al.: "Atlas of Pneumatic Tires Equilibrium Shapes Nomographs". Moscow *1967*.

[26] KOUTNY, F., "Meridian des aufgepumpten Reifens I", Plaste u. Kautschuk, **18**, *1971*, S. 282.

[27] KOUTNY, F., "Meridian des aufgepumpten Reifens II", Plaste u. Kautschuk, **18**, *1971*, S. 680.

[28] KOUTNY, F., "Mathematical Methods in the Theory of Tires"(Czech), Plastikářský bulletin, *1976*, p. 165.

[29] KOUTNÝ, F., "Calculations for Cross-Ply Tires I ", International Polymer Science and Technology, **9**, *1982*, No. 5/T65.

[30] KOUTNY, F., "Calculations for Cross-Ply Tires II ", International Polymer Science and Technology, **9**, *1982*, No. 2/T67.

[31] FRANK, F. - ELLIS, J.R.: A.S.A.E. Report No. 2, September *1966*.

[32] www.tufo.com

[33] KOUTNÝ, F., "Pneumatic Toroidal Springs" (Czech), Strojnícky časopis, **33**, *1982*, p. 477.

[34] KOUTNY, F., "Über die Druckexpansion der Radialkarkasse beim Aufbau", Kautschuk + Gummi, Kunststoffe, **35**, *1982*, S. 501

[35] KOUTNÝ, F., "Geometry of a Cordless Tire ", Plasty a kaučuk, **8**, *1971*, p. 110.

[36] JANDIK, M. – KOUTNY, F., "Nomograms for Equilibrium Profiles of Radial Tyres", International Polymer Science and Technology, **1**, *1974*, No. 5/T75.

[37] KOUTNY, F., "Static Calculations of Radial Tires", Plasty a kaučuk, **10**, *1973*, p. 360.

[38] KOUTNÝ, F., "Static Belt Tension in Belted Tires", Plasty a kaučuk, **8**, *1971*, p. 365.

[39] www.koutny-math.com (Miscellany | Strength).

[40] ODSTRČIL, J. – KOUTNÝ, F.: Introductory Study to Tire Vibrations" (Czech). VÚGPT Report No. 695. Zlín *1968*.

[41] KOUTNÝ, F., "Elastic Behavior of Car Tires. Measurement of Radial Stiffness" (Czech). VÚGPT Report No. 813/6, Zlín *1969*.

[42] KOUTNY, F., "Load-Deflection Curves for Radial Tyres", Applied Mathematical Modelling, *5*, *1981*, p. 422.

[43] KOUTNY, F., "Cornering radial tyres", Applied Mathematical Modelling, **7**, *1983*, p. 139.

[44] BRDIČKA, M. – HLADÍK, A.: "Theoretical Mechanics". Academia, Prague *1987*.

[45] GREGUŠ, M. – ŠVEC, M. – ŠEDA, V.: "Ordinary Differential Equations" (Slovak), ALFA Bratislava *1985*.

[46] ZIKA, V. – KOUTNY, F., "Use of Fourier Analysis for Designing Tyre Treads", International Polymer Science and Technology, *15*, 1988, No. 3, T/50.

[47] LANDAU, L. D. – LIFSHITZ, E. M.: "Theory of Elasticity. Theoretical Physics VII" (Russian). Moscow *1965*.

[48] WESTERMANN, S. – PETRY, F. – THIELEN, G.: "Impact of Fundamental Contact Mechanics on Development ", Tire Technology International, The Annual Review *2004*, p. 68.

[49] FEYNMAN, R., P. – LEIGHTON, R. B. – SANDS, M.: The Feynman Lectures on Physics (Chapter 12). Addison-Wesley, *1966*.

[50] KOUTNÝ, F., "On Dynamic Behavior of Radial Tires", Plasty a kaučuk, 32, *1995*, p. 262.

[51] LÁZNIČKA, L., "Construction and Properties of Radial Tires" (Czech), PhD Thesis, UTB Zlin, *2007*.

[52] KOUTNY, F., "Analytical Comments on Radial Tires Nonuniformity ", Tire Science and Technology, **24**, *1996*, pp. 132-152.

[53] KOUTNY, F., "Gürtelreifengeometrie und ihre Konsequenzen", Kautschuk + Gummi, Kunststoffe, **31**, *1978*, S. 156.

[54] ANDĚL, J., "Foundations of Mathematical Statistics," (in Czech) SNTL Prague *1978*.

[55] LÁZNIČKA, L. – KOUTNÝ, F., "Rolling Resistance in Truck Tires", Plasty a kaučuk, **41**, *2004/No 11-12*, p. 11.

[56] KOUTNÝ, F., "Impact of Inflation Pressure and Load on Rolling Resistance of Radial Tires ", Plasty a kaučuk, **34**, *1997*, p. 4.

[57] LÁZNIČKA, L. – KOUTNÝ, F., "Pneumatic Tire as a Vertical Dynamic Element in Vehicle", Plasty a kaučuk, **42**, *2005/No 3-4*, p. 8.

[58] KOUTNY, F., "Stochastic Elements in the Carcass of a Radial Tyre", International Polymer Science and Technology, **6**, *1979*, No. 5, T/69.

[59] KOUTNÝ, F., "Statistical Analysis of some Disturbances of Tire Uniformity ", Plasty a kaučuk, **16**, *1979*, s. 243.

[60] KOUTNÝ, F. – LÁZNIČKA, L., "On Radial Uniformity of Tires ", Plasty a kaučuk, **42**, *2005/No 7-8*, p. 6.

[61] KOUTNÝ, F. – LÁZNIČKA, L., "Quasistatic Uniformity of Tires – Distribution and Correlation", Plasty a kaučuk, **42**, *2005/No 9-1*, p. 8.

[62] BATHELT, H., Zeitschrift für angewandte Mathematik und Mechanik, **53**, *1973*, S. 675.

[63] KOUTNY, F. – ZATLOUKAL, A., "Aquaplaning", International Polymer Science and Technology, **3**, *1976*, No. 10, T/92.

[64] KOUTNY, F., "A Model for Tire Wear", Rubber Chemistry and Technology, **64**, *1991*, p. 683.

[65] KOUTNÝ, F. – ČEVELÍK, R., "Nonlinear Regression in Physical Analyses of Polymers", Plasty a kaučuk, **26**, *1990*, p. 367.

[66] KOUTNÝ, F., "Circumferential Stiffness of Tire Belts", Plasty a kaučuk, **10**, *1973*, p. 109.

[67] KOUTNY, F. – SINDELAR, M., "Experimental Study of the Stiffness of the Cord- reinforced Rubber", International Polymer Science and Technology, **3**, *1976*, No. 10, T/92.

[68] KOUTNY, F. – SYCHA, A. – MATUCHA, P., "Experimental Study of the Circumferential Stiffness of Tyre Belts", International Polymer Science and Technology, **6**, *1979*, No. 8, T/42.

[69] KOUTNY, F., "Bending Stress in the Cord of Radial-ply Tyres", International Polymer Science and Technology, **2**, *1975*, No. 12, T/7.

INDEX